Louisiana Transportation Research Center

Final Report 651

Finite Element Analysis of the Lateral Load Test on Battered Pile Group at I-10 Twin Span Bridge

by

Murad Y. Abu-Farsakh
Ahmad Souri
Mohsen Amirmojahedi

LTRC

4101 Gourrier Avenue | Baton Rouge, Louisiana 70808
(225) 767-9131 | (225) 767-9108 fax | www.ltrc.lsu.edu

TECHNICAL REPORT STANDARD PAGE

1. Title and Subtitle
Finite Element Analysis of the Lateral Load Test on Battered Pile Group at I-10 Twin Span Bridge

2. Author(s)
Murad Y. Abu-Farsakh, Ahmad Souri, and Mohsen Amirmojahedi

3. Performing Organization Name and Address
Louisiana Transportation Research Center
4101 Gourrier Avenue
Baton Rouge, LA 70808

4. Sponsoring Agency Name and Address
Louisiana Department of Transportation and Development
P.O. Box 94245
Baton Rouge, LA 70804-9245

5. Report No.
FHWA/LA.17/651

6. Report Date
November 2021

7. Performing Organization Code
LTRC Project Number: 13-3GT
SIO Number: DOTLT1000103

8. Type of Report and Period Covered
Final Report
Mar 2016 – Feb 2021

9. No. of Pages
236

10. Supplementary Notes
Conducted in Cooperation with the U.S. Department of Transportation, Federal Highway Administration

11. Distribution Statement
Unrestricted. This document is available through the National Technical Information Service, Springfield, VA 21161.

12. Key Words
Lateral behavior of piles, numerical analysis, battered pile, pile group, p-y curve, soil-pile interaction

13. Abstract
The design of pile foundations to resist lateral loads is essential in offshore structures and bridge foundations. The lateral behavior of piles has been studied in the past by experimental investigations coupled with analytical and numerical methods. The problem is complex due to the nonlinearities from soil behavior, gap formation, and pile-soil-pile interaction in pile groups (or the group effect). In this work, the finite element (FE) modeling was used to study the lateral behavior of pile groups. The FE method is robust and allows incorporating the necessary aspects for studying the behavior of pile groups. The nonlinear material behavior was incorporated using nonlinear constitutive models. The pile-soil interface was modeled using the zero-thickness surface-surface interaction, which provided the capability for modeling the gap behind the piles, and the transfer of interface normal and frictional stresses. The group interaction was facilitated through the interaction of stress fields around the piles, and by the continuity of the FE mesh.

The lateral behavior of three pile group (PG) configurations (vertical, battered, and mixed) with a similar number of piles were evaluated under static and dynamic loading. In the static analysis, the case study of the M19 pier foundation field test was used to verify the FE models. A parametric investigation for the effect of pile spacing and clay soil type was performed. The results showed that the lateral stiffness of the battered and mixed PGs was significantly higher than the vertical PG (+120%, +50%, respectively). The lateral load was found unevenly distributed among the piles in all PGs, and the exterior piles carried 1.5-2% higher load than the interior piles. The influence of the group effect vanished at pile spacings greater than 5D (D is pile width). Also, the influence of pile spacing was more prominent along the load direction. In the dynamic analysis, the PGs behavior was evaluated in barge impact simulations. The results showed that the battered and mixed PGs had similar and large lateral stiffness, which resulted in limited pile cap displacement and large deformation in the barge bow. The weak lateral stiffness of the vertical PG allowed the development of significantly larger impact force and pile cap displacement compared to the battered and mixed PG.

3D FE numerical analyses and parametric studies were also performed to develop models to evaluate the p-y curves for clayey and sandy soils using tangent hyperbolic models based on soil and pile properties. Regression analyses were performed on results of parametric study to develop formulas for evaluating the ultimate lateral bearing capacity factor (N_p) and reference displacement of p-y curve (y_{50}) in clay soils. A combination of tangent hyperbolic and power function model was developed to evaluate the p-y curves in sand soils based soil and pile properties. These p-y curve models can be effectively implemented into any FE pile design software such as FB-MultiPier, LPILE, Midas, CSIBridge, and SAP2000.

Results of laboratory UU tests were used to develop correlations to estimate the strain at 50% stress level (ε_{50}) based on soil properties (i.e., S_u, PI, LI). The comparison between the models' values and measurements are somehow reasonable. In addition, the results of FE parametric study for p-y curve in sand were analyzed to develop a formula to estimate the coefficient of subgrade reaction (k) based on soil and pile properties. For simplification, the estimation of k for different sand consistency, soil condition, and friction angle were presented in a table and a figure. The results of k values are comparable with the values recommended by FHWA.

Project Review Committee

Each research project will have an advisory committee appointed by the LTRC Director. The Project Review Committee is responsible for assisting the LTRC Administrator or Manager in the development of acceptable research problem statements, requests for proposals, review of research proposals, oversight of approved research projects, and implementation of findings.

LTRC appreciates the dedication of the following Project Review Committee Members in guiding this research study to fruition.

LTRC Administrator/Manager

Zhongjie "Doc" Zhang, Ph.D., P.E.
Pavement and Geotechnical Research Manager

Members

Zheng Fu, Kelly Kemp, Xuyong Wang, Jesse Rauser,
Miranda Perkins, and Arturo Aguirre

Directorate Implementation Sponsor

Christopher P. Knotts, P.E.
DOTD Chief Engineer

Finite Element Analysis of the Lateral Load Test on Battered Pile Group at I-10 Twin Span Bridge

By
Murad Y. Abu-Farsakh,
Ahmad Souri, and Mohsen Amirmojahedi

Louisiana Transportation Research Center
4101 Gourrier Avenue
Baton Rouge, LA 70808

LTRC Project No. 13-3GT
SIO No. DOTLT1000103

conducted for

Louisiana Department of Transportation and Development
Louisiana Transportation Research Center

November 2021

Abstract

The design of pile foundations to resist lateral loads is essential in offshore structures and bridge foundations. The lateral behavior of piles has been studied in the past by experimental investigations coupled with analytical and numerical methods. The problem is complex due to the nonlinearities from soil behavior, gap formation, and pile-soil-pile interaction in pile groups (or the group effect). In this work, the finite element (FE) modeling was used to study the lateral behavior of pile groups. The FE method is robust and allows incorporating the necessary aspects for studying the behavior of pile groups. The nonlinear material behavior was incorporated using nonlinear constitutive models. The pile-soil interface was modeled using the zero-thickness surface-surface interaction, which provided the capability for modeling the gap behind the piles, and the transfer of interface normal and frictional stresses. The group interaction was facilitated through the interaction of stress fields around the piles, and by the continuity of the FE mesh.

The lateral behavior of three pile group (PG) configurations (vertical, battered, and mixed) with a similar number of piles were evaluated under static and dynamic loading. In the static analysis, the case study of the M19 pier foundation field test was used to verify the FE models. A parametric investigation for the effect of pile spacing and clay soil type was performed. The results showed that the lateral stiffness of the battered and mixed PGs was significantly higher than the vertical PG (+120%, +50%, respectively). The lateral load was found unevenly distributed among the piles in all PGs, and the exterior piles carried 1.5-2% higher load than the interior piles. The influence of the group effect vanished at pile spacings greater than 5D (D is pile width). Also, the influence of pile spacing was more prominent along the load direction. In the dynamic analysis, the PGs behavior was evaluated in barge impact simulations. The results showed that the battered and mixed PGs had similar and large lateral stiffness, which resulted in limited pile cap displacement and large deformation in the barge bow. The weak lateral stiffness of the vertical PG allowed the development of significantly larger impact force and pile cap displacement compared to the battered and mixed PG.

3D FE numerical analyses and parametric studies were also performed to develop models to evaluate the p-y curves for clayey and sandy soils using tangent hyperbolic models based on soil and pile properties. Regression analyses were performed on results of parametric study to develop formulas for evaluating the ultimate lateral bearing capacity factor (N_p) and reference displacement of p-y curve (y_{50}) in clay soils. A combination of

tangent hyperbolic and power function model was developed to evaluate the p-y curves in sand soils based soil and pile properties. These p-y curve models can be effectively implemented into any FE pile design software such as FB-MultiPier, LPILE, Midas, CSIBridge, and SAP2000.

Results of laboratory UU tests were used to develop correlations to estimate the strain at 50% stress level (ε_{50}) based on soil properties (i.e., Su, PI, LI). The comparison between the models' values and measurements are somehow reasonable. In addition, the results of FE parametric study for p-y curve in sand were analyzed to develop a formula to estimate the coefficients of subgrade reaction (k) based on soil and pile properties. For simplification, the estimation of k for different sand consistency, soil condition, and friction angle were presented in a table and a figure. The results of k values are comparable with the values recommended by FHWA.

Acknowledgments

This research project was funded by the Louisiana Department of Transportation and Development (DOTD) (SIO No. 1000103) and the Louisiana Transportation Research Center (LTRC Project No. 13-3GT). The help and support of Zhongjie Zhang, Ph.D., at LTRC is gratefully acknowledged.

Implementation Statement

This study aimed at evaluating the performance of pile groups subjected to static and dynamic (barge impact) lateral loading using finite element (FE) numerical modeling. Three pile group (PG) configurations with a similar number of piles were considered (i.e., vertical, battered, and mixed). FE parametric study was conducted to investigate the effect of pile spacing and clay soil type on the performance of PGs. The FE analyses were also used to develop models for p-y curves in clayey and sandy soils. The findings of this study can be implemented in the design of pile groups of different configurations as summarized below:

- The results of axial reaction (F_{axial}) per pile versus the applied lateral load presented in Figures 51, 61, and 62 for the three PGs can be used to estimate the contribution of each pile within the row/column of pile group for inclusion in the pile design.

- The distribution of lateral load per pile presented in Figure 52 for the three PGs can be used to calculate the contribution of each pile from the total applied lateral load for use in the lateral analysis and design of the pile.

- The developed p-multipliers presented in Tables 13 thru 15 and Figures 74 thru 78 for vertical, battered, and mixed PGs, respectively, which are applied to p-y curves, can be used to incorporate the group effect when designing pile groups of different pile spacing.

- The effect of barge speed impact on the piles' peak lateral displacement for the different PG configuration can be estimated using the results presented in Figure 92.

- The effect of barge speed impact on the piles'peak shear force for the different PG configuration can be estimated using the results presented in Figures 96, 100, and 101.

- The effect of barge speed impact on the contribution of piles and pier columns to the total resisting force for the different PG configuration can be estimated using the results presented in Figure 97.

- The effect of barge speed impact on the contribution of piles' peak axial force for the different PG configuration can be estimated using the results presented in Figures 104 and 105.

- The effect of non-centric barge impact on the peak lateral displacement, peak shear force, and the contribution of piles and pier columns to the resisting force can be evaluated using the results presented in Figures 112, 113, and 114, respectively.

- The developed nonlinear hyperbolic tangent function model for p-y curve in clay soil (Equation 79) can be implemented in any pile analysis software such as FB-MultiPier, LPILE, Midas, CSIBridge, and SAP2000 to evaluate the lateral behavior of piles driven in clayey soils.

- The developed nonlinear hyperbolic tangent/power function model for p-y curve in sand soil (Equation 85) can be implemented in any pile analysis software such as FB-MultiPier, LPILE, Midas, CSIBridge, and SAP2000 to evaluate the lateral behavior of piles driven in sandy soils.

- The developed models for estimating the strain at 50% stress (ε_{50}) based on typical soil properties (i.e., Su, PI, LI) presented in Figures 156, 157, 158, 160, 161, and 162, can be used to estimate the ε_{50} as an input parameter for use in different p-y curve models in clays.

- The proposed values for the coefficient of subgrade reaction, k, in Table 21and Figure 163 can be used to estimate k for different sand consistencies and soil conditions for use as an input parameter in different p-y curve models in sands.

Table of Contents

List of Tables

List of Figures

Introduction

Piles are one type of deep foundations that are designed to resist vertical loads as well as lateral loads. Their long, beam-like shape allows transfer of vertical loads to the soil thru side friction and tip bearing. Piles are usually used in group form with a pile cap (i.e., concrete thick slab) on top, which supports the superstructure elements above ground. Some of the purposes of using pile foundations are: (1) carry the superstructure elements and transfer vertical and lateral loads to the soil, (2) resist uplift or overturning for mats below water table, (3) control settlements for mats and spread footing over compressible soils, (4) support offshore structures by transmitting loads thru water to underlying soil [1]. Depending on the soil type, piles are installed either by driving (hammering) or by pre-boring (augured or drilled).

The design of piles is mainly based on vertical load capacity. However, design for lateral resistance has become necessary especially for cases where considerable lateral loads are present as in offshore structures, bridge abutments, and foundations near slopes. The lateral capacity of single piles and pile groups has been well investigated by field experiments, centrifuge (lab tests), analytical methods, and numerical methods (e.g., [2], [3], [4], [5], [6], [7], [8], [9]). The beam on elastic foundation theory provides a simplified analogy for the problem of pile-soil system subjected to lateral loads [10]. The system is idealized (in 2-D space) as a long beam (pile) supported by a series of independent elastic springs (soil) (Figure 1). In order to solve the problem, assumptions are needed for springs' stiffness. For example, Winkler [11] assumed constant linear spring stiffness, while others assumed nonlinear spring stiffness after experiments proving the latter case (e.g. [2]). The nonlinear soil spring stiffness is referred to as 'p-y curve', which relates the soil reaction to pile deflection at certain depth.

The assumption regarding the soil model allows solving the problem either analytically or by using numerical methods. The analytical solution is based on solving the beam differential equation for the pile-soil system using appropriate boundary conditions. The numerical approach is used in the case of nonlinear spring stiffness of soil, which requires iterative procedure. Solutions using the two mentioned approaches are available for the single pile case. For pile groups, single pile solutions can be extended by adjusting the soil spring stiffness to account for the effect of nearby piles, which is called the group effect. The influence of the group effect can be explained by the overlapping of stress

zones from the nearby piles when the group is subjected to lateral load. The group effect apparently reduces soil stiffness compared to the isolated single pile case.

Figure 1. Spring idealization of soil in the laterally loaded pile problem

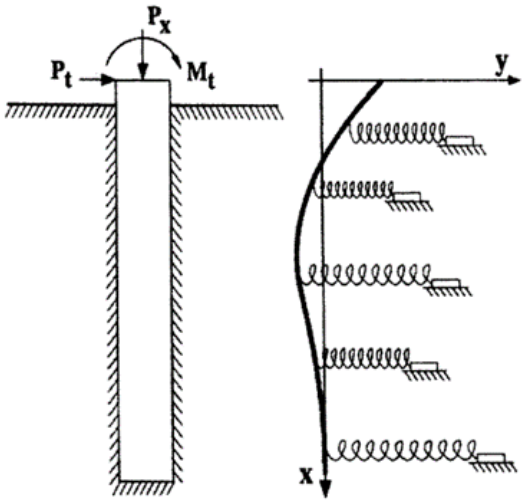

Numerically, the group effect is accounted for using reduction factors called ‘p-multipliers’ that are applied to the soil spring stiffness. The reduction factors for pile groups are deduced by comparing the soil resistance in case of a pile in a group to the soil resistance in the isolated single pile case. Those factors are empirical and have recommended values based on previous experiments.

Recently, the user of finite element (FE) numerical analysis has become one of the powerful methods for solving complex problems especially with the huge leap in the computational power and speed of computers. Experimental studies for pile groups are expensive and can be limited, and the FE method can provide a practical, affordable, and reliable alternative to the experimental approach. It has the capability to study and analyze problems in 1, 2, or 3-D space. The use of the FE method for the pile-soil problem allows for modeling of the several aspects of nonlinearity in the problem such as pile and soil material nonlinearity, multilayered soil, pile-soil gapping, interface friction, and pile group effect. Furthermore, the use of 3-D pile group models allows for studying non-uniform pile group spacing. When experimental results are limited, an FE model can be used to extract valuable results after being verified using the available results from the experiment. However, the FE method requires understanding of the problem mechanics and strong knowledge in numerical modeling.

The lateral behavior of pile groups can be well studied using the FE method. While the experimental approach is reliable, it can be limited and expensive for large-scale problems. The analytical approach is limited by assumptions and the size of the problem. The established numerical approaches based on p-y curves are reliable and well tested. However, these methods have a semi-empirical nature, and the soil springs work in 1-D space only.

Literature Review

Static Lateral Behavior of Single Piles

The lateral behavior of pile foundations is an interaction problem between the pile and the surrounding soil. This is usually faced in offshore platforms as well as bridge foundations crossing waterways. The lateral forces acting on the foundation is resisted by the rigidity of the piles and the soil surrounding it. The problem can be visualized as a deflecting beam (pile) resting on continuous support along its length (soil). The interaction between the pile and the soil is interdependent and nonlinear at large deflections. The lateral pile deflection depends on the soil reaction, which is also a function of the pile deflection.

Several methods are established for analysis of the lateral behavior of piles. For single pile, the main approaches are: Winkler approach, the *p-y* curve method, elastic solutions, and the finite element method. In the following sections, each approach is briefly reviewed.

Winkler Model

The differential equation (1) governing the pile-soil system was first introduced by Hetenyi [10]. The solution starts by assuming a beam resting on elastic foundation (Winkler foundation) is subjected to horizontal forces and axial forces (Figure 2).

$$\frac{\boldsymbol{d^2M}}{\boldsymbol{dx^2}} + \boldsymbol{P_x}\frac{\boldsymbol{d^2y}}{\boldsymbol{dx^2}} - \frac{\boldsymbol{dV_v}}{\boldsymbol{dx}} = \boldsymbol{0} \qquad [1]$$

Furthermore, the differential of the bending moment function is related to the pile deflection as:

$$\frac{d^2M}{dx^2} = E_pI_p\frac{d^4y}{dx^4}$$
$$\frac{dV_v}{dx} = p \qquad [2]$$

Figure 2. Analysis of beam resting on elastic foundation [10]

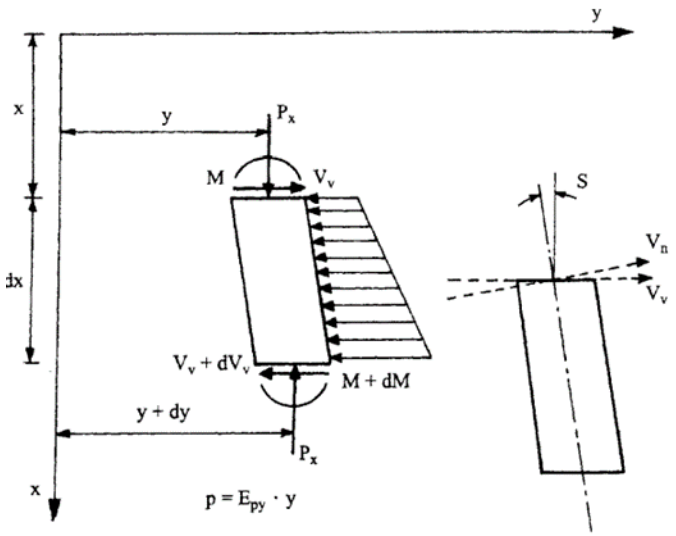

The variation in shear force is equal to the soil resistance (p), which is assumed as a distributed load. The Winkler hypothesis assumes that the soil reaction is a function of the pile deflection (y) as:

$$p = E_{py} * y \quad [3]$$

Where E_{py} is the soil's modulus of subgrade reaction (Force/Length/Length). In literature, the modulus of subgrade reaction is estimated from the modulus of subgrade reaction and the pile size D (diameter, width) as:

$$E_{py} = k_h * D \quad [4]$$

The value of the lateral subgrade reaction modulus k_h is a function of the depth. Palmer and Thomson [12] suggested a nonlinear (exponential) relation for k_h over depth assuming a maximum value at pile tip. Terzaghi [13] suggested a constant value for k_h over depth, and that the vertical and horizontal subgrade reaction moduli of the soil are the same. He estimated the value of k_h using the subgrade modulus from plate load test. Matlock and Reese [2] suggested that k_h for the soil is linearly varying with depth for granular and normally consolidated (NC) soils. Gill and Demars [14] suggested other variations for k_h with depth such as step function, hyperbolic function, and exponential function.

The final form of the beam equation is obtained by substituting the previous equations (2, 3, and 4) into equation (1) yields:

$$E_p I_p \frac{d^4y}{dx^4} + P_x \frac{d^2y}{dx^2} - p(x) + W = 0 \quad [5]$$

where W is the load on the upper portion of the pile.

A general solution to the differential equation is achieved by assuming (1) no axial loading, (2) E_pI_p constant, and (3) constant soil modulus E_s as:

$$y = e^{\beta x}(\xi_1 \cos \beta x + \xi_2 \sin \beta x) + e^{-\beta x}(\xi_3 \cos \beta x - \xi_4 \sin \beta x) \quad [6]$$

where $\xi_{1,2,3,4}$ are solution constants, and β is given as $\beta = \sqrt[4]{\frac{E_s}{4E_pI_p}}$.

Solutions for several pile cases can be achieved by introducing boundary conditions to equation (6). For example, for long piles, the first term in equation (6) vanishes and the solution for pile's deflection, slope, bending moment, shear, and soil reaction is obtained using equation (7) [15].

$$\begin{aligned} y &= \frac{2P_t\beta}{\alpha} C_1 + \frac{M_t}{2E_pI_p\beta^2} B_1 \\ S &= \frac{2P_t\beta^2}{\alpha} A_1 - \frac{M_t}{E_pI_p\beta} C_1 \\ M &= \frac{P_t}{\beta} D_1 + M_t A_1 \\ V &= P_t B_1 - 2M_t\beta D_1 \\ p &= -2P_t\beta C_1 - 2M_t\beta^2 B_1 \end{aligned} \quad [7]$$

where A, B, C, D are constants obtained from solution tables found in the reference.

Another solution for the governing differential equation is found by assuming no axial load, and a linear variation of soil modulus with depth (8). The method utilizes non-dimensional parameters (A_x, B_x) which can be obtained from charts. The method is useful but requires several trails to achieve convergence. The differential equation for the pile-soil system can also be solved using the finite difference method and computer.

$$y = A_y \frac{P_t T^3}{E_p I_p} + B_y \frac{M_t T^2}{E_p I_p}$$

$$S = A_s \frac{P_t T^2}{E_p I_p} + B_s \frac{M_t T}{E_p I_p}$$

$$M = A_m P_t T + B_m M_t$$

$$V = A_v P_t + B_v \frac{M_t}{T} \quad [8]$$

$$T = \sqrt[5]{\frac{E_p I_p}{k_{py}}}$$

$$Z_{max} = \frac{L}{T}$$

P-y Curve Method

Soil stresses surrounding the pile in the loaded and unloaded cases are shown in Figure 3. For the unloaded case, the stresses are the same around the pile; however, when the pile is deflected under lateral load, the stress distribution becomes uneven. The pile deflection increases the soil resistance at pile front (in movement direction) and decreases it at the back of the pile. Integration of the stresses around the pile yields net reaction force from the soil at certain depth.

Figure 3. Distribution of soil stresses around the pile

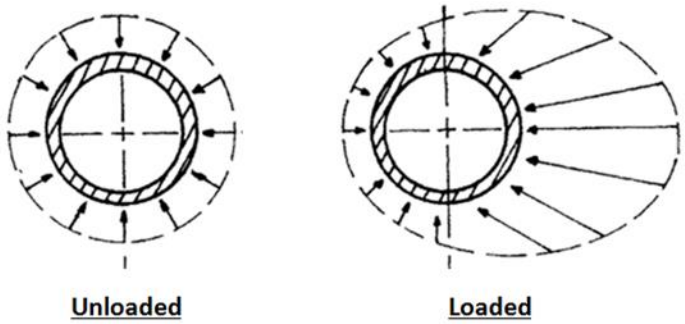

A p-y curve is a representation of soil resistance that gives the magnitude of soil reaction force at a certain depth as a function of soil deflection due to lateral pile deflection. The

terminology came after the use of plots of soil resistance force (p) as a function of the lateral deflection (y), as shown in Figure 4.

Figure 4. Illustration of the p-y curve concept

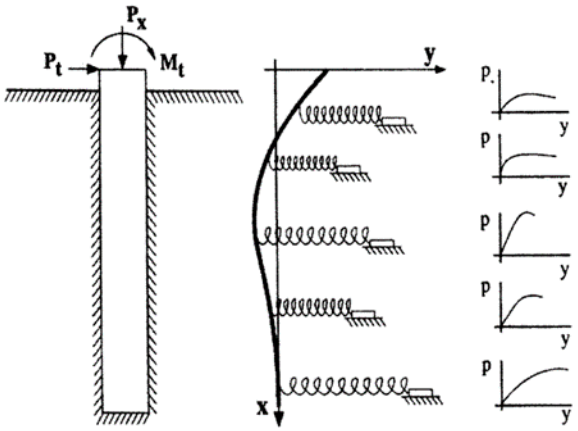

The p-y curve is initially linear and has a final flat portion at the ultimate resisting force. The initial portion is related to the initial soil modulus in the stress-strain curve. While the ultimate resistance, p_u, is related to the soil strength in bearing mode. The p-y curve is affected by the type of loading: static, sustained (long-term), and cyclic loading. For NC clays, the soil resistance decreases under sustained loading due to consolidation. Under cyclic loading, degradation in the soil resistance may occur and should be accounted for prior to the use of p-y curves from the static case, especially for cohesive soils.

In the differential equation of pile-soil system, the p-y curve is used to determine the soil reaction (p). The differential equation for the system is solved using finite difference or finite element techniques with the appropriate boundary conditions. The boundary conditions of the system depend on the type of loading (e.g. lateral force, moment loading), rotation at top of pile (fixed head, partially restrained, free head), and shear force at pile toe (whether its zero or certain value). Implementation of the p-y curves is found in software packages such as COM624P, FB-MultiPier, LPILE, Midas, CSIBridge, and SAP2000.

Construction of p-y Curves. Experimentally, the p-y curves can be obtained using strain gage (SG) data in instrumented piles (e.g., [16]). The SG measurements are used to calculate the bending moment at points over the pile length. Bending moment as a function of pile's length is found by a polynomial fit. By integrating the bending moment function, one can obtain the pile deflection (y) as a function of depth. Furthermore, the soil reaction (p) can be obtained by differentiating (twice) the bending moment function.

Finally, using the *p* and *y* values at selected depths, a family of p-y curves can be constructed. Reese and Cox [17] presented a slightly different approach. They used the experimental data to obtain values for deflection, slope, bending moment, and shear force. Then they used the non-dimensional method by Matlock and Reese [2] to solve for E_{py} as a function of depth. In addition, several methods were proposed to construct p-y curves from in-situ tests, such as dilatometer [18], cone penetrometer [19], and pressuremeter [20].

P-y Curves for Clay. P-y curves for clays can have different shapes depending on the clay type (stiff, soft). The earliest method to obtain p-y curves for clays was proposed by McClelland and Focht [21]. This method was based on experimental studies and utilized the stress-strain data from triaxial tests for samples confined at the overburden pressure. The soil resistance was estimated using the maximum normal stress (in the stress-strain curve), and the corresponding soil deflection was estimated using the strain at corresponding stress level.

Later, Matlock [22] proposed a method to obtain p-y curves for soft clays in presence of water. The p-y curve in this method is divided into three parts: initial straight portion, nonlinear portion, and final flat portion resembling the ultimate resistance p_u. This method requires soil properties such as undrained shear strength, S_u, and the strain at one half of maximum principal stress difference. The initial slope in the p-y curve can be determined from experiments or using suggested values. The nonlinear portion is constructed using equation (9).

$$\frac{p}{p_u} = 0.5\left(\frac{y}{y_{50}}\right)^{1/3} \qquad [9]$$

where the maximum value for *p* is reached at $y=8y_{50}$, y_{50} is estimated as $y_{50} = 2.5\varepsilon_{50}.b$, and p_u is the smallest value from equation (10).

$$p_u = \left[3 + \frac{\gamma'}{c} + \frac{J}{b}z\right]cb$$
$$p_u = 9cb \qquad [10]$$

The method also proposed modifications to the p-y curve for cyclic loading case to account for the loss in soil resistance. Figure 5 shows p-y curves for both cases of loading.

Figure 5. Characteristic p-y curves for static and cyclic loading for soft clay in water [22]

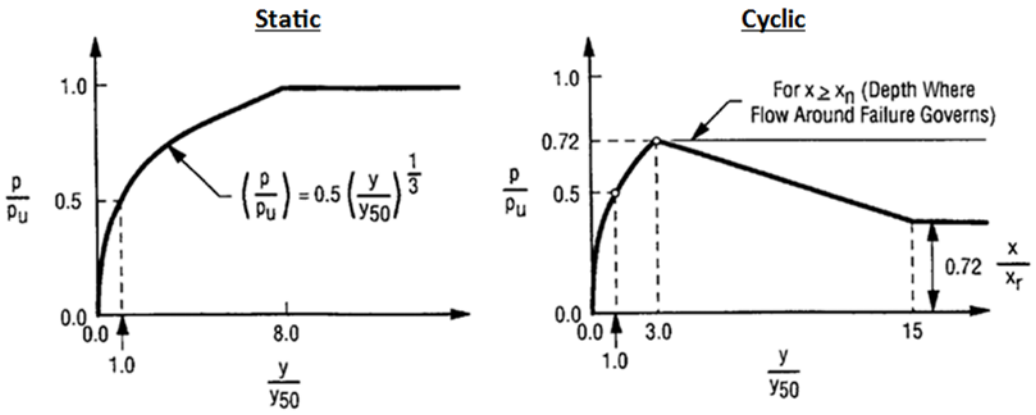

In a similar way, methods for constructing p-y curves for the cases of stiff clay in the presence of water [3], and stiff clay with no water ([23], [4]), were proposed.

P-y Curves for Sands. The difference between sands and clay soil is that sands do not exhibit softening behavior at large deformations or under cyclic loading. Reese et al. [24] proposed a procedure to construct p-y curves for sands. The strength of sand is estimated using the friction angle ϕ, which can be determined from in-situ or from triaxial tests. The p-y curve for sands is composed of 4 parts: initial sloping part, parabolic part, straight part, and final flat part at the ultimate soil resistance, see Figure 6. The slope of the initial part K_{py} is determined experimentally or from recommended values as in Reese et al. [15]. The parabolic part is determined using equation (11).

$$p = \bar{C} y^{1/n} \ , \ \bar{C} = \frac{p_m}{y_m^{1/n}} \qquad [11]$$

where p_m and y_m are defined next.

Figure 6. Construction of p-y curves for sand [24]

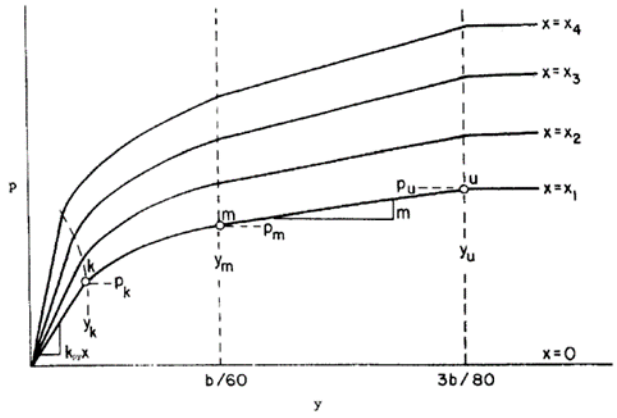

The straight part that comes after the parabolic part is the line connecting between the two points with p values of

$$p_u = A_s p_s \quad \text{or} \quad p_u = A_c p_s$$
$$p_m = B_s p_s \quad \text{or} \quad p_m = B_c p_s \qquad [12]$$

where A, B are non-dimensional constants accounts for the variation in the ultimate soil resistance with depth. The constants are determined from charts created for static load (lower case 's') and cyclic load cases (lower case 'c').

Finally, the flat part is determined by the ultimate soil resistance p_u given as the smaller of the following:

$$p_u = \gamma z \left[\frac{K_0 \tan\phi \tan\beta}{\tan(\beta-\phi)\cos\alpha} + \frac{\tan\beta}{\tan(\beta-\phi)}(b + z\tan\beta\tan\alpha) + K_0 z \tan\beta(\tan\phi \sin\beta - \tan\alpha) - K_A b \right] \qquad [13]$$

$$p_u = K_A b\gamma z(\tan^8\beta - 1) + K_0 b\gamma z \tan\phi \tan^4\beta$$

where γ is soil unit weight, z is the depth for p-y curve, ϕ is soil friction angle, $\beta = 45 + \phi/2$, b is pile size, α is defined as $\alpha = \phi/2$ for loose sand and $\alpha = \phi$ for dense sand, and K_o, K_A are the at-rest and active coefficient of lateral earth pressure, respectively.

Comments on the p-y Curve Method. The advantage of the p-y curve approach over the Winkler approach is that the nonlinearity of soil is incorporated. However, the p-y curve method has disadvantages such as (1) there is no coupling between adjacent p-y

curves (i.e. the continuous nature of soil is omitted), (2) construction of p-y curve requires in-situ testing, and (3) it has semi-empirical nature.

Elastic Continuum Solutions

Poulos and Davis [25] obtained the solution for the laterally loaded piles under static load treating the soil as an elastic continuum. The pile is assumed as thin rectangular vertical strip with constant flexibility. Soil displacements were estimated using Mindlin's solution for horizontal displacement of a point within a semi-infinite mass caused by horizontal point load. The solution assumptions were (1) homogeneous, isotropic, elastic soil, (2) the soil pressure at any point does not exceed the ultimate pressure, (3) the shear stress at pile sides is neglected, and (4) soil-pile separation is not considered. The solution starts with the following system of equations:

$$\{y\} = \frac{D}{E_s} . [I] . \{p\} \qquad [14]$$

Where $\{y\}$ is the column vector of soil displacements, D is pile diameter, E_s is soil modulus, $[I]$ is matrix of factors from Mindlin's solution, and $\{p\}$ is the column vector of horizontal load between soil and pile.

The previous equations are substituted in the beam differential equation. Then, the system of equations is solved using the finite difference technique. Poulos and Davis [25] indicated that higher soil reactions that exceed the ultimate soil resistance developed near the top due to the elastic assumption. In that case, he suggested using iterations in the solution to ensure that the maximum soil reaction possible at any point does not exceed the ultimate resistance.

Later, Sun [26] used the modified Vlasov model by Vallahban and Das [27] for analysis of beams on elastic foundations and presented a numerical solution for laterally loaded piles. The soil in this model is considered homogeneous elastic continuum. The solution approach used variational calculus principles to obtain the differential equation for the pile-soil system. Soil displacements were assumed a function of radial distance from the pile. Sun compared his solution to the elastic solution by Poulos and Davis [25], and showed an agreement between the two solutions with a slight difference. Sun's solution is powerful; however, it requires determination of several factors and moderate computational effort and is limited to single layered soils. Later, Basu et al. [28] extended

Sun's solution for single soil profile to multi-layer soil profile. They also improved Sun's solution by assuming different soil displacement fields in radial and angular directions.

In a similar approach to Sun [26], Guo and Lee [29] developed a closed form solution for laterally loaded piles in homogeneous elastic soil medium. Their approach differed from Sun's in the simplified stress field which ignored higher order stress components. Guo and Lee [29] indicated that their solution excelled Sun's solution in its modeling accuracy for cases with Poisson's ratio greater than 0.3.

Strain Wedge Model

The strain wedge model developed by Norris [30] assumes that the pile is resisted by a 3-D passive soil wedge in front of it. The side friction on the sides is considered in this model as part of the total lateral resistance. The model was improved later by Ashour et al. [8] for multilayered soil, and to account for pile head conditions (i.e. fixed or free). It assumes that the soil in front of the pile is in similar conditions to triaxial test; in which the horizontal stress from the pile resembles the deviatoric stress in the triaxial test. The model parameters are horizontal soil strain, horizontal stress change, and the nonlinear soil modulus. These parameters are analogous to those used in the beam on elastic foundation solution: pile deflection (y), soil reaction force (p), and modulus of subgrade reaction (E_{py}). The geometry of passive wedge is characterized by the mobilized friction angle ϕ_m, which evolves gradually with pile deflection until it reaches the maximum value of soil friction angle ϕ, see Figure 7.

The main assumption in this model is the linear variation of pile deflection with depth. The depth of passive wedge is assumed initially and then determined by an iterative procedure. The strain wedge model is also capable of solving the problem of multilayered soil by dividing the passive wedge into sublayers that can have different soil properties, see Figure 8.

Figure 7. Illustration of the strain wedge concept [8]

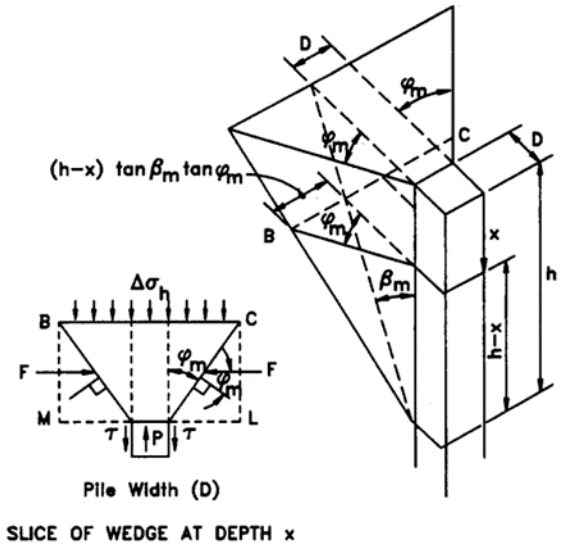

The main assumption in this model is the linear variation of pile deflection with depth. The depth of passive wedge is assumed initially and then determined by an iterative procedure. The strain wedge model is also capable of solving the problem of multilayered soil by dividing the passive wedge into sublayers that can have different soil properties (see Figure 8).

Figure 8. The passive wedge for multilayered soil in strain wedge model [31]

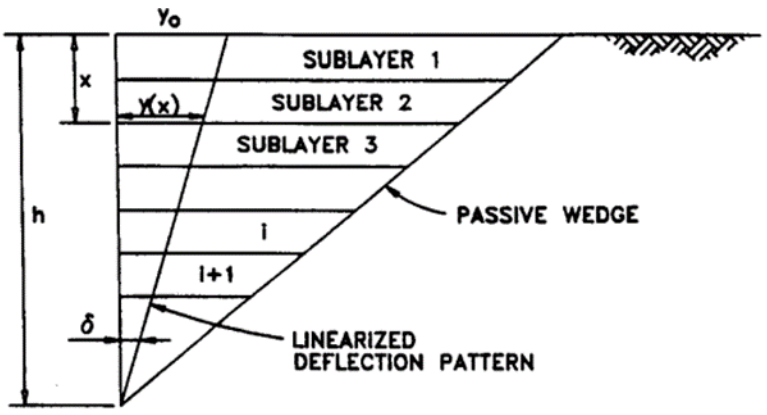

The procedure starts by determining the horizontal stress level (SL) from the strain using a power function which relates the stress level with axial strain. The function is normalized using ε_{50} which is the strain at 50% stress level (from stress-strain curve in triaxial test). SL is defined as the ratio of mobilized horizontal stress to the ultimate horizontal stress that the soil can carry. Using SL, one can determine the mobilized

friction angle and the horizontal stress increase $\Delta\sigma_h$ from equation (15) (assuming passive conditions for soil resistance)

$$SL = \frac{\Delta\sigma_h}{\Delta\sigma_{hf}} = \frac{\tan^2(45 + \phi_m) - 1}{\tan^2(45 + \phi) - 1} \quad [15]$$

where ϕ_m is the mobilized friction angle, $\Delta\sigma_h$ is the change in horizontal stress corresponding to ϕ_m, ϕ is the maximum friction angle for soil, $\Delta\sigma_{hf}$ is the maximum change in horizontal stress corresponding to the ultimate soil resistance (i.e. at maximum ϕ).

Estimation of ϕ_m from equation (15) is for sands. For clay soil, the model assumes undrained conditions and further estimates the change in pore water pressure to find the effective stresses. The mobilized friction angle is found using equation (16):

$$\tan^2\left(45 + \frac{(\bar{\phi}_m)_i}{2}\right) = \frac{(\bar{\sigma}_{vo} + \Delta\sigma_h - \Delta u)_i}{(\bar{\sigma}_{vo} - \Delta u)_i} \quad [16]$$

where $\bar{\sigma}_{vo}$ is the effective overburden stress, and Δu is the excess pore water pressure.

The resistance force per unit length of pile is determined using equation (17):

$$p_i = (\Delta\sigma_h)_i \overline{BC}_i S_1 + 2\tau_i D S_2 \quad [17]$$

where $S_{1,2}$ are shape factors, τ is the shear stress on pile sides, D is pile size.

$\overline{BC}$ is given as (from geometry of the passive wedge, see Figure 7)

$$\overline{BC} = D + (h - x)2 \tan\beta_m \tan\phi_m \quad [18]$$

where h is the passive wedge depth, x is the depth of soil segment, β_m is the base angle of passive wedge ($\beta_m = 45 + \phi_m/2$).

Having p_i, y_i (= $[h - x_i] \times \delta_i$) can be estimated for each sub layer. The subgrade modulus, E_s, is determined as $E_s = p_i/y_i$.

The value of pile head load is estimated using equations as in Norris [30], depending on pile head condition (i.e. free, fixed). Finally, the profiles of pile deflection, soil reaction, and bending moment are determined.

The advantages of the strain wedge model are it addresses the nonlinearity of soil reaction and the subgrade modulus. It is effective since it utilizes basic soil properties (ϕ, S_u, ε_{50}) that are easy to obtain. Another advantage for strain wedge model over Winkler model is the interdependence of soil reactions between each soil segment within the wedge, which is achieved thru the total wedge depth (h). Furthermore, the model is capable of analyzing multi-layered soil. Ashour et al. [8] indicated that strain wedge model can be used to verify conventional p-y curves, since it defines its own parameters from the stress-strain curve from triaxial tests. He also pointed that no unique p-y curves for certain soil type exists due to several factors affecting the pile-soil problem. Ashour and Norris [32] used the strain wedge model and showed that different p-y curves can be obtained for the same soil type. Their study concluded that the p-y curve, in addition to soil properties, is a function of pile stiffness, pile head fixity, embedment depth of pile head, and pile cross section shape. The weaknesses of the strain wedge model are (1) it is suitable only for statically loaded piles, and (2) it does not address the effect of pile-soil gapping.

Static Lateral Behavior of Pile Groups

The lateral behavior of piles in group differs from single pile due to the influence of the pile-soil-pile interaction. The soil resistance in case of pile groups is reduced due to the group effect, see Figure 9. The soil located within the overlapping zones of the stress bulb is subjected to additional stresses (compared to isolated single pile case). In addition, movement of leading pile reduces the confining stress behind it. Furthermore, soil gapping may occur due to pile movement away from the soil especially in cohesive soils. This combination of overlapping of stress zones along with gapping reduces the resistance of the pile in group configuration.

Figure 9. Illustration of the pile group effect

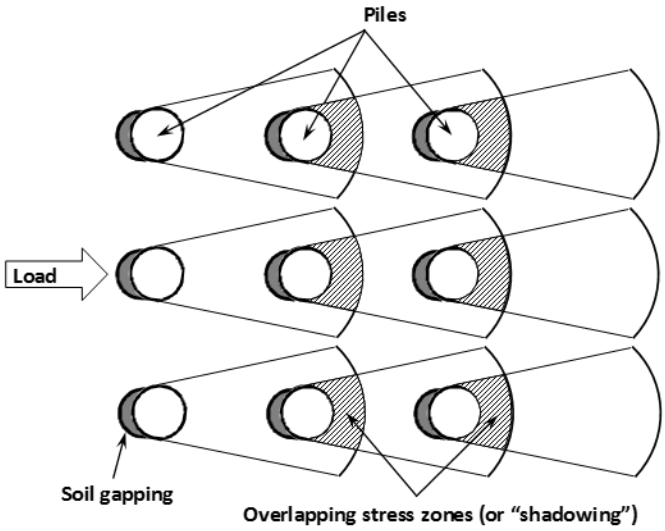

Poulos and Davis [25] used his solution, assuming elastic soil continuum, to estimate the group effect using pile-soil-pile interaction factors. The interaction factor reflects the additional passive pile displacement due to active pile displacement. Plots of interaction factors for two-pile groups as function of spacing were presented for cases with different boundary conditions (e.g. fixed head, free head), and flexible/rigid piles. Variation of interaction factors with different parameters showed: (1) larger interaction effect for leading piles (in loading direction) compared to side piles, (2) decreasing interaction with higher slenderness ratio, (3) increasing interaction with higher pile stiffness, and (4) increasing interaction with smaller pile spacing. Poulos and Davis [25] indicated that the solution for two-pile group can be extended for pile groups with more than two piles, and the total displacement for a pile in group considering the group effect is found by superposition. For example, for a group with n piles subjected to horizontal load only, the deflection of pile i is estimated using equation (19) as:

$$u_i = u_0 \left[\sum_{i,j}^{n} \left(P_j * \alpha_{ij} \right) + P_i \right] \qquad [19]$$

where u_i is the total displacement of pile i in the group, u_o is the unit displacement of single pile subjected to unit horizontal load, P_j is the load on pile j, P_i is the load on pile i, α_{ij} is the interaction factor between piles i and j.

Leung and Chow [33] presented a semi-theoretical solution for pile groups considering the pile-soil-pile interaction. Their solution utilized the p-y curve approach for individual

pile response. The pile is divided into segments and the stiffness matrix for single pile-soil system is determined. The pile-soil-pile interaction is estimated using Mindlin's solution, and the soil displacement is assumed to be in the horizontal direction only. The total soil displacement at a node is estimated using equation (20).

$$y_i = \sum_{j}^{n} f_{ij} * P_{sj} \quad [20]$$

where y_i is soil displacement at node *i*, f_{ij} is the flexibility factor for displacement at node i due to unit horizontal load at node *j*, P_{sj} is the horizontal force at node *j*.

The flexibility factors in the previous equation are obtained from Mindlin's equation for the influence of a unit horizontal point load in a homogeneous isotropic elastic half-space. The vector of soil displacements at all nodes in the group is found as in equation (21) as:

$$\{y_s\} = [F_s] * \{P_s\} \quad [21]$$

Equation (21) is substituted in the force-deformation matrix of pile group system assuming (1) pile and soil displacements are equal, and (2) pile force equals soil force but with a negative sign. The global load-displacement equations for the pile group-soil system is given as in equation (22) as:

$$\left([K_p] + [K_s]\right) * \{y_s\} = \{Q\} \quad [22]$$

where K_p and Ks are the stiffness matrix for the pile and soil, respectively, y_s is the deflection of soil at pile nodes, Q is the vector of external horizontal forces.

Leung and Chow [33] solution was in good match with Poulos and Davis [25] solution. However, the first tends to overpredict pile shear force and bending moment at large deflections.

Strain Wedge Model for Pile Groups

Ashour et al. [31] extended the single pile strain wedge model and added the capability to solve for pile groups. The model extension accounts for the group effect by estimating the additional soil stresses due to the overlapping of passive soil wedges. This is achieved by determining the area of overlap for a pile's wedge with surrounding piles' wedges (Figure

10). The additional stresses from the surrounding piles result in larger deflection at certain load compared to the isolated pile case.

Figure 10. Soil wedge overlap in pile groups for strain wedge model [31]

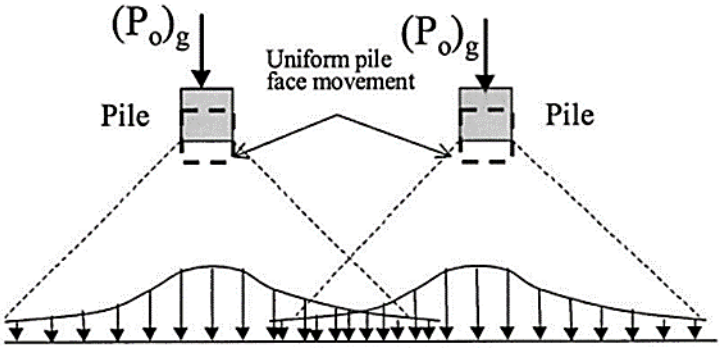

The strain wedge solution for pile groups starts by analyzing each pile in the group individually [8]. The overlapping between piles' wedges is determined from the resulted passive wedges geometry for all piles in the group. The increased stress level SL_g in the passive wedge for pile i in the group is estimated using the empirical relationship in equation (23).

$$\left(SL_g\right) = SL_i\left(1 + \sum R_j\right)^{1.5} \leq 1 \qquad [23]$$

where SL_i is the stress level from single pile solution, R_j is the ratio between the length of overlapped portion of passive wedge face and the total length of the passive wedge face from neighboring pile j.

The final value of SL_g is determined by iterative procedure, and consequently a modified fanning angle (ϕ_m) is obtained for the pile group. The solution proceeds by constructing subgrade modulus profile over pile length, which represents the influence of the group effect.

The advantage of strain wedge model for pile groups is that it implicitly accounts for the group effect without using empirical factors such as p-multipliers, which are applied to p-y curves for pile groups (see next section). Furthermore, the response of each pile in a group can be assessed individually and can be unique for each pile, unlike the p-multipliers approach which assumes similar response for all piles in the same row.

Pile Groups Behavior using P-Multipliers

The p-multiplier is a factor that modifies (softens) single pile p-y curve to obtain the p-y curve for a pile-in-group, which was first introduced by Brown et al. [34]. The p-multiplier simplifies the design of pile groups by predicting their response using p-y curves for single piles. It is defined as the ratio of lateral load resisted by a pile-in-group and causes a certain deflection, to the lateral load resisted by isolated single pile at the same deflection, see Figure 11. The value of p-multiplier is usually less than or equal to unity.

Figure 11. The p-multiplier concept [34]

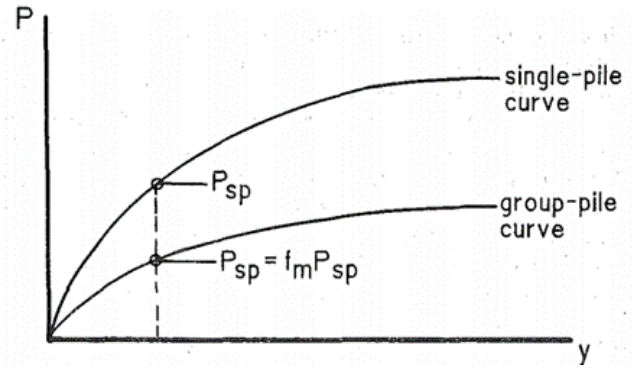

The p-multiplier concept is analogous to the group efficiency factor [1], which is defined as the ratio of the ultimate lateral capacity of a pile-in-group to the ultimate lateral capacity of an isolated single pile.

Several studies showed that the p-multiplier in pile groups is a function of soil type, soil profile, pile spacing in both directions (longitudinal and transversal), pile location in the group (inside or outside pile), pile group deflection, and depth (e.g., [5], [35], [36], [37], [38], [39]). It should be noted here that, in practice, the p-multipliers usually assume a constant value over the pile length.

Table 1. Reported p-multipliers in literature

Reference	Group size	s/D	*p*-multipliers			Soil type
			Leading row	2nd row	Trailing row	
Brown et al. [34]	3x3	3	0.7	0.6	0.5	clay
Brown et al. [5]	3x3	3	0.8	0.4	0.3	sand
McVay et al. [40]	3x5	3	0.8	0.4	0.3	dense sand
		3	0.65	0.45	0.3	loose sand
		5	1.0	0.85	0.7	sand
Ruesta and Townsend [20]	4x4	3	0.8	0.3	0.3	sand
McVay et al. [35]	3x3-3x7	3	0.8	0.4	0.3	sand
Rollins et al. [41]	3x3	3	0.78	0.59	0.45	clay
		3.3	0.81	0.61	0.46-0.51	
		4.4	0.9	0.8	0.73	
		5.6	0.94	0.88	0.77	
Ilyas et al. [42]	4x4		0.65	0.49	0.46	clay
Chandrasekaran et al. [43]	3x3	3	0.61	0.41	0.44	clay
AASHTO [44]	-	3	0.8	0.4	0.3	-
		5	1.0	0.85	0.7	-

In general, closer pile spacing in both directions leads to higher group interaction, and hence, smaller p-multiplier value. This was observed in experimental and numerical studies (e.g., [45], [43], [39]). In the same context, the group effect is larger for piles located in the interior columns of the group compared to the piles on the edges or corners. This is because a smaller number of piles participates in the overlapping of stress zones (e.g., [20]).

Table 1 shows p-multipliers reported by a number of experimental studies. Figure 12 and Figure 13 present the suggested values for p-multipliers at different pile spacing.

Figure 12. Suggested p-multiplier vs. pile spacing for the leading row

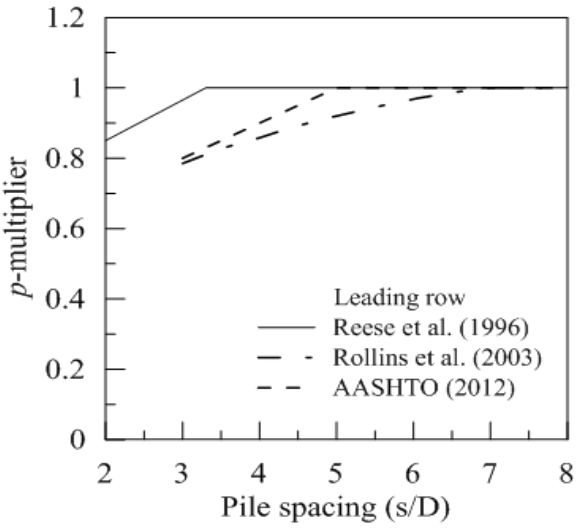

Figure 13. Suggested p-multiplier values for the second and trailing rows with pile spacing

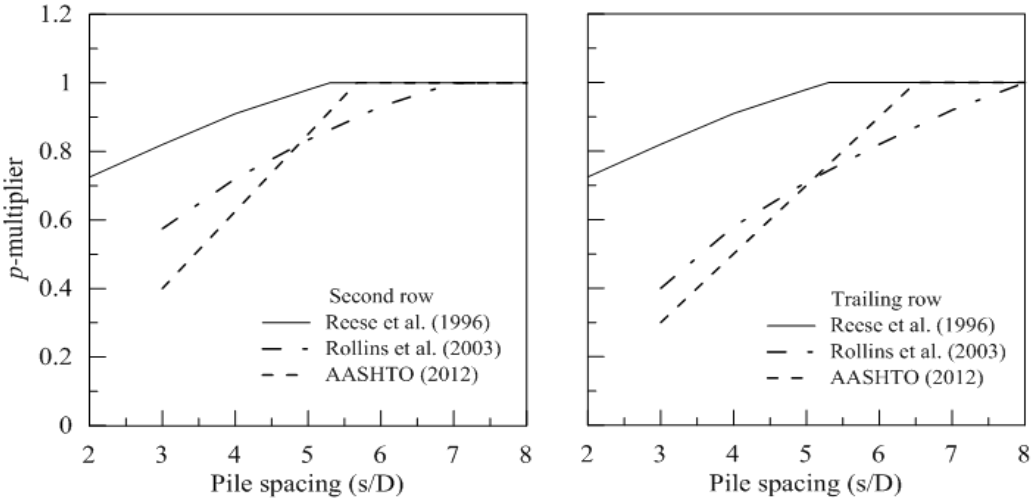

The influence of pile group deflection is related to the size of mobilized stress zones. At small deflections, the stress zones are not fully developed and minimal overlapping occurs. With increased deflection, the stress zones gradually continue to evolve so that the group interaction fully mobilizes. This is also noticed on the value of p-multipliers, which start at values close to unity at low deflection, and gradually degrade with larger deflection (e.g., [31] , [39], [46]). Therefore, p-multiplier values at relatively small pile deflections might not be reliable for design purposes. The variation of p-multipliers with depth is also related to the size of stress zones. At greater depths, the stress zones are smaller and hence the influence of the group effect is less (e.g., [47], [45]).

The effect of group configuration is more evident in case of non-square groups (i.e., the number of rows and columns not equal). The lateral resistance of non-square pile group differs according to the direction of loading. This effect is clearly observed in case of pile groups in single line arrangement. The lateral resistance of such pile groups is larger when the loading direction is perpendicular to the line of arrangement (e.g., [45], [37], [43]). This is related to the size of mobilized soil zone and area of overlapped stress zones. For example, for a pile group in single line arrangement, the mobilized soil zone is wider when the direction of loading is perpendicular to the line of arrangement (Figure 14). Also, the group effect is smaller in this case of loading (perpendicular to the line of arrangement) compared to in-line loading direction due to smaller overlapped stress zones.

Figure 14. Stress zones around pile groups loaded in-line and transverse to piles arrangement [45]

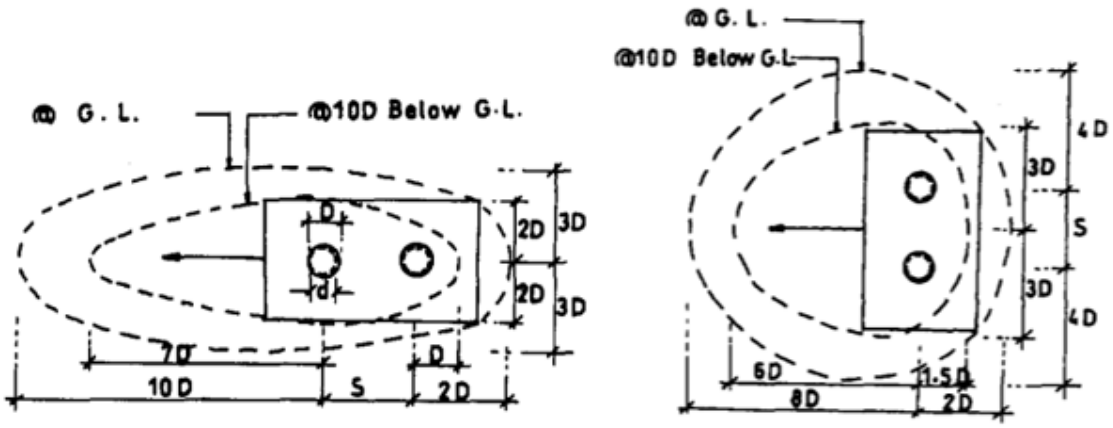

Dynamic Lateral Behavior of Single Piles

The dynamic lateral behavior of piles differs from the static behavior in the inclusion of inertia and damping effects. The equation of motion for the pile considering the inertia effect and ignoring the pile's material damping is written as:

$$EI\frac{d^4y}{dx^4} + \mu_p\ddot{y} + P_s(x,y) = Q(x) \qquad [24]$$

where y is pile deflection, $\ddot{y}$ is the acceleration, μ_p is the mass per unit length of pile, *EI* is the flexural rigidity of the pile, $P_s(x,y)$ is the soil reaction per unit length, and $Q(x)$ is the external load acting on pile.

The soil reaction includes both the static and damping resistance. Assuming compatibility at the soil pile interface, the soil reaction is then a function of pile deflection and deflection rate. Neglecting the soil inertia, the equilibrium equation for the soil component is given as:

$$P_s(x,y) - k(x)y - c(x)\dot{y} = 0 \qquad [25]$$

where $\dot{y}$ is the deflection rate, $k(x)$ is the static soil stiffness, and $c(x)$ is the soil's viscous damping coefficient.

Substituting equation (25) into equation (24) gives the general equation of motion for the pile-soil system as:

$$EI\frac{d^4y}{dx^4} + \mu_p\ddot{y} + k(x)y + c(x)\dot{y} = Q(x) \qquad [26]$$

Equation (26) can be solved by assuming the pile under harmonic lateral excitation and solved in the frequency domain using the suitable boundary conditions. The lateral deflection of the pile (y) is assumed to be harmonic in the form $y(x,t) = y(x)exp(i\omega t)$, in which ω is the cyclic frequency. Thus, the equation for the pile-soil system is rewritten:

$$EI\frac{d^4y}{dx^4} + \left[k^*(x) + i\omega c(x) - \mu_p\omega^2\right]y(x,\omega) = Q(x) \qquad [27]$$

There are two types of soil damping considered in equation (27): material (hysteretic) damping, and viscous (radiation) damping. The effect of material damping can be observed under cyclic load conditions, in which the damping ratio is estimated from the area enclosed by the hysteresis loop. Material damping is frequency independent and difficult to separate from the static material stiffness. Therefore, the static stiffness and material damping are usually combined and represented by the complex stiffness $k^*=k(1+i\eta)$, where η is the hysteretic damping ratio. On the other hand, viscous damping is frequency dependent and can be modeled as a dashpot with its coefficient estimated by assuming that the radiation energy is fully absorbed by the dashpot.

There are two main approaches used in literature to solve the pile-soil system equations: continuum, and Winkler approach. The continuum approach considers the pile and soil as continuous domain and accounts for radiation damping. However, this approach neglects two main aspects of the problem: the soil plasticity and gap formation. The Winkler approach builds on Winkler's hypothesis by modeling the soil as a separate element with stiffness and damping properties.

Using the continuum approach, Novak [48] presented an approximate analytical solution for the lateral dynamic resistance of single piles. He assumed an infinite cylindrical pile embedded in an infinite soil cylinder. The cylinder is discretized into infinitesimal slices (circular discs) that extend to infinity in a plane strain condition. The dynamic soil reaction was obtained for the pile under harmonic motion considering the damping properties of the soil (material and radiation). The differential equation for the problem is then solved in the frequency domain. It was concluded from the solution that pile foundations have higher natural frequency than shallow foundations, and the dynamic stiffness and damping are insensitive to the vibration frequency for piles with slenderness ratio greater than 25. Later, Nogami and Novak [49] used the same solution technique and presented analytical expressions for the dynamic soil reaction for piles subjected to vertical, horizontal, rotational, and torsional vibrations.

On the other hand, Winkler's approach has been used more often by researchers for its ability to account for soil nonlinearity, damping, and gap formation. Gazetas and Dobry [50] presented a simplified realistic method for estimating the lateral dynamic stiffness of piles. They solved the problem for fixed-head piles subjected to harmonic excitation. They assumed that the additional damping resistance only affects the magnitude of the static deflection pile while the deflected shape remains the same. They estimated the dynamic pile resistance by assuming a single spring (static stiffness) and dashpot (damping) at the top of the pile. The static spring stiffness is obtained using the established static approaches such as the p-y curve method. The overall dashpot constant was estimated from the material and radiation damping coefficients of soil. The overall dashpot constant was found by integrating over the pile length.

Nogami and Kanagai [51] presented a time-domain solution for the dynamic lateral resistance of piles using Winkler's soil spring approach. They estimated the dynamic soil reaction by modeling the soil as a series of springs and dashpots connected to a mass (Figure 15).

Figure 15. Illustration of the Winkler soil model by Nogami and Kanagai [51]

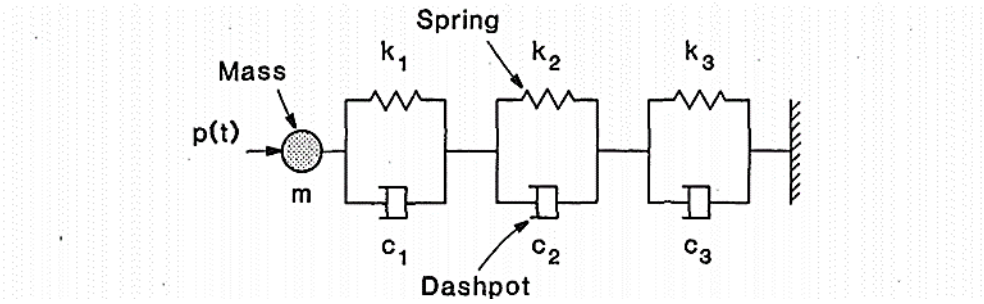

In the figure, *p(t)* is the pile-soil interaction force, m_s represents the mass of soil element, k_n is the spring stiffness, c_n is the dashpot coefficient. The dynamic soil reaction at time t_i is estimated as:

$$p_i = m_s\ddot{u}_i + ku_i + d_i \qquad [28]$$

where $m_s\ddot{u}_i$ is the inertial resistance of the soil element, ku_i is the increment in soil resistance from the spring and dashpot combined, d_i is the mobilized soil reaction from the previous time steps.

The pile-soil domain is divided into slices and the beam differential equation for the pile combined with Eq.28 is solved in time using numerical integration scheme.

Later, Nogami et al. [52] built on and improved the solution by Nogami and Konagai [51]. They divided the soil model into two elements: near field (accounting for the nonlinear soil behavior near the pile) and far field (accounting for the elastic behavior and damping away from the pile). Additionally, they introduced an interface model to account for the gap formation (Figure 16). El-Naggar and Novak [53] used the concept from Nogami et al. [52] by assuming the soil model comprised of inner and outer field elements. For the inner field element, they used the solution by Novak and Sheta [54] for the stiffness of the nonlinear spring, while for the outer field they used the solution from Novak [48]. They also accounted for the soil gapping by introducing separate elements for the front and back of the pile with the use of no tension springs. Using El-Naggar and Novak [53] model and regression analysis, El-Naggar and Bentley [55] proposed a simplified formula for the dynamic soil resistance (dynamic p-y curves) as a function of the static reaction and load frequency, as shown below:

$$P_d = P_s \left[\alpha + \beta a_o^2 + \kappa a_o \left(\frac{\omega y}{d}\right)^n\right] \quad [29]$$

where P_d, P_s are the dynamic and static soil reactions, a_o is the dimensionless frequency, y is pile deflection, d is pile diameter, and α, β, κ, n are fitting parameters.

Figure 16. Illustration of the pile-soil model by Nogami et al. [52]

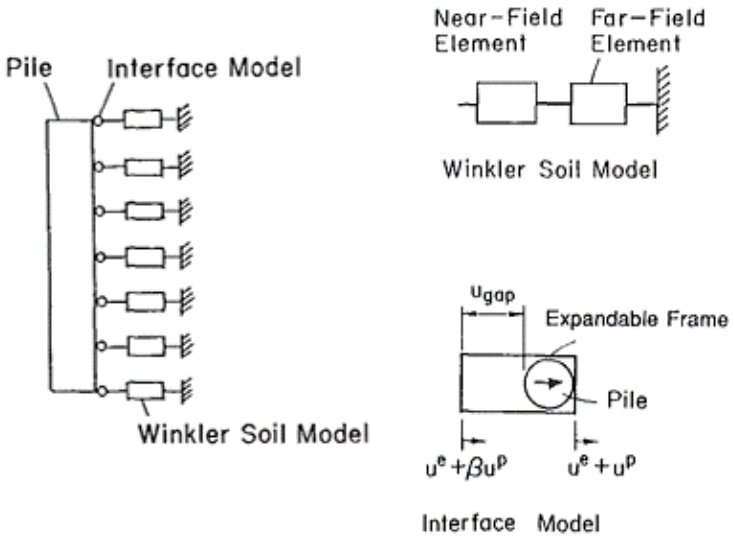

The value of P_d in the equation is limited to the ultimate soil resistance that can be estimated using one of the established methods (e.g., [22]). Validations of the dynamic p-y curve model showed that the model works better with loading frequencies greater than 4 Hz where the dynamic effects are more prominent.

In summary, the dynamic lateral behavior of piles requires additional considerations over the static behavior for the influence of pile and soil inertia, and soil damping. The inertial effects are incorporated by adding the inertia terms for the mass of pile and soil elements in the beam differential equation. Soil damping influences the pile behavior by two mechanisms: hysteretic soil behavior or material damping, and radiation damping. Material damping is accounted for by using the complex form for the soil stiffness and is considered frequency independent. The radiation damping accounts for the energy dissipation at the far region from the pile.

Dynamic Lateral Behavior of Pile Groups

In addition to the group effect from the static behavior, the dynamic lateral behavior of pile groups is influenced by the stress waves emitted from the source piles. The problem was approached in several ways such as the analytical solution (e.g., [56]); dynamic interaction factors based on analytical solutions (e.g., [57], [58], [59], [60]); and dynamic interaction factors based on Winkler soil model (e.g., [53], [61]).

Kaynia and Kausel [56] presented a rigorous numerical solution for the dynamic resistance of pile groups. The solution was used to evaluate the validity of the superposition assumption and the dynamic interaction factors for pile groups. The dynamic interaction factor is defined as the ratio of the displacement of the passive pile due to the dynamically loaded active pile to the displacement of the pile under static load [58]. One of the interesting conclusions from the study was that piles closer to the center of the footing carry the largest share of loading. The study also indicated that the dynamic pile group behavior is highly frequency dependent, and the superposition assumption is valid for low-frequency dynamic loads.

Dobry and Gazetas [57] defined the dynamic interaction factor as the ratio of the displacement of the passive pile due to the active pile motion to the displacement of the active pile under dynamic loading. They assumed that the stress waves over the length of the source pile are emanated at the same time (i.e., no phase lag) and travels away from the pile's axis in a cylindrical fashion. The displacement field from the source pile periphery was estimated using the wave equation

$$y(r) \cong A\frac{1}{\sqrt{r}}\exp\left(-\frac{\beta\omega r}{V_s}\right)\exp\left[i\omega\left(t-\frac{r}{V_s}\right)\right] \qquad [30]$$

where A is the displacement amplitude at the source, r is the radial distance from the pile axis, β is the damping ratio, V_s is the shear wave velocity.

The dynamic interaction factor was found as the ratio of the displacement at the passive pile located at a radial distance (r) to the displacement at the source pile using radial distance ($r = 0$). The dynamic interaction factors were found for the cases of two piles in-line ($\theta = 0$) and side-by-side ($\theta = 90°$) and interpolated for the cases of piles located at angles ($0 < \theta < 90°$). Later, Gazetas et al. [58] presented plots for the dynamic interaction factors using Dobry and Gazetas [57] solution. The dynamic interaction factors were in complex form, and were influenced by frequency, piles spacing, damping ratio, and pile-soil stiffness ratio.

In a similar approach, Makris and Gazetas [59] obtained an expression for the dynamic interaction factors using the solution for the equation of motion in the frequency domain. Mylonakis and Gazetas [60] followed the same approach by Makris and Gazetas [59] to obtain the dynamic interaction factors. The difference in their solution was in the displacement field functions for the source pile and the receiver pile, respectively.

El Naggar and Novak [53] used a slightly different approach by modeling the pile-pile interaction using a viscoelastic spring. They used the expression of the attenuation function from Dobry and Gazetas [57] to estimate the displacement at the passive pile due to the displacement of the active pile. The group interaction force is then added to the equation of motion in the outer field element and the system of equations is solved for two piles (Figure 17).

Figure 17. Viscoelastic spring model for pile group interaction [53]

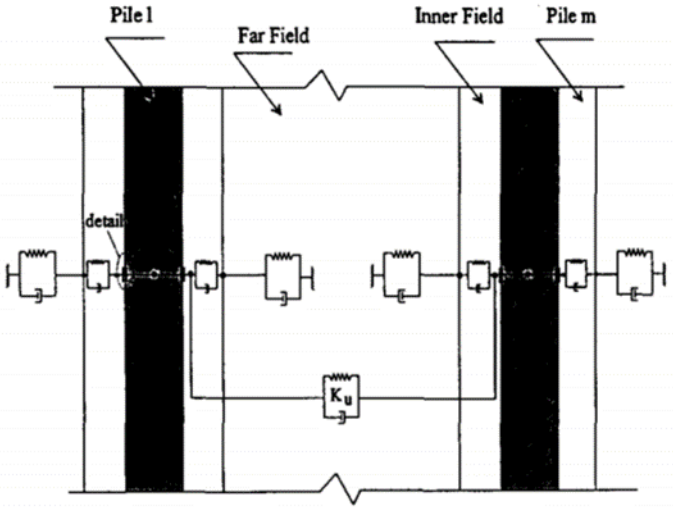

Mostafa and El Naggar [61] attempted to extend the p-multiplier concept for the dynamic behavior of pile groups. They conducted a parametric study using the dynamic p-y curve formula by El Naggar and Bently [55] and investigated the influence of several parameters on the p-multipliers, and concluded that the p-multipliers increase with increased pile spacing, deflection, stiffness ratio, and pile size. They also found that pile installation method and head-fixity condition have major influence on the p-multipliers.

Estimating Parameters of p-y Curve Models

Different soil types (clay versus sand) usually require different input parameters for the p-y curves. Table 2 presents summary of input parameters for available p-y curves. Usually, effective unit weight, γ'_w, undrained shear strength, S_u, and strain factor, ε_{50}, are needed for clayey soils. However, the required p-y parameters for sandy soils are γ'_w, friction angle, φ, and initial stiffness of p-y curve (or modulus of subgrade reaction), E_{py}.

Table 2. Summary of input parameters for available p-y curves

Soil type	Method	Input
Soft clay	Matlock [22]	Effective unit weight γ'_w, Undrained shear strength S_u, strain factor ε_{50}
Stiff clay w/ free water	Reese et al. [3]	γ'_w, S_u, p-y subgrade modulus k , ε_{50}
Stiff clay w/o free water	Reese and Welch [4]	γ'_w, S_u, ε_{50}
Sand	Reese et al. [24]	γ'_w, friction angle φ, k
Sand	Murchison and O'Neill [62]	γ'_w, φ, k
Silt (cemented c- φ soil)	Murchison and O'Neill [62]	γ'_w, Undrained cohesion c_u, φ, k, ε_{50}

Initial Stiffness of p-y Curve in Sands

The performance of piles under lateral loading has been investigated by many researchers. The use of Winkler's model [11] is a simple method based on replacing the elastic soil medium by a series of infinitely close independent springs, where the modulus of subgrade reaction, E_{py} can be defined as:

$$E_{py} = \frac{p'}{y} \quad [31]$$

where p' is the soil resistance (force per unit length of the pile) and y is lateral displacement. Terzaghi [13] performed plate load tests on 1ft. × 1ft. plates on top of the soil, and measured the coefficient of subgrade reaction, $\overline{k_{s1}}$, as:

$$\overline{k_{s1}} = \frac{p}{y} \quad [32]$$

where p is force per unit area, and y is lateral displacement. For rectangular plates Terzaghi [13] showed that:

$$k_{s1} = \overline{k_{s1}} \frac{L + 0.5}{1.5L} \quad [33]$$

Terzaghi [13] applied this concept for piles assuming that k_{s1} in horizontal direction is roughly identical to the beams resting on the horizontal surface of the same soil. Assuming "L" is infinite, the value of k_{s1} can be obtained as:

$$k_s = \frac{\overline{k_{s1}}}{1.5B} \quad [34]$$

Therefore:

$$E_{py} = \frac{\overline{k_{s1}}}{1.5} \quad [35]$$

Which leads to the values of E_{py} for different soils presented in Table 3.

Table 3. Values of E_{py} MPa (tsf) based on Terzaghi [13]

Sand	**Loose**	**Medium**	**Dense**
Dry or moist sand, limiting values	1.3-3.8 (13-40)	3.8-19 (40-200)	19-64 (200-667)
Dry or moist sand, proposed values	2.5 (27)	8.3 (87)	32 (333)
Submerged sand, proposed values	1.6 (17)	5.1 (53)	19 (200)
Clay	**Stiff**	**Very stiff**	**Hard**
Values of unconfined compressive strength, q_u KPa (tsf)	96-192 (1-2)	192-383 (2-4)	>383 (>4)
limiting values	3.2-6.4 (33-66)	6.4-12.8 (66-133)	>12.8 (>133)
proposed values	4.8 (50)	9.6 (100)	19.2 (200)

It should be noticed here that the E_{py} values obtained by Terzaghi are for the case when the soil stiffness is replaced by springs with constant stiffness, which included many simplifications.

Terzaghi [13] realized that the modulus of elasticity in sands increases linearly with depth, which can be described as follows:

$$E_{py} = n_h x \quad [36]$$

Terzaghi [13] used the deformation due to contact pressure, p', of a medium with modulus of Elasticity, E_s, for a distance of 3B to evaluate n_h as follows:

$$n_h = \frac{A\,\gamma'}{1.35} \quad [37]$$

Considering the range of effective unit weight of dry or moist sand between 1.6 g/cm^3 (dense) and 1.2 g/cm^3 (loose), and for submerged sand between 0.8 and 1.2 g/cm^3; the ranges of n_h can be obtained as shown in Table 4.

Table 4. Values of the constant of horizontal subgrade reaction, n_h MN/m3 (tcf)

Sand	Loose	Medium	Dense
Dry or moist sand, values of n_h	0.95-2.8 (3.0-8.9)	3.5-10.9 (11.1-37)	13.8-27.7 (44-88)
Submerged sand, values of n_h	0.57-1.7 (1.8-5.5)	2.2-7.3 (6.9-23.1)	8.7-17.9 (27.7-55.5)

It should be noted here that the obtained values E_{py} from Terzaghi estimations are for the case of constant stiffness in p-y curves. However, based on the p-y curve concept, the value of E_{py} starts with higher value, known as k_{ini} and the soil behavior nonlinearity can be addressed by decreasing E_{py} as the pile deflection progresses, as shown in Figure 18. It is obvious from the figure that the value of k_{ini} should be higher than the constant k values suggested by Terzaghi [13].

Figure 18. Nonlinear behavior of p-y curve

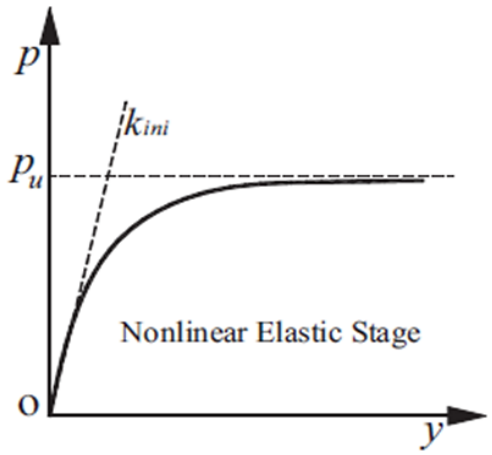

Other researchers proposed some equations for estimating the value of k in case of elastic soil behavior. Vesic [63] derived a relationship between the modulus of subgrade reaction E_{py} for the beam resting on elastic foundation (Winkler) and the pile and soil elastic properties as follows:

$$E_{py} = \frac{0.65E_i}{(1-\nu_s^2)}\left[\frac{E_i D^4}{E_p I_p}\right]^{1/12} \quad [38]$$

where E_i is initial soil modulus of elasticity, ν_s is Poisson's ratio of the soil, D is the pile width, and E_p I_p is the flexural rigidity of the pile.

The use of a constant value for k in analyzing the lateral behavior of piles is not accepted. Due to nonlinearity of soil behavior, the modulus of subgrade reaction E_{py} in the p-y curves varies as the pile deflection progresses. Reese et al. [24] reported that although E_{py} is related to the soil stiffness, E_s, it is not a soil property and its variation is a result of the soil-structure interaction.

Reese et al. [24] performed experimental field tests on piles instrumented with strain gauges. The measurements of strain gauges were used to calculate the bending moment using the following formula, which utilizes the elastic pile stiffness E_p and the sections' second moment of area, I_p:

$$M(x) = \frac{E_p I_p(\varepsilon_t - \varepsilon_c)_x}{h} \quad [39]$$

where ε_t and ε_c are the strains at the tension side and compression side, respectively; and h is the horizontal distance between the strain gage pair in the pile's section. Using a suitable curve fitting technique, the function of bending moment profile was, which was then differentiated twice to obtain the corresponding soil resistance profile. The profile of pile deflection, y, can be constructed using strain gauges or inclinometer measurements. When strain gauges are used, the profile of y can be evaluated by double integrating M as follows:

$$y(x) = \iint \frac{M(x)}{E_p I_p} dx \quad [40]$$

Similarly, when inclinometers are used, the pile's slope measurements are directly obtained. Then, using curve fitting, the slope function θ(x) is integrated once to obtain the

pile's deflection, y, with depth. The p-y curves at any depth (x) can then be obtained by combining the soil resistance, p, and the corresponding y value at different depths.

Reese et al. [24] recommended values for n_h based on their field study on open-ended piles driven in Mustang Island as summarized in Table 5. Here $k = n_h$ with $E_{py} = n_h x$. It should be noted here that Reese et al. [24] also proposed values of n_h for clayey soils. The values of nh suggested by Reese et al. [24] have been used in softwares like LPILE, in to calculate the lateral behavior of piles in sand and stiff clays in the case of presence of free water.

Table 5. Values of horizontal subgrade reaction, n_h, proposed by Reese et al. [24] for static and cyclic loading in sand

n_h MN/m^3 (tcf) [lb/in^3]	Relative density		
	Loose	Medium	Dense
Below the water table	5.4 (17) [20]	16 (52) [60]	34 (108) [125]
Above the water table	6.8 (22) [25]	24 (78) [90]	61 (194) [225]

Based on the work of Murchinson and O'Neill [62], API [64] suggests estimating n_h for p-y curves in sands from the internal friction angle (ϕ) as shown in Table 6.

Table 6. API [64] recommended values for n_h

n_h MN/m^3 (tcf) [lb/in^3]	Friction angle (ϕ)			
	25°	30°	35°	40°
Below the water table	5.4 (17) [20]	10.9 (35) [40]	22 (69) [80]	45 (143) [165]
Above the water table	5.4 (17) [20]	14 (43) [50]	37 (117) [135]	73 (233) [270]

Kim et al. [65] performed experimental measurements on the pre-installed and driven piles embedded in Nak-Dong River sand (medium and medium dense sand), located in South Korea, under monotonic lateral loadings. Based on their results, they found out that the value of nh depends on relative density of sand, pile installation method, and pile head restraint conditions. They back-calculate the values of n_h as shown in Table 7 for each pile installation and pile head restraint conditions. Their results of n_h were similar to the lower bound values recommended by Terzaghi [13].

Table 7. Values of n_h in sands proposed by Kim et al. [65]

n_h in MN/m^3 (tcf) [lb/in^3]	Relative density		
	Loose	Medium	Dense
Preinstalled (Free head)	-	4.329 (14) [16]	12 (38) [44]
Preinstalled (Fixed head)	-	21.1 (67) [78]	32.5 (103) [120]
Driven (Free head) (Driving energy 0.5J)	-	9.524 (30) [35]	18 (57) [66]
Driven (Free head) (Driving energy 1.0J)	-	16.45 (52) [61]	24 (76) [88]
Driven (Free head) (Driving energy 1.5J)	-	24.675 (79) [91]	30 (95) (111)

*Values for dry sand used in this test (medium sand with D_r=50% and unit weight of 13.13 KN/m^3 and medium dense sand D_r=73% and unit weight of 13.72 KN/m^3)

Based on Kim et al. [65] results on piles in sand, application of load-transfer curves by Reese et al. [24] and API [64] models result in stiffer responses with calculated pile head displacements being about 42% and 60% of the measured values, as shown in

Figure 19. Load transfer curves for Nak-Dong River sand for the depth of three pile diameters [65]

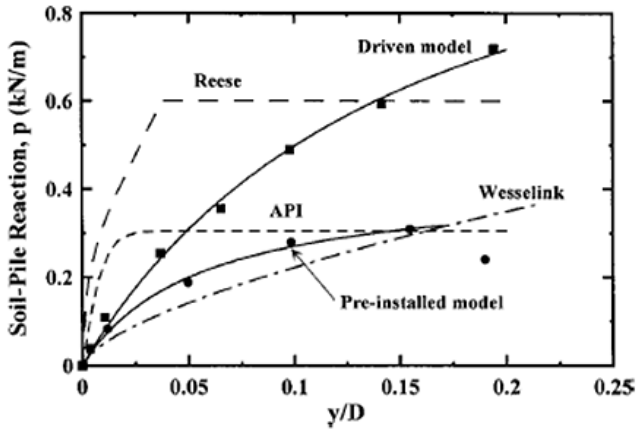

Georgiadis et al. [66] performed tests on model piles of three different diameters and flexural stiffnesses in a centrifuge apparatus to evaluate the lateral behavior of prototype pilesr under lateral loading in sand. They noticed that a value of n_h =11000 kN/m^3 is appropriate for medium dense to dense sand. They showed that the values of n_h recommended by Reese et al. [24] for submerged sand gave significantly higher initial p-y stiffnesses than those obtained experimentally for the dry sand.

Rajashree and Sitharam [67] suggested that the initial stiffness, ki, of the p-y curves is twice the value of ks proposed by Vesic's relationships and is given by the following equation:

$$k_i = \frac{1.3E_i}{(1-\nu_s^2)}\left[\frac{E_i D^4}{E_p I_p}\right]^{1/12} \quad [41]$$

Georgiadis and Georgiadis [68] argued that the value of $\nu_s = 0.5$ for undrained loading, and therefore, the value of k_i depends primarily on E_i since the term $(D^4/(E_p I_p))^{(1/12)}$ is approximately constant for most piles. Following current practice in the development of p-y curves, where the soil deformability is represented by the strain ε_{50} at 50% of the failure stress, the initial elasticity modulus E_i can be related to the elasticity modulus at 50% of the failure stress, E_{50}. This is achieved through the following well known hyperbolic expression for triaxial compression [18]:

$$E_s = E_i\left(1 - \frac{R_f \sigma}{\sigma_f}\right) \quad [42]$$

where σ is deviatoric stress, E_s is elastic modulus at deviatoric stress σ, σ_f is deviatoric failure stress, and R_f is the ratio of deviatoric failure stress over deviatoric ultimate stress, commonly taken as 0.8. Setting $R_f = 0.8$ and $\sigma/\sigma_f = 0.5$ into above equation, the relationship $E_i = 1.67E_{50}$ is obtained. Finally, the equation for k_i will be given as:

$$K_i = 3E_{50}\left[\frac{E_{50} D^4}{E_p I_p}\right]^{1/12} \quad [43]$$

Majority of existing research assumes that the initial stiffness (ki) increases linearly with depth (z) for sand deposit (i.e., [64], [69]), i.e., m=1 in below equation [70]:

$$k_i = n_i\left(z/z_{ref}\right)^m \quad [44]$$

For the overconsolidated dense sand deposits discussed by Li et al. [70], the derived p-y curves showed that the value of the initial stiffness for each depth increases insignificantly with depth. To determine the distribution of initial stiffness with depth for the overconsolidated dense sand, a power function is fitted to the in-situ measured profile of q_c with a depth down to 20 ft. They found that $10.9(z/z_{ref})^{0.35}$ fits well, where $z_{ref} = 3$ frt. Accordingly, the value of m in the above equation was recommended to be 0.35 based on correlation between k_i and q_c. This value agrees with recent studies performed by Sorensen et al. [71] and Kallehave et al. [72], which suggest that the value of m ranges from 0.3 to 0.7.

With respect to the value of n_i in Equation 44, several researchers (e.g., [66]) found that the value of initial stiffness in sand deposit is heavily overestimated by API [64], and the recommended values by Georgiadis et al. [66] and Kim et al. [65] agree well with those given by Terzaghi [13]. Therefore, n_i = 3394 psi (23.4 MPa) corresponding to z = 3 ft. (i.e., z ≈ 3D) was recommended for the overconsolidated dense sand deposit.

ε_{50} for p-y Curves in Clays

The p-y curves in clays can be described by the ultimate soil resistance, p_u, y_{50}, and the equation for the p-y curve, as described in Figure 20.

Figure 20. Description of p-y curve for clays

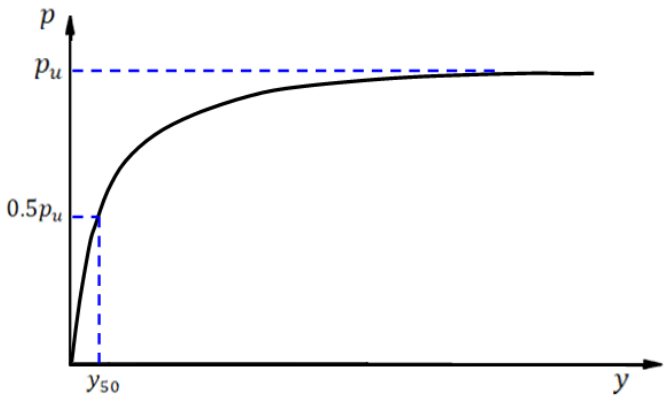

Based on Matlock [22] equation for soft clay below water, the equation of p-y curves is given as follows:

$$p = 0.5p_u \left(\frac{y}{y_{50}}\right)^{\frac{1}{3}} \leq p_u \quad [45]$$

Here y_{50} refers to the pile deflection at 50% of ultimate soil resistance (p_u) in the p-y curve. So when y reaches the value of y_{50}, the value of $p = 0.5p_u$, and when $y = 8y_{50}$, the value of $p = p_u$. It is commonly used in the p-y curve models for clays (e.g., [3], [22], [73], [74], [75]). y_{50} can be estimated using the soil property (ε_{50}) and the pile width (D) as follows:

$$y_{50} = A\varepsilon_{50}D \quad [46]$$

where A is a constant, ε_{50} is known as characteristic strain, which is the axial strain corresponding to the undrained shear strength, S_u in the UU test. Different values for A were proposed in the literature; Matlock [22] assumed A = 2.5, Reese et al. [3] used A = 1.0, Stevens and Audibert [76] suggested A = 8.9D-0.5, Dunnavant and O'Neil [74] found that A depends on the pile-soil relative stiffness and proposed A = 0.0063 $[(E_p.I_p)/(E_s.L^4)]^{-0.875}$, where $E_p.I_p$ is pile rigidity, E_s is the soil modulus, and L is pile length. Wu et al. [75] argued that A is approximately equal to the bearing capacity factor (N_p) for normally consolidated clays. As shown in Figure 21, the value of S_u/E_s can be replaced by ε_{50}.

Figure 21. Evaluation of ε_{50} from UU test.

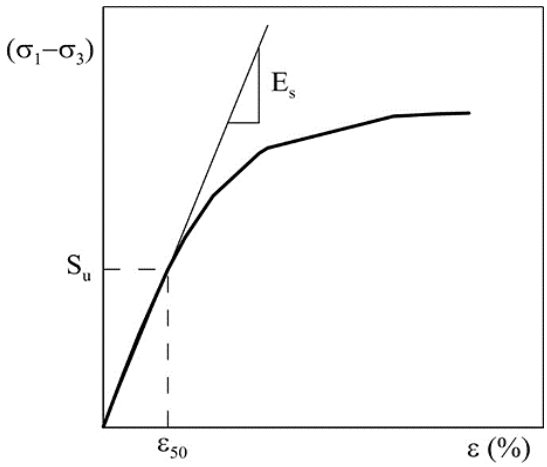

Typical stress-strain curves for normally consolidated (N.C.) clay and overconsolidated (O.C.) clay are presented in Figure 22. Also shown in figure are the secants modulus, E_s. The value of S_u for a particular test is constant; therefore, when E_s is large (at the beginning of stress-strain curve), the value of ε is small. The sharp increase in ε as E_s becomes smaller is evident in the figure. The decrease in the E_s/S_u parameter with the increase in ε is shown in Figure 23 for both normally and overconsolidated clays. Since S_u is a constant for a particular case, the curves reflect the decay in E_s.

Analytical studies presented earlier revealed the relevance of the stress-strain curve to p-y curves, in which ε_{50} was selected as the single parameter to characterize the stiffness of the stress-strain curves. The p-y curves are closer to the p-axis for smaller values of ε_{50}. Thus, the values of pile deflection will be smaller for smaller ε_{50}, especially at relatively light loads. For the relatively heavy loads, the values of ultimate soil resistance, p_u, based on values of S_u, control the results.

Figure 22. Typical stress-strain curves for NC and OC clays [3]

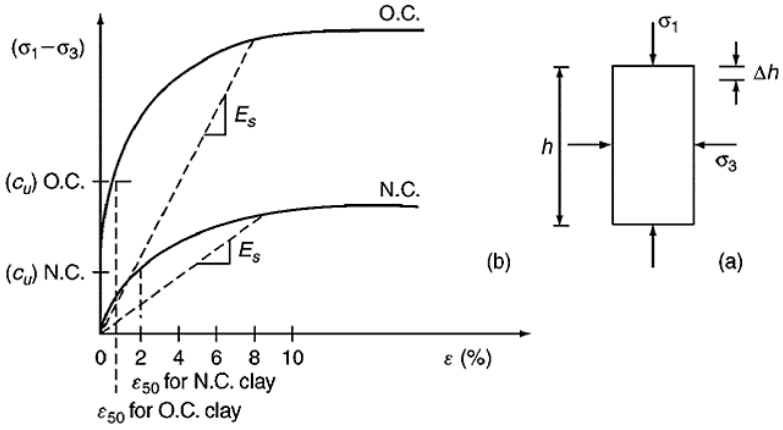

Figure 23. The ratio of E_s/S_u versus axial strain, ε [3]

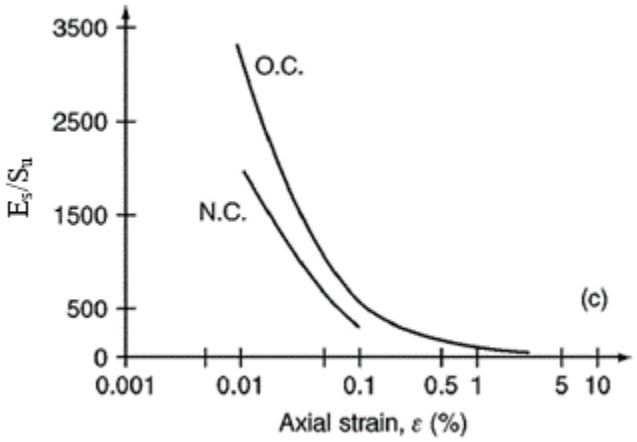

In case triaxial tests are not available on the clay for a particular site, there is some guidance in literature on how to select the value of ε_{50}. Skempton [77] studied the settlement of footings on clay and noted that the ratio E_s/S_u ranged from 50 to 200. Since $E_s = S_u/\varepsilon_{50}$ was assumed by Skempton, his values of ε_{50} ranged from 0.02 to 0.005. Matlock [22] performed experiments in soft clays and found from laboratory tests that the values of ε_{50} ranged between 0.005 and 0.20, with the smaller value being applicable to brittle or sensitive clays and the larger value applicable to disturbed soil or unconsolidated sediments. Reese, et al. [3] performed experiments on piles in stiff clays and recommended smaller values of ε_{50} than the values suggested by Matlock. Based on experimental results and the work of Skempton [77], Reese et al. [3] recommended

values of ε_{50} for N.C. clays, as shown in Table 8, and for O.C. clays, as shown in Table 9. The values recommended by FHWA for clays are presented in Table 10 [78].

Table 8. Representative values of ε_{50} for normally consolidated clays [3]

Consistency of Clay	Average value of undrained shear strength, psf (kPa)	ε_{50}
Soft	< 1000 (48)	0.020
Medium	1000 – 2000 (48 – 96)	0.010
Stiff	2000 – 4000 (96 – 192)	0.005

Table 9. Representative values of ε_{50} for overconsolidated clays [3]

	Average value of undrained shear strength, psf (kPa)		
	1044 – 2088 (50 – 100)	2088 – 4177 (100 – 200)	6265 – 8354 (300 – 400)
ε_{50}	0.007	0.005	0.004

Table 10. FHWA representative values of ε_{50} for clays [78]

Consistency of Clay	Average value of undrained shear strength, psf (kPa)	ε_{50}
Soft	250 – 500 (12 – 24)	0.020
Medium	500 – 1000 (24 – 48)	0.010
Stiff	1000 – 2000 (48 – 96)	0.007
Very stiff	2000 – 4000 (96 – 192)	0.005
Hard	4000 – 8000 (192 – 383)	0.004

In summary, the stiffness of clay and ε_{50} values should be determined by laboratory tests or by appropriate in situ tests for each site. However, in the absence of tests, values of ε_{50} may be obtained from values of undrained shear strength. Proper selection of ε_{50} value is important when computing deflection under lateral loading, especially for relatively small loads. Errors in ε_{50} are less important in computing the maximum bending moment.

Objectives

The objectives of this research can be summarized as follows:

- Develop a three-dimensional finite element model to simulate the lateral behavior of battered pile group foundations, and verify the model using the results of a unique static lateral load test that was conducted at I-10 Twin Span Bridge.
- Investigate the lateral behavior of battered pile group foundations subjected to static loads as compared to vertical single and pile group foundations.
- Investigate the lateral behavior of battered pile group foundations subjected to dynamic loads due to barge impact.
- Develop p-y curves for different soil types for use in the analysis and design of battered pile group foundations subjected to lateral loads.
- Develop guidance to select parameters and p-y curves for application in FB-MultiPier, Midas and CSIBridge/SAP2000 softwares.
- Develop rationale values of p-multipliers to incorporate the group effect in the design and analysis of battered pile group foundations subjected to lateral loads.
- Evaluate the contribution of axial loads carried by battered piles.

Scope

The objectives of this research study were achieved through conducting finite element numerical analysis. For this purpose, several three-dimensional (3D) finite element models were developed to evaluate the lateral behavior of three pile group (PG) configurations (vertical, battered, and mixed) of similar number of piles under static and dynamic lateral loading. The results of the unique full-scale lateral load test that was conducted at M19 eastbound pier foundation of the I-10 Twin Span Bridge was used to verify the 3D FE models. The nonlinear behavior of soils was incorporated using nonlinear constitutive models. The pile-soil interface was modeled using the zero-thickness interface model available in ABAQUS, which has the capability to model the gap behind the piles and the transfer of interface normal and frictional stresses.

An FE parametric was conducted on the three PG configurations to investigate the effect of row/column pile spacing and type of clay soil on the performance of pile groups in terms of group effect, p-multipliers, lateral displacement, the contribution of axial, lateral and shear forces per pile, and lateral stiffness of PGs.

A 3D FE dynamic analysis was conducted to evaluate the effect of barge impact of different speeds on the lateral performance of the three PG configurations in terms of peak lateral displacement, peak axial reaction, peak shear force, lateral stiffness of PGs, and the contribution of piles and pier columns to the total resisting force.

3D FE numerical analyses and parametric studies were also performed to develop hyperbolic p-y curve models for both clayey and sandy soils based on the soil and pile properties. Regression analyses were performed on the results of FE study to develop formulas for evaluating the ultimate lateral bearing capacity factor (N_p) and reference displacement (y_{50}) needed for the hyperbolic p-y curve model in clay soils. A combination of tangent hyperbolic and power function model was developed for the p-y curves in sandy soils based soil and pile properties.

The results of laboratory UU tests were collected from the LTRC geotechnical laboratory and DOTD material laboratory for use to develop correlations to estimate the strain at 50% stress level (ε_{50}) based on soil properties (i.e., Su, PI, LI). In addition, the results of FE study on p-y curves in sand were analyzed to develop a formula to estimate the coefficient of subgrade reaction (k) based on soil and pile properties. The k values for different sand consistency, soil condition, and friction angle were evaluated.

Methodology

Finite Element Modeling

A three-dimensional (3-D) finite element (FE) analysis was used in this study to simulate the lateral behavior of single and pile groups (vertical and battered). This method allows for modeling and analyzing complex engineering problems that are not possible to solve using traditional methods. The advantages of using FE method are: ability to model linear and nonlinear material response, ability to include more than one material type in the problem, ability to include surface-to-surface interaction between different geometries, ability to solve static or dynamic problems, and the ability to perform FE parametric studies. However, there are some limitations for the FE method such as it requires strong knowledge and expertise in the numerical methods, the output is highly dependent on the modeling choices by the user, and it requires a long time to solve large size problems.

For the current study, it was necessary to use the 3-D FE analysis. The pile-soil-pile interaction is a 3-D problem in which the surrounding piles influence the lateral response of the pile in interest. Moreover, the pile- pile spacing is a major factor in the pile-soil-pile interaction problem and can be varied in two directions (i.e., row spacing and column spacing). The components of the FE model are: problem geometry, materials constitutive model, applied loads, boundary conditions, and interface behavior. These components will be described in details in the following sections.

Problem Geometry

Establishing geometry of the FE model is the first step in the FE simulation, which is considered the basis for creating the FE mesh for the problem. The input geometry for the current study has two main parts: pile group part, and soil body part (Figure 24). Owing to the symmetry of the problem, only half of the pile group and soil body is considered in the FE model. The pile group part is composed of the pile cap and a set of piles (in 4x2 or 4x3 arrangement), which are either vertical or battered. The dimensions of the pile group model follow the design of the M19 pier foundation of the I-10 twin span bridge. Each pile has a square cross-section with 3 ft. width and is 110 ft. long. The pile to pile spacing will vary throughout the study, which will be described later in the discussion and results section. The pile cap is 7 ft. thick and has varying planar dimensions depending on the pile to pile spacing.

Figure 24. Example of pile group and soil body FE models

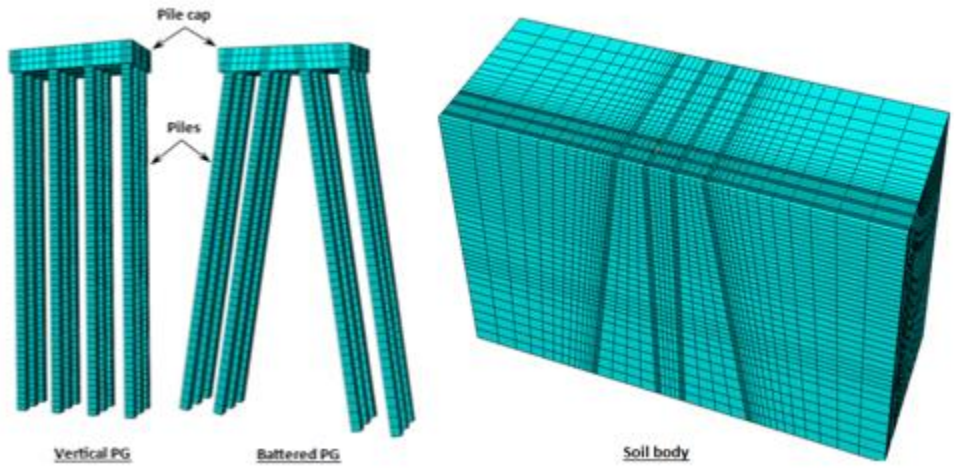

The soil body part is a solid block with cutout holes for each pile. The soil body can be treated as a single layer or multiple layers. A multiple layer soil body has planar divisions (in the global horizontal direction) for each soil layer and assumes full bond between different layers at the interface. Each layer can be assigned with different constitutive model and parameters. The dimensions of the soil body vary depending on the pile to pile spacing and are determined by finding the least dimension at which the deformation in the boundary elements is negligible.

Another special pile group model is used in the study to obtain the soil resistance for single piles. This model is composed of three piles: vertical, negative battered, and positive battered (Figure 25). The pile to pile spacing at the pile cap level is 10D (where D is the pile width), which is considered large enough to eliminate pile-soil-pile interaction. The pile's behavior in this model is assumed as the equivalent for an isolated single vertical or battered pile. The reasons for using this model is to closely simulate the fixed head pile condition in a similar way to the pile group, and save time by running single model to obtain results for three single pile cases.

Applied Load

Two types of load were applied in the FE models: gravity load and lateral load. In the initial state, the gravity load (or self-weight) should be in equilibrium with the stresses in the soil. Initializing the soil stresses is necessary because the stiffness in the constitutive models exists only under confining stress. The initial equilibrium is achieved by applying the gravity load and a predefined stress field in the soil (i.e., geostatic stress). An

acceptable equilibrium state is obtained once the deformation in the soil body due to the gravity load is negligible. The gravity load is defined by providing the gravitational acceleration (g = 32.2 ft/s^2), the density for all materials, and the direction, which is the vertical (i.e., z-dir). The lateral load is applied at the side of the pile cap to produce lateral deformation. It is defined as uniform distributed area load and is assumed in the global horizontal direction parallel to the symmetry plane.

Figure 25. Special pile group FE model for single pile results

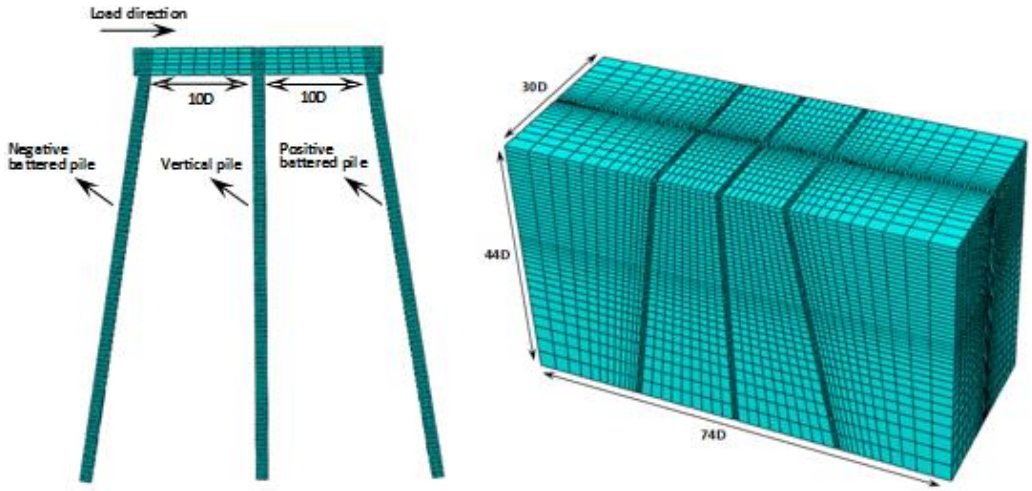

Boundary Conditions

The global static equilibrium in the FE model is enforced by applying boundary conditions. The boundary conditions are displacement constraints used on the soil body boundaries and on the symmetry plane, see Figure 26. The pin-type boundary condition was used for the far boundaries to restrain the displacement in all directions. The roller-type boundary condition was used for the symmetry plane, which constrains the displacement in one axis and the rotations on the other axes. For example, a roller-type boundary condition for the x-direction restrains the displacement in the x-direction and rotations in the y- and z- directions.

Figure 26. Displacement boundary conditions used for the soil model

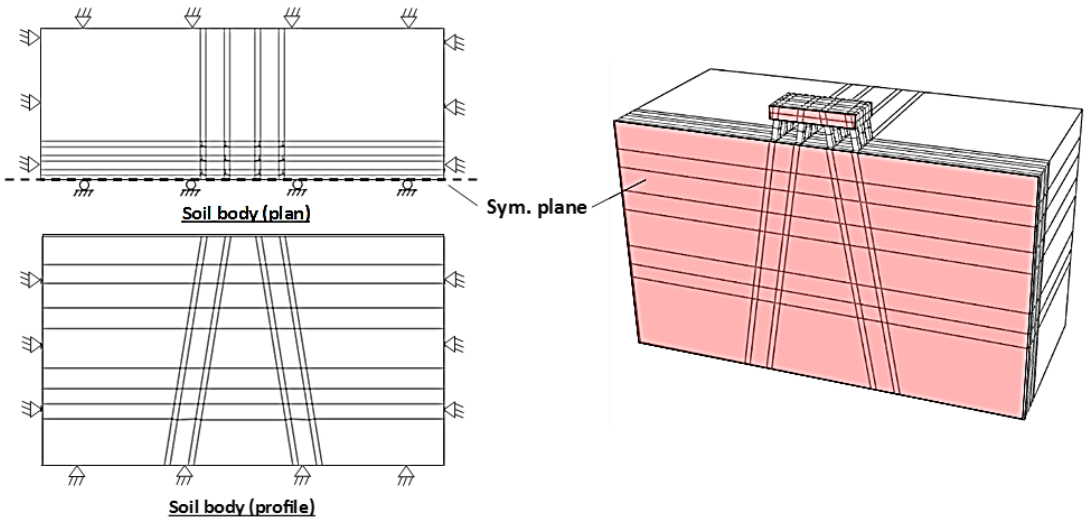

Pile-Soil Interface Model

The pile-soil interface is modeled using the contact feature in ABAQUS. There are two main mechanisms at the interface that is considered: the normal (to surface) behavior, and the tangential behavior (see Figure 27). The normal behavior refers to the interaction between the pile and soil in the direction of surface normal, which comes in the form of separation or interpenetration. For the pile-soil problem, the normal behavior should allow separation (i.e. the tensile stress is not transmitted to the soil, and hence pile-soil gap forms), and prevent interpenetration (i.e. on pile movement, bearing stress is transmitted and the soil moves at equal distance). The normal behavior is referred to as "hard contact". The magnitude of the normal stress is found by an iterative numerical procedure, which determines the global equilibrium state after an incremental pile displacement.

The tangential behavior refers to the interaction in the direction parallel to the pile-soil surface, which can be in the form of sticking or sliding (Figure 27). For the pile-soil problem, the tangential behavior in sticking mode transfers the shear stress to the soil with no relative pile-soil displacement. In sliding mode, the transferred shear stress is limited to the maximum limit with the occurrence of relative pile-soil displacement. The maximum shear stress limit for sliding (τ_{lim}) is governed by the Coulomb friction criteria characterized by the friction coefficient (μ) and the user defined ultimate friction stress (τ_{max}). The Coulomb friction criteria defined the limit as $\tau_c = \mu \sigma_n$, where σ_n is the mean

stress at the interface, μ is the coefficient of interface friction (= tan 2/3ϕ), and ϕ is the friction angle of soil.

Figure 27. Illustration of the pile-soil interface model

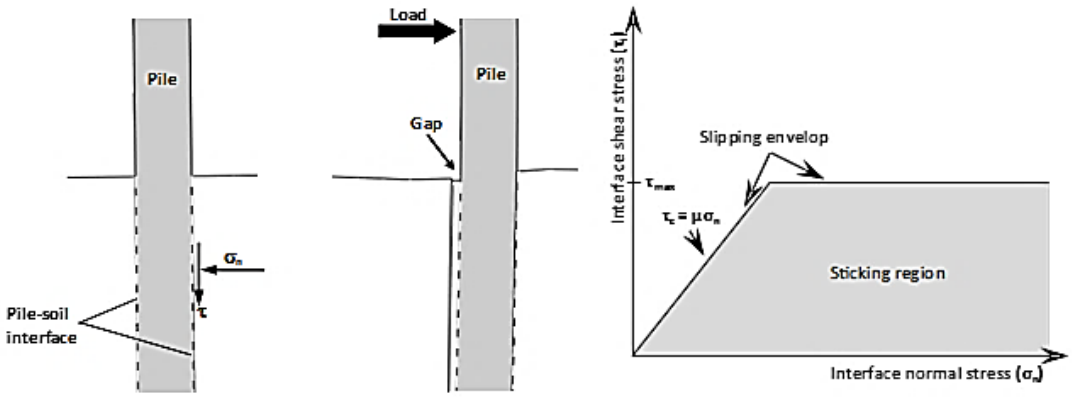

Steel Reinforcement Model

The concrete piles have main steel reinforcement (or rebars) in the form of prestressed steel strands. Each strand has 0.6-in. diameter and made of low relaxation Grade 270 steel wires [79]. In 3-D FE, the rebars geometry can be represented by either beam (line) elements (for individual rebars) or shell elements (for rebars layers). The interaction between rebars elements and concrete elements is modeled using the embedded elements technique [80]. In this technique, the nodes of the embedded (rebars) elements are tied to the host (concrete) elements nodes. Another advantage of the embedded elements technique is the ability to define the prestress force in rebars elements. The prestress force enforces an initial state of compression in the concrete elements, which eliminates the possibility of premature concrete failure in tension. The structural behavior of the embedded shell elements also mimics the behavior of individual rebars, which only carries axial forces [80]. The actual prestress force magnitude (35.1 kips per rebar) is estimated following AASHTO bridges design standards and considering 20% prestress loss from the design value. Figure 28 shows the rebars FE model and pile section detail. Each shell layer resembles nine strands for a total of 36 strands in the pile's section. The layers are positioned at 3 in. from the pile's faces.

Figure 28. Illustration of pile's section detail and rebars FE model

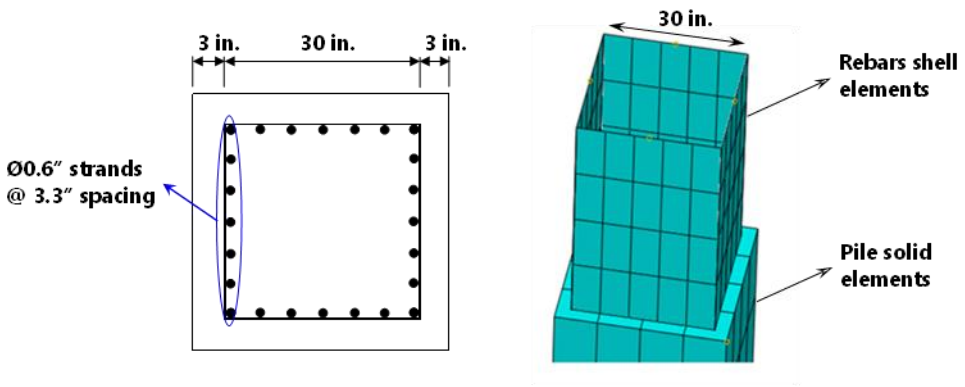

Material Constitutive Models

One of the advantages of the FE method is the ability to simulate various types of materials behavior. This is achieved by defining the constitutive model for each material, which governs the linear/non-linear stress-strain material response at the element level. The constitutive model is based on a mathematical function that relates the stress rate to the strain rate. The material constitutive models used in the FE simulation will be discussed in the following sections.

Concrete. The concrete nonlinear behavior was modeled using the concrete damaged plasticity model (CDP) available in ABAQUS. This model is plasticity based and features distinct material behavior in both tension and compression. The distinction in the concrete's tensile and compressive behavior is necessary due to the large contrast in the tensile and compressive concrete strength (typically $(f_c'/f_t') \approx 10$). The CDP model applies damage to the concrete material (i.e. reduction in the concrete elastic modulus) once failure (in tension) or yielding (in compression) is exceeded.

In damage mechanics, the effective stress ($\bar{\sigma}$) is obtained from the Cauchy stress (σ) using the scalar damage variable d as $\bar{\sigma} = (1 - d)\,\sigma$. The effective stress is used in the yield and the plastic potential functions for plasticity calculations. Numerically, the damage effect is applied to the elastic stiffness as:

$$D^{el} = (1 - d)D_0^{el} \qquad [47]$$

where D^{el} and D_0^{el} are damaged and undamaged elastic stiffness, respectively. The damage variable d is a function of two damage variables for tension d_t and

compression d_c. For multiaxial conditions, it is estimated from the damage variables d_t and d_c using the multiaxial stress factor r as:

$$(1-d) = \big(1 - d_t.(1 - w_t.r)\big).(1 - d_c.(1 - w_c.r))$$

$$r(\sigma) = \frac{\sum_1^3 \langle \sigma_i \rangle}{\sum_1^3 |\sigma_i|} \qquad [48]$$

Where $\langle\ \rangle$ are the Macauley brackets, w_t and w_c are weight factors. The damage variables d_t and d_c in the CDP model are function of plastic strains ($\varepsilon_t^{pl}, \varepsilon_c^{pl}$), and assume values in the range ($0 \leq d \leq 1$). These variables are usually determined from extensive experimental tests on concrete. In this study, concrete models available in literature are used to obtain the damage variables versus strain, as shown in Figure 29 (e.g., [81], [82]).

Figure 29. Compression damage and tension damage variables versus strain

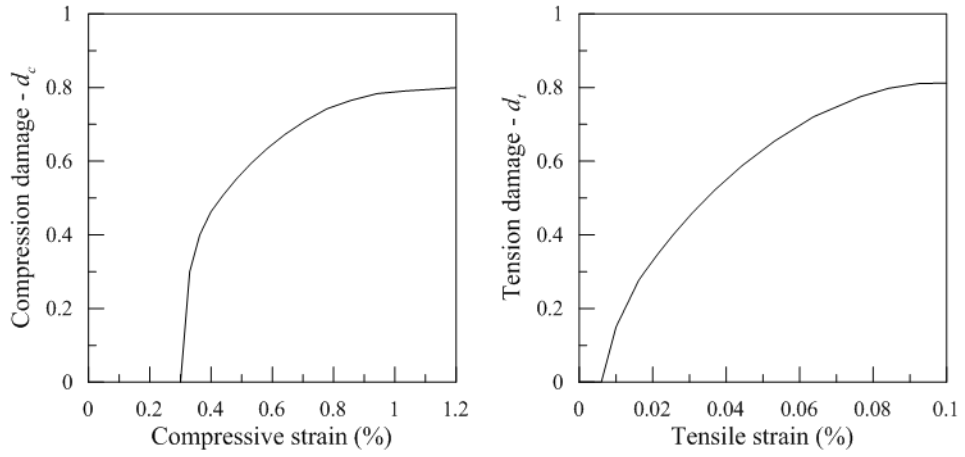

In the tension zone, the model assumes linear elastic behavior up to the failure stress σ_{to} (i.e., onset of cracking in concrete), and then followed by gradual softening in the plastic zone (called tension stiffening). In CDP model, tension stiffening is defined by providing values of the post failure stress (i.e., $\sigma > \sigma_{to}$) as a function of the cracking strain (ε_t^{ck}). The cracking strain is estimated from the total strain (ε_t) and the elastic strain.

In compression, the model assumes linear elastic behavior up to the initial yield stress, σ_{co}. In the plastic region, the concrete exhibits some hardening up to the ultimate compressive strength, σ_{cu} followed by softening. The stress-strain curve for the compression region is obtained using the analytical model by Mander et al. [81], and

following the work of Pam and Park [83] for prestressed concrete piles. The stress-strain curves for compression and tension zones are presented in Figure 30.

Figure 30. Stress-strain curves in (a) compression, and (b) tension

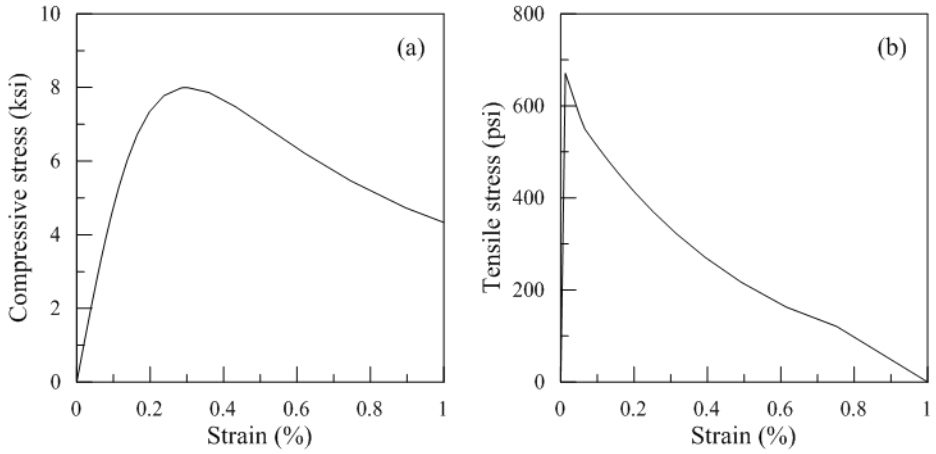

The yield function for the CDP model is the one proposed by Lubliner et al. [84] with some modifications by Lee and Fenves [85] for the evolution of strength in tension and compression. The function is given in terms of effective stress values as:

$$f = \frac{1}{1-\alpha}[\bar{q} - 3\alpha\bar{p} + \beta\langle\hat{\sigma}_{max}\rangle - \gamma\langle-\hat{\sigma}_{max}\rangle] - \bar{\sigma}_c \quad [49]$$

where $\bar{q}$ is the deviatoric component of the effective stress, $\bar{p}$ is the hydrostatic component of the effective stress, α and γ are material constants, $\hat{\sigma}_{max}$ is the maximum principal stress, and β is given as:

$$\beta = \frac{\bar{\sigma}_c}{\bar{\sigma}_t}(1-\alpha) - (1+\alpha) \quad [50]$$

where $\bar{\sigma}_t$ and $\bar{\sigma}_c$ are the effective tensile and compressive cohesion stress, respectively. The model assumes a non-associative flow rule for the calculations of the plastic strain rate.

The input parameters for the CDP model are the stress-strain curves (tension, compression parameters), the damage variables as a function of cracking/ inelastic strains, the elastic modulus, and Poisson's ratio.

Steel. The material behavior of the reinforcement steel in the prestressed concrete piles is modeled using the classical elastoplastic von Mises model. This model is suitable for metals that exhibit similar behavior under monotonic tensile or compressive loading [86]. The model assumes isotropic linear elastic behavior up to the yield stress point. The plastic behavior is triggered by the yield surface which is mathematically written as:

$$f = J_2^2 - k^2 \qquad [51]$$

where J_2 is the second invariant of the deviatoric stress tensor ($=\sqrt{3/2\ s_{ij}s_{ij}}$), s_{ij} is the deviatoric stress tensor, k is estimated from the uniaxial yield strength as $\sqrt{2/3}\ \sigma_y$. The yield function has the shape of a cylinder in the 3-D principal stress space, and the radius of the cylinder is k, see Figure 31.

Figure 31. Von Mises yield surface in the 3-D principal stress space

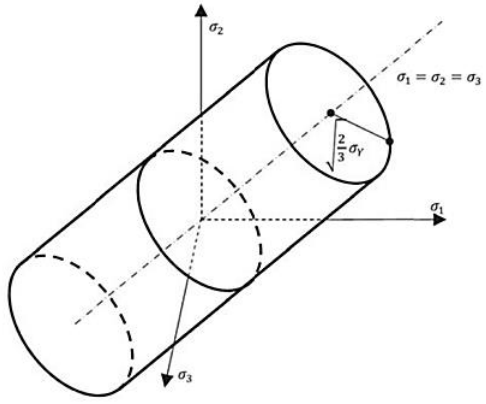

Clay. Natural clays tend to have a certain degree of anisotropy which develops during deposition, one-dimensional consolidation, and any subsequent straining (e.g., [87]). There are two forms of anisotropy in soils: inherent anisotropy from natural deposition, and induced anisotropy due to straining. The anisotropic modified Cam clay (AMCC) model is able to account for the anisotropic behavior of clays. The AMCC model is based on the modified Cam-clay (MCC) model, which is derived from the critical state soil mechanics [88]. It incorporates a specialized rotational hardening rule for the yield surface, which allows simulating the anisotropy of naturally deposited soils [89]. The yield function for multi-dimensional stress space of the AMCC model in terms of effective stress as suggested by Dafalias et al. [90] is given as:

$$f = \frac{3}{2}(s_{ij} - p'\alpha_{ij})(s_{ij} - p'\alpha_{ij}) - (M^2 - \frac{3}{2}\alpha_{ij}\alpha_{ij})p'(p'_0 - p') \quad [52]$$

where p' is the effective hydrostatic (or mean) stress component ($p'=\sigma_{ii}/3$), s_{ij} is the deviatoric stress, M is the slope of critical state line in the triaxial stress space, p'_0 is the preconsolidation pressure, α_{ij} is the non-dimensional deviatoric anisotropy tensor. The critical state line slope M acquires different values for triaxial compression (M_c) and extension (M_e). This can be achieved by means of the Lode angle (θ). Using Argyris et al. [91] proposition, the slope of the critical state line in the multi-dimensional stress space can be adjusted according to the following formula:

$$M = \left[\frac{2n}{(1+n) - (1-n)cos3\theta}\right] M_c \quad [53]$$

where $n = M_e/M_c$ (0.8 is typically assumed), triaxial compression occurs when θ=0, and triaxial extension occurs when $\theta = \pi/3$.

The kinematic hardening variable is the anisotropy tensor α_{ij}, which represents the inclination of the yield surface in the stress space as shown in Figure 32.

Figure 32. AMCC yield surface shape in the triaxial stress space

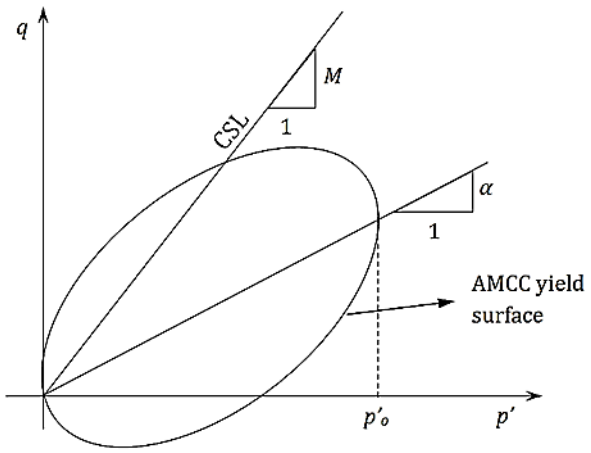

The inherent part of soil anisotropy is incorporated by defining an initial value for α_{ij}, while the induced part develops during elastoplastic loading. The initial value for α_{ij} tensor components can be estimated from the initial stress state condition. The induced anisotropy develops during loading with the evolution of the anisotropy tensor α_{ij} is given as:

$$\dot{\alpha_{ij}} = \langle L \rangle \left(\frac{1+e_0}{\lambda-\kappa}\right) C \left(\frac{p'}{p'_0}\right)^2 \left|\frac{\partial \Pi}{\partial \sigma_{ii}}\right| \left[\sqrt{\frac{3}{2}(r_{ij}-x\alpha_{ij})(r_{ij}-x\alpha_{ij})}\right] \left(\alpha_{ij}^b - \alpha_{ij}\right) \qquad [54]$$

where C and x are material constants which control the evolution rate, α_{ij}^b is the bounding anisotropy tensor which limits the values of α_{ij} to guarantee the existence of real stress states σ_{ij}. The model parameters C and x are typically determined from CKo triaxial test results.

Sand. The well-known Drucker-Prager (DP) constitutive model is best suited for pressure dependent materials [86]. Cohesionless materials such as sand are known to have small cohesion strength, negligible tensile strength, and become stronger with increasing confining pressure (i.e. pressure dependent).

The elastic part of the DP model is governed by the hypoelastic stress-strain relationship, similar to AMCC model. The plastic strain is triggered by the DP yield surface, which has a distorted cone shape in the 3-D stress space as shown in Figure 33. The yield function of the DP model is given as:

$$f = t - p' tan\beta - d \qquad [55]$$

where p' is the mean component of the effective stress, **d** is the internal cohesion, β is the friction angle for the DP model, which is related to the friction angle for Mohr Coulomb criteria [tan β = (6sin ϕ)/(3 – sin ϕ)], and t is the deviatoric stress measure defined as:

$$t = \frac{q}{2}\left[1 + \frac{1}{K}\left(1 - \frac{1}{K}\right)\left(\frac{r}{q}\right)^3\right] \qquad [56]$$

where $q = \sqrt{\frac{3}{2}s_{ij}s_{ij}}$, r $= \sqrt[3]{\frac{9}{2}s_{ij}s_{jk}s_{ki}}$, K is the ratio of yield in triaxial extension and triaxial compression (typically K =0.8).

Figure 33. Drucker-Prager yield surface in the 3-D stress space

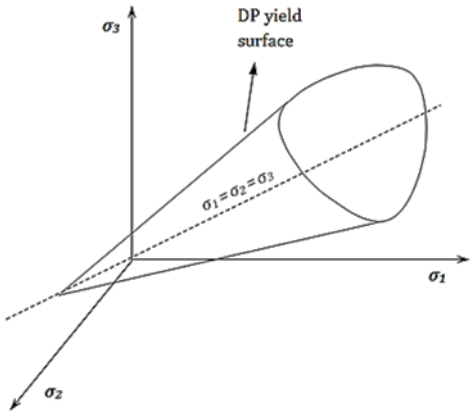

A non-associative flow rule is assumed in the DP model, which controls the dilative behavior during the plastic flow. The plastic potential function is given as:

$$\Pi = t - p' tan\psi \qquad [57]$$

where ψ is the angle of dilation, which is typically $\psi = \phi/3$.

Simulation of Barge Impact

Introduction

Vessel-bridge collisions have become a serious issue due to the increasing number of inland vessels passing underneath bridges over waterways, especially after several serious accidents since the 1960s. For example, one of the catastrophic incidents was the collapse of the Sunshine Skyway Bridge in Florida in 1980 after the collision of a freighter into one of the bridge piers [92]. The current AASHTO bridge design guideline requires all bridge components in a navigable waterway crossing to be designed for vessel impact [44]. Determination of loads from vessel-bridge collision should consider factors such as size, type, and frequency of vessels passing, bridge and channel geometry, available water depth, vessel speed and direction, the structural response of the bridge [93]. The AASHTO design impact force (equivalent static force) from barges is estimated using empirical relations based on kinetic energy (KE) and barge bow crush depth (a_B)

$$KE = \frac{C_H W_B V_B^2}{29.2} \qquad [58]$$

$$a_B = 10.2\left(\sqrt{1+\frac{KE}{5672}}-1\right) \quad [59]$$

$$P_B = \begin{cases} 4112a_B \ , & \text{for } a_B < 0.34 \\ 1349 + 110a_B \ , & \text{for } a_B \geq 0.34 \end{cases} \quad [60]$$

where KE is the kinetic energy (kip-ft.), C_H is the hydrodynamic coefficient (= 1.05 for draft ≥ 0.5 ft., 1.25 for draft ≤ 0.1 ft.), W_B is the barge weight (ton), V_B is the barge speed (ft./s), a_B is the bow crush depth (ft.), P_B is the equivalent static impact force (kips).

In the past two decade, several numerical and experimental studies investigated the impact load from barges and the factors affecting it such as speed, pier column shape and width, vessel weight, and bow stiffness (e.g., [94], [95], [96], [97], [98]). The main focus of these studies was to propose and validate a simplified model to predict the impact load magnitude. The most versatile studies were performed by the research group at the University of Florida, in which they used both experimental and numerical methods to study and validate the prediction models for the barge impact problem ([94], [99]). Their numerical results indicated that the current AASHTO equivalent static force model underestimates the magnitude of impact force for low to moderate energy impacts and overestimates it for high energy impacts. They also found that the shape of the impacted pier has a significant influence on the peak impact force [99].

In this study, FE numerical models were developed to study the lateral behavior of pile groups subjected to barge impact using the case of pier M19 of the I-10 twin span bridge. In these models, the superstructure, pile group foundation, and the soil body were included for the vertical, battered, and mixed pile group cases.

Additional Considerations for Dynamic FE Simulations

Modeling of Far Boundaries. For problems with semi-infinite domains, the FE model boundaries defined with displacement constraints have to be far enough from the studied region to eliminate their influence on the response. The optimum mesh size is selected as the smallest mesh at which the influence on the response becomes negligible. This approach is commonly used for static problems. However, for dynamic problems another issue arises from the reflection of stress waves by the boundaries, which interferes with the model response. This issue is avoided by using a combination of spring and dashpot

elements connected to the ground at the boundaries (Figure 34). The spring elements provide the reaction to satisfy the global force equilibrium, while the dashpot elements provide the dissipation mechanism for the stress waves traveling toward the domain boundaries.

Alternatively, ABAQUS library provides a special type of elements called “infinite elements” (Figure 34). The infinite elements, which are similar to the standard solid continuum elements in their nodal structure, have modified numerical formulation that dissipates the energy from the stress waves akin to a dashpot. In the current study, the linear infinite elements with eight nodes (CIN3D8) was used on the far boundaries of the soil body.

Figure 34. Modeling of FE model boundaries in dynamic problems using spring-dashpot elements or infinite elements

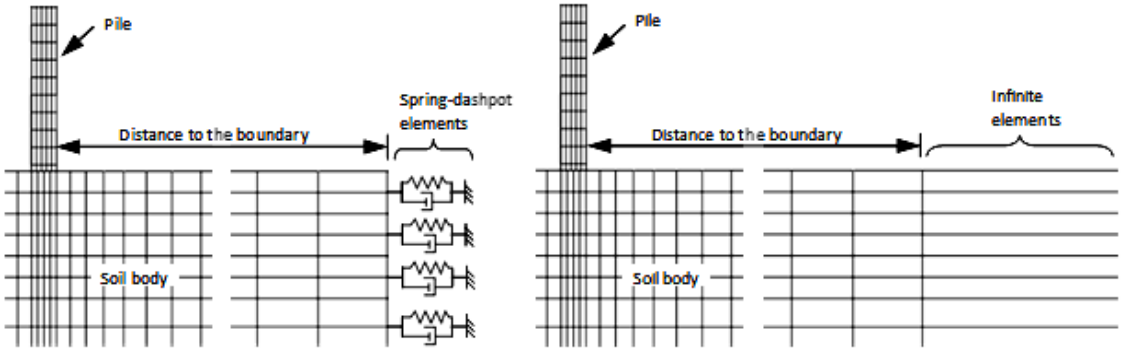

Material Damping. Damping is one of the energy dissipation mechanisms that cause the attenuation of propagating stress waves. The influence of damping in soils is more prominent during cyclic events such as earthquakes or vibrations. The damping property for soils is represented by the damping ratio (ξ), which can be estimated from the results of cyclic shear tests [100]. The main factors affecting the damping ratio in soils are the strain amplitude, effective confining stress, void ratio, and number of cycles.

In FE modeling, the effect of damping can be incorporated using the Rayleigh damping model, which is a simplified approach to introduce damping in FE models. The Rayleigh damping model approximates the damping matrix [C] in the dynamic governing equation as a linear combination of the mass [M] and stiffness [K] matrices [101]:

$$[M]\{\ddot{u}\} + [C]\{\dot{u}\} + [K]\{u\} = \{F\} \quad [61]$$

$$[C] = \alpha[M] + \beta[K] \quad [62]$$

where $\ddot{u}$, $\dot{u}$, and u are the acceleration, velocity, and displacement vectors, respectively, $\{F\}$ is the external force vector, α and β are the mass and stiffness proportional damping constants.

The damping ratio (ξ) is estimated using α and β in the two-parameters Rayleigh damping model as:

$$\xi_i = \frac{\alpha}{2\omega_i} + \frac{\beta\omega_i}{2} \quad [63]$$

where *i* is the mode number, and ω_i is the circular frequency. The first term in the RHS of equation is the mass proportional part of the Rayleigh model, which mainly dampens the response in the low-frequency range; while the second term is the stiffness proportional part mainly dampens the response in the high-frequency range. The equation estimates the damping parameters (α and β) at a certain frequency. However, the FE model response covers a range of frequencies. Therefore, the damping is introduced for the selected frequency range 1-10 Hz, which typically applies for soils. For frequency range damping, the constants α and β are alternately determined as [102]:

$$\bar{\xi} = \frac{\frac{\alpha}{2}\ln\left(\frac{\omega_1}{\omega_n}\right) + \frac{\beta}{4}(\omega_n^2 - \omega_1^2)}{\omega_n - \omega_1} \quad [64]$$

$$Var(\bar{\xi}) = \frac{(\omega_n - \omega_1)\left[\frac{\alpha^2}{4}\left(\frac{1}{\omega_1} - \frac{1}{\omega_n}\right) + \frac{\beta^2}{12}(\omega_n^3 - \omega_1^3) + \frac{\alpha\beta}{2}(\omega_n - \omega_1)\right] - \bar{\xi}^2}{(\omega_n - \omega_1)^2} \quad [65]$$

To solve for α and β in Equations 64 and 65, an average value for the damping ratio is assumed first, and then the constants are determined using an iterative procedure to minimize the variance.

Data Sampling and Filtering. The numerical solution using explicit schemes proceeds in very small increments, which is dependent on the smallest element size and the propagation speed of stress waves. Requesting data output at every time increment results

in huge output file size, which makes the access time for the computer very long and consumes the computer's main memory. Therefore, the user chooses to store the output data at spaced time intervals, which usually referred to as sampling. Care must be taken when choosing the frequency of sampling to avoid the signal corruption by aliasing (Figure 35). Aliasing occurs due to the sampling of the source signal at a frequency below the limit defined by the Nyquist sampling rate (f_{Nyq}) and the maximum frequency (f_{max}) of interest in the source signal.

Figure 35. Sampling can lead to signal corruption by aliasing

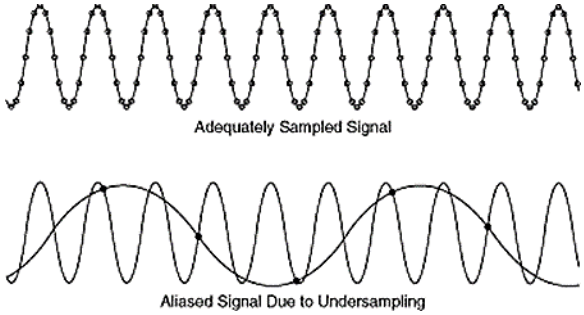

To avoid aliasing the following rules apply: $f_s > 2f_{max}$, and $f_{Nyq}=f_s/2$; where f_s is the sampling frequency. The value of f_{Nyq} defines the minimum sampling frequency to avoid signal corruption by aliasing. For the barge impact problem, the frequency range of interest is within 1-10 Hz, and therefore, the chosen sampling frequency is 100 Hz.

The output from the dynamic FE analysis in the postprocessing contains a spectrum of frequencies with unwanted components in the high-frequency range, which referred to as noise. Noise can be removed from the signal using a low-pass digital filter, which performs mathematical operations to remove the frequency content above a user-defined frequency limit called the cutoff frequency. Examples of well-known low-pass digital filters are the Butterworth and Chebyshev filters. Ideally, it is desired that the digital filter removes all frequencies above the cutoff frequency from the signal. The cutoff frequency can be determined by several approaches such as the residual analysis method [103], and the Jackson knee method [104].

In this study, the residual analysis method was adopted for its simplicity and ease of implementation in spreadsheets. In this method, the signal is filtered at regularly increasing cutoff frequencies (i.e., 1, 2, 3..., up to 0.5 fs), and then the residual is estimated for each filtered signal as:

$$R(f_c) = \sqrt{\frac{\sum(X_i - \hat{X}_i)^2}{N}} \quad [66]$$

where X_i and $\hat{X}_i$ are the unfiltered and filtered signal data points, respectively, and N is the total number of signal data points.

The residual function $R(f_c)$ is then plotted against the cutoff frequency f_c to graphically determine the optimal cutoff frequency. The Butterworth digital filter was used in this study for its availability and simplicity. This is because it requires defining only the cutoff frequency unlike the Chebyshev filter, which requires defining two additional constants.

Discussion of Results

Verification of the Static Load Test at M19 Pier Foundation

The developed FE model was used to simulate the static load test that was conducted at the M19 eastbound pier of the I-10 Twin Span Bridge over Lake Pontchartrain, LA [105]. A 3-D model of the M19 pile group foundation was developed and verified using the experimental results from the field test. The results obtained from the field test are limited to (1) displacement profiles for some piles, (2) and bending moment at two elevation level from strain gages. The FE simulation provided additional results for each pile in the pile group such as complete bending moment profile, axial and shear forces profiles, and visualization of damage zones. Furthermore, the soil resistance was deduced from the shear force profile from FE.

Description of the Lateral Load Test of M19 Pier Foundation

The static lateral load test is briefly described here. For more details, the reader can refer to Abu-Farsakh et al. [105]. The lateral load test was conducted on the M19 eastbound pier of the I-10 Twin Span Bridge. The pier comprised of 24 prestressed concrete battered piles arranged in 4×6 configuration (Figure 36). The adjacent rows of piles were battered at slope of 1H:6V, so that two rows were battered to the southeast and the other two to the northwest. Each pile was 110 ft. long (at casting) and had 3 ft. × 3 ft. square section. The pile spacing at the cap level was 4.3D between rows and 2.5D between columns. The average embedded length of the piles was 87 ft., and the mudline was located 11 ft. from the bottom of the pile cap. The pile cap dimensions were 44 ft. L × 42.5 ft. W × 7 ft. D. Figure 36 presents the layout and numbering of the piles for the pile group foundation. Numbers are used for columns, and L/ML/MT/T refers to leading, middle-leading, middle-trailing, and trailing rows, respectively. A column refers to the piles arranged in the line parallel to the lateral load direction; while a row refers to the piles arranged in the transverse direction to the lateral load. Some of the piles were instrumented with strain gages (SGs) and/or in-place inclinometers (IPI) (Figure 36). The SGs were initially installed in pairs at 16 and 21 ft. from the pile top at the time of casting. Considering an average cutoff length of 6.5 ft. in the piles, the final location of the SGs was estimated at 9.5 and 14.5 ft. from the bottom of the pile cap. The inclinometers were installed over the pile length at the following levels: 5, 15, 25, 35, 45, 65 ft. from the bottom of the pile cap.

Figure 36. Schematic of the lateral load test setup, and piles numbering and instrumentation (After Abu-Farsakh et al. [105])

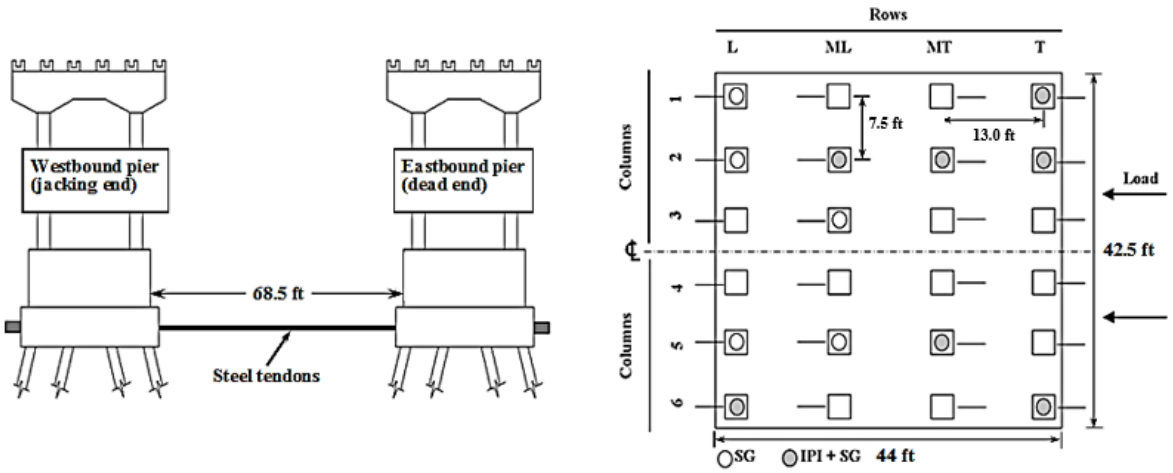

The lateral load test was conducted by pulling the eastbound and westbound piers toward each other using high strength steel tendons run through two 4-in. PVC pipes installed in both pile caps. The steel strands were first anchored at the dead-end side, and then were threaded one-by-one through the two 4-in. PVC pipes from the dead-end at the M19 eastbound pier toward the hydraulic jacks of the live-end at the M19 westbound pier. The total lateral load was applied incrementally and designed to reach a maximum of 2000 kips. However, the maximum load achieved was 1870 kips because one of the strand jacks reached its maximum stroke.

The subsurface soil conditions for the M19 pier were characterized by means of in-situ and laboratory tests; this includes soil boring, laboratory testing, standard penetration tests (SPT), and cone penetration tests (CPT). The site investigation revealed that the subsurface soil stratigraphy consists mainly of medium-to-stiff silty clay to clay soil down to about 100 ft. deep with a layer of medium dense sand between 38 and 49 ft. below the mudline. A dense sand layer was found at depths greater than 100 ft. below the mudline. Figure 37 shows the soil stratigraphy and the CPT profile.

Finite Element Model Description

A 3-D geometry of the M19 pier and the soil domain was created using the ABAQUS software (Figure 38). Owing to the symmetry in both load and geometry, only half of the M19 pier foundation was modeled. Roller-type boundary conditions were applied at the soil domain boundaries and the symmetry plane as shown in Figure 38. The dimensions

of the soil domain were 220 ft. L x 80 ft. W x 120 ft. D. The size of the soil domain was checked to be large enough to eliminate the boundary effects. The mesh was designed to be finer near the piles and gradually become coarser near the boundaries. The geostatic (or in-situ) stresses were first established by applying gravity load on both soil and pile models, and then performing a static equilibrium step. Once equilibrium was achieved, the lateral load was applied incrementally on the side of the pile cap as: 570, 770, 970, 1180, 1580, 1745, 1870, 2500, 3500, 4500, 5500 kips. The lateral load increments up to 1870 kips followed the field test loading sequence. The soil-pile interaction was introduced using ABAQUS's contact feature, which allows soil-pile separation and models frictional behavior at the interface. The frictional behavior was governed by the classical Coulomb friction law with coefficient of interface friction, $\mu = \tan \delta = 0.5$, where δ is the angle of interface friction.

Figure 37. Soil stratigraphy and CPT profile

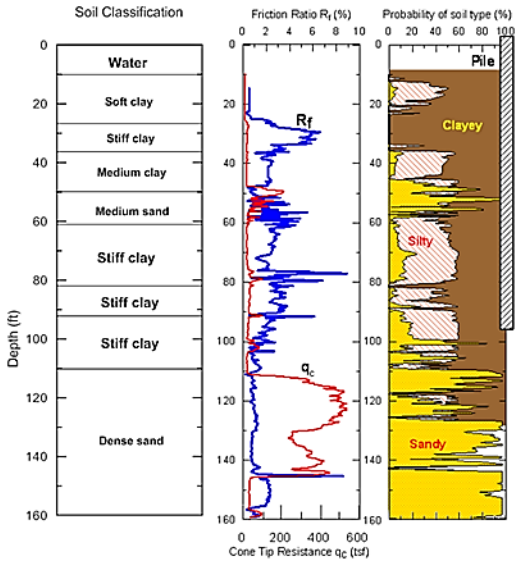

Pile Group Model. The pile group model comprised of 10206 linear continuum brick elements (C3D8R). Two constitutive laws for the concrete were used at the same time: linear elastic, and concrete damaged plasticity (CDP). The main advantage in CDP is it allows distinct behavior in tension and compression, which is a major aspect of the concrete material behavior that allows better simulation of the nonlinear concrete behavior. The linear elastic law was chosen for the pile cap, and the CDP model was used for the piles. The value of Poisson's ratio for both linear elastic and CDP models was 0.2.

Figure 38. Geometry and mesh of the FE model for the battered pile group

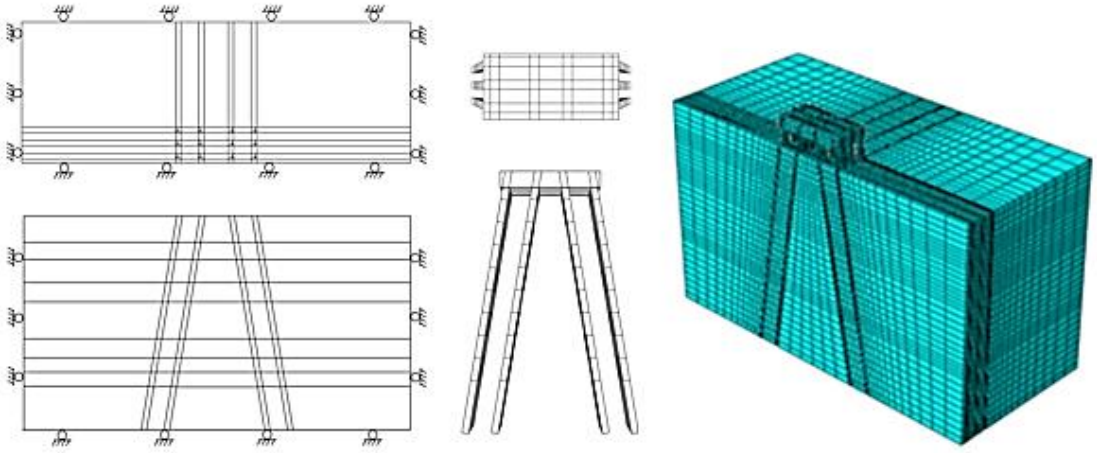

Steel Reinforcement in Piles. The piles were built with prestressed steel strands as the main reinforcement. Each steel strand was made of seven-wire, low relaxation Grade 270 bundled steel strands, and had a diameter of 0.6 in. The total number of strands per pile was 36 spaced at 3.3 in., and the concrete cover was 3 in. The estimated prestress force per strand after considering the prestress losses was 35.1 kips. The steel reinforcement was modeled using embedded shell elements (S4R), as described earlier. The von Mises elastic-perfectly plastic model was used to describe the behavior of the steel material. The elastic properties used were Young's modulus E_s = 29000 ksi, Poisson's ratio ν = 0.2, and the yield stress was 234 ksi [79].

Soil Models. The soil domain was composed of eight layers: six clay and two sand layers. The soil domain was modeled using linear continuum brick elements (C3D8R) with a total of 72160 elements. The constitutive laws for the soil layers were the Anisotropic Modified Cam-clay (AMCC) model for clays [90], and the Drucker-Prager elastic-perfectly plastic model for sand. The parameters for both AMCC and DP models and the soil layering are summarized in Table 11. The parameters (κ, λ, K_o, β) were estimated with the aid of the CPT results and correlations found in the reference for CPT [106]. For the DP model, d' represents the cohesion in the sand material, which was assumed 10 psf to avoid numerical problems. The constants x and C were reasonably assumed following Dafalias et al. [90].

Table 11. AMCC and DP model parameters

Soil Type	Depth from Mudline (ft.)	Total Unit Weight (pcf)	Poisson's ratio (ν)	K_0	AMCC						DP		
					α_{ini}	M	κ	λ	χ	C	κ	β	*d*' (psf)
Soft Clay	0-15	123	0.25	0.95	0.034	0.9	0.03	0.14	1.33	4	-	-	-
Stiff Clay	15-25	119	0.20	0.85	0.111	1.1	0.01	0.12	1.33	4	-	-	-
Medium Stiff Clay	25-38	108	0.25	0.73	0.219	1.0	0.02	0.13	1.33	4	-	-	-
Medium Sand	38-49	120	0.38	0.70	-	-	-	-	-	-	0.003	53	10
Stiff Clay	49-70	113	0.20	0.65	0.271	1.2	0.01	0.12	1.33	4	-	-	-
Stiff Clay	70-81	122	0.20	0.65	0.271	1.2	0.01	0.12	1.33	4	-	-	-
Stiff Clay	81-99	128	0.20	0.60	0.363	1.2	0.01	0.12	1.33	4	-	-	-
Dense Sand	>99	124	0.40	0.60	-	-	-	-	-	-	0.003	58	10

Results and Discussion

The FE model was verified using the results from the lateral load test conducted on the M19 pier (i.e., displacement profiles from IPIs, and bending moments from SGs). Furthermore, additional lateral load was applied in the FE model to induce more deformation and to study the lateral behavior of the battered pile group under extreme load conditions. In addition to deflected shapes and bending moments, internal forces such the axial and shear forces in the piles, soil resistance, and p-y curves were extracted.

Load-Displacement Curves. The lateral load versus displacement for the pile cap and the average for each row in the pile group are presented in Figure 39. Recall that the maximum lateral load from the field test was 1870 kips. Good agreement was observed between the FE results and the field test measurements. The cap displacement from the experiment at 1870 kips was 0.65 in. compared to 0.76 in. from the FE model. In the FE simulation, the lateral load was further increased until the piles were severely damaged. The maximum lateral load achieved in the FE model was 5500 kips, which resulted in pile cap displacement of 2.9 in. Figure 39 also depicts the average lateral load carried by the piles in each row, which shows that the middle rows (ML, MT) carried larger lateral load compared to the leading (L) and trailing (T) rows. It is noticed that rows ML and MT carried approximately similar load percentage, which also applies to rows L and T. At 5500 kips, the average lateral load percentage carried by each row was 22%, 31%, 28%, and 20% in rows L, ML, MT, and T, respectively. The distribution of lateral load per row observed for battered piles is different than the case of vertical piles groups. For vertical pile groups, the largest share of lateral load is usually carried by the leading row followed by the 2nd, 3rd, and 4th rows, respectively (i.e., [20], [47], [107]). The difference can be attributed to the effect of batter angle, which modifies the mechanism of lateral resistance

in battered piles. In vertical case, the pile resists the lateral load by carrying shear load only, while in the battered case the pile carries both axial and shear loads.

Figure 39. Load-displacement curve at pile cap level

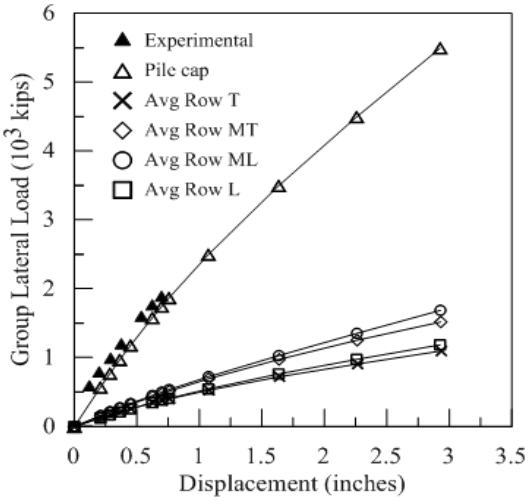

Damage in Piles. The CDP constitutive law introduces damage by reducing the concrete modulus when tension and/or compression exceed the strength limit. In the current FE study, only damage from tension was observed since the tensile strength is significantly smaller than the compressive strength. The first elements to get damage were in row MT piles at 3500 kips, and located 5 ft. below the pile cap. Figure 40 shows the damage progression in the piles with lateral load. The damage was first appeared in row MT at 3500 kips, followed by rows T and L at 4500 kips, and finally in row ML at 5500 kips. At 5500 kips, the damaged area expanded to elements further below the 5 ft. The FE analysis was aborted at a total lateral load less than 6000, which suggests that the 5500 kips is the maximum lateral load of the pile group.

The damage sequence in the rows can be explained by investigating the axial load carried in each pile. Figure 41a summarizes the variation of the axial load in each pile with increasing group lateral load. In the figure, positive axial load means compression; while negative is tension. The axial loads in the leading rows (L and ML) were in compression and increased with increasing the lateral load; while in the trailing rows (T and MT), the axial loads increased in tension. Additionally, it is noticed that the edge piles (column 1) were subjected to the largest magnitude of axial loads among other piles in the same row. For the damage sequence, piles in row MT were the first to get tension damage due to the relatively large tensile axial load, which in combination with bending moment initiated

tension-damage earlier than other rows. The second to experience tension-damage was the trailing row (T), which was subjected to a lesser tensile axial load. Lastly, the leading rows (L and ML) exhibited damage at later stages due to the compressive axial load, which counteracts the action of the bending moment. Moreover, within the same row, the edge piles (column 1) received more damage compared to the interior piles (columns 2 and 3) due to the larger bending moment. For example, Figure 41b shows the bending moments developed at the top of piles in the leading row (L). The edge pile (L1) carried larger bending moment (8% more) compared to the interior piles (L2 and L3).

Figure 40. Damage progression in the piles with increased loading

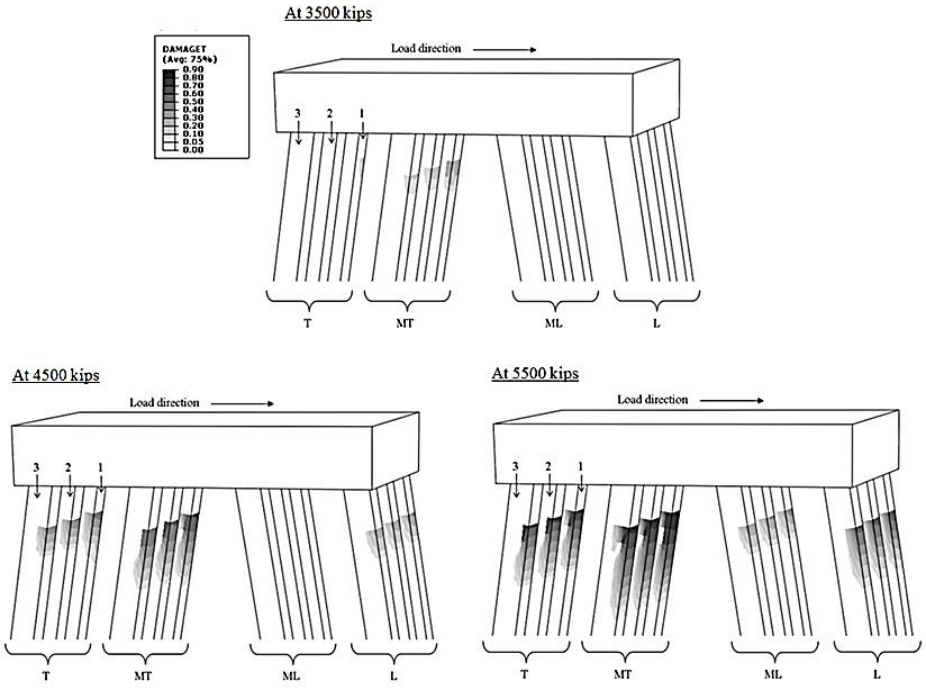

Lateral Displacement Profiles. The lateral deformation profiles for piles L6, ML2, MT2, T1, and T2 are shown in Figure 42. Note that the results of pile L6 from the full-scale test are compared to the mirror or symmetry pile L1 from the FE model. The deflected shapes are shown for two load levels: 1870 kips from the field test and FE, and 5500 kips from FE analyses only. Good agreement can be observed between the FE results and field test at 1870 kips. It can be noticed that the majority of the deformation occurred within the clay layers (11 - 49 ft.), and diminished at the (medium dense) sand layer located at 49 - 60 ft. below the mudline.

Figure 41. Variation of the axial reaction and bending moment in row L

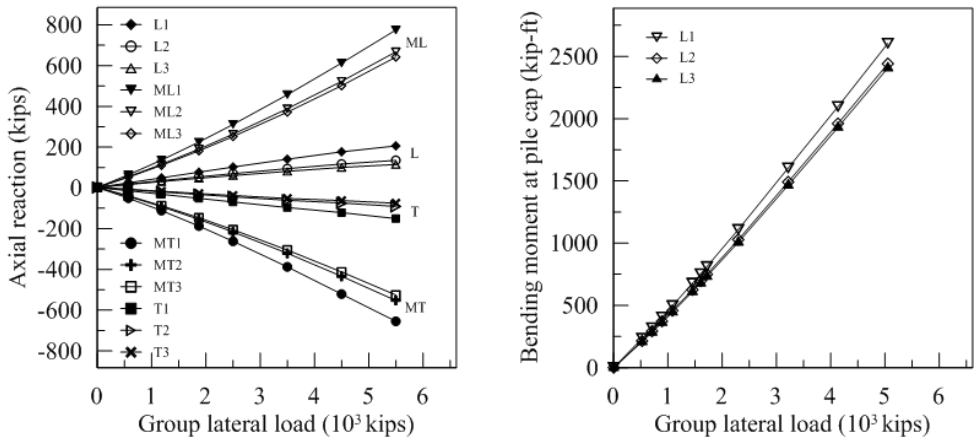

Figure 42. Displacement profiles for instrumented piles

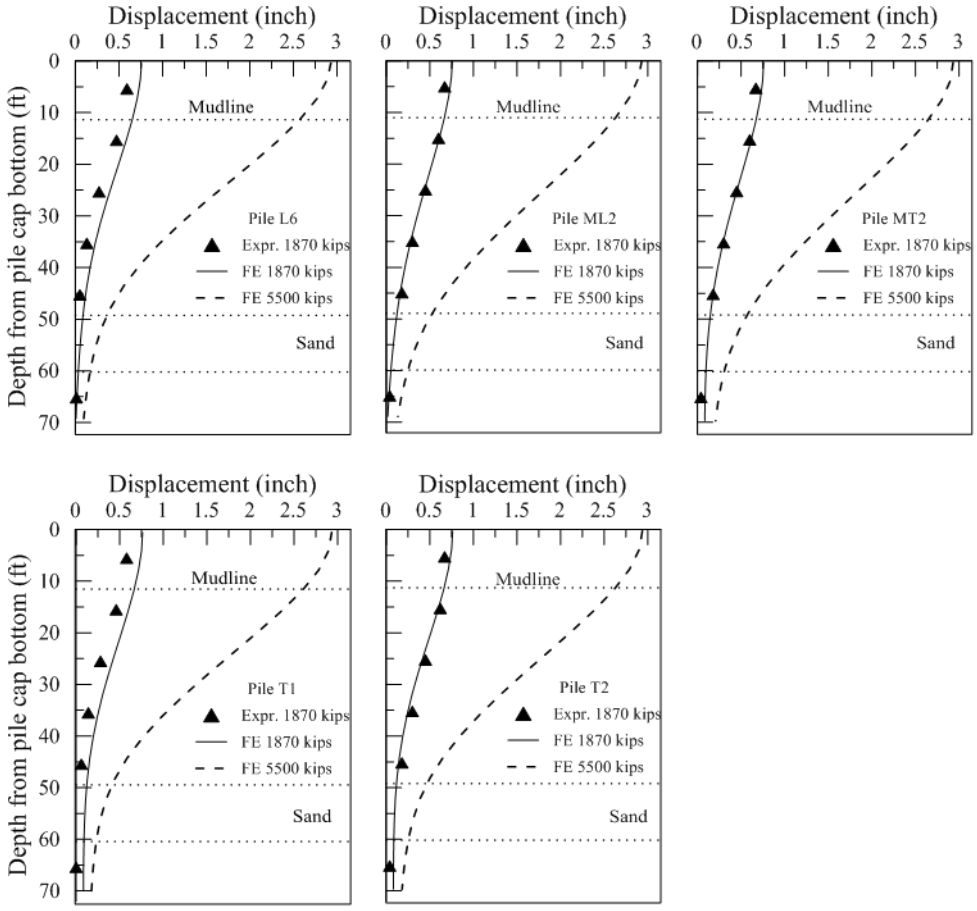

Bending Moment Profiles. The bending moments from the field test were deduced from the strain gage readings at 9.5 ft. and 14.5 ft. from the bottom of pile cap for the instrumented piles. The 3-D FE analysis provides the results of bending moment, axial force, and shear force for defined cross sections in the piles. Figure 43 presents the comparison between the field results and the FE bending moments at lateral loads of 570 kips and 1745 kips. Good agreement is observed between the field and FE results. The bending moment profiles from FE show that the inflection point (i.e., zero moment) was located within 21-25 ft. from the bottom of the pile cap. The location of the maximum positive moment was at the pile cap connection; while the maximum negative moment was located at 39-45 ft. from the bottom of the pile cap. Within the same column, the leading and trailing rows (L and T) had shallower inflection and maximum negative moment points compared to the middle rows (ML and MT), as shown in Figure 44a. Within the same row, the inflection and maximum negative moment points were slightly shallower for the edge piles (column 1), see for example the bending moment profiles for row L piles in Figure 44b. It is also noticed that both points (inflection and maximum negative moment) shift deeper with increasing lateral load, as noticed in Figure 44c.

Figure 43. Bending moment results from strain gages and FE profiles for instrumented piles

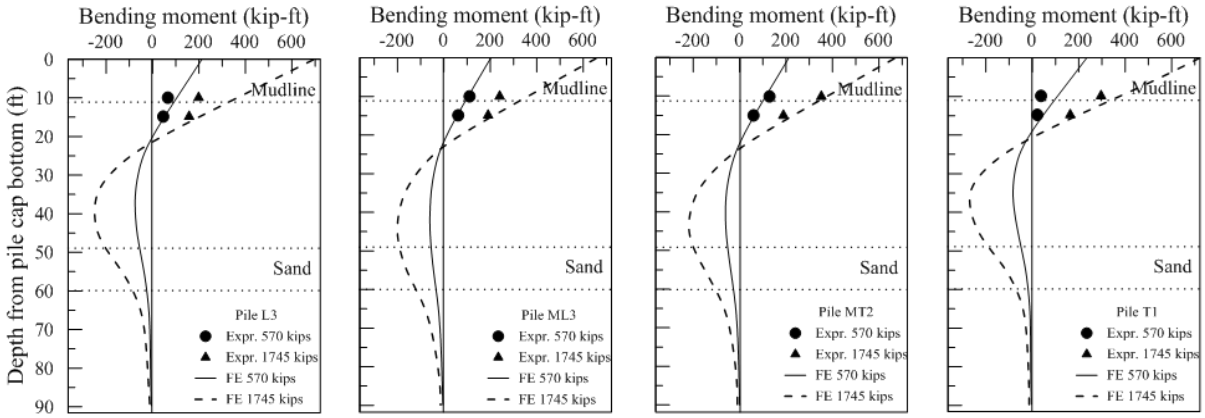

Soil Resistance. The soil resistance was investigated in terms of the soil resistance profiles and the p-y curves. The soil resistance profile was obtained using the traditional method by double differentiating the bending moment curve, which is fitted using a high-order polynomial fit (i.e., [42], [108], [109]). Figure 45 presents the soil resistance profiles for the column 2 piles. The profiles show that the soil resistance changed direction at an approximate depth of 45 ft. in all piles. The soil resistance increased with increasing lateral load in all piles, but at different rates. The largest increase in soil resistance was in the leading row pile L2, which is mainly due to the group effect. The

resistance was also influenced by soil layering; this can be noticed in the larger resistance in layer 2 (stiff clay, 15-25 ft.) compared to layer 3 (medium stiff clay, 25-38 ft.). In addition, a sharp increase in the resistance at 5500 kips was noticed in the sand layer, which can be attributed to the larger stiffness of the sand layer compared to the clay layers.

Figure 44. Bending moment profiles for (a) column 2 piles, (b) row L piles, (c) pile L2

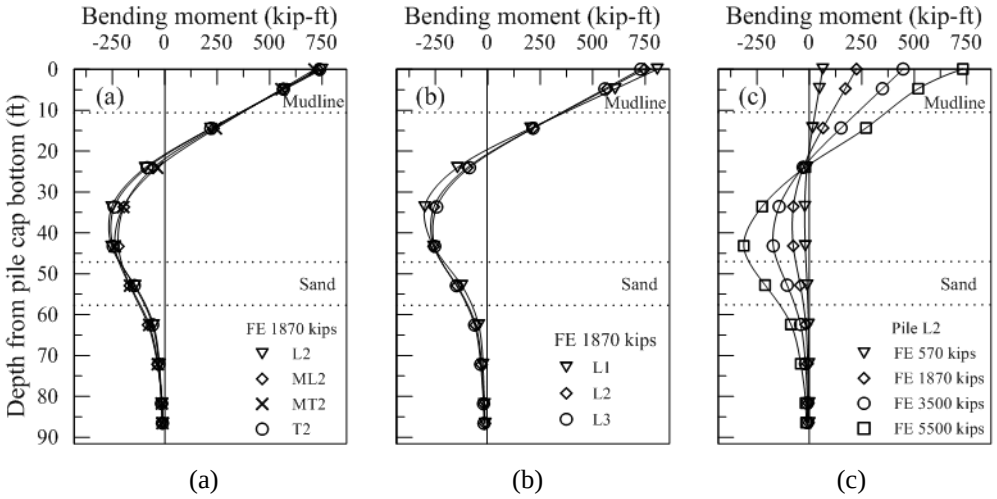

(a) (b) (c)

Figure 45. Soil resistance profiles for column 2 piles

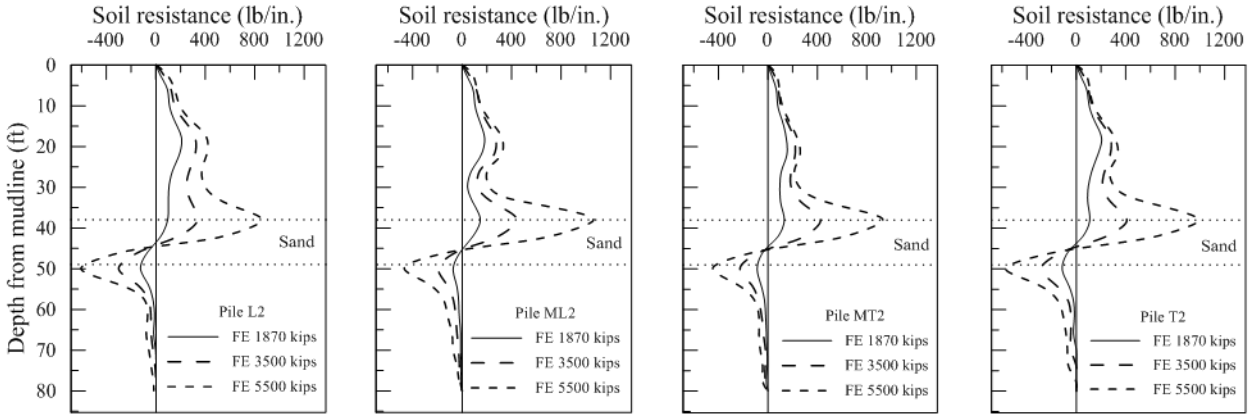

The soil resistance was also investigated using the p-y curves. A p-y curve represents the soil resistance per unit pile-length versus displacement at certain depth. Only the p-y curves for column 2 and row ML are presented here, and the following discussion applies to other columns/rows as well. Figure 46 presents the p-y curves for column 2 piles at different depths. The p-y curves for pile L2 in the leading row were stiffer than those in

other rows (ML2, MT2, and T2). In addition, the p-y curves for piles ML2 and T2 were approximately similar and stiffer than pile MT2, which had the lowest soil resistance.

Figure 46. p-y curves for column 2 piles

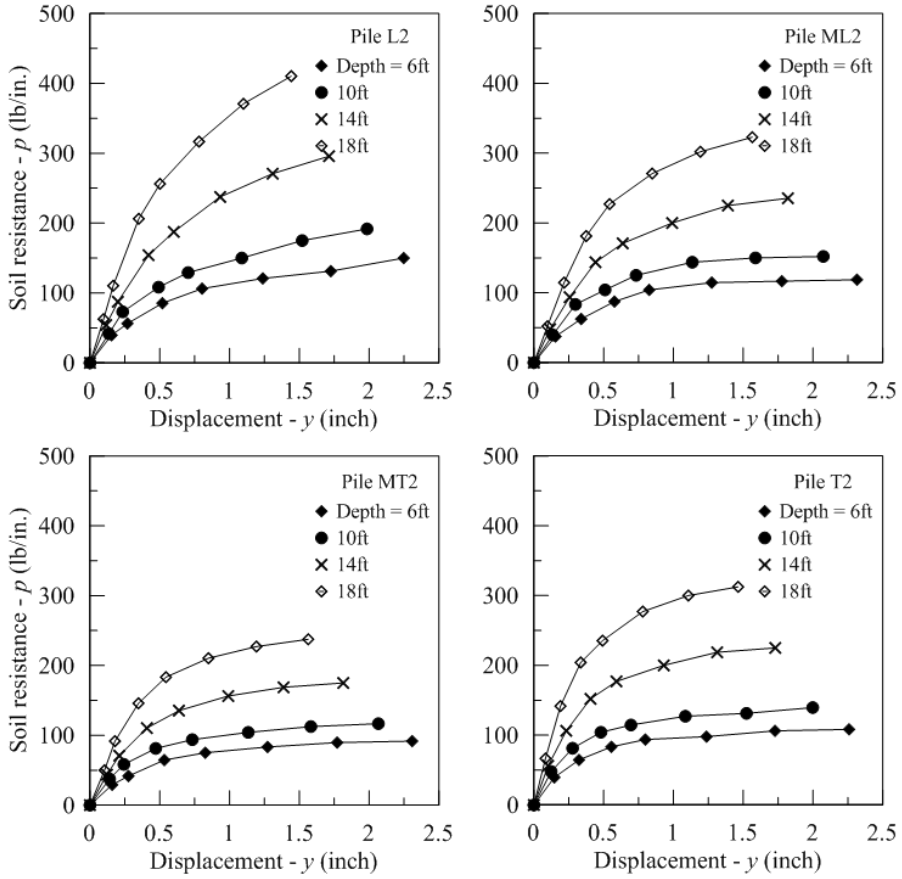

Figure 47 compares the p-y curves for column 2 piles and row ML piles at depth of 10 ft. The comparison also includes the p-y curve for an isolated single vertical pile, single positive battered pile, and single negative battered pile. The p-y curves for single pile cases show that the single positive battered pile was subjected to slightly higher soil resistance as compared to the vertical and negative battered cases, which can be attributed to the effect of the batter angle. Within the same column (Figure 47a), the soil resistance was notably reduced for all piles in the group as compared to the single pile case due to the group effect. The largest reduction in the soil resistance was in row MT followed by rows T then ML, and finally row L. Within the same row (Figure 47b), the soil resistance was the largest in the edge pile ML1 followed by ML2 and ML3, which had almost the same p-y curves.

Figure 47. Comparison of p-y curves for (a) column 2 piles and (b) row ML piles

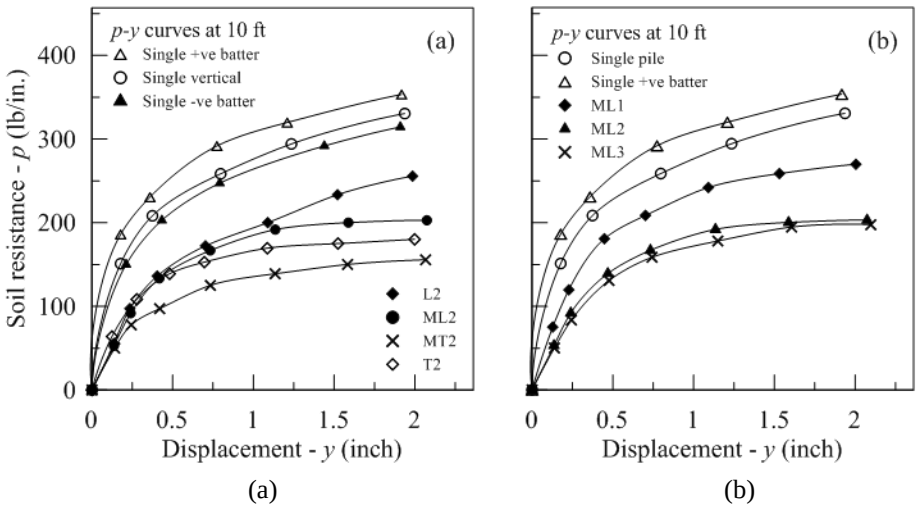

(a) (b)

The influence of the group effect is quantitatively evaluated using the p-multiplier concept. Brown et al. [5] defined the p-multiplier as the factor that reduces the p-y curve from a single pile case to the p-y curve of a pile-in-group. The typical value of p-multiplier is less than unity. The p-multiplier is affected by pile group arrangement (i.e. number of rows and columns), piles spacing (row and column spacing), and soil properties (e.g., [39], [40], [43]). Table 12 summarizes the p-multipliers for all piles in the current study obtained using the p-y curves at depth of 10 ft., in which the p-y curve for the single vertical pile was taken as the reference case. The p-multipliers in Table 12 represent the average values of p-multipliers calculated at displacements of 1, 2, and 3 in., following the suggestions from previous studies. McVay et al. [107] reported that 0.79-1.18 in. lateral displacement is needed to develop the average p-multipliers. Ashour and Ardalan [39] showed that the p-multiplier value stabilizes at lateral displacements greater than 1 in.

Table 12. Summary of p-multipliers at 10 ft. depth

	Row			
	L	ML	MT	T
Column 1	0.96	0.78	0.57	0.72
Column 2	0.74	0.59	0.46	0.55
Column 3	0.70	0.57	0.43	0.51
Average	0.80	0.64	0.49	0.59

The p-multipliers were the highest in the edge piles (column 1) followed by the interior columns 2 and 3 for which the multipliers were almost the same. The average p-multiplier was largest in the leading row L followed by rows ML, T, and MT, respectively. The p-multipliers for the current study are comparable to those from experimental studies on vertical pile groups with 4-rows (e.g., [42], [43]). The p-multipliers from the study by Ilyas et al. [42] were 0.65, 0.49, 0.42, 0.46; and from the study by Chandrasekaran et al. [43] were 0.76, 0.56, 0.46, 0.54 for the 1st, 2nd, 3rd, and 4th row, respectively. The most notable similarity is in the value of the p-multiplier for the 3rd row, which was the lowest multiplier among other rows. The slightly higher p-multipliers for the battered pile group for the current study can be attributed to the larger row spacing, which was 4.3D in the current study versus 3D in the referenced studies

Effect of Pile Group Configuration on the Static Lateral Behavior of Pile Groups

The lateral performance of three pile group (PG) configurations (vertical, battered, and mixed) is investigated here using the 3-D FE modeling for comparison. The study is an extension to a previous field and numerical investigations for the lateral performance of the battered pile foundation at M19 pier of the I-10 Twin Span Bridge ([109], [110]). The three FE models are based on the M19 battered pile group case study, in which the same cap size, pile spacing, material models, concrete and soil parameters were used. The comparison of lateral performance considered: load-displacement curves, axial load, damage in piles, bending moment, soil resistance, and back-calculated p-y curves and p-multipliers

Description of Finite Element Models

Three FE models were developed using the ABAQUS software for the three pile group configurations: vertical PG, battered PG, and mixed PG. The Vertical and Mixed PGs models were developed based on the Battered PG model of the M19 pier foundation presented in Figure 36 and Figure 38, and using the same subsurface soil condition as described in Figure 37. The three FE models have similar characteristics as will be described next, with the only difference is in the piles' inclination (or configuration).

The FE models resembled half of the foundation geometry exploiting the symmetry to reduce the solution cost. The pile group (including the cap) and soil body were created

from two separate meshes using the 8-nodes linear continuum brick element (C3D8R). The soil mesh was designed so that the element size increased gradually in the direction away from the pile group. The number of elements for the pile group mesh was ~10500, and ~72000 for the soil mesh. The geometry and dimensions of the three FE models are shown in Figure 48. The soil domain boundaries were located far away from the pile group to eliminate their influence on the response. The connection between the piles and the cap was assumed fixed-head connection. The main steel reinforcement in the piles was included in the FE models to introduce the prestress force. This was achieved using the embedded shell elements (S4R), which was numerically formulated to simulate rebars [80]. Each row of steel tendons in the pile section was replaced by one shell with a total of four shells per pile in a box shape (see Figure 28).

Figure 48. Geometry and dimensions of FE models

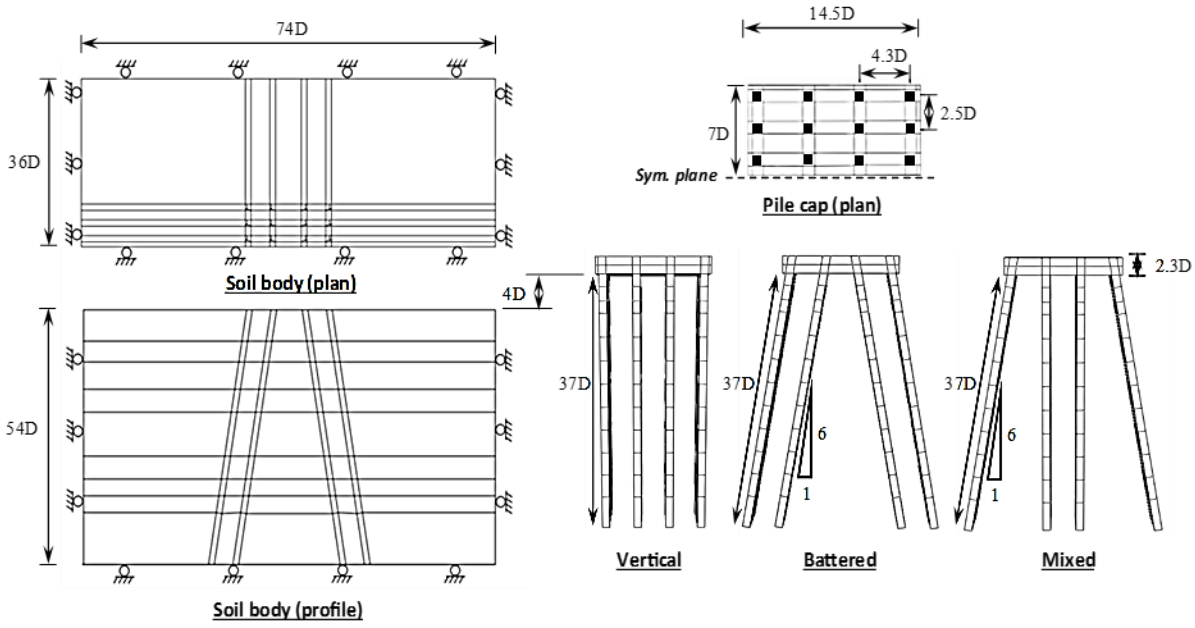

The laterally loaded pile is a nonlinear problem due to the nonlinear material behavior of concrete piles and surrounding soils, and gap formation at the pile-soil interface (e.g., [7], [22]). In this section, the nonlinear materials' behavior of the vertical, battered and mixed PGs were incorporated using the advanced material constitutive models for concrete, soils, and pile-soil interaction that were described in the Methodology section. The soil layering and soil parameters for the AMCC and DP models were presented earlier in Table 11.

Results of Load-Displacement Curves

The comparison between the load-displacement responses for the vertical, battered and mixed PGs is presented in Figure 49. Under the same lateral load, the vertical PG exhibited lower lateral resistance compared with the battered and mixed PGs, which was due to the additional lateral resistance from the battered piles. For instance, at the maximum load, the displacement in the vertical PG was 11 in.; while it was 3 in. in the battered PG and 6.5 in. in the mixed PG. The figure also depicts the average lateral load carried by each row in the PGs. It is noticeable that the load distribution is affected by the presence of battered piles. In the vertical PG, the largest load share was carried by the leading row L (31% at max load) followed by rows ML (24%), MT (23%), and T (22%). For the battered PG, the middle rows carried larger share with 31% and 28% for rows ML and MT, and 22% and 19% for rows L and T, respectively. For the mixed PG, the load share distribution was 36%, 17%, 18%, and 29% for rows L, ML, MT, T, respectively. The load share percentages indicate that the lateral load is likely to be closely distributed in vertical PGs, and nonuniformly distributed in the battered and mixed PGs.

Figure 49. Load-displacement response for the vertical, battered, and mixed pile groups

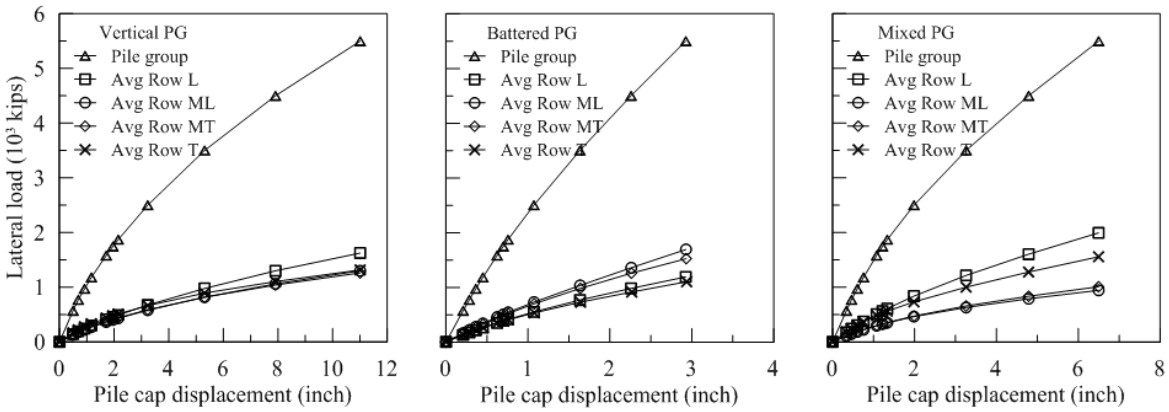

The lateral stiffness of the PGs are compared in Figure 50. It can be noticed that the lateral stiffness decreased nonlinearly with displacement in all PGs at a similar rate. The relative stiffness results show that the battered PG was 120% stiffer than the vertical PG, while for the mixed PG it was about 48% stiffer.

Results of Axial Reaction in Piles

The results of axial reaction (F_{axial}) per pile versus the group lateral load (H) are shown in Figure 51. Note that the positive sign means the force is compressive (i.e. push in); while

the negative sign means it is tensile (i.e., pull out). It can be seen that the axial load in a pile and its mirror pile are similar in magnitude and different in load sign (assuming the mirror axis passes between the middle rows and perpendicular to load direction). For example, the axial reaction in pile L1 and its mirror pile T1 are similar in magnitude, but different in load sign. In any row, the axial reaction for all PGs was the largest in the piles within the edge column (i.e., column 1), which was due to the weaker influence of group effect. The results also show that the average axial reaction per row differs between the PGs. In the vertical PG, the axial reaction was largest in the leading and trailing rows (L and T) with a row average of 8% and stabilized with increased lateral load. In the battered PG, the axial load was largest in the middle rows (ML and MT) and increased linearly with lateral load from 10% to 12.5%. For the mixed PG, the largest axial reaction was in rows L and T with 8.5% row average. One interesting observation was that the axial reaction was compressive in row MT and tensile in row ML in the mixed PG, which is opposite to the observation in the vertical and battered PGs.

Figure 50. Comparison of the PGs lateral stiffness

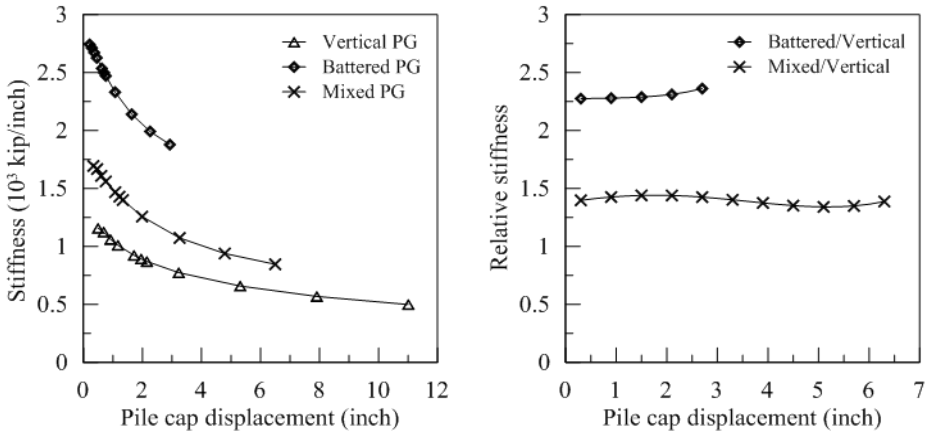

Figure 51. Variation of the axial reaction in the piles

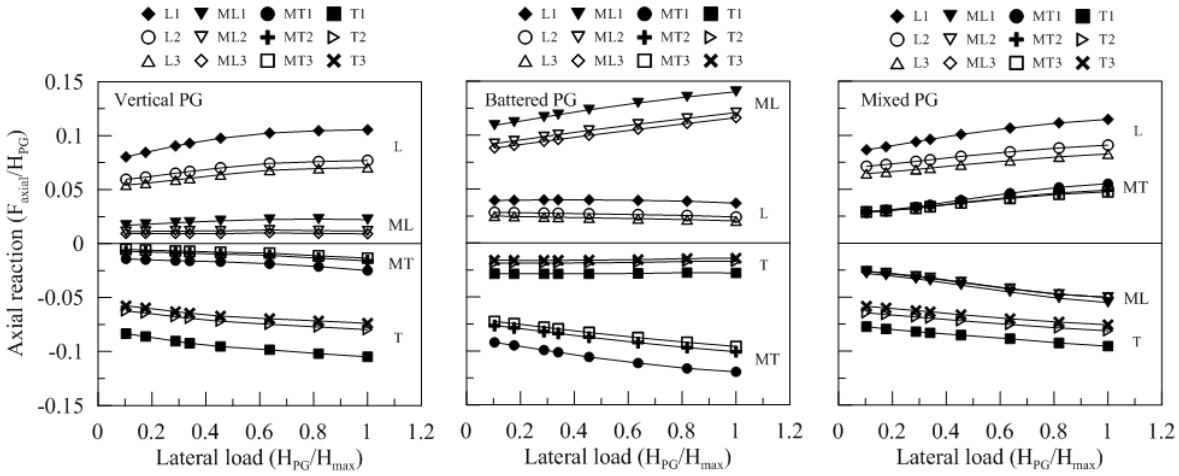

Results of Lateral Load Distribution

The lateral load distribution per pile for all PGs is depicted in Figure 52. It should be noted here that the sum of piles' loads (in the plots) for each PG is 50%, which is due to the fact that the FE model represents half of the PG foundation. For the vertical PG case, the lateral load share varied only in rows L and T and remained fairly constant in rows ML and MT. The lateral load in row T decreased steadily to reach a similar load as in rows ML and MT; while in row L the load kept increasing. In the battered PG case, the lateral load distribution exhibited slight variation with lateral load while keeping same order for rows share. In a similar way to axial load, rows ML and MT carried a larger share of lateral load compared to rows L and T. For the mixed PG, a larger contrast in load share is noticed between rows L, T, and ML, MT (2-3%) compared to the vertical and battered PGs. The load share in rows L and T exhibited notable variation, similar to the vertical PG case. When comparing pile columns, the edge column (column 1) exceeds columns 2 and 3 load share by 0.5-1.0% for all PGs.

Results of Bending Moment

The variation in bending moment (BM) at the pile-pile cap connection is shown in Figure 53. The BM in the vertical PG kept increasing with increasing the lateral load and was higher than battered and mixed PGs. In the battered PG, the rate of increase in BM was much less compared to other PGs. Similar to previous observations, piles in the edge column (column 1) carried higher BM magnitude compared to columns 2 and 3.

A comparison of BM profiles is shown in Figure 54. The figure shows that the point of BM inflection (i.e., sign change) was located at a similar depth in all PGs (7-8D). The area under the BM curve was largest in the case of vertical PG, and it took greater depth to approach zero value (32D). In the battered PG case, the area under the BM curve was less, and it approached zero at a shallower depth (25D). For the mixed PG, the area under the BM curve varied between the piles with row T piles carrying the lowest BM, and the depth at which the BM approached zero was 30D.

Results of Soil Resistance Profiles

The soil resistance profiles in each pile were obtained using the double differentiation of bending moment curve technique (e.g., [42], [108], [109]). Figure 55 presents the soil resistance profiles for all piles in the PGs. It should be noted that the zero-depth reference in the figure is the mudline. The sign convention in the figure refers to the acting direction of soil resistance. Positive resistance value means it acted in a direction opposite to pile movement direction, and vice versa. The figure shows that the profiles are similar for all piles in the same PG. The soil resistance in all PGs switched to a decreasing trend within the sand layer, which is due to the high stiffness of sand material. The depth at which the soil resistance changed sign was deeper in the vertical PG (18-20D) compared to 15D in the battered PG and 16-18D in the mixed PG. The soil resistance diminished at shallower depth in the battered PG (20D) compared to the vertical and mixed PGs, which reached to depths (29D). On the side of positive resistance, the vertical PG mobilized greater soil resistance in front of the piles compared to other PGs (58% greater than battered PG, and 43% greater than mixed PG, based on average area under the curves).

Results of p-y Curves

The variation of normalized soil resistance (p) with lateral pile displacement (y) at a certain depth is a nonlinear curve called “p-y curve.” In this FE study, the p-y curves were generated using the soil resistance and pile deflection values. Figure 56 presents the p-y curves for all PGs obtained at a selected depth of z/D=4.6. Each sub-figure contains p-y curves for piles in the group and for isolated single piles (vertical, positive battered and negative battered). When comparing p-y curves for the PGs with single piles, the influence of the group effect is noticeable in the softer p-y curves in all PGs. The columns 2 and 3 piles had softer p-y curves compared to column 1 piles (edge piles) due to the higher influence of the group effect from neighboring columns. When comparing piles

rows, the soil resistance was highest in the leading row. The middle rows (ML and MT) had similar p-y curves in all PGs.

The p-y curves from the FE solution allows for back-calculating the p-multipliers, which provide quantitative measure for the group effect in PGs [34]. The p-multiplier is defined as the ratio of soil resistance for a pile-in-group (p_g) to the soil resistance for an isolated single pile (p_{single}) at certain displacement (y), and typically assumes values less than unity. Figure 57 displays the variation of p-multipliers with pile displacement in all PGs. Overall, the p-multipliers were higher and more stable with displacement in the battered PG, which was due to the increased in pile-pile spacing with depth. The vertical and mixed PGs had closely similar p-multipliers for rows ML, MT, T, and notably differ for row L, which was higher in the mixed PG. The largest change in the p-multiplier is noticed in row T for all PGs. This indicates that soil resistance mobilized early in row T with limited influence from the group effect, and then gradually decreased due to the movement of piles in the rows ahead.

The p-multipliers averaged over the displacement are summarized in Table 13, Table 14, and Table 15 for the vertical, battered, and mixed PGs, respectively. The p-multipliers for column 1 (edge column) is notably higher than columns 2 and 3 in all PGs with 0.2 difference. This observation leads to the conclusion that the average p-multiplier for a row would decrease with increasing number of columns. This is due to the fact that there are only two edge columns in any PG, and their influence on the average p-multiplier would decrease with increasing the number of interior columns.

Figure 52. Comparison of the lateral load distribution

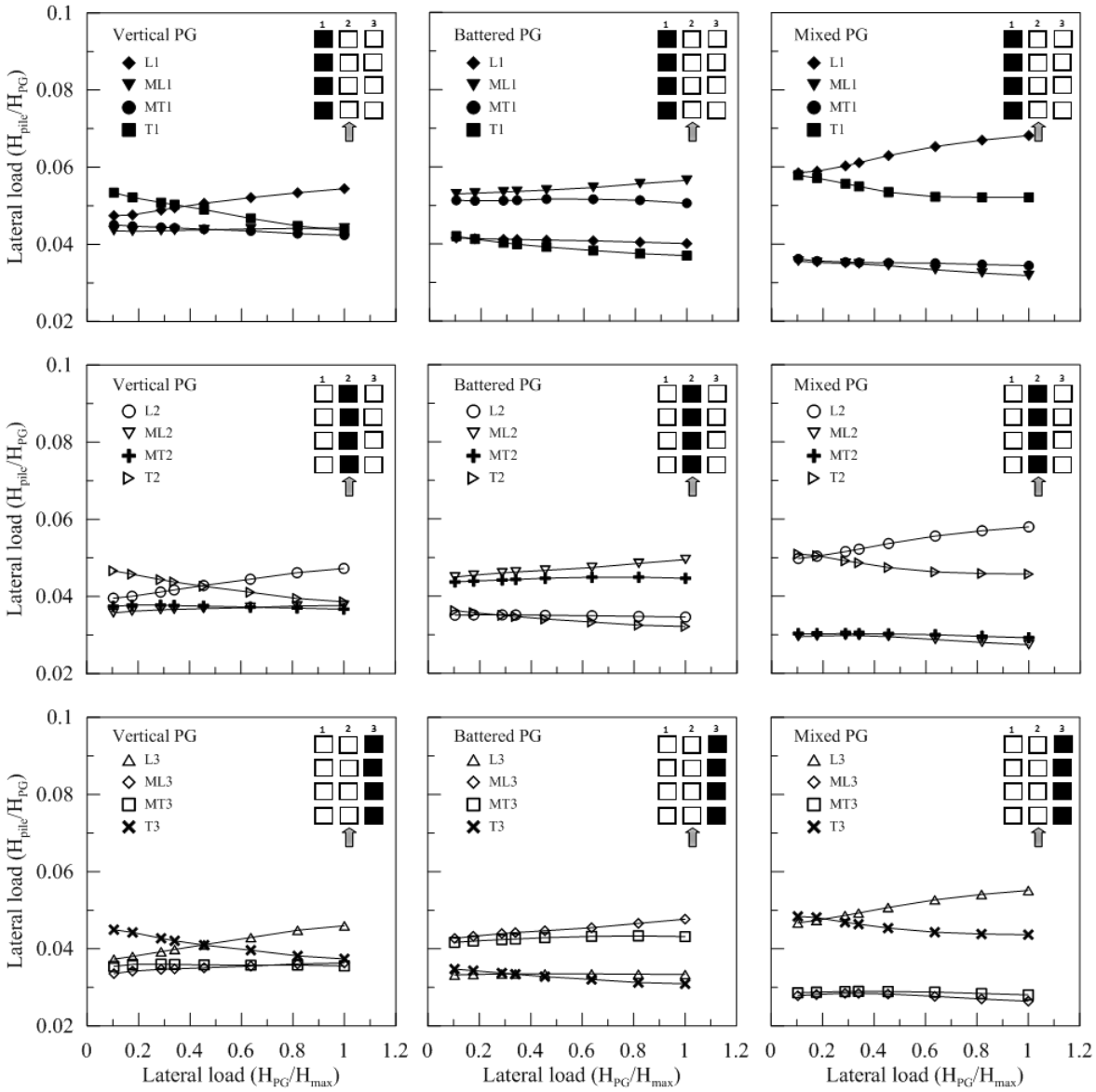

Figure 53. Bending moment variation with lateral load at the pile cap connection

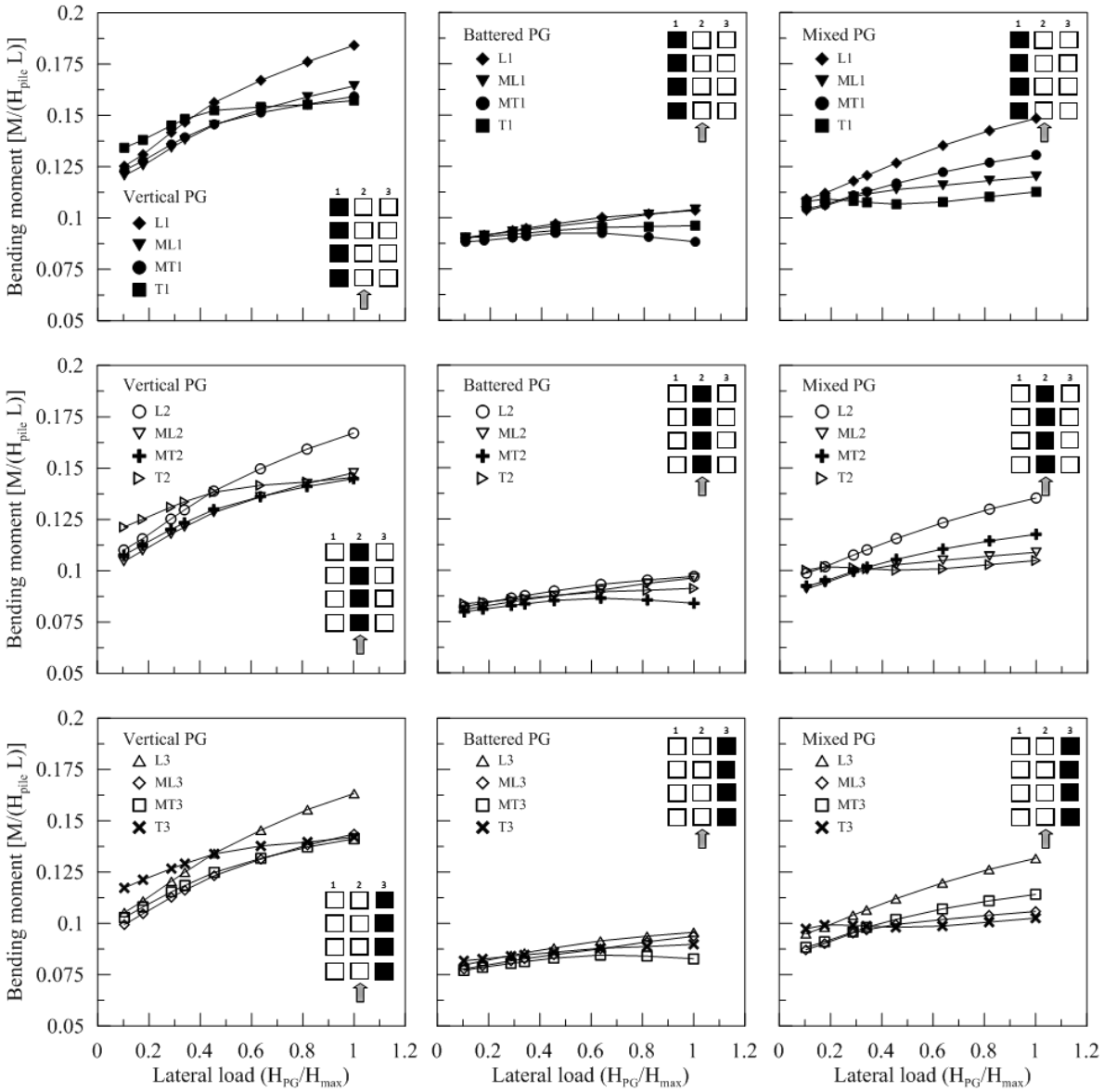

Figure 54. Bending moment profiles at 5500 kips

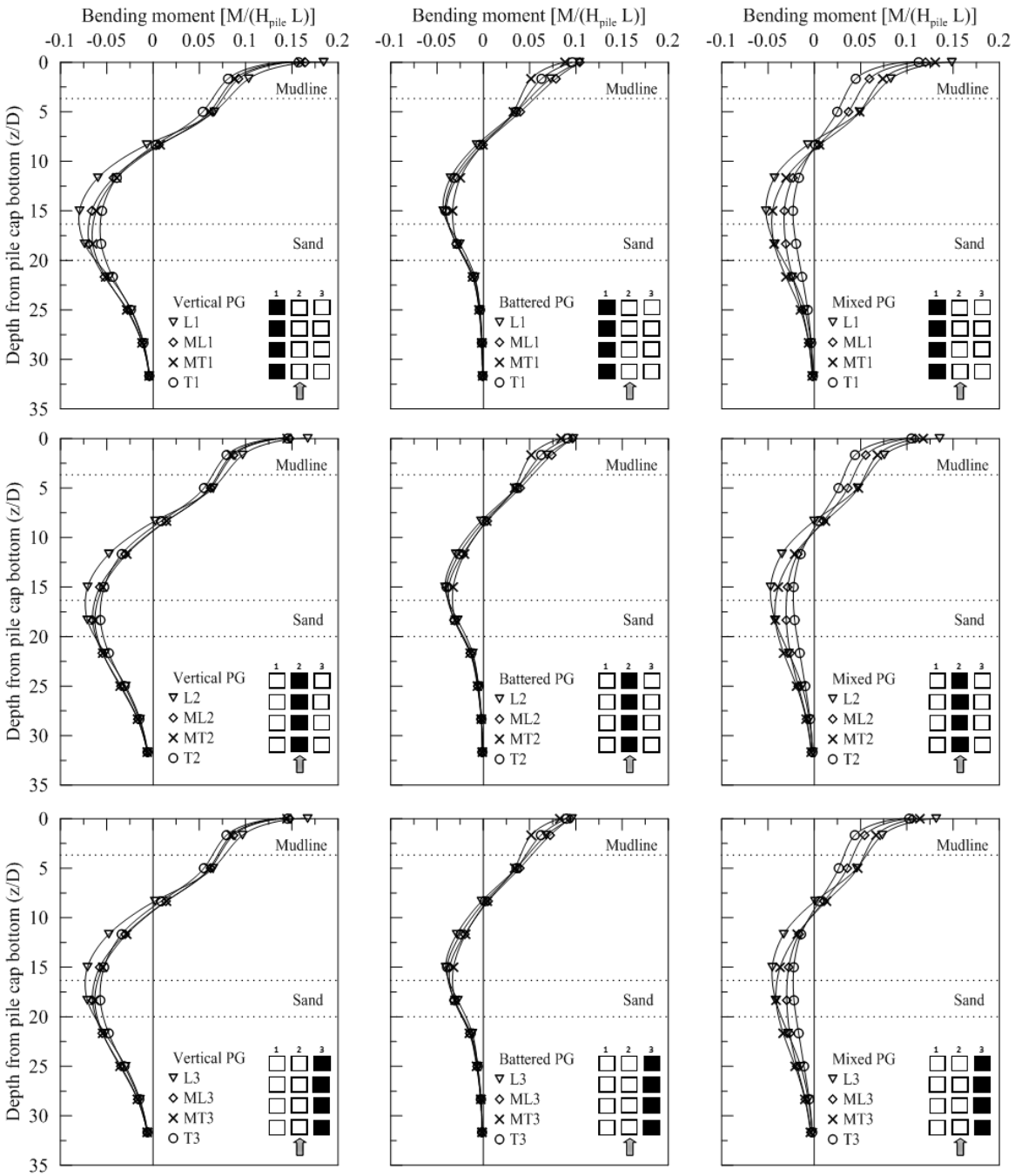

Figure 55. Soil resistance profiles at 5500 kips

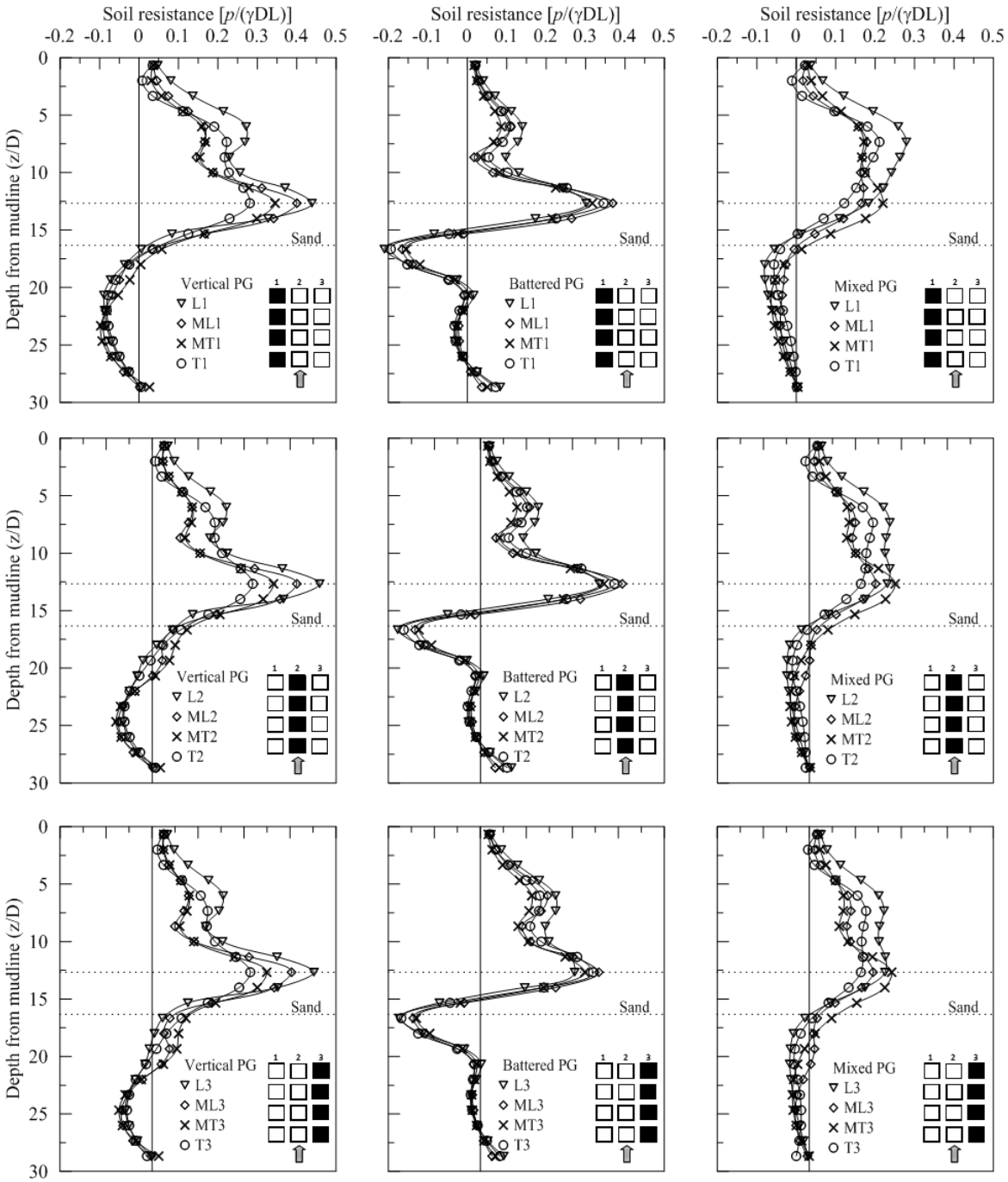

Figure 56. Calculated p-y curves at a depth z/D = 4.6

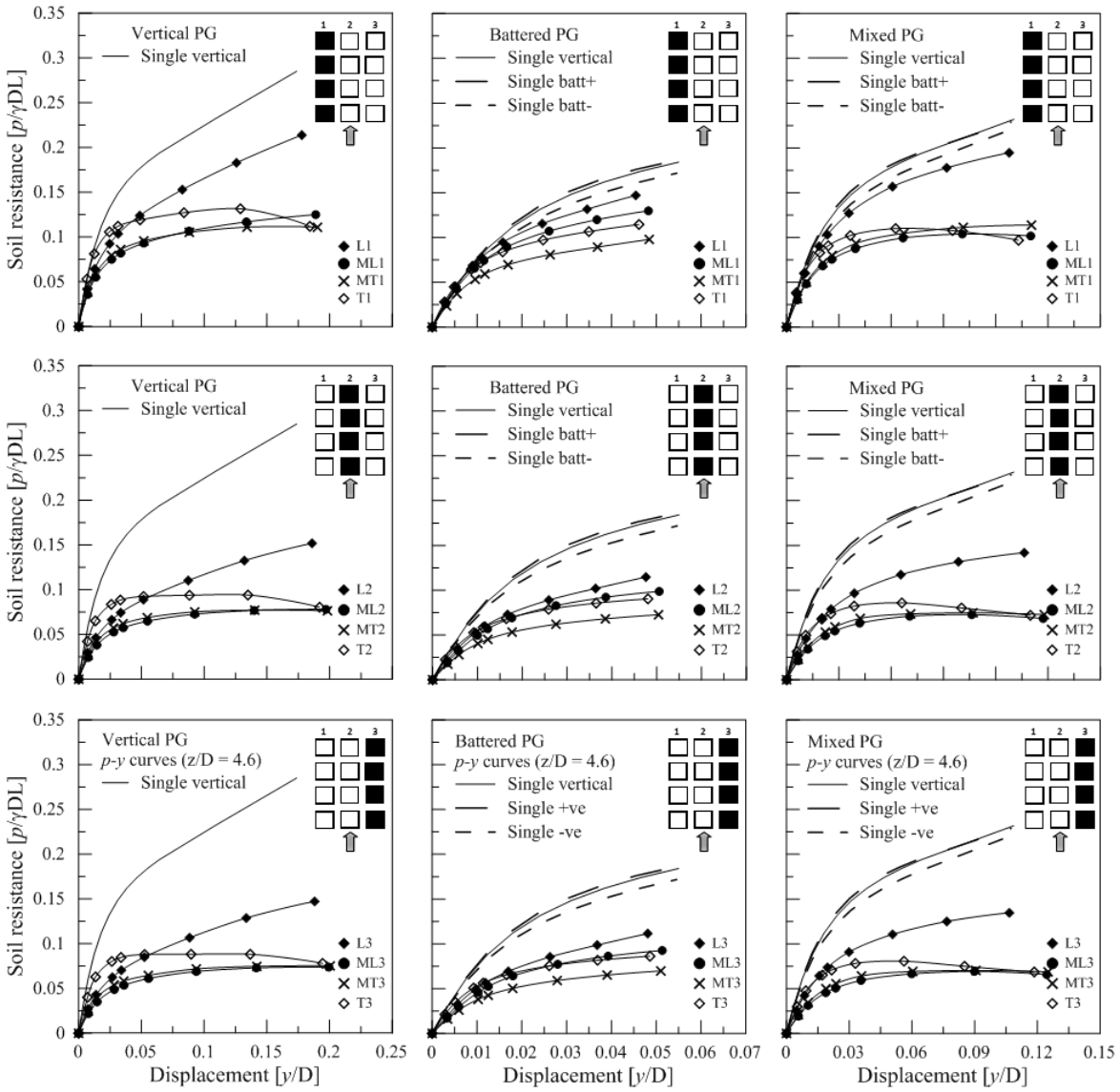

Figure 57. Back-calculated p-multipliers at depth z/D = 4.6

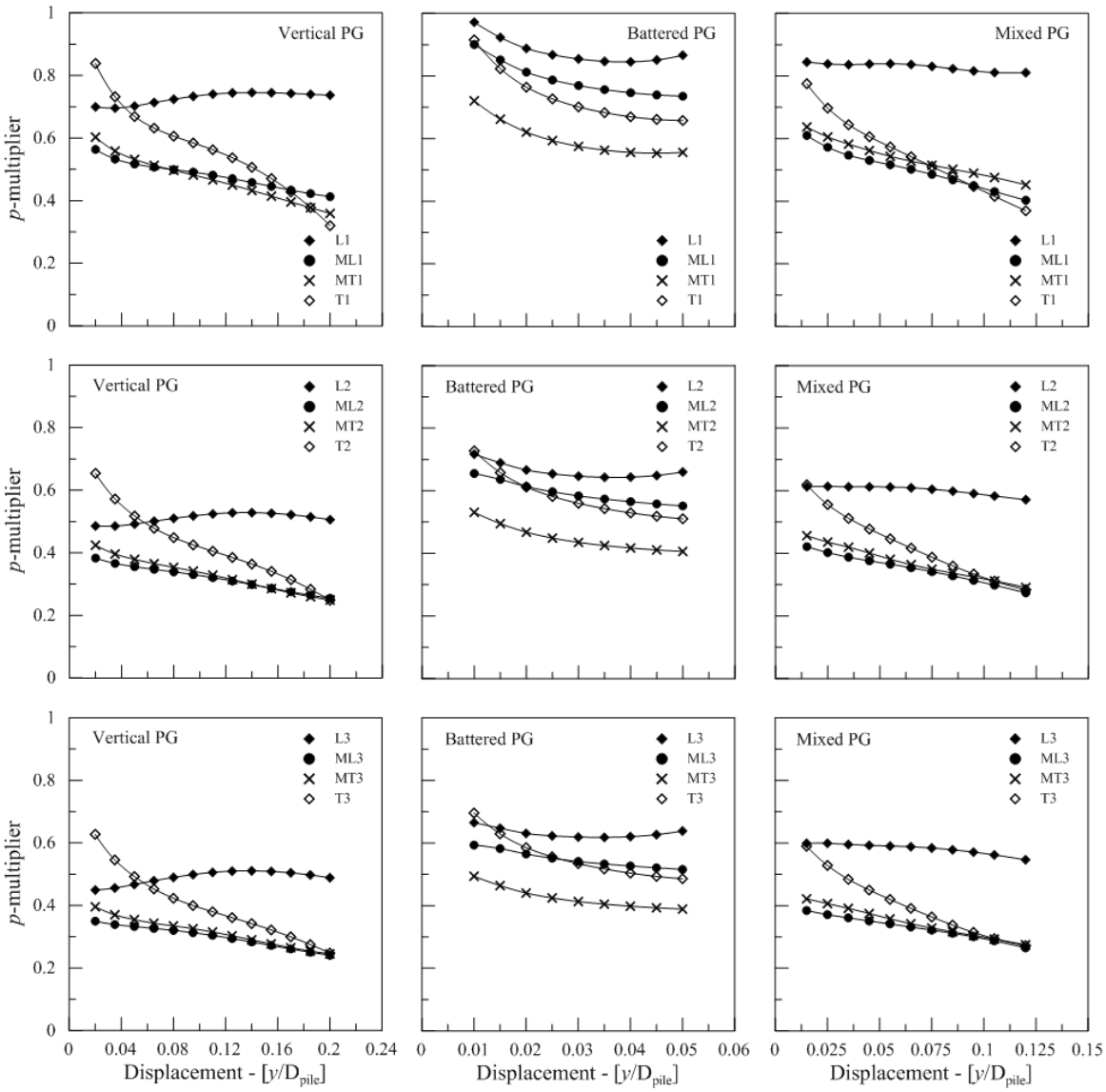

Table 13. Average p-multipliers for vertical PG at depth z/D=4.6

	Row			
Column	L	ML	MT	T
1	0.73	0.49	0.48	0.59
2	0.51	0.32	0.34	0.44
3	0.49	0.30	0.32	0.42
Row average	0.58	0.37	0.38	0.48

Table 14. Average p-multipliers for battered PG at depth z/D=4.6

	Row			
Column	L	ML	MT	T
1	0.89	0.81	0.62	0.77
2	0.67	0.60	0.46	0.61
3	0.64	0.55	0.43	0.58
Row average	0.73	0.65	0.51	0.65

Table 15. Average p-multipliers for mixed PG at depth z/D=4.6

	Row			
Column	L	ML	MT	T
1	0.87	0.54	0.57	0.61
2	0.63	0.37	0.39	0.47
3	0.61	0.35	0.37	0.44
Row average	0.70	0.42	0.44	0.51

Finite Element Parametric Study

Finite element parametric study was conducted to investigate the effect of pile spacing and clay soil type on the lateral behavior of pile groups (vertical, battered, and mixed). To study the effect of pile spacing, three pile group (PG) types are considered at three pile spacings. In addition, a pile group composed of four vertical piles in one line at similar pile spacings is also studied. For the effect of soil type, clay strength parameters corresponding to soft, medium, and stiff clays are considered. The variables investigated are the axial reaction, shear force, pile group efficiency, and p-multipliers.

Finite Element Models

Geometry and FE mesh. The FE parametric study was conducted on three PG types: vertical, battered, and mixed. Each PG comprised of eight concrete piles in a 4x4 arrangement, in which each pile had a square cross-section and measured 3 ft. wide (D) and 110 ft. long. Due to model symmetry, the FE model resembled half of the PG geometry. The three pile spacings (S) considered were: 3D, 5D, and 7D as measured from the pile cap level (Figure 58). The soil body was created from single soil material and was sized large enough to eliminate the influence of boundaries. The interaction between the PG and soil models was governed by the interface model. The total number of solid continuum brick element with 8 nodes (C3D8R) used was ~70000.

Figure 58. PGs FE models used in the parametric study

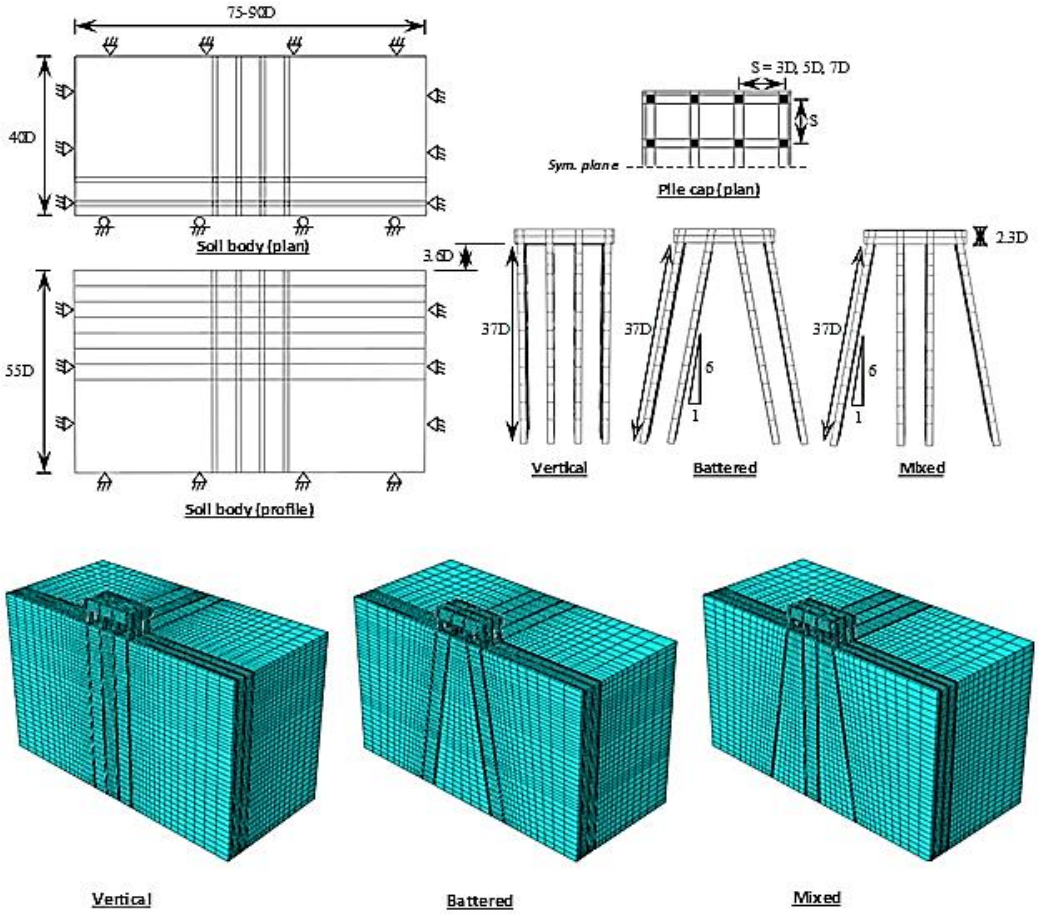

In addition to the three PGs, a group composed of four vertical piles arranged in single line was studied. The influence of pile spacing and clay soil type for this PG was investigated for two loading conditions. The first is when the loading direction is concurrent with the line of piles (termed as single-column); while the second is when the loading is transverse to the line of piles (termed as single-row), as shown in Figure 59. Similar to the previous PG models, the pile spacings was varied from 3D to 7D, and the PG and soil body models were made of two separate FE meshes. The total number of solid elements (C3D8R) used was ~50000.

Table 16 summarizes the pile groups cases considered in the parametric study. Each PG type was analyzed at three pile spacings (3D, 5D, 7D) and three clay soil types (soft, medium, stiff), which resulted in a total of nine unique cases per PG.

Figure 59. Dimensions and FE models for the single row PG

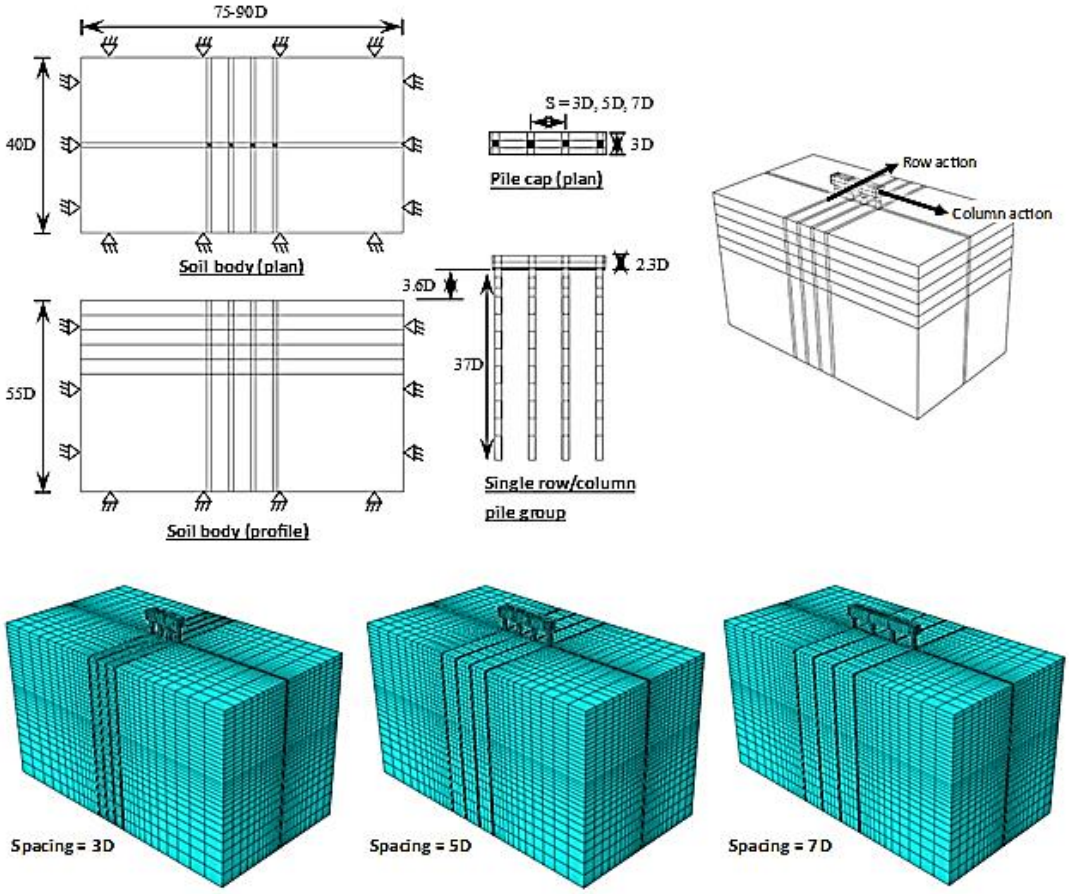

Table 16. PG cases considered in FE parametric study

Pile group type	Pile-pile spacing (w.r.t pile size D)	Clay soil type
Vertical	3, 5, 7	Soft, Medium, Stiff clay
Battered	3, 5, 7	Soft, Medium, Stiff clay
Mixed	3, 5, 7	Soft, Medium, Stiff clay
Single column	3, 5, 7	Soft, Medium, Stiff clay
Single row	3, 5, 7	Soft, Medium, Stiff clay
Total number of cases = 45		

Material Constitutive and Interface Models. The constitutive models that were described in the Methodology, were used in the FE parametric study. The concrete behavior was modeled using the elastoplastic CDP constitutive model, and the clay soil was modeled using the AMCC model. The AMCC model parameters for the three clay soil types: soft, medium, and stiff are summarized in Table 17. The soil strength and stiffness properties for each clay category were obtained from the literature ([111], [112])

and were used to estimate the clay model parameters. The pile-soil interface was modeled using the contact feature described in Methodology assuming interface friction coefficient μ = 0.5, and slipping shear stress limit of τ = 2000 psf.

Table 17. Clay soil material properties used in the parametric study

Soil type	Unit weight (pcf)	Undrained shear str. s_u (psf)	Poisson's ratio (ν)	K_o	AMCC model parameters						
					e_o	α_{ini}	M	κ	λ	x	C
Soft clay	120	250	0.25	1.0	0.8	0.03	0.6	0.030	0.17	1.33	4
Medium clay		750			0.8	0.03	0.8	0.010	0.11	1.33	4
Stiff clay		1500			0.8	0.03	1.4	0.007	0.09	1.33	4

Results of FE Parametric Study

The effect of pile spacing on the axial reaction, piles' shear, pile group efficiency, and p-multipliers are reported here for the medium clay soil only. This is because the influence of clay soil type vanishes by the normalization of the axial reaction, piles' shear, and pile group efficiency results. Therefore, the effect of clay soil type is discussed only for the p-multipliers.

Effect of Pile Spacing on Axial Reaction. The axial reaction here refers here to the net change in the axial force in the piles due to lateral load. The axial force in total remains compressive in the piles due to the self-weight of the structure. The axial reaction was obtained at the pile cap elevation at four pile cap displacements (0.5, 1.0, 1.5, 2.0 in.). Figure 60 describes the definition of the axial reaction in the PGs. The results for axial reaction was normalized using the group lateral load (H_{PG}) at the corresponding pile cap displacement. The influence of pile cap displacement on the axial reaction is investigated in Figure 61. It can be seen that the normalized axial reaction was fairly constant in all PGs, and therefore considered independent of the pile cap displacement.

Figure 60. Definition of the axial reaction in the PGs

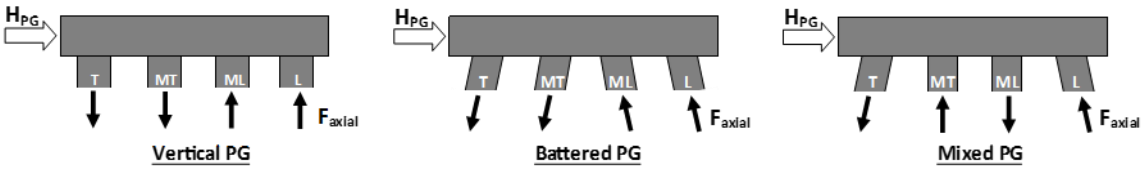

Figure 61. Effect of pile cap displacement on axial reaction

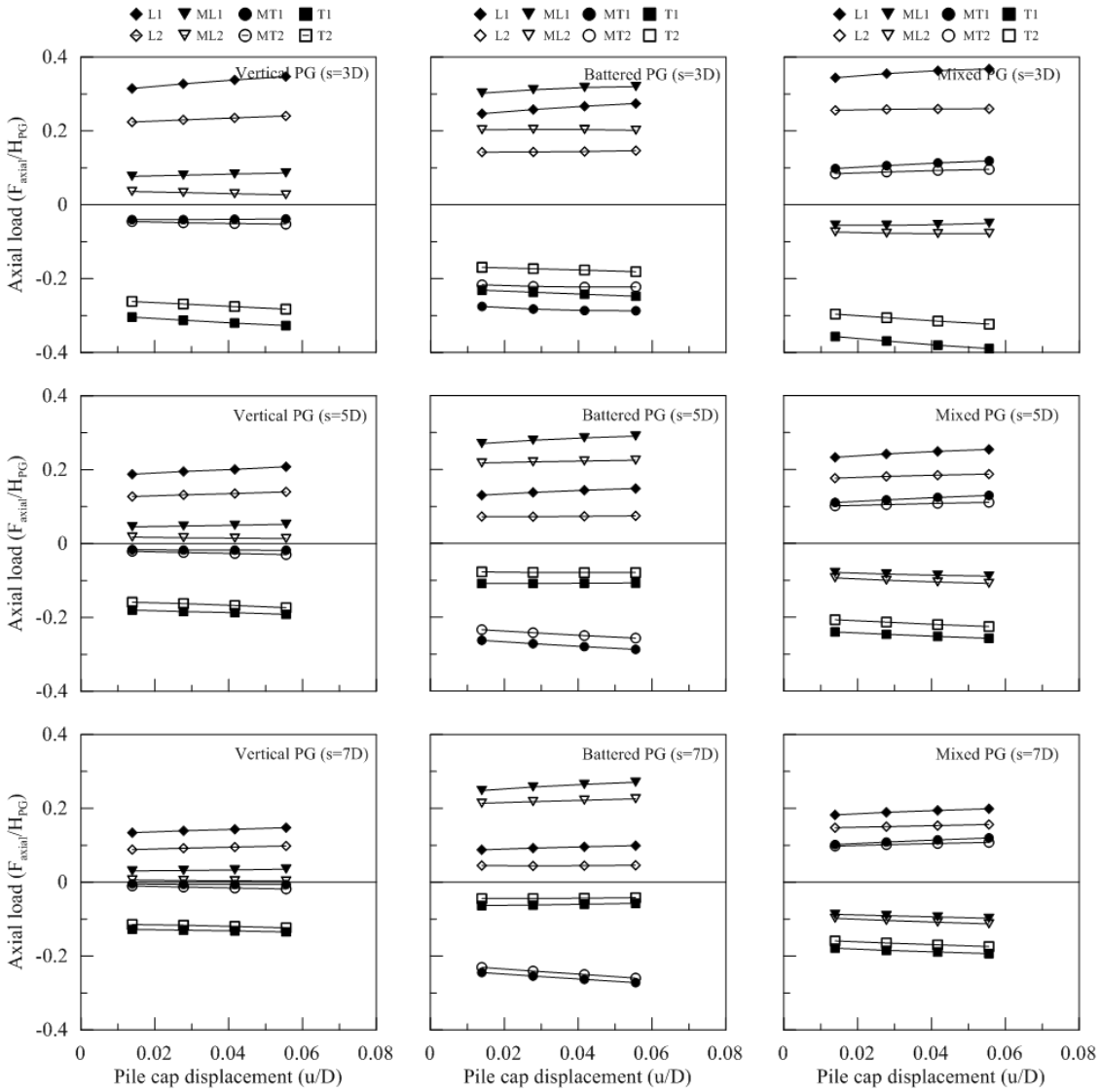

The effect of pile spacing on the normalized axial reaction is depicted in Figure 62 and Figure 63. The axial reaction is expected to decrease at larger pile spacing due to increase in moment arm. In the vertical PG, the significant percentage of axial reaction was found on the leading and trailing rows (L, T) with an average of 57% at 3D spacing. The axial percentage of reaction decreased with increasing the pile spacing in all piles. The largest decrease was in the leading and trailing rows at an average of 34% when the spacing increased from 3D to 7D. In the middle rows (ML, MT), the percentage of axial reaction was relatively small at 10%, and the percentage dropped to 4% at 7D spacing.

Figure 62. Effect of pile spacing on normalized axial reaction per pile

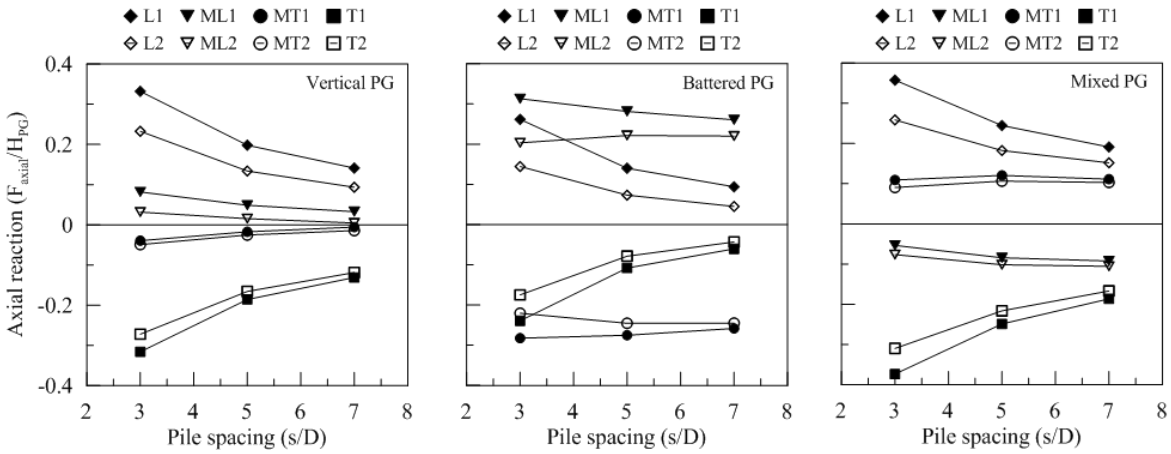

Figure 63. Effect of pile spacing on normalized axial reaction per row

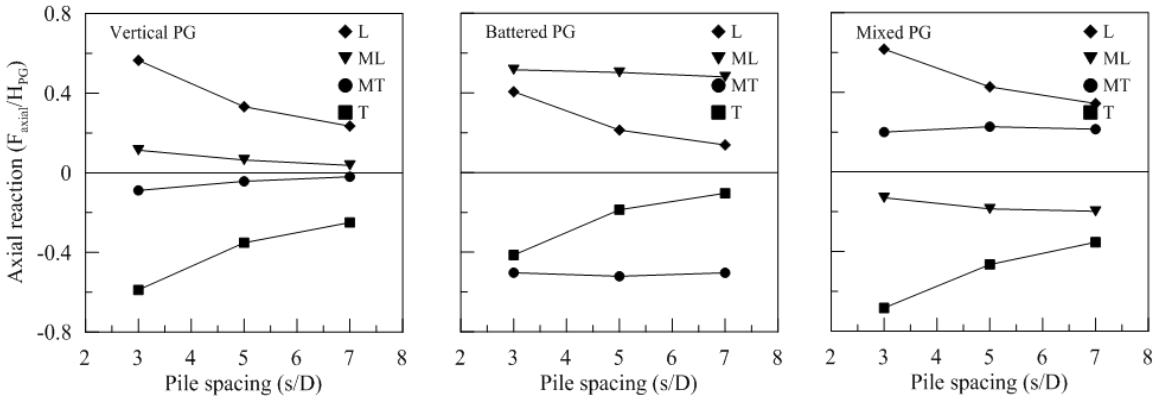

In the battered PG, the percentage of axial reaction was significant in all piles with an average of 40% in the leading and trailing rows and 50% in the middle rows at 3D spacing. The decrease in axial reaction when spacing increased was notable only in the leading and trailing rows with 28% reduction on average; while in the middle rows the average percentage remained fairly constant.

In the mixed PG, the percentage of axial reaction was higher in the leading and trailing rows with an average of 65% at 3D spacing, which is dropped 30% when the spacing increased to 7D. The middle rows showed a slight change in the percentage and remained around 20%. Moreover, the axial reaction in rows ML and MT was tensile and compressive, respectively, which was in contrary to the observation in the vertical and battered PGs. The common observation in the three PG cases is that the axial reaction

significantly decreased only in the leading and trailing rows when the pile spacing increased.

Effect of Pile Spacing on Piles' Shear. The pile shear (V) refers here to the internal shear component normal to the pile's major axis, as depicted in Figure 64. Following this definition, the sum of shears in all piles in the vertical PG will be equivalent to the group lateral load (H_{PG}); while it is not in the cases of battered and mixed PGs. The results of piles' shear at the pile cap elevation are presented in Figure 65 for pile cap displacements of 0.5, 1.0, 1.5, and 2.0 in. Similar to axial load, the piles' shear was normalized using the group lateral load (H_{PG}). The figure shows that the piles' shear was slightly affected by the cap displacement, in which it decreased with the increase of displacement in some piles.

The effect of pile spacing on the piles' shear per row is presented in Figure 66. In the vertical PG, the pile spacing increase from 3D to 7D caused a slight change in piles shear (<1%). In the battered PG, the shear increased 2% in rows L and ML, and less than 1% in rows MT and T. In the mixed PG, the shear increased 1.5% in all rows. The change in piles shear observed was very small in all PGs with no clear trend, and therefore the influence of pile spacing is considered negligible on the piles' shear per row.

Figure 64. Pile shear definition in the pile groups

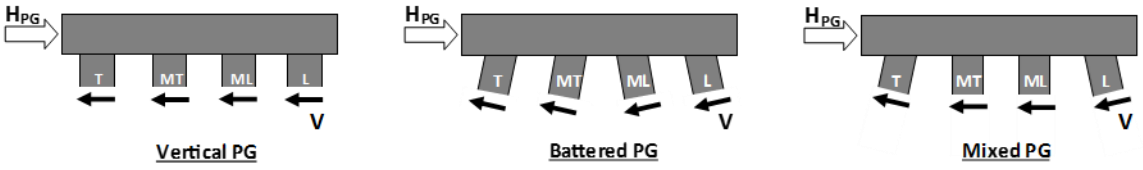

Effect of Pile Spacing on Group Efficiency. The pile group efficiency is a simple measure of the pile group load capacity in reference to the sum of individual pile capacities [defined as: $Eff_{PG} = H_{PG} / (n \cdot H_{single})$]. Where H_{PG} is the lateral capacity of the pile group, H_{single} is the lateral capacity of single pile, and n is the number of piles in the group.

The lateral capacity is defined as the magnitude of lateral load that causes certain displacement at the pile cap (for pile group) or pile top (for single pile). The lateral capacities of the pile groups at different pile cap displacements (0.5, 1.0, 1.5, 2.0 in.) are presented in Figure 67. The figure also shows the sum of individual pile capacity (n

.H_{single}) at similar displacements for number of piles n = 16 (recall that the studied PGs have 4 rows and 4 columns). The individual pile capacity was obtained from a separate FE model for single pile with similar pile and soil model properties. The pile group efficiency was estimated and presented at different displacements in the bottom plots in Figure 67. It can be seen that the pile group efficiency remained constant at different pile cap displacements in all pile groups.

Figure 65. Effect of displacement on normalized pile shear

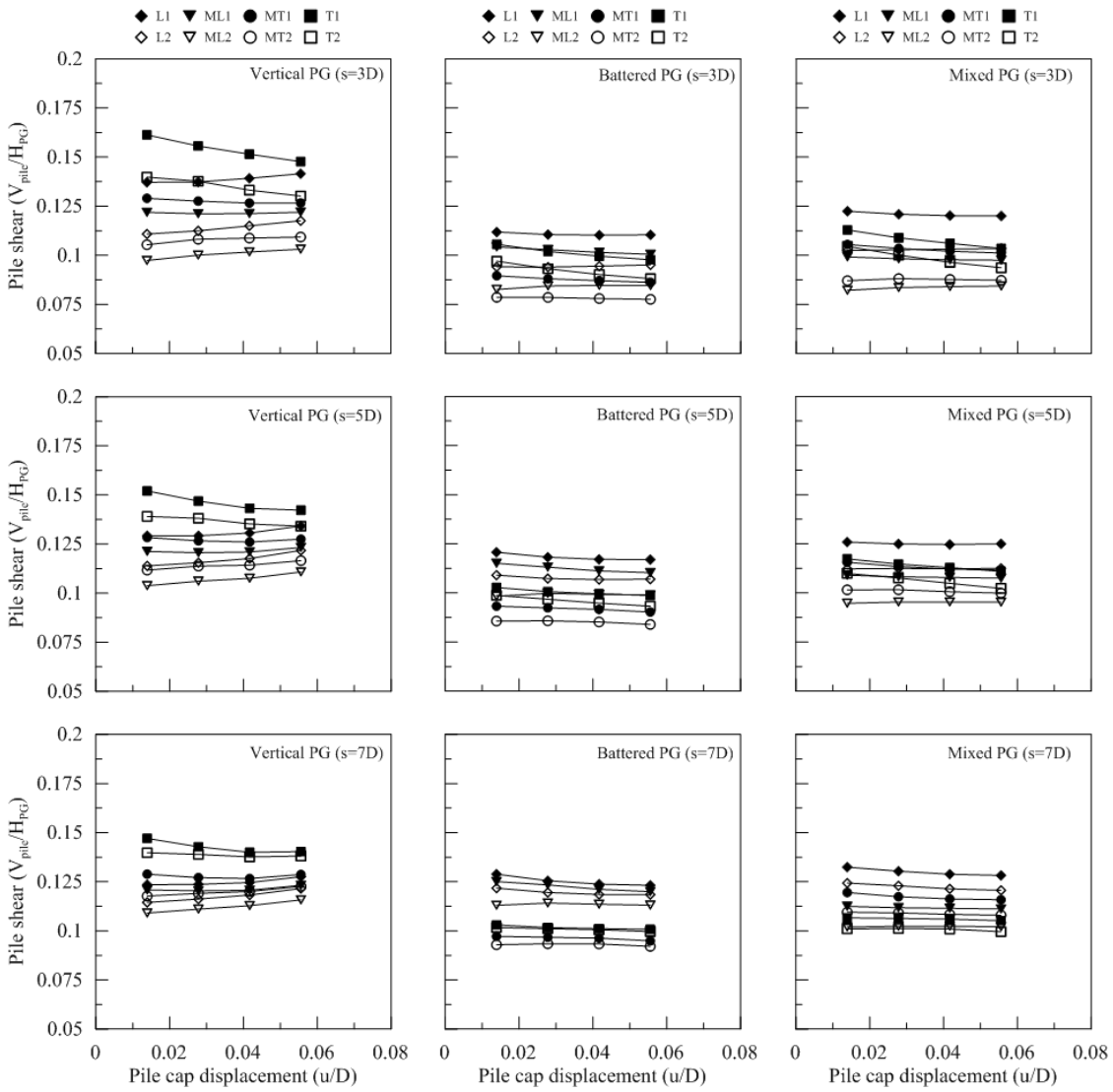

Figure 66. Effect of pile spacing on normalized pile shear

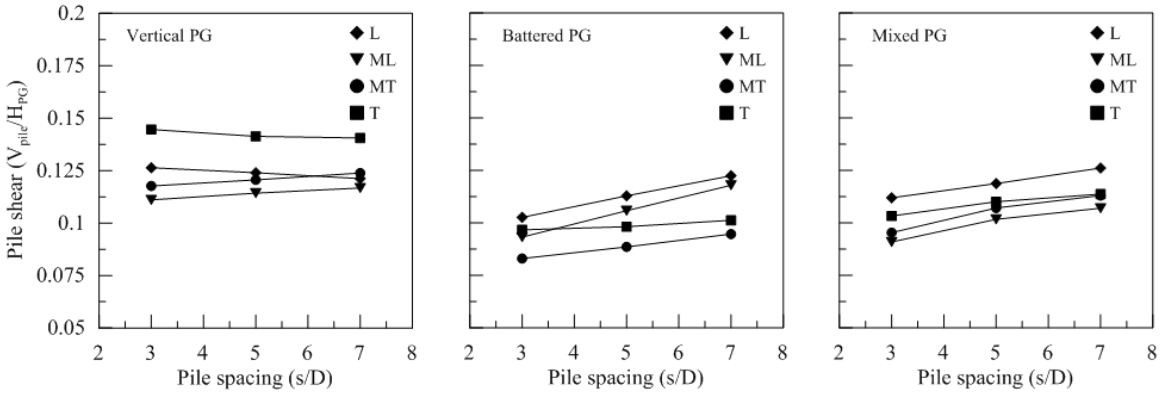

Figure 67. Variation of the lateral capacity and group efficiency with displacement

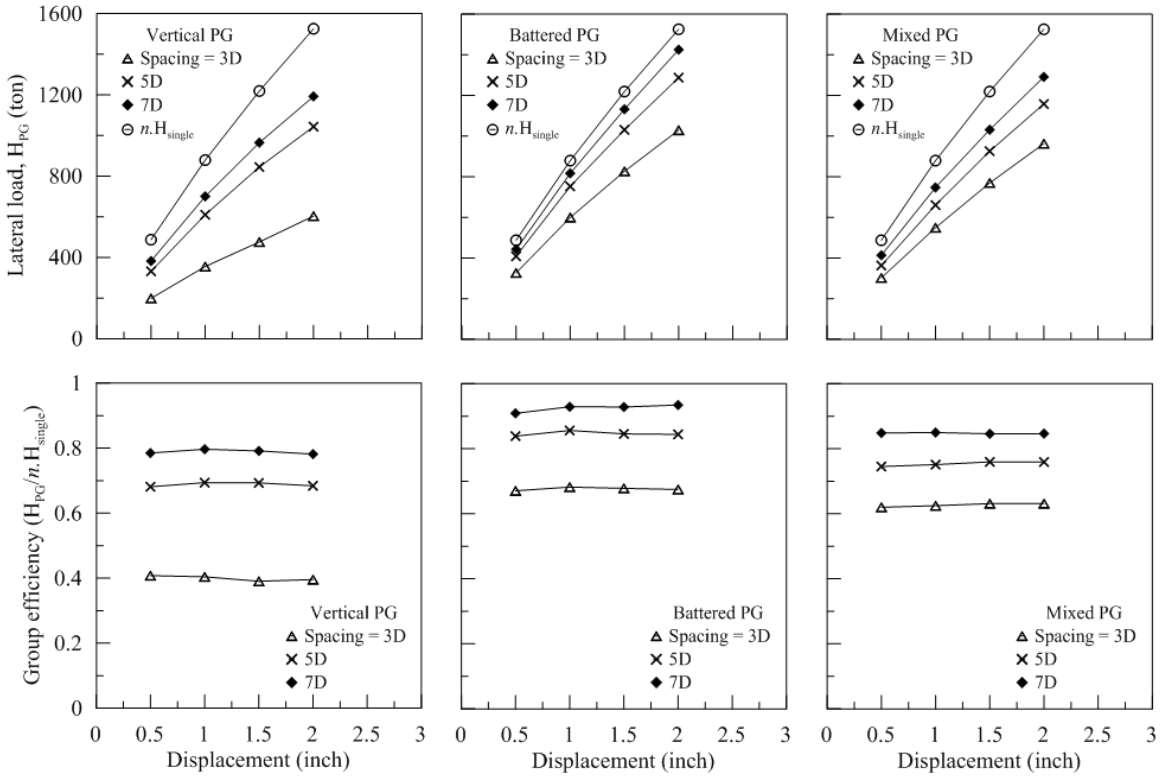

The comparison of PG efficiency at different pile spacing is presented in Figure 68. In general, increasing pile spacing resulted in higher efficiency for all PGs types. This follows the fact that the group effect become weaker at larger spacing, and the lateral capacity of each pile in the group is closer to the individual pile capacity. The battered PG had the highest efficiency followed by the mixed and vertical PGs, respectively. The largest improvement in PG efficiency was in the vertical PG at 28% when the spacing

increased from 3D to 5D as compared to 12% and 16% in the mixed and battered PGs, respectively. When the spacing was increased from 5D to 7D, the percent improvement was less than 10% in all PGs. The latter indicates that the influence of the group effect becomes minimal at pile spacings greater than 5D [113]. The efficiency results for the vertical PG suggests that switching to mixed or battered PG configuration at 3D spacing is an alternative design option to increase the PG lateral capacity in addition to increasing pile spacing.

Figure 68. Effect of pile spacing on the group efficiency

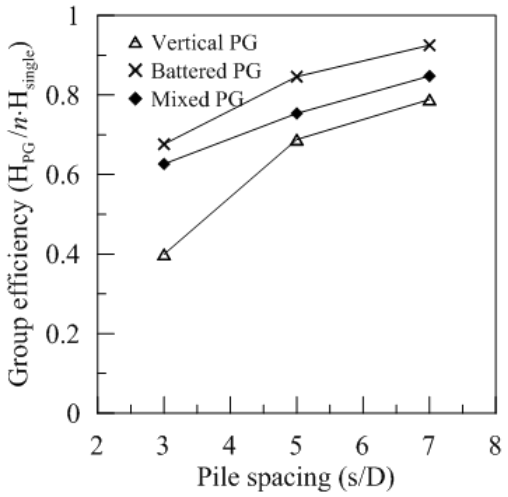

Effect of Pile Spacing on p-multipliers. The p-multiplier is a scalar that accounts for the group effect in the beam-spring FE modeling (e.g., FB MultiPier, Ensoft GROUP). This factor is applied to p-y curves for a single pile to obtain the p-y curves for a pile-in-group. In order to back-calculate the p-multiplier from the FE model, the p-y curves at several points over depth were obtained for the single pile and pile-in-group cases, and then the p-multiplier is averaged over the depth (Figure 69). However, this approach is laborious and time-consuming when analyzing multiple pile group cases. Instead, a time-efficient procedure was adopted in this study to back-calculate the p-multipliers. This procedure starts with the soil resistance profiles for the single pile and pile-in-group at a presumed displacement (Δy), as illustrated in Figure 70. Then, the soil resistance ratio of the pile-in-group to the single pile (p_g/p_s) is estimated over depth. The p-multiplier is estimated from the average of soil resistance ratios over the influence depth (~15D). The pile top/pile cap displacement (Δy) was assumed 0.1D, which was selected to ensure a fully mobilized soil resistance.

Figure 69. Estimation of p-multipliers following the definition in literature

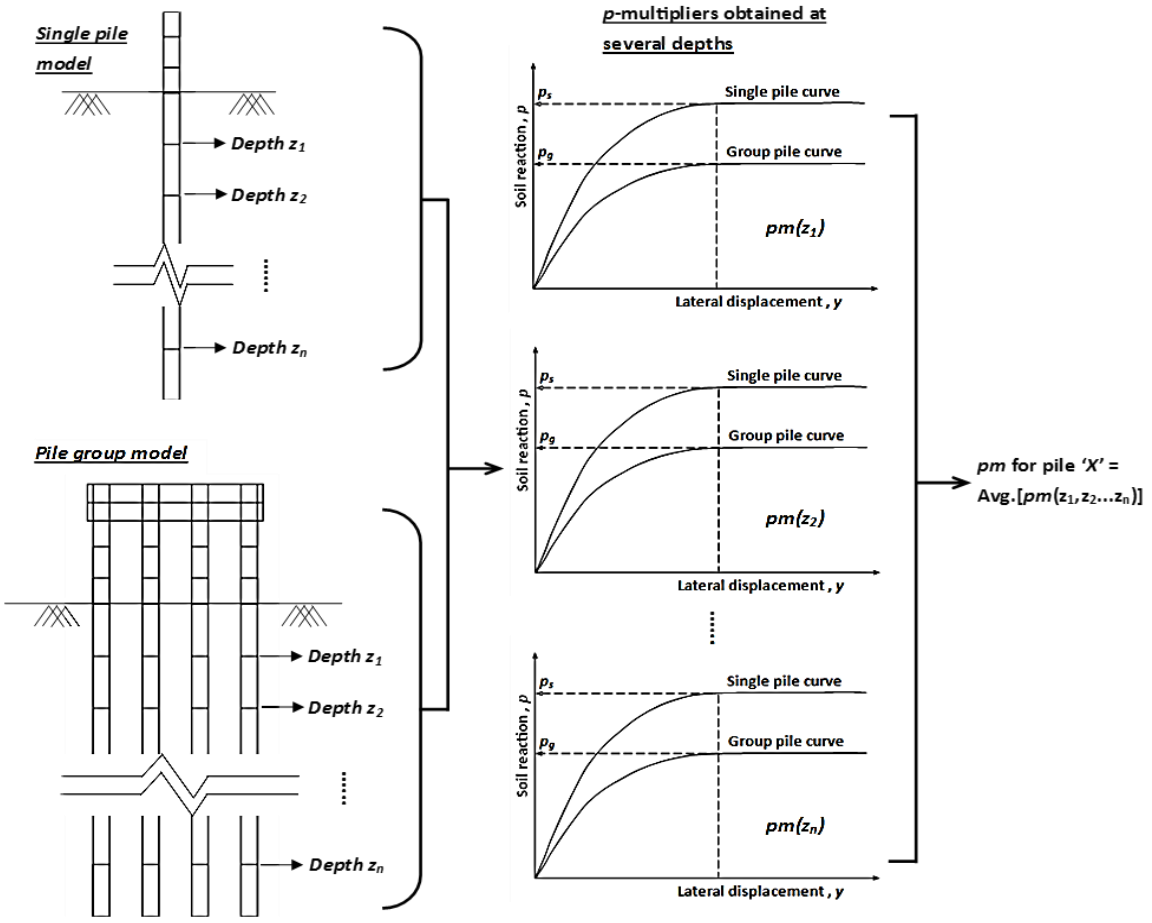

The soil resistance profiles for different pile spacings (3D, 5D, and 7D) in medium clay soil for the vertical, battered, and mixed PGs are shown in Figure 71, Figure 72, and Figure 73, respectively. The profile from the single pile model used for p-multipliers calculation is presented in the top left plot. The effect of pile spacing is clearly seen when the figures of 3D spacing are compared to the figures of 5D and 7D spacings. The mobilized soil resistance in the pile groups increased at larger pile spacing, which resulted in p-multipliers closer to 1.0.

The results of p-multipliers versus spacing are presented in Figure 74, which are averaged for each pile row, following the practice of reporting p-multipliers as a function of spacing and pile location (e.g., [44]). The largest increase in the p-multipliers in all pile groups was when the pile spacing increased from 3D to 5D. At 5D spacing, the average increase in p-multipliers was more notable in rows ML, MT, T with 0.3-point increase, and at a lesser degree in the leading row (L) with 0.2-point increase, approximately. Further the increase in pile spacing from 5D to 7D resulted in a smaller increase in p-

multipliers with 0.1-point increase on average. The latter indicates that the influence of group effect significantly diminishes at pile spacings of greater than 5D.

The results for the single column and single row pile groups are presented in Figure 75. Again, increasing pile spacing resulted in higher p-multipliers, and the largest increase was when the spacing increased from 3D to 5D. For the single column group, the p-multipliers were slightly higher compared to the vertical pile group (Figure 74), which is expected due to the absence of neighboring piles. At 7D spacing, the p-multipliers approximately reached the unity value (1.0). Similar to the vertical pile group, the row with the highest p-multipliers was row L, followed by rows T, MT, and ML, respectively.

Figure 70. Proposed procedure for estimation of the p-multiplier using soil resistance profiles

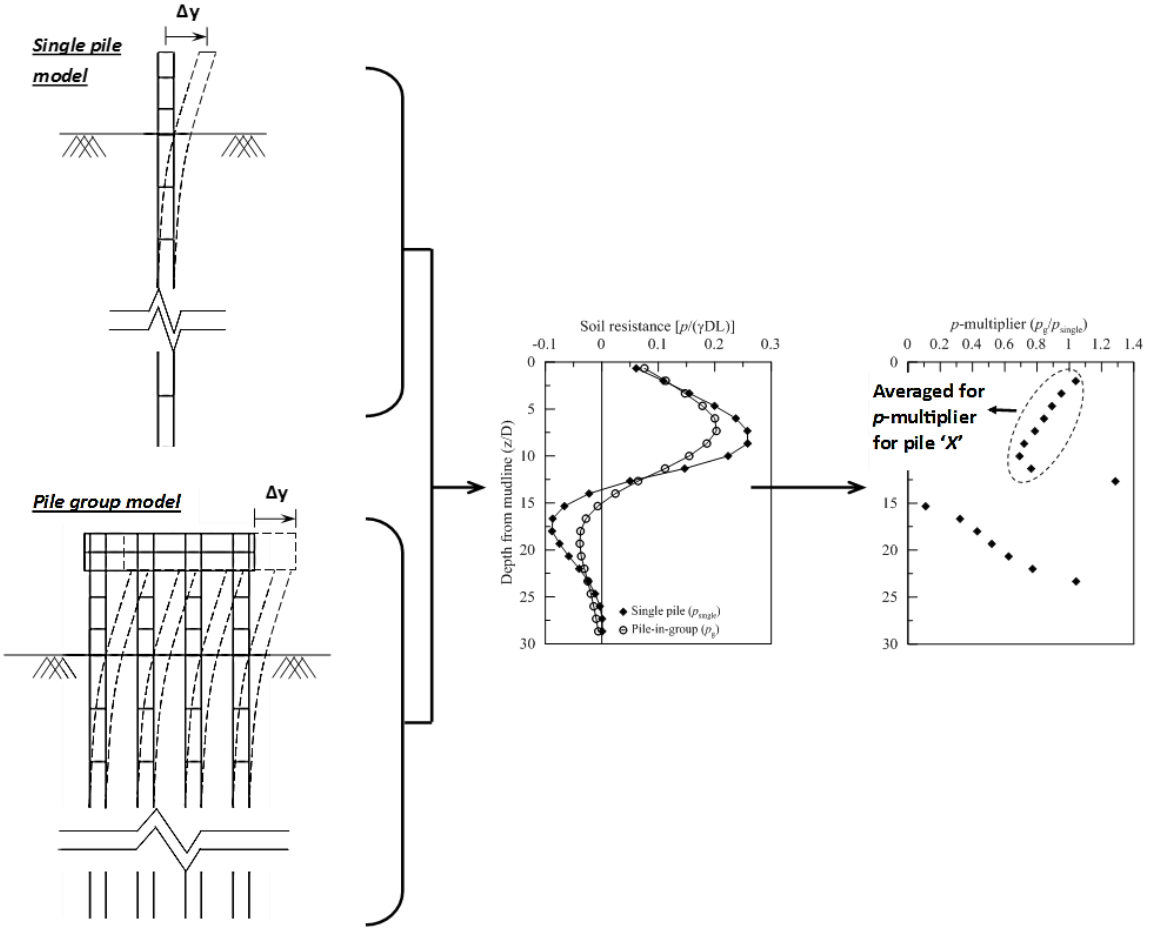

Figure 71. Soil resistance profiles for pile groups at 3D spacing

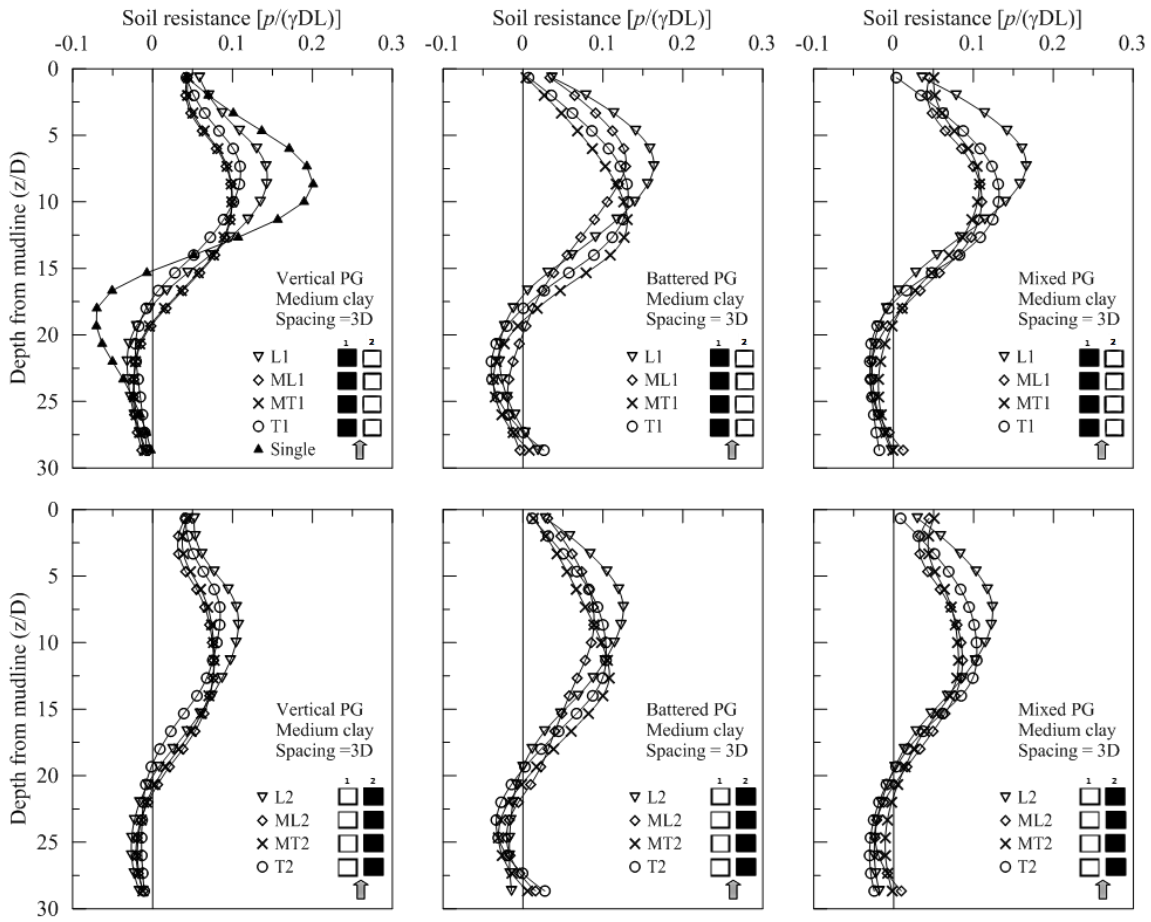

For the single row group, the influence of the group effect was notably weaker as compared to the single column group. The p-multipliers at 3D spacing were greater than 0.8 and reached to unity at 5D spacing. The p-multipliers at 3D spacing was the highest in all pile groups at similar spacing. Notice that piles 1 and 4 had higher p-multipliers than piles 2 and 3 because they are located at the edges of the pile group. The single row group results suggest that pile spacing in the loading direction can be used solely to determine the p-multipliers for the cases when pile spacing in the transverse (to the load) direction is greater than 3D.

Figure 72. Soil resistance profiles for pile groups at 5D spacing

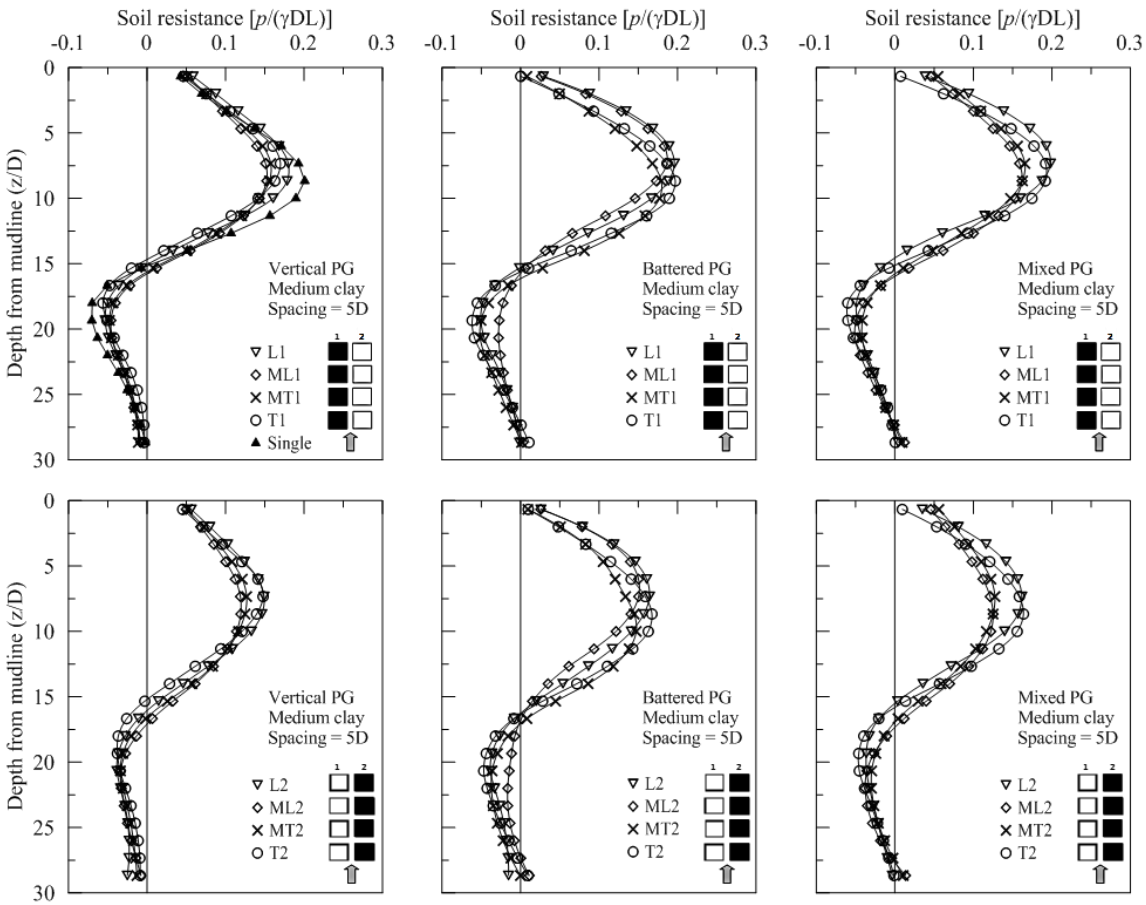

Figure 73. Soil resistance profiles for pile groups at 7D spacing

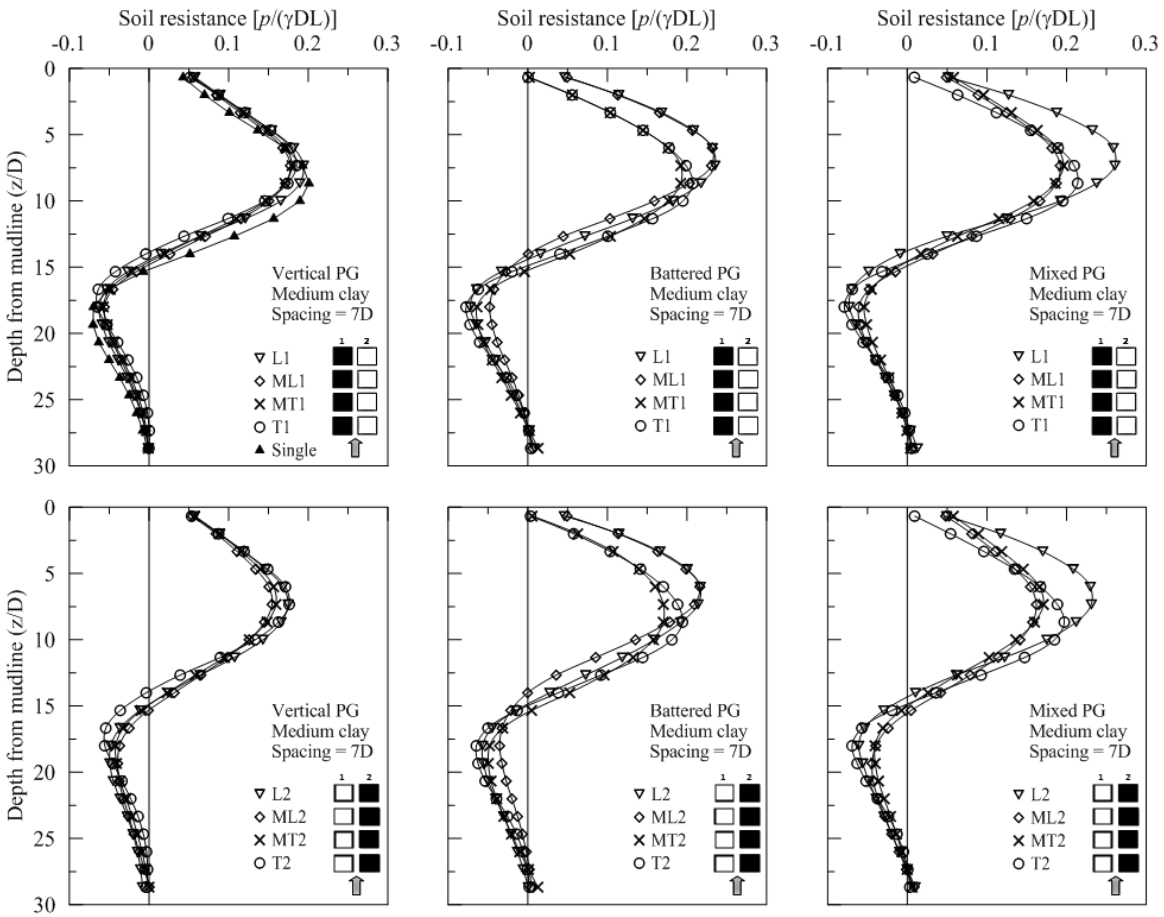

Figure 74. Effect of pile spacing on p-multipliers for vertical, battered, and mixed pile groups

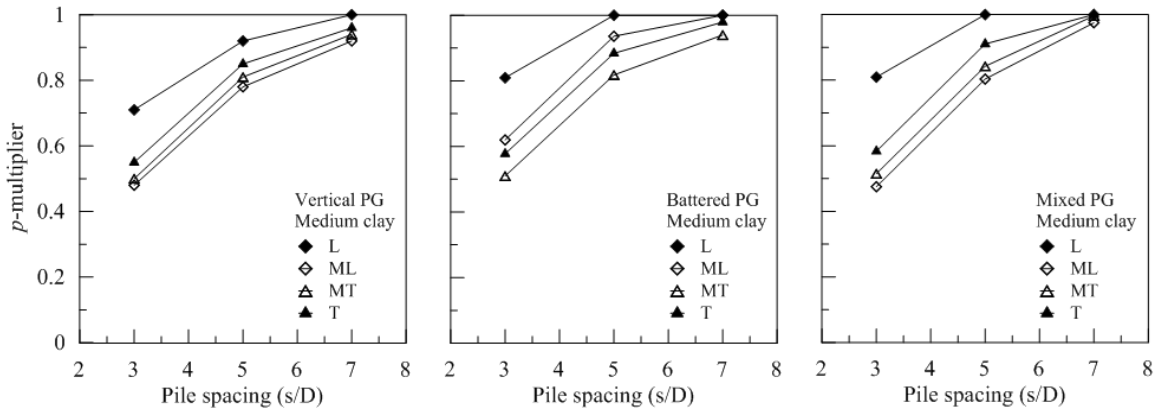

Figure 75. Effect of pile spacing on p-multipliers for single column and single row pile groups

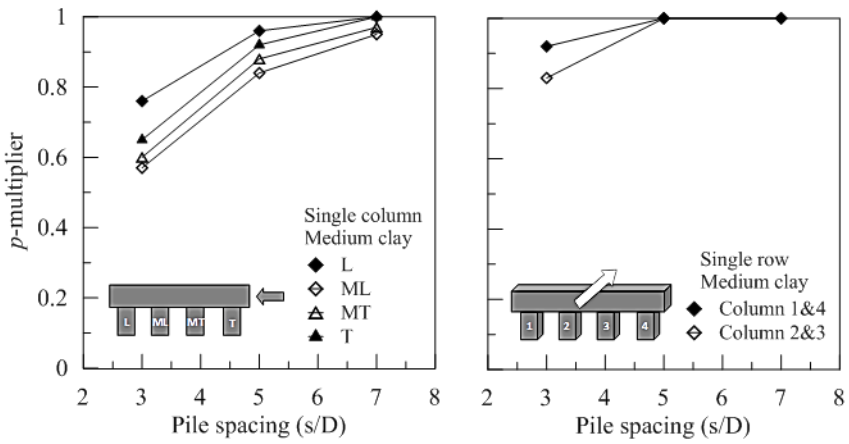

Effect of Clay Soil Type on P-Multipliers. The recommended p-multipliers in literature are given for two main soil categories; sandy or clay soils. In the current study, the focus is on clay soils, which were classified into three types; soft, medium, and stiff based on consistency. The soil strength and stiffness properties for each clay category were obtained from the literature ([111], [112]), which were used to estimate the clay model parameters presented earlier. The results for the effect of clay soil type on p-multipliers in the pile groups are shown in Figure 76, in which the average p-multipliers per row are presented. It can be noticed that the influence of clay soil is also affected by the pile spacing. At pile spacing 3D, the p-multipliers increased (0.1-point) steadily and consistently when the clay soil became stiffer. At pile spacing 5D, the p-multipliers increased consistently only in the vertical PG, while in the battered and mixed PGs they increased only when the clay type was changed from soft to medium. At pile spacing 7D, the influence of clay type became negligible.

The influence of clay soil type on the single column/row pile groups is shown in Figure 77 and Figure 78, respectively. For the single column pile group, the effect of clay soil type was closely similar to the vertical PG, but the increase in the p-multipliers was slightly less (0.08-point). For the single row pile group, the influence of clay soil type is noticed only at pile spacing 3D, which follows the previous observation in Figure 75 that the group effect vanishes at pile spacings greater than 5D for single row pile groups.

Figure 76. Effect of clay soil type on p-multipliers for vertical, battered, and mixed pile groups

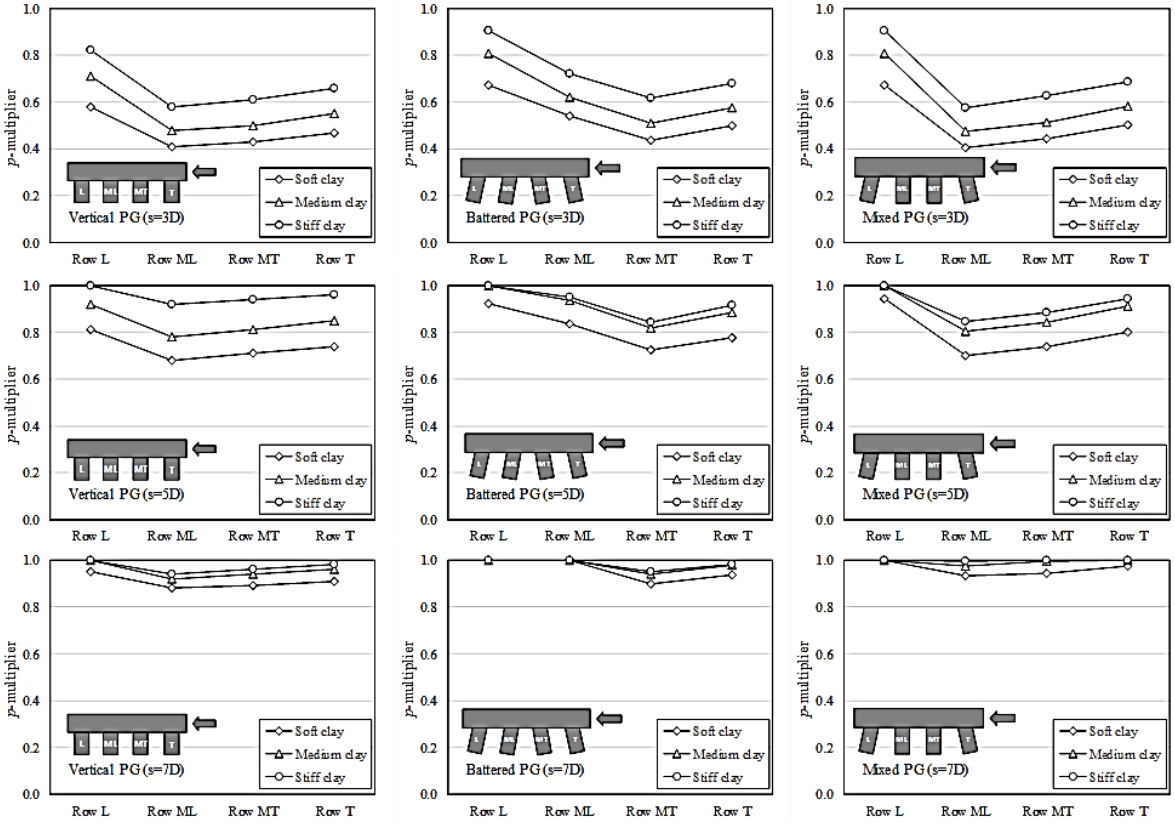

Figure 77. Effect of clay soil type on p-multipliers for single column pile group

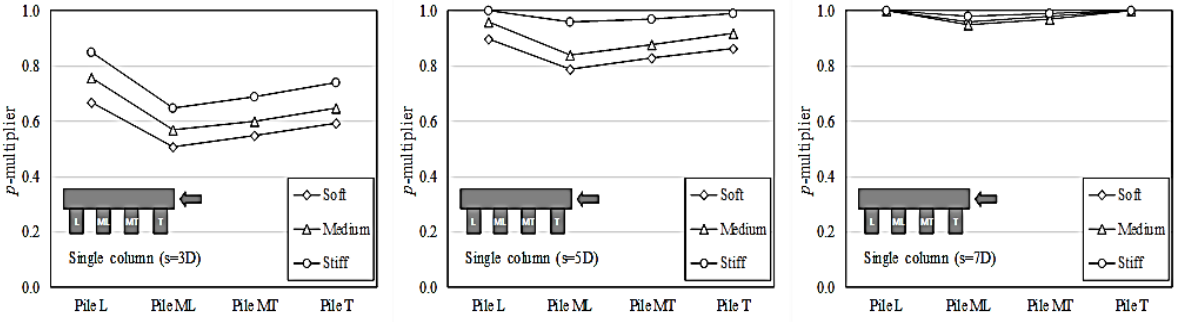

Figure 78. Effect of clay soil type on p-multipliers for single row pile group

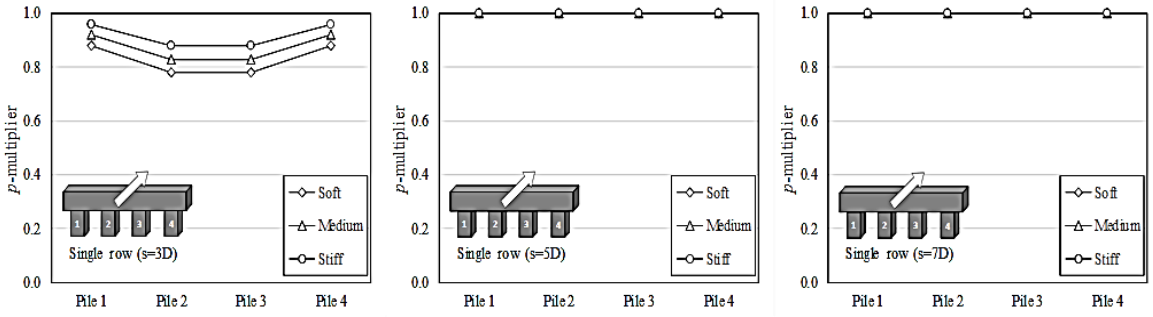

Dynamic Lateral Behavior of Pile Groups Subjected to Barge Impact

In this study, the lateral behavior of three types of pile groups (vertical, battered, and mixed PGs) was simulated, evaluated and compared. The FE models for the barge impact comprised of several components that will be discussed in the following sub-sections. In addition, the results of FE simulation of the statnamic test of test pile TP7 is presented, which was used to verify the soil model parameters.

Study Cases

This study was conducted on three types of pile groups (vertical, battered, and mixed) being hit by the barge at different speeds: 2 knots (3.37 ft./s), 4 knots (6.75 ft./s), and 6 knots (10.12 ft./s). These speeds represent slow to moderate level navigation speeds for barges [44]. The barge weight was maintained at 1873 tons in all cases. In the FE models, the barge was set to hit the middle of the pile cap, which was determined from the mean water level for the M19 pile group foundation (Figure 79). The design barge specs by AASHTO suggests that the draft for fully loaded barge is 8.7 ft. In the horizontal plane, the centerline axis for the barge was aligned with the cap central axis.

Figure 79. Positioning of the barge and impact point

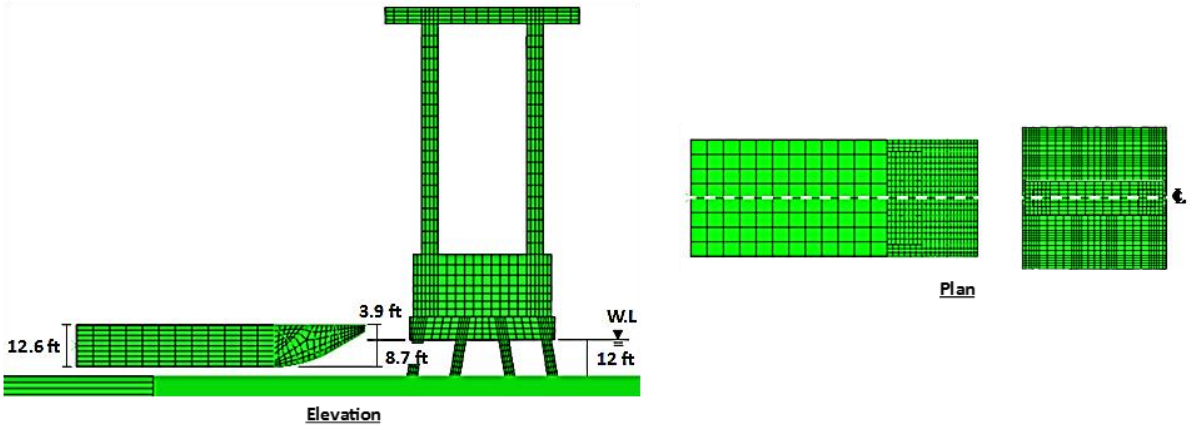

Barge FE Model

The JH barge has been used in many FE simulations of barge impact (e.g., [94], [95], [96], [97], [98]). The standard JH barge specs per AASHTO guidelines was used in the current study [44]. The actual barge dimensions are 195 ft. L x 35 ft. W x 12 ft. D, and the total weight is 1873 tons for fully loaded barge. The JH barge body can be separated into two main regions: the bow rake and the cargo region (Figure 80). The entire JH barge is built from trusses and steel plating. In this study, the bow rake model was built of 3-D beam and shell elements. The beam elements were used to model the internal truss frames; while the shell elements modeled the outer steel plating. The total number of truss frames was 14 spaced at 2.16 ft. in the lateral direction (Figure 81).

Figure 80. FE model for the Jumbo Hopper barge

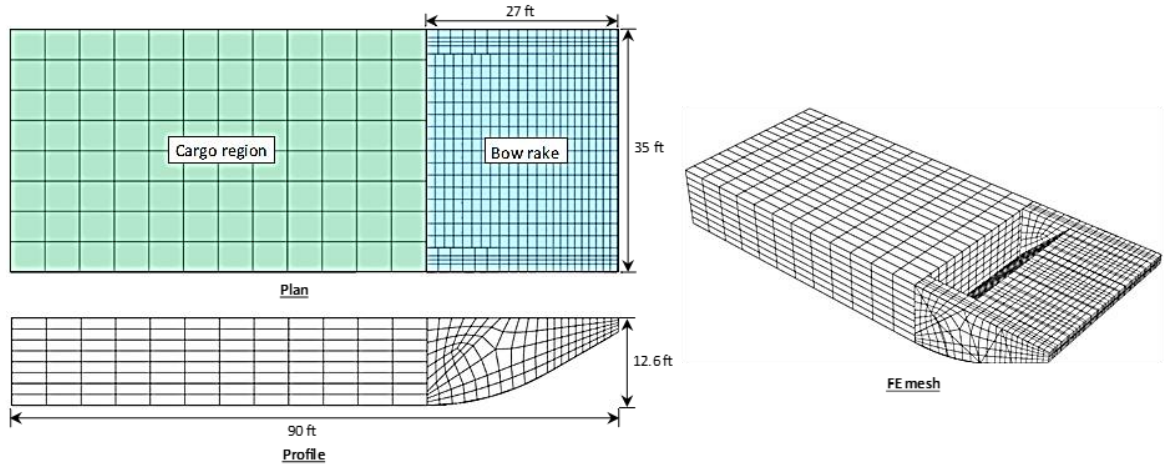

Figure 81. Bow rake FE model details

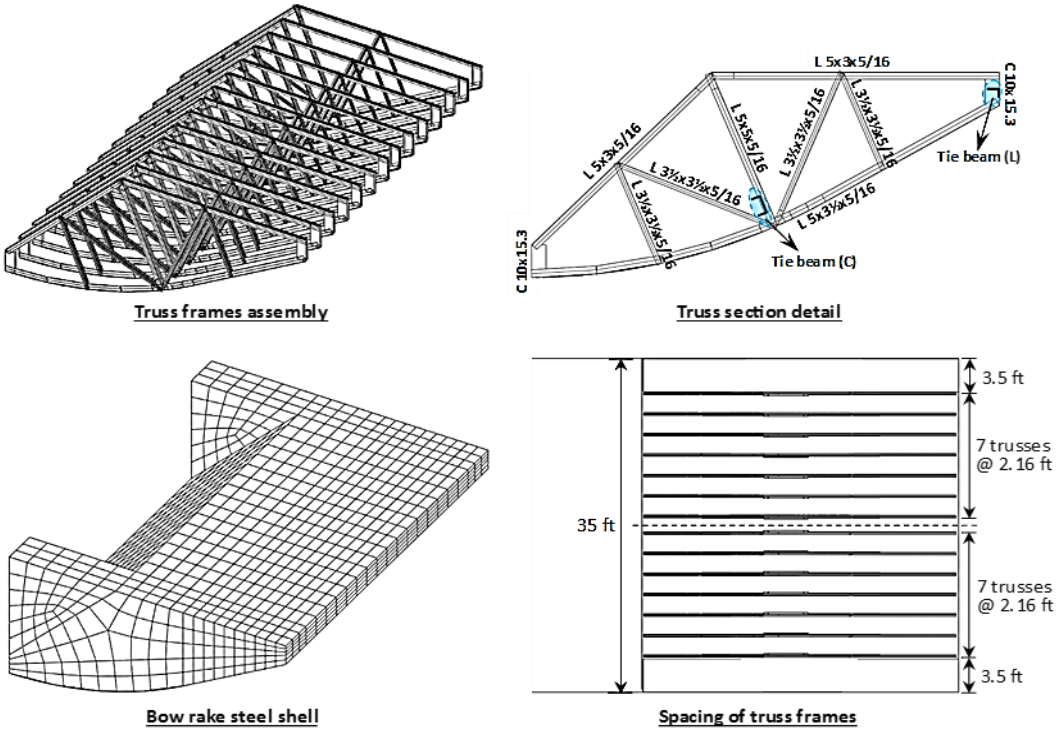

Each truss frame was built from A36 steel beams with L and C structural shapes. The frames were mirrored at the barges' center line and laterally braced by two tie beams (L & C shaped) at the front of the bow and at the bottom of the diagonal member, respectively. All components of the truss frame were modeled using 3-D beam elements (B23), and the beam junctions were numerically constrained to simulate the effect of stiffened joints. The outer shell was built from A36 steel plating with 3/8" thickness and modeled using 3-D shell elements (S4R). The total number of elements used in the bow rake model was ~3200.

The cargo region was modeled as a solid block of A36 steel with a total weight of 1873 tons. The elements used were the 3-D solid continuum elements (C3D8R) with a total number of ~500 elements. The bow rake and cargo region were numerically tied using numerical constraints so that they behave as a single unit.

The A36 steel material behavior was simulated using the elastoplastic von Mises constitutive model. The A36 steel elastic properties used in the model were the Young's modulus, E_{st} = 29000 ksi, and the Poisson's ratio, ν = 0.26.

Pile Group and Bridge Pier FE Model

The M19 pier foundation design was used to study the lateral behavior of the three pile groups subjected to barge impact. The FE model was created from three main components: the pier superstructure, the bridge deck and girders, and the pile group foundation.

Pier Superstructure. The concrete pier superstructure comprised of the protection wall, columns, and the seating beam for girders (Figure 82). The pier superstructure was modeled as a solid part using the 3-D solid continuum element (C3D8R) with a total of ~2200 elements. The concrete material behavior was assumed linear elastic with the elastic properties Young's modulus E_c = 3800 ksi and Poisson's ratio ν = 0.2. The unit weight of concrete used in the model was 150 pcf.

Figure 82. Geometry and FE mesh for the pier superstructure

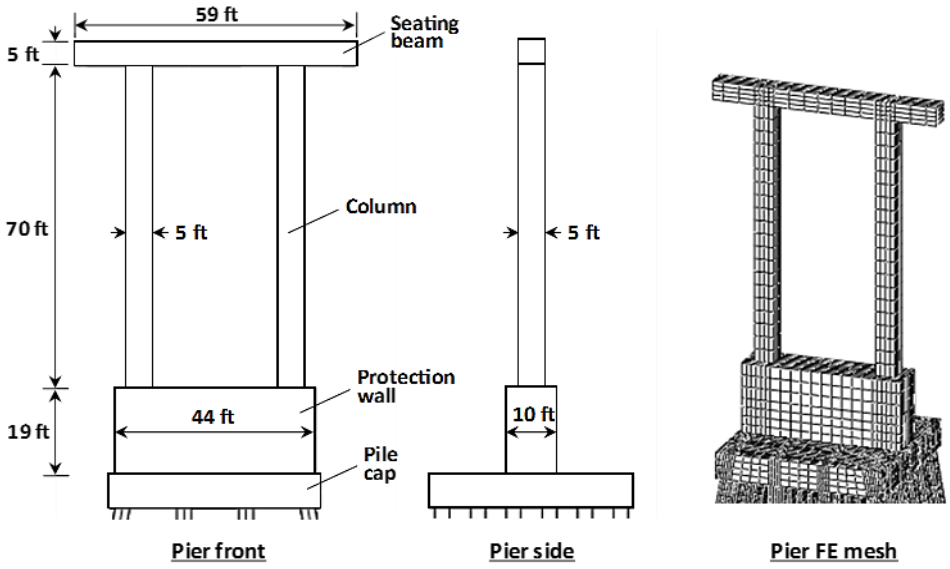

Girders and Bridge Deck. The pier superstructure supported 12 girders and two concrete decks. The girders used in the M19 case were the LG-78 concrete girders spaced at 10.75 ft. and had 200 ft. span length. The section detail for LG-78 girders was simplified in the FE model to an approximate I-section in terms of cross-sectional area and second moment of area. The concrete decks were modeled as solid slab of 8 in. thickness using 3-D shell elements (S4R) and connected to the girders using tie constraints (Figure 83). The concrete material for the girders and decks was assumed

linear elastic with similar elastic properties to the pier superstructure (E_c = 3800 ksi, and ν = 0.2). The unit weight of concrete for girders and deck used in the model was 150 pcf.

Figure 83. Girders and deck FE model

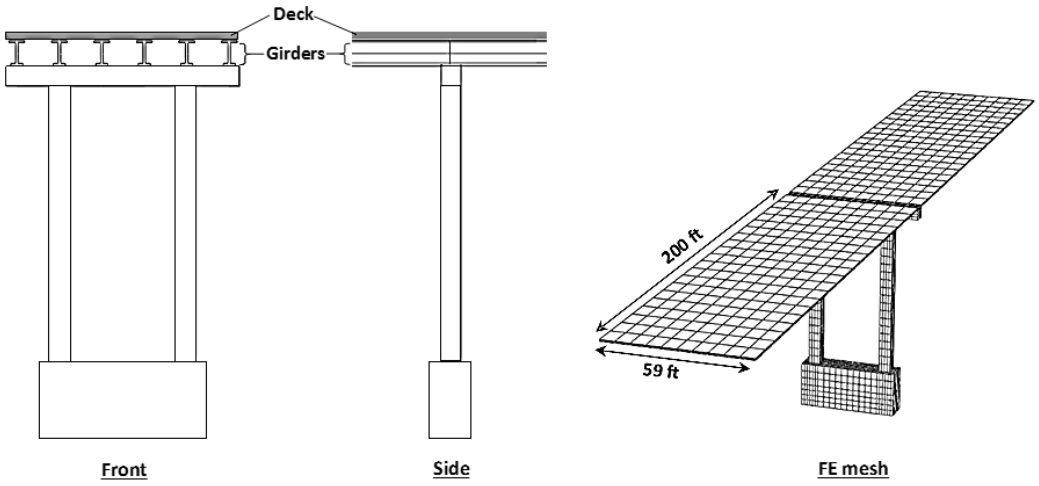

Pile Group Foundation. The M19 pile group foundation comprised of 24 battered piles and the pile cap. In addition to battered pile group, FE models developed and analyzed for vertical and mixed pile groups were for barge impact (Figure 84). The geometry and dimensions of the pile group models were adapted from the M19 battered pile group. The prestressed concrete piles had 3 ft. square section and 110 ft. in long. The pile cap was built of cast-in-place concrete and measured 44 ft. × 42.5 ft. × 7 ft. The main steel reinforcement (Grade 270 steel) in the piles comprised of 36 x 0.6″-dia. steel tendons. The pile group including the pile cap that was modeled as a single mesh using the 3-D solid continuum element (C3D8R) with a total of ~21000 elements. The main steel reinforcement was modeled using the embedded shell elements (S4R), which allowed to incorporate the prestress force in the piles. The concrete material was modeled using the Concrete Damaged Plasticity (CDP) constitutive model (described earlier). The concrete elastic properties for piles were E_c = 5000 ksi and ν = 0.2. The steel material was modeled using the elastoplastic von Mises model with the elastic properties: E_s = 29000 ksi and ν = 0.26.

FE Soil Models. The soil profile identified earlier for M19 site was used here too. The soil layering was divided into six clay layers and two sand layers. The FE mesh for the soil layer was built from two types of elements: the standard elements, and the infinite elements. The standard elements were the 3-D solid continuum elements (C3D8R) and were assigned to the central part with elastoplastic material behavior. The infinite

elements (CIN3D8) were used on the far boundaries to provide the equilibrium reaction and absorb the propagating stress waves, as discussed earlier. The total number of elements used in the soil body was ~153000. The clay material behavior was modeled using the Modified Cam Clay (MCC) model; while the sand material behavior was modeled using the Drucker Prager model (DP). The material parameters for both models are summarized in Table 18. The soil model parameters used in the barge impact problem were verified using the results of the statnamic test discussed in the following section. Additionally, material damping for the soil material was introduced using the two-parameter Rayleigh damping model described earlier. The Rayleigh damping parameters (α, β) were estimated for an average damping ratio $\xi = 2\%$ over the frequency range 1-10 Hz. The damping parameters obtained from the iterative procedure were $\alpha = 0.1$, $\beta = 0.0013$.

Figure 84. Pile group geometry and FE models (D is pile width = 3 ft.)

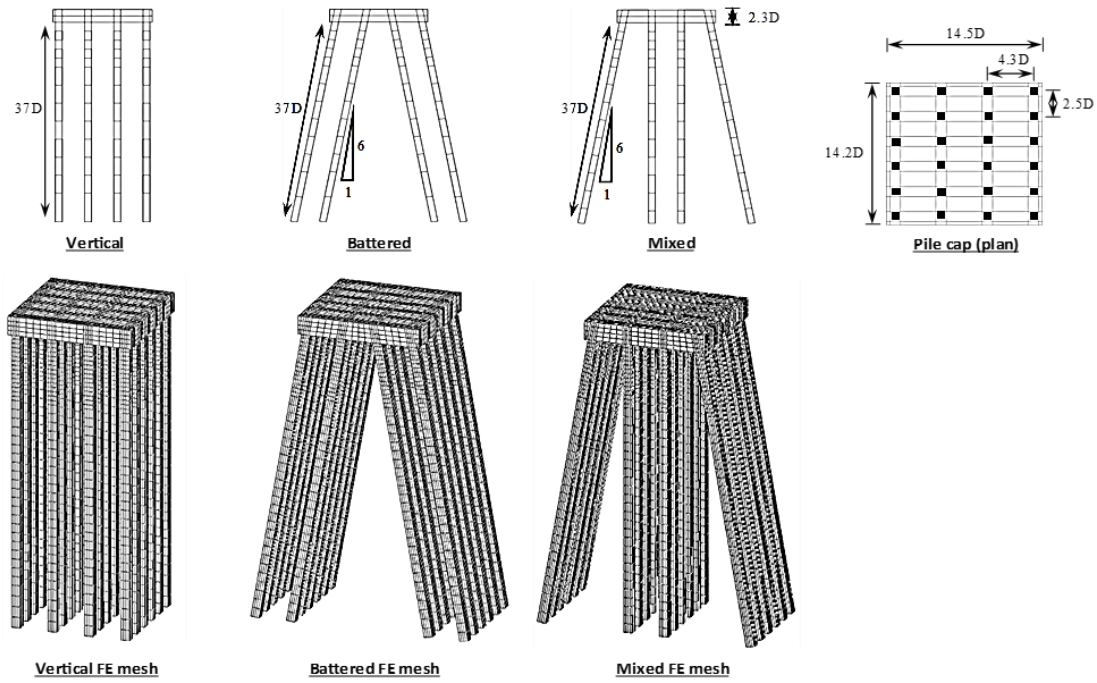

Table 18. MCC and DP model parameters used in the barge impact FE models

Soil Type	Depth from mudline (ft)	Unit weight (pcf)	Poisson's ratio (ν)	MCC			DP		
				E (ksf)	M	λ	E (ksf)	β	d (psf)
Soft Clay	0-15	123	0.40	52	0.9	0.14	-	-	-
Stiff Clay	15-25	119	0.40	239	1.1	0.12	-	-	-
Medium Clay	25-38	108	0.40	259	1.0	0.13	-	-	-
Medium Sand	38-49	120	0.40	-	-	-	360	53	10
Stiff Clay	49-70	113	0.40	528	1.2	0.12	-	-	-
Stiff Clay	70-81	122	0.40	637	1.2	0.12	-	-	-
Stiff Clay	81-99	128	0.40	637	1.2	0.12	-	-	-
Dense Sand	>99	124	0.40	-	-	-	720	58	10

Verification of Soil Parameters from Statnamic Test Results

The soil and damping parameters were verified to ensure realistic responses in the pile group models subjected to a barge impact. During the construction of M19 pile foundation, a statnamic test was performed on test pile TP7, which was located 135 ft. west of the M19 pier. A FE model was developed for pile TP7 to simulate the statnamic test, in which the soil model and damping parameters in Table 18 were used. The experimental and FE pile response was compared to verify the response from the soil model.

The TP7 driven near the M19 pier was 36-in. squared prestressed concrete pile and 123 ft. in total length with similar specs to the piles of M19 pier foundation. The statnamic test on TP7 was conducted in five consecutive load cycles with increasing peak load after each cycle (Figure 85a). In this study, the test results of TP7 were used to verify the soil model parameters and the pile response in the FE models. The displacement time history and load-displacement response measurements from the linear variable differential transformer (LVDT) are shown in Figure 85b, and Figure 85c, respectively. The peak load for the first cycle was 33 kips and increased up to 115 kips in the fifth cycle. The peak displacement during the first cycle was 2 in. and reached to 10 in. during the fifth cycle.

Figure 85. Results of statnamic test on TP7: (a) load time history, (b) displacement time history at loading point, and (c) load-displacement curves

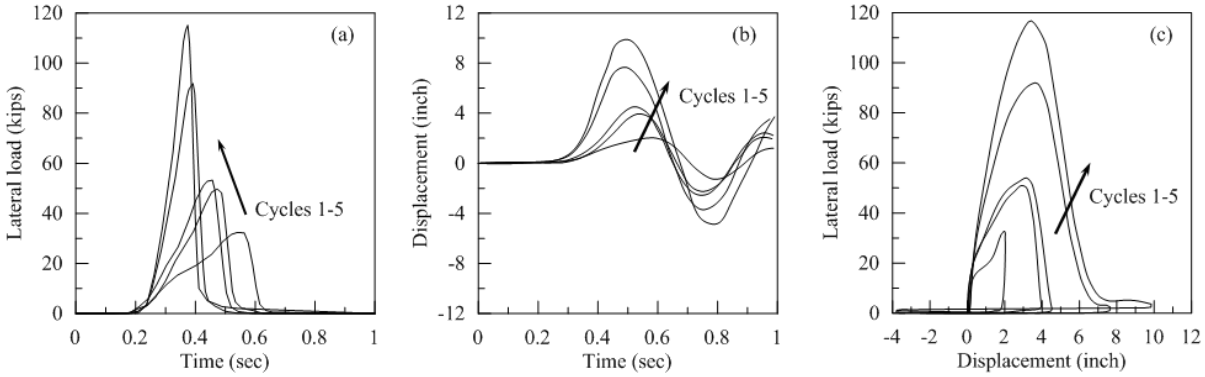

FE Model of TP7. A FE model was developed for the TP7 to verify the soil constitutive model parameters and damping constants. The model comprised of the pile and soil body (Figure 86). The pile was modeled using the solid continuum element (C3D8R) with the main steel reinforcement modeled using the embedded shell elements (S4R). The soil body was modeled using the solid continuum elements (C3D8R) for the central region (blue color in Figure 86) and using the infinite elements (CIN3D8) for the outer boundary regions (green color). The number of elements used was ~2300 for the pile and ~50000 for the soil.

Figure 86. Pile TP7 geometry and FE model

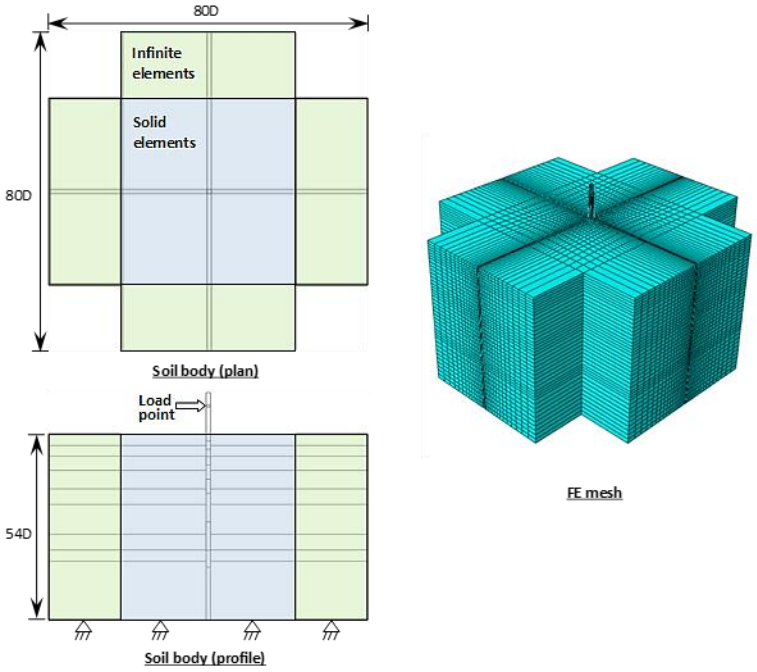

The statnamic load was applied as uniformly distributed load over a strip area of 1ft. width on the pile surface so that the center of the area corresponds to the loading point in the in-situ test, and included a dummy first step to establish the geostatic stress equilibrium (Figure 87). The load amplitudes for the five load cycles (Figure 85a) were imported into the FE model and used to vary the distributed load magnitude with time. The FE simulation was conducted in five consecutive loading steps, similar to the in-situ test. The duration of statnamic load cycle was less than 1.0 seconds, and there was 20-30 min gap after each cycle to reset the statnamic device and allows the pile's free oscillation to vanish prior to the next load cycle. The duration for each load step was fixed at 3.0 seconds, which was verified to be long enough to stop the free oscillation of the pile (Figure 87).

Results of Statnamic Simulation. The pile displacement at the loading point was used to verify the response from the FE model. Figure 88 compares the results of pile displacement for each load cycle from the statnamic test and the FE model, which demonstrates very good agreement for the first three cycles. For cycles 4 and 5, there is a notable difference (0.7-0.9 in.) in the peak displacement between the FE model and the statnamic tests, which can be attributed to pile damage. The statnamic test report showed that the strain gage readings at depth 16 ft. from the mudline were very high (>7000μ strain), which is a sign of pile damage.

Figure 87. Pile displacement response throughout the simulation steps

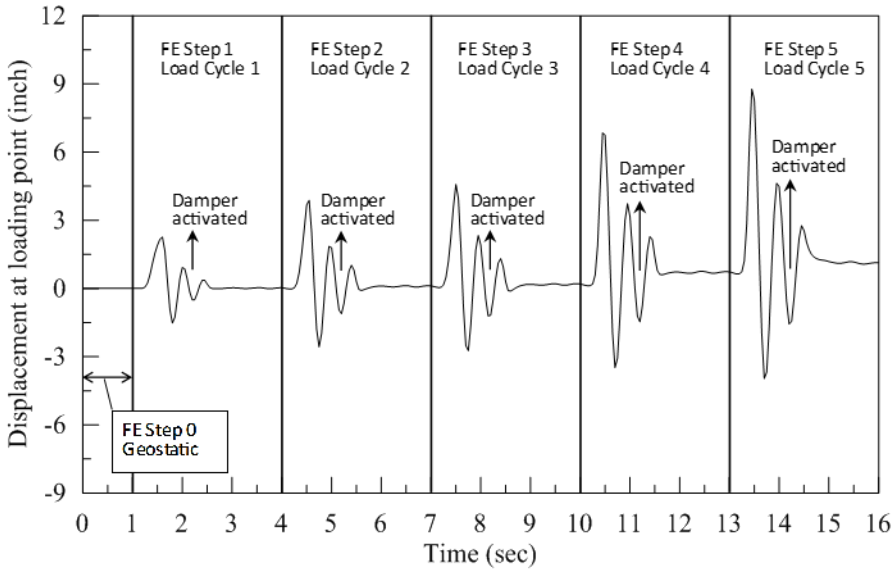

Figure 88. Pile displacement results at the loading point from the statnamic test and FE model

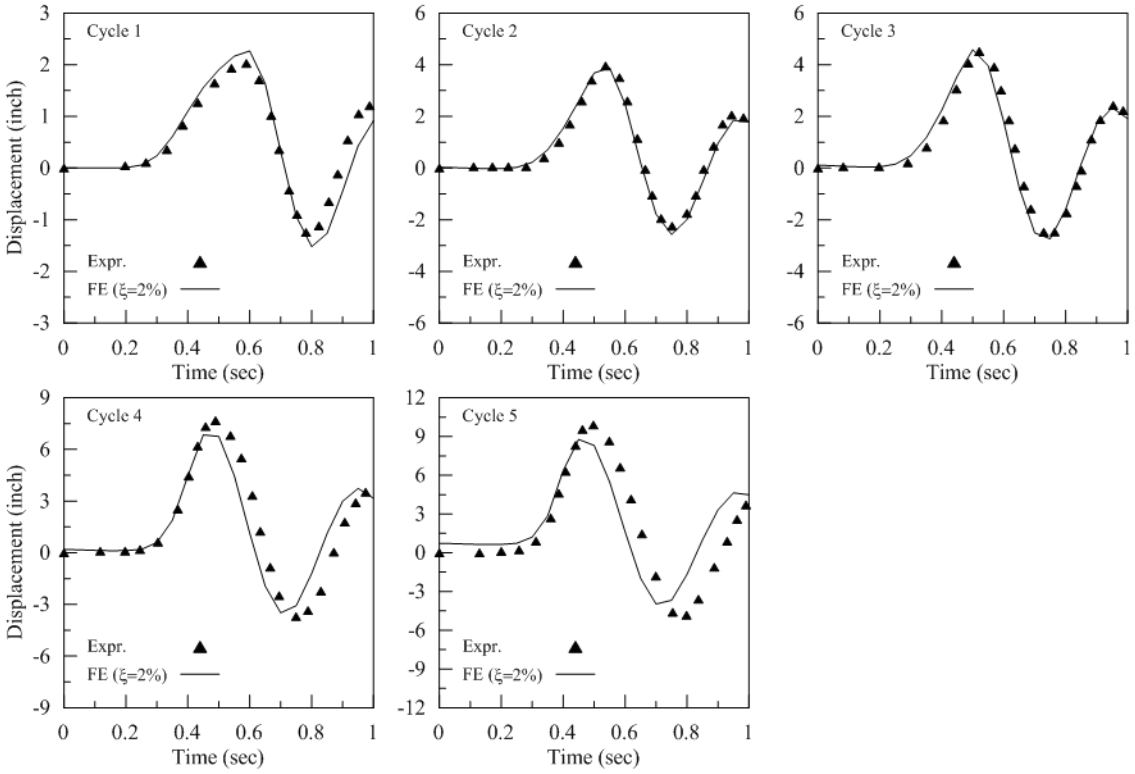

Loads and Solution Steps

The loads applied in the barge impact problem were gravity and artificial damping loads. The gravity load was applied to the soil body, pier superstructure, girders and deck, and pile group. The impact load by the barge was introduced by assigning an initial velocity in the horizontal direction to generate barge momentum. The artificial damping loads were introduced to eliminate the oscillations in the whole model induced by the gravitational acceleration, which were removed after the oscillations ceased, so they don't influence the model response during the barge impact.

The barge impact problem was solved in two steps with two seconds step duration: the equilibrium step 1, and the impact step 2 (Figure 89). In step 1, the model is brought to near static condition by allowing the soil to reach a state of geostatic stress equilibrium and dissipating the oscillations caused by the gravitational acceleration. The barge is initially positioned at a distance so that the impact occurs after the end of the first step, which is estimated from the barge velocity and the step time of two seconds. At the end of step 1, the impact is imminent and the barge bow is barely in touch with the pile cap.

In step 2, the barge impact progresses until the barge momentum dissipated and rebounds away from the pile group.

Figure 89. Illustration of steps for simulating the barge impact problem

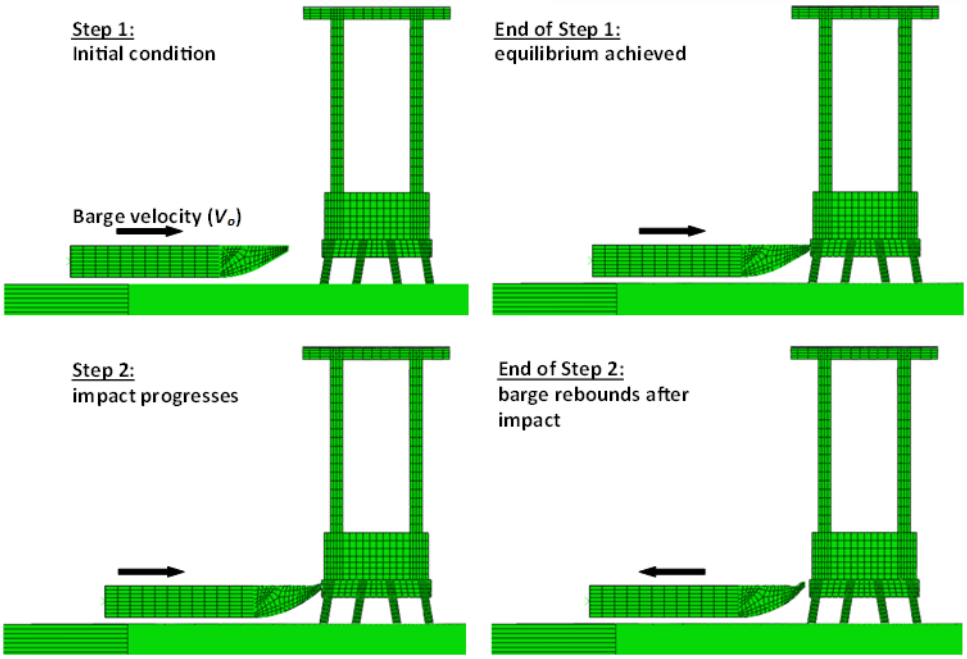

Results of Lateral Displacement

The resulted lateral displacement history at the pile cap and pier top elevations from the barge impacts for all cases are presented in Figure 90. The displacement history exhibits a large peak in the first 0.2-0.4 seconds as a response to the impact force, and subsequent smaller peaks corresponding to the free oscillations of the structure. It is noticed that the displacement vanished for the battered and mixed PGs after 2 seconds; whereas it returns to a non-zero value for the vertical pile group. The latter observation is referred to the gap formation in the front soil and to the significant damage in the piles (Figure 91). The damage contours plot is shown only for the vertical PG; while the battered and mixed PGs were free of damage for all impact cases.

The peak displacement at the pile cap was notably higher (2-8.4 in.) in the vertical PG; while in the battered and mixed PGs, the peak displacement remained within 2-2.5 in. at all barge speeds. The magnitude of peak displacement was mainly affected by the impact force, which is dependent on the lateral PG stiffness and the barge bow stiffness. The barge's kinetic energy is dissipated in the impact by two mechanisms: (1) PG

displacement, and (2) barge bow deformation. The PG displacement depends on the lateral PG stiffness, which is a function of PG type and soil resistance. When the PG stiffness is relatively low, a greater portion of the impact energy is dissipated in the PG displacement, while for very stiff PGs, the significant portion of the impact energy is absorbed by the bow deformation.

The lateral stiffness of the vertical PG is lower than the battered and mixed PGs, therefore, the impact generated greater lateral force and greater pile cap displacement for vertical PG. The relationship between the peak displacement and barge speed is presented in Figure 92. A linear relation between the displacement and speed is noticed in the vertical PG. In the battered and mixed PGs, the results show that the displacement was almost constant with the increased barge speed.

The barge bow deformation can be separated into two parts: elastic and inelastic. As shown in Figure 93, the bow deformation reaches a peak value and then recedes to a lower plateau. The difference between the peak and the plateau represents the elastic bow deformation, whereas the value at the plateau corresponds to the inelastic deformation. It can be noticed from the figure that the inelastic bow deformation in the vertical PG case was significantly lower than the battered and mixed PGs for the barge speeds greater than 2 knots. For example, at barge speed 6 knots, the inelastic bow deformation was 3.5 in. for the vertical PG versus 40-42 in. in the battered and mixed PGs.

Figure 90. Displacement history results

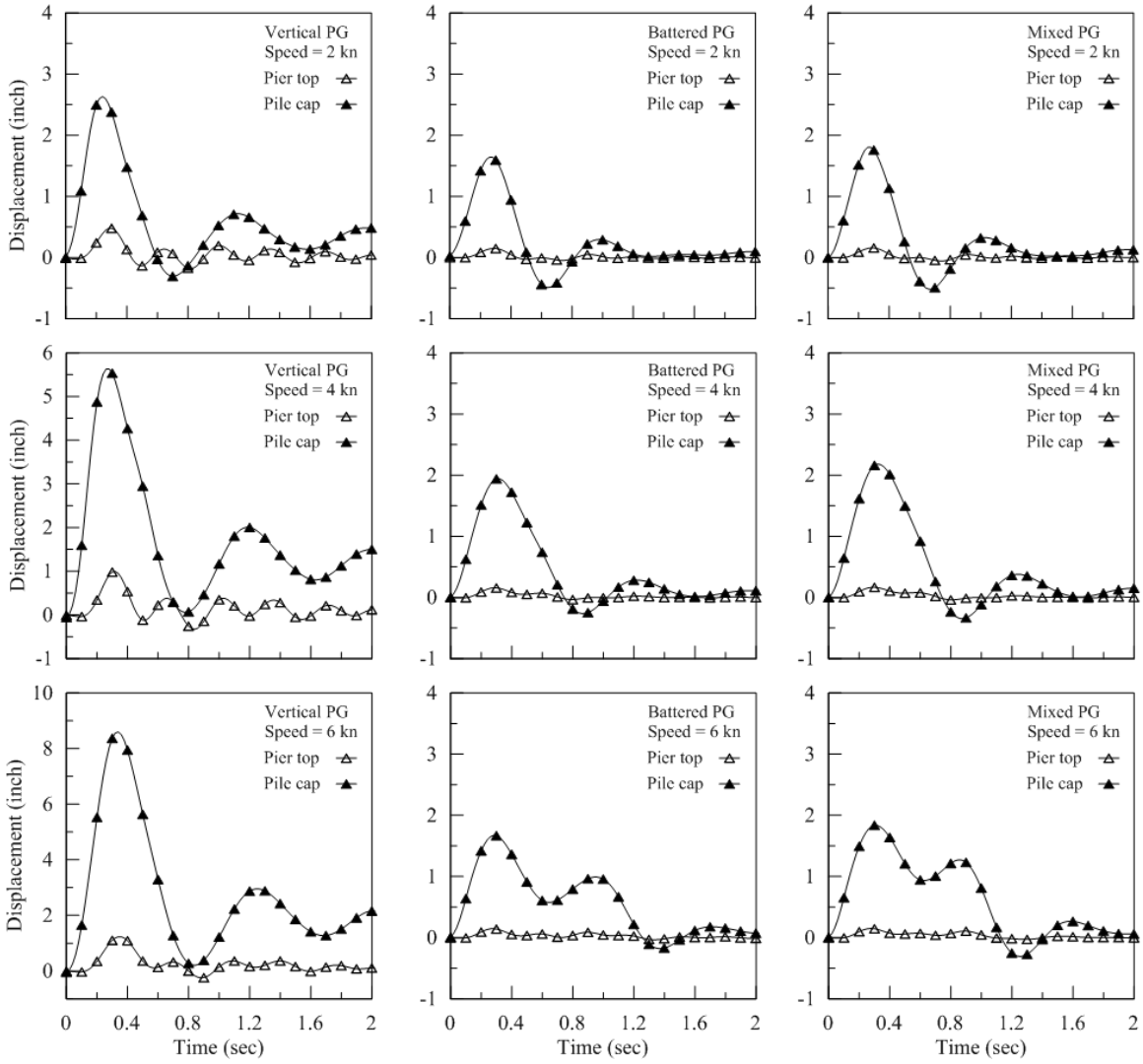

Results of Shear Force and Impact force

The definition of the shear force in the piles and pier columns is illustrated in Figure 94. The results of shear force history in all piles and pier columns is shown in Figure 95. The sum of shear force represents the total impact force. The impact force in the vertical PG case was notably higher than the battered and mixed PGs. The vertical PG behavior facilitated the generation of greater lateral force from the impact by absorbing more kinetic energy. The lower stiffness of the vertical PG allowed greater lateral displacement and greater damage levels in the piles. On the other hand, the battered and mixed PGs absorbed less kinetic energy due to the higher stiffness, which forced the barge bow to greatly deform and absorb significant amount of kinetic energy. The force history in the

vertical PG peaks at a higher rate than the other PGs. It can be noticed that the force in the piles in the vertical PG returns to a negative value at the end of the impact, which was due to the damage in the piles. The damage in the piles was located on the tension side in the piles and created a negative balance in the pile shears. The negative pile shears were countered by a net positive shear in the pier columns. In the battered and mixed PGs, the duration of the first peak was longer due to the bow deformation. At barge speed 6 knots, the force history for both PGs shows two consecutive force peaks indicating that the collision was highly inelastic.

Figure 91. Damage contours for the vertical PG after the impact

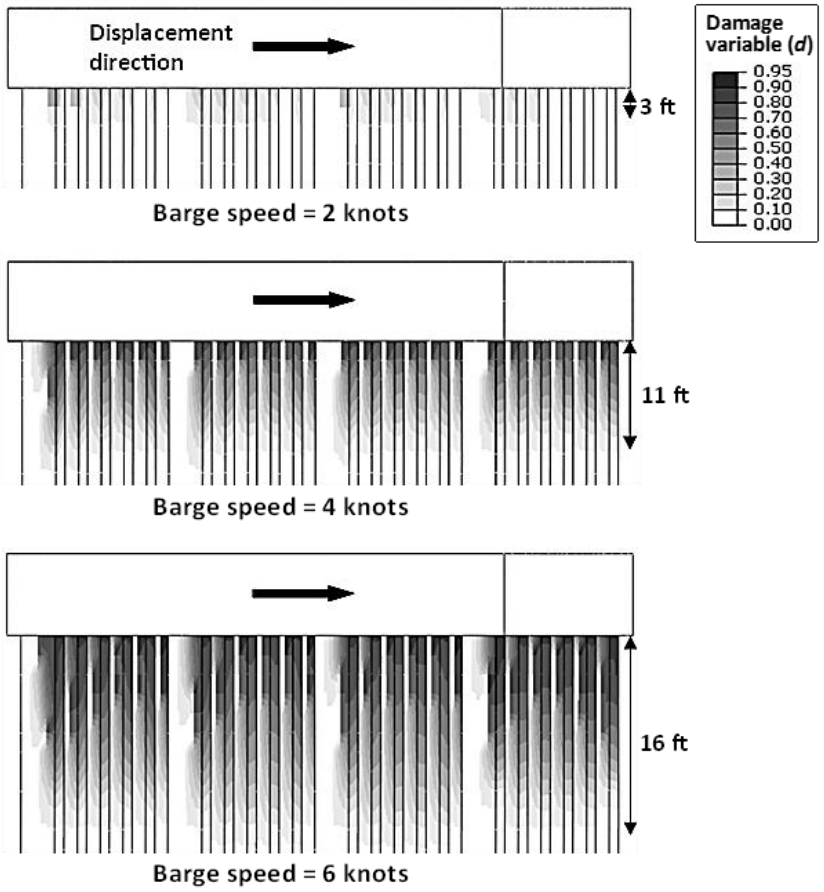

Figure 92. Peak displacement at different barge speeds

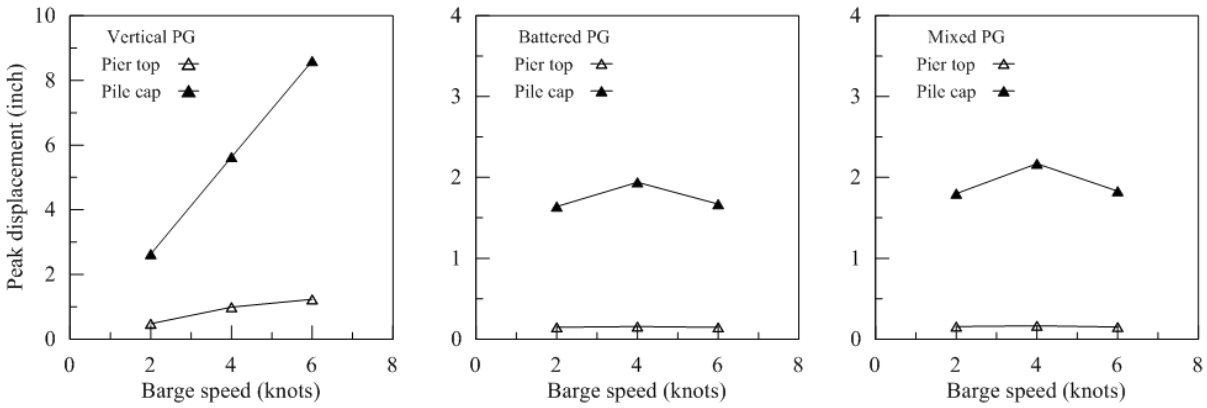

Figure 93. Barge bow deformation history results

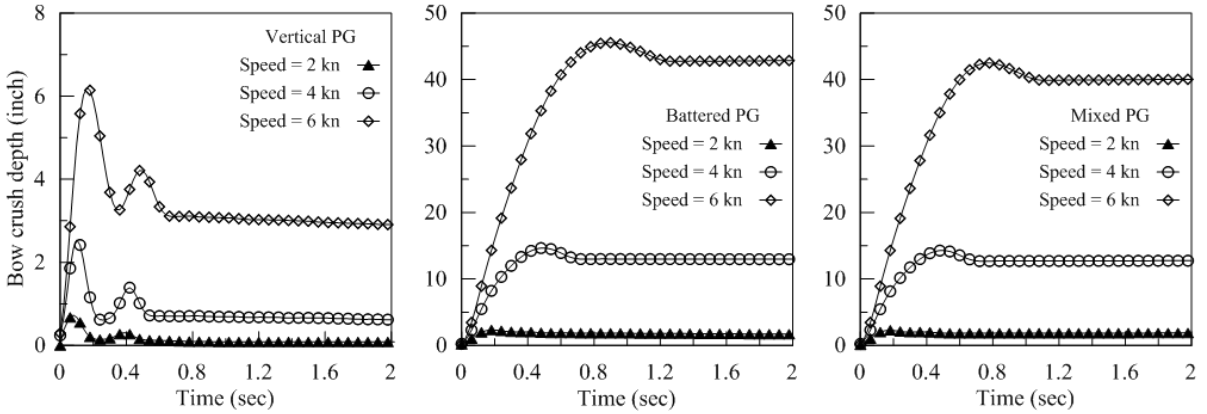

Figure 94. Free body diagram illustrating the internal shear forces in the pier

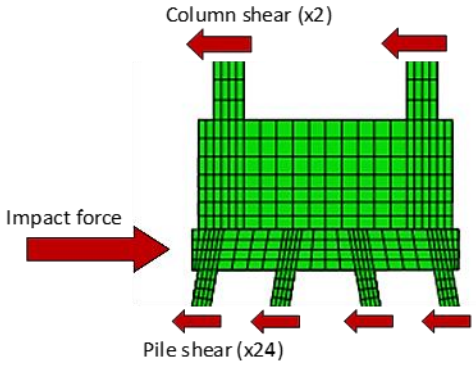

Figure 95. Results of shear force history

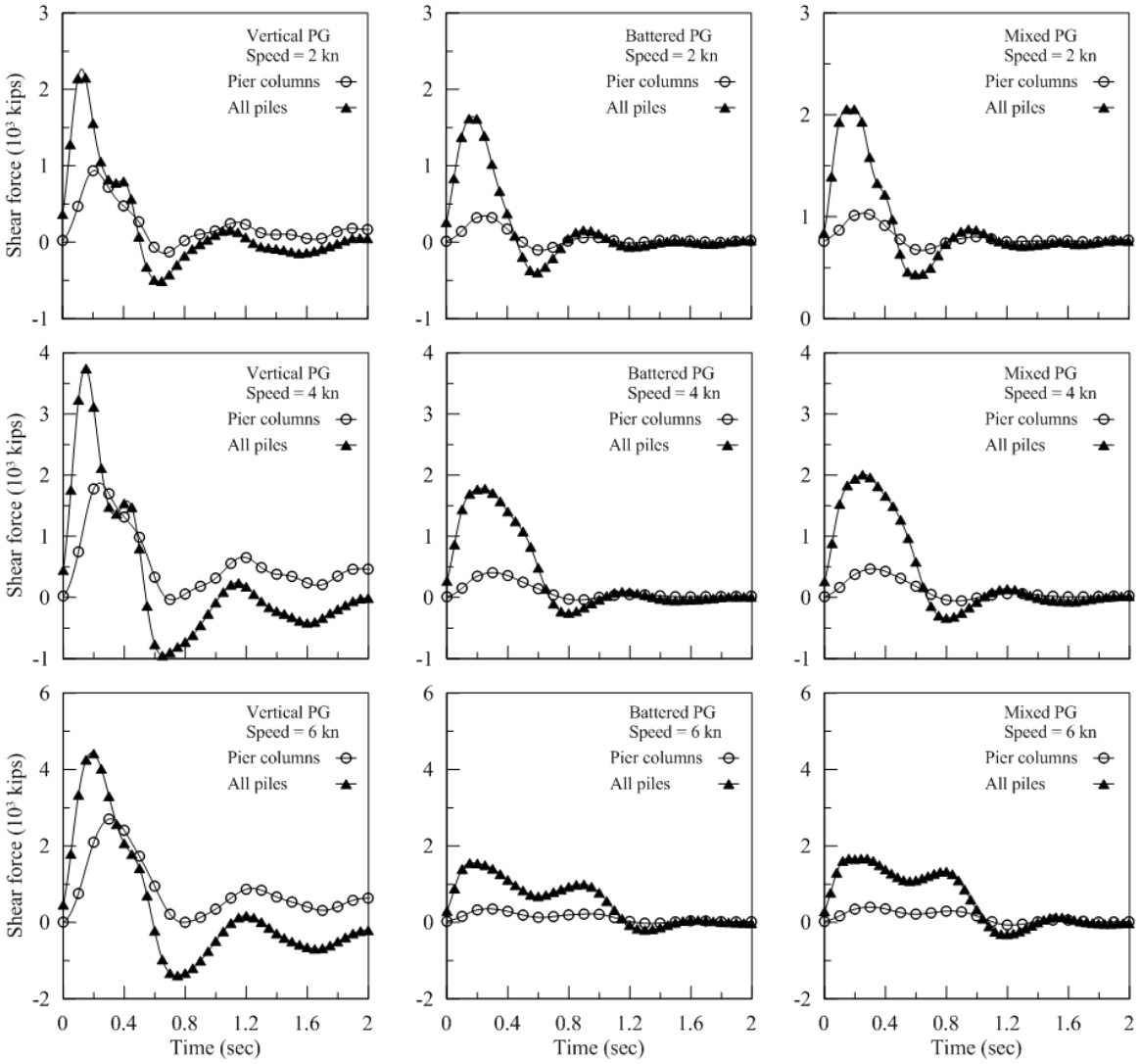

The peak shear force in the piles and pier columns versus barge speed are presented in Figure 96. The results show that the peak force increased linearly with barge speed in the vertical PG, while it remains fairly constant in the battered and mixed PGs. The contribution from the foundation and superstructure in the total resisting force is depicted in Figure 97. The results show that the force ratio carried by the piles was constant (82%) in the battered and mixed PGs; while in the vertical PG the force ratio decreased from 75% to 65% when the barge speed increased. This is mainly due to piles damage, which weakened the piles in the in the vertical PG.

A comparison between the peak impact force from the FE analysis and prediction models by AASHTO [44] and Consolazio et al. [99] is shown in Figure 98. As discussed earlier,

the AASHTO's impact force prediction model is a function of the barge's mass, speed, and bow crush depth; while Consolazio's prediction model is a function of the pier-barge contact width only. It can be seen that the Consolazio's prediction model works well for the vertical PG case but highly over-predict the impact forces for the battered and mixed PG cases. This indicates that the lateral stiffness of pile group is an influence factor that needed in the prediction models. On the other hand, the AASHTO's model under-predict the impact force in all cases, especially in the vertical PG case.

Figure 96. Results of peak shear versus barge speed

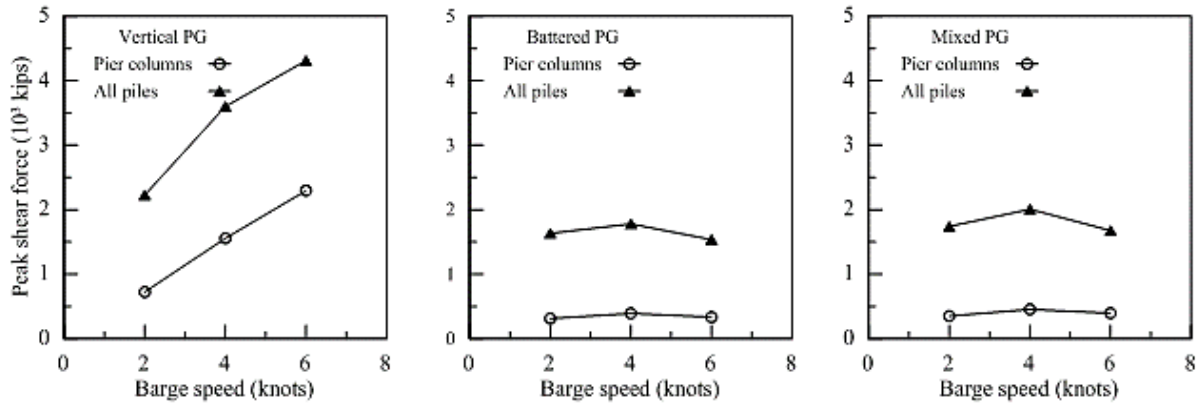

Figure 97. Contribution of piles and pier columns in the resisting force

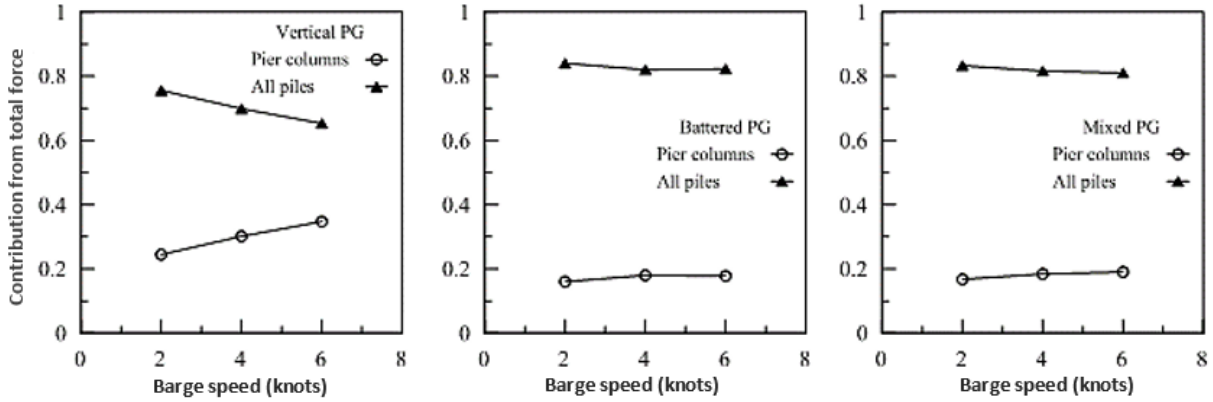

Figure 98. Peak impact force vs force prediction models

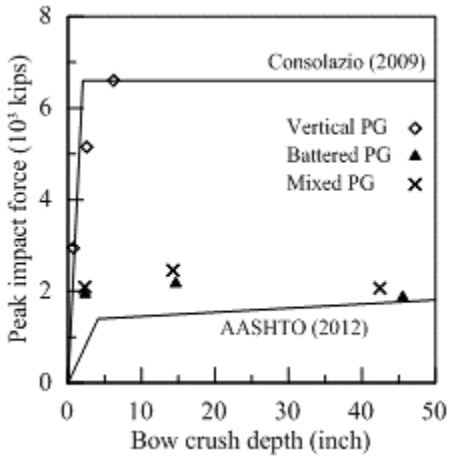

The contribution of each pile to the total shear force from the barge impact was investigated for the for the vertical, battered, and mixed PGs. Figure 99 presents the results of shear contribution history per pile at the barge speed of 4 knots, in which each subplot presents the results for piles in the same row (L, ML, MT, T). Similar results pattern were obtained for the barge speeds of 2 and 6 knots, but with different magnitudes. The figure includes the results for half of the 24-piles due to symmetry about the pile cap centerline. The figure reveals slightly higher shear force contribution of the piles in the edge column (col. 1), which was also observed in the previous results for statically loaded PGs and the reason for it was the influence of the group effect. The ratio of the peak shear force in each pile to the total shear force is presented in Figure 100. The contribution of the edge column was fairly constant for all barge speeds and notably higher in the battered and mixed PGs. On average, the percentage difference in the shear force ratio between the edge column (col. 1) and the interior columns (col. 2 and 3) was 0.6% in the vertical PG, 1.7% in the battered PG, and 1.5% in the mixed PG.

The contribution of each pile row to the total shear force is presented in Figure 101. In the vertical PG, the row L had the highest percentage (27%) followed by row T (25%), and rows ML and MT (24% each). The battered PG rows had close percentages at about 25%, which is different distribution to what we observed from the static analysis. However, the mixed PG had the largest contrast between the rows with 28% in rows L and T, and 22% in rows ML and MT.

Figure 99. Piles' shear force history results at barge speed = 4 knots

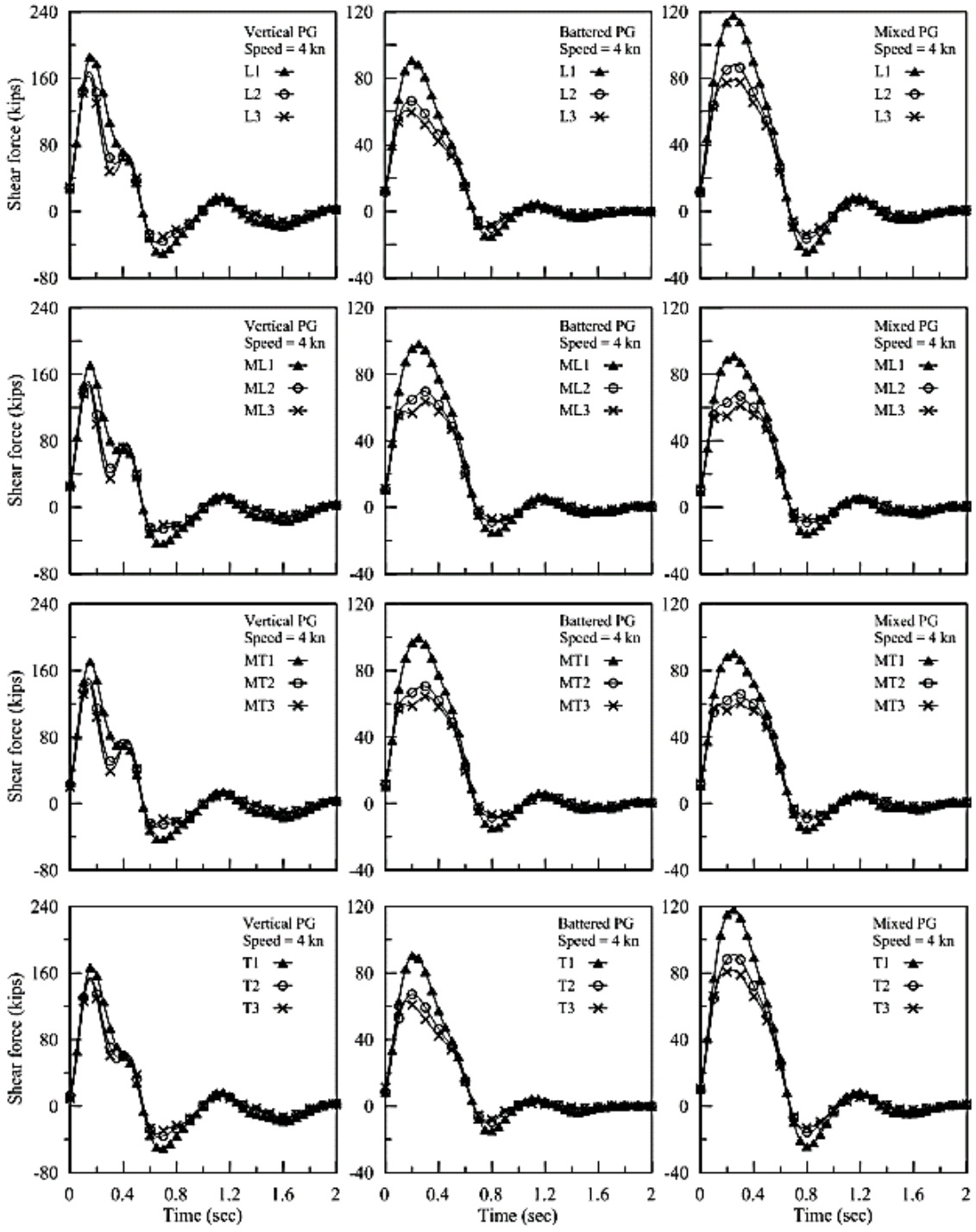

Figure 100. Summary of piles' peak shear force ratio for each pile

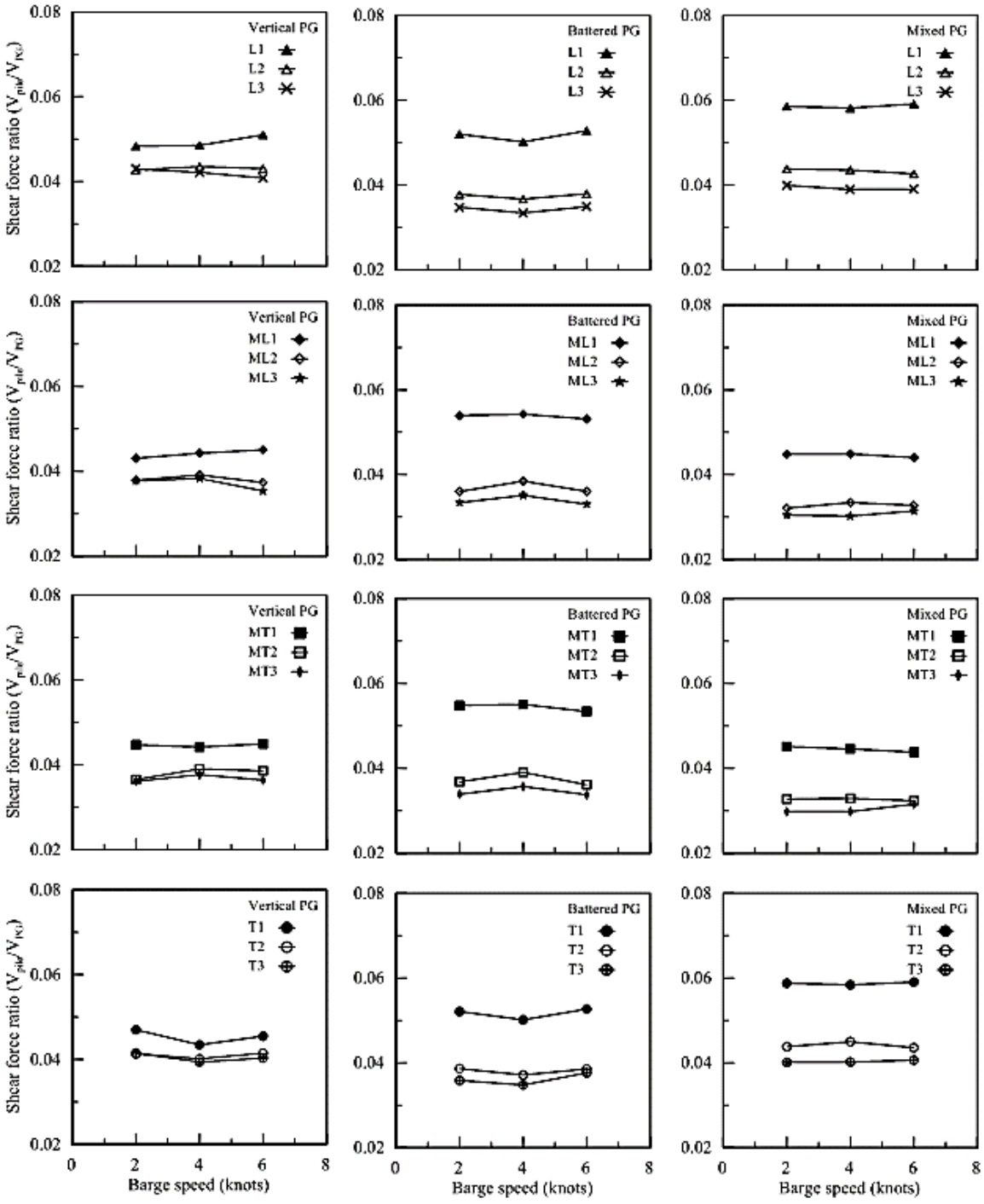

Figure 101. Distribution of shear force per row

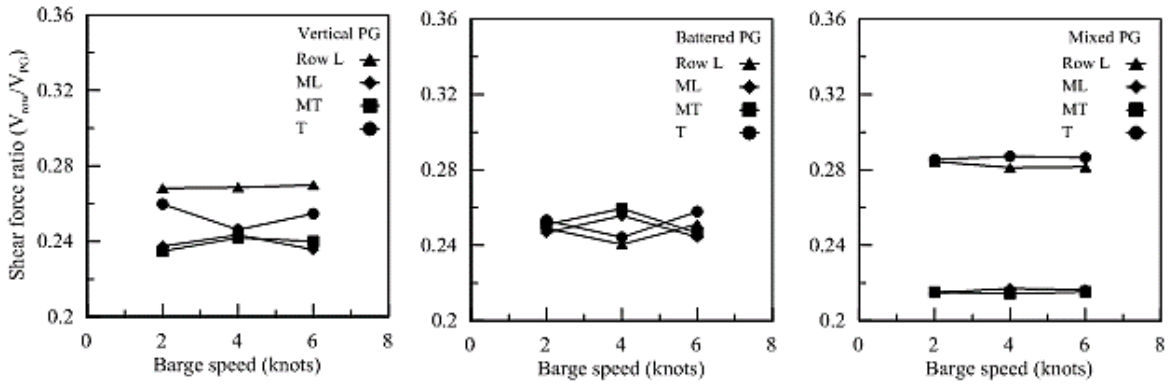

Results of Axial Reaction

The definition of the axial reaction developed in the piles is illustrated in Figure 102. The results of axial reaction history generated in each pile at a barge speed of 4 knots is shown in Figure 103. Similar results pattern were obtained for the barge speeds of 2 and 6 knots, but with different magnitudes. In the figure, positive force indicates the force action is compressive in the piles, whereas negative means the force action is tensile.

Figure 102. Free body diagram illustrating the axial reactions in the piles

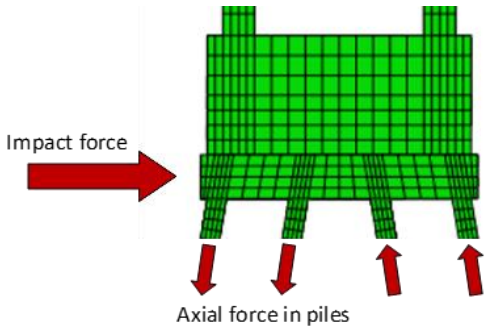

The magnitude and direction of the axial reaction is affected by the PG type and row location. In vertical PG, the axially active piles can be noticed from the difference in the force magnitude. The piles in rows L and T had a significant magnitude of axial reaction compared to rows ML and MT for the cases with barge speeds 2 and 4 knots. For the case with barge speed 6 knots, the large pile cap displacement and piles' damage influenced the PG behavior so that the piles in rows L and ML generated a greater compressive reaction. In battered PG, all of the PG rows were axially active with notably higher

contribution from the middle rows (ML and MT). In the mixed PG, all rows were axially active with closely similar contribution from all rows.

Figure 103. Results of axial force history at barge speed = 4 knots

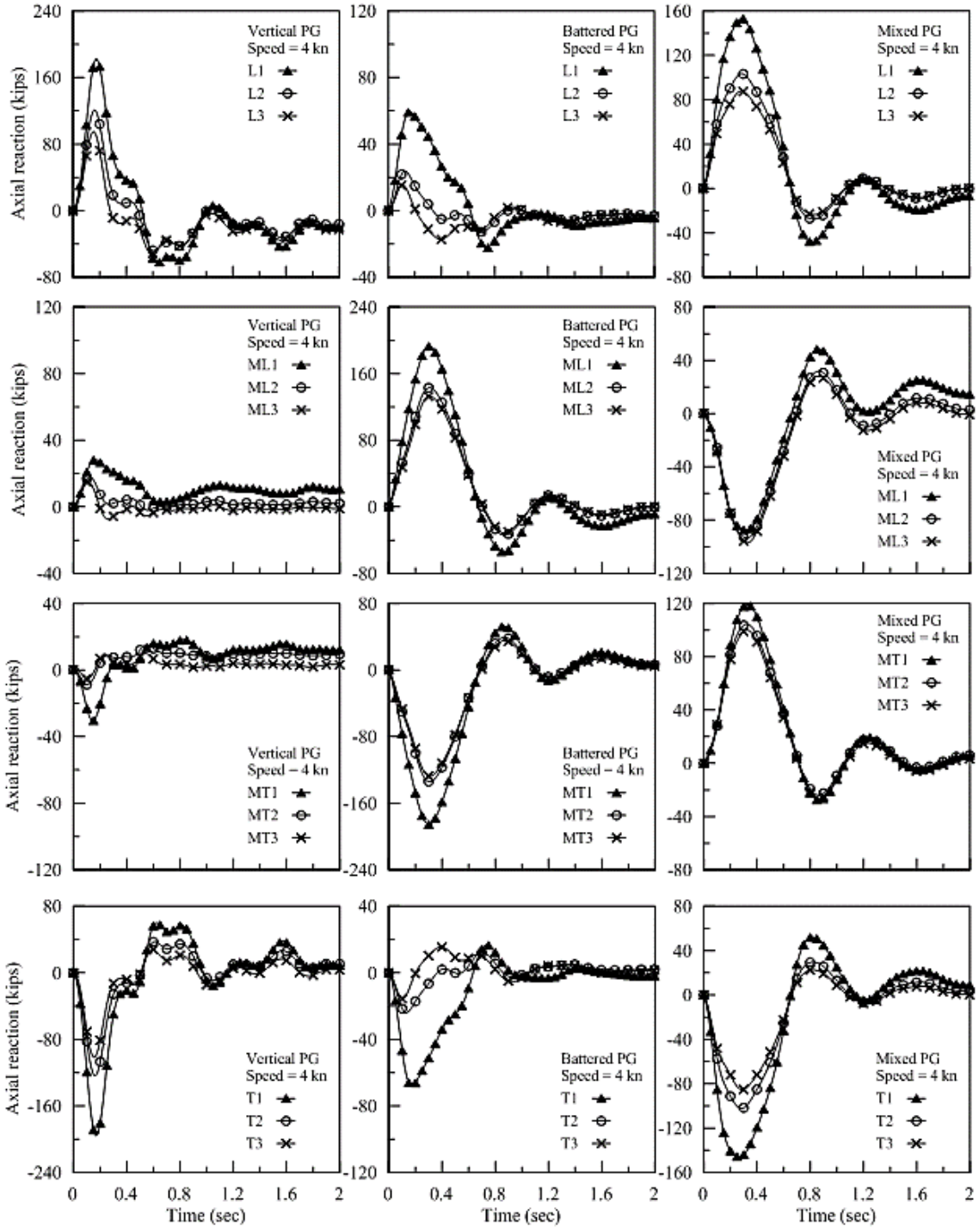

The ratio of peak axial reaction per pile to the total shear in the piles is summarized in Figure 104. This figure shows the percentage of axial reaction generated in reference to the total shear in the PG. The force ratio in the rows L and T in the vertical PG were similar (3-5%) for the cases with barge speed 2 and 4 knots; while it was relatively small (<1%) in the in the middle rows (MT, ML). The force ratio in row L and ML showed a sharp increase in the case of barge speed 6 knots, which can be referred to the large pile cap displacement (9 in.) and piles' damage. The piles in the edge column (col. 1) had a 2% higher force ratio compared to the interior columns. In battered PG, the force ratio in the middle rows (ML, MT) was 6% higher than rows L and T, and the edge column piles had 2% higher ratio than the interior columns. However, in mixed PG, the pile rows had closely similar force ratio at about 15%.

The force ratio per row is presented in Figure 105, which is estimated by the sum of force ratio of all piles within the row. The vertical PG results show that rows L and T were the axially active rows at 23%; while the contribution was limited from the middle rows (ML, MT) at 3%. In battered PG, all the rows were axially active with the middle rows (ML, MT) having the higher axial reaction at 50% compared to 12% in rows L and T. However, in mixed PG, the rows had a closely similar force ratio at 33%.

Results of Bending Moment

The direction of action illustrated in Figure 106 indicates a positive sign for the BM. The results of piles' bending moment (BM) at the pile cap elevation at a barge speed of 4 knots is shown in Figure 107. Similar results pattern were obtained for the barge speeds of 2 and 6 knots, but with different magnitudes. The results of BM history show closely similar response and contribution from all piles in the PGs. Looking at the peak BM, the piles in the vertical PG had notably higher BM than the piles in the other PGs, which was due to the large pile cap displacement. The contribution of peak BM for each pile was calculated and presented in Figure 108. The BM ratio in the figure was obtained by normalizing the peak BM for the individual pile using the PG shear (VPG), pile length (L=110 ft.), and the number of piles in the PG (n=24). The results show that the piles in the edge column (col. 1) had higher BM ratio in all PGs. The difference in BM between the edge column and the interior columns was 1.3% in the vertical PG, 2.3% in the battered PG, and 2.2% in the mixed PG.

The ratio of BM per row was also calculated and presented in Figure 109, which gives an idea about the BM distribution between the rows. The figure shows that the leading row (L) had the highest BM ratio (69-72%) in all PGs. In vertical PG, the BM ratio was

closely similar in rows ML, MT, and T (58-61%). In battered PG, the BM ratios were 71, 57, 61, and 67% in rows L, ML, MT, and T, respectively. However, in mixed PG, the BM ratios were 72, 65, 62, and 68% in rows L, ML, MT, and T, respectively.

Figure 104. Summary of piles' peak axial force ratio

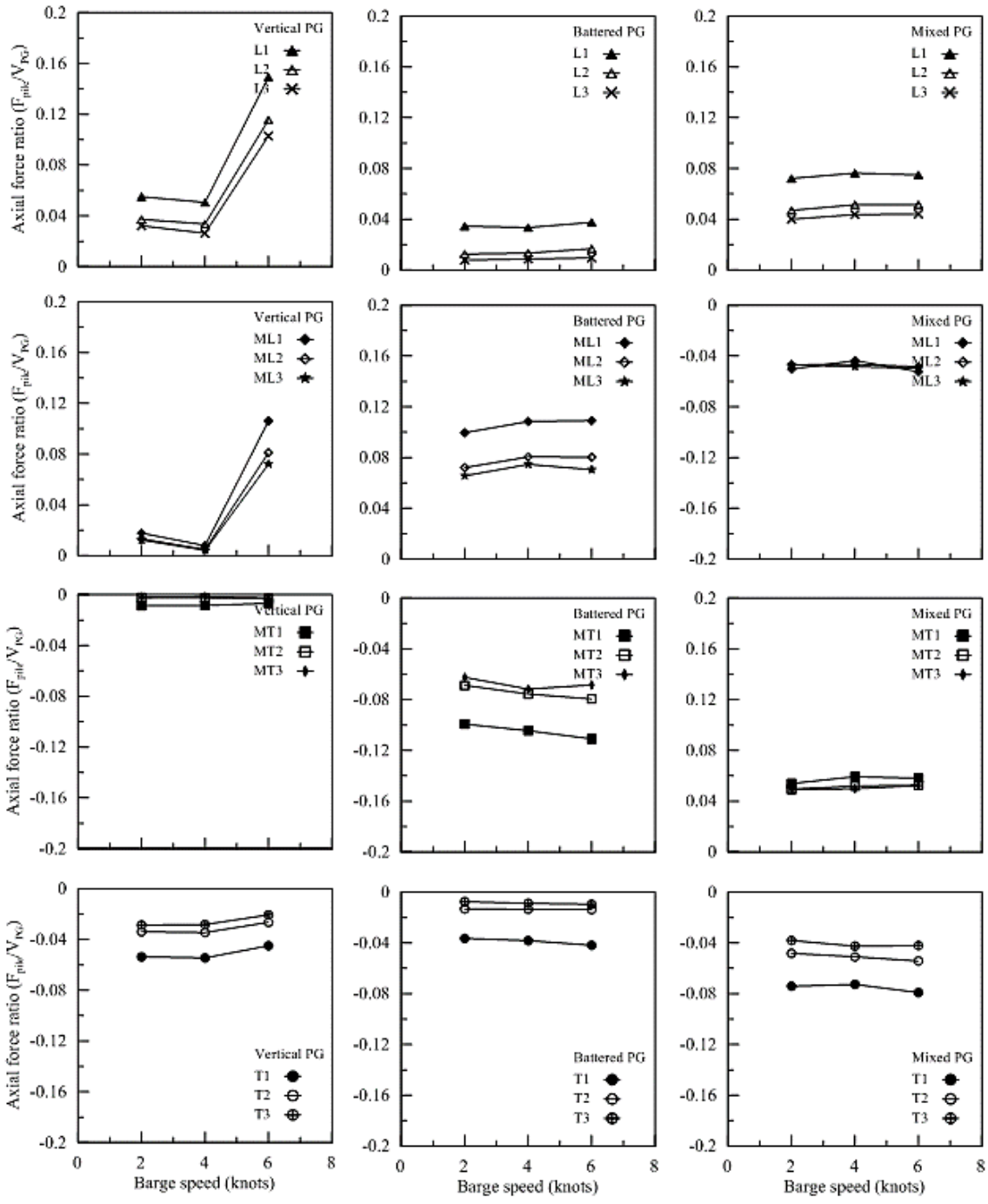

Figure 105. Summary of axial force ratio per row

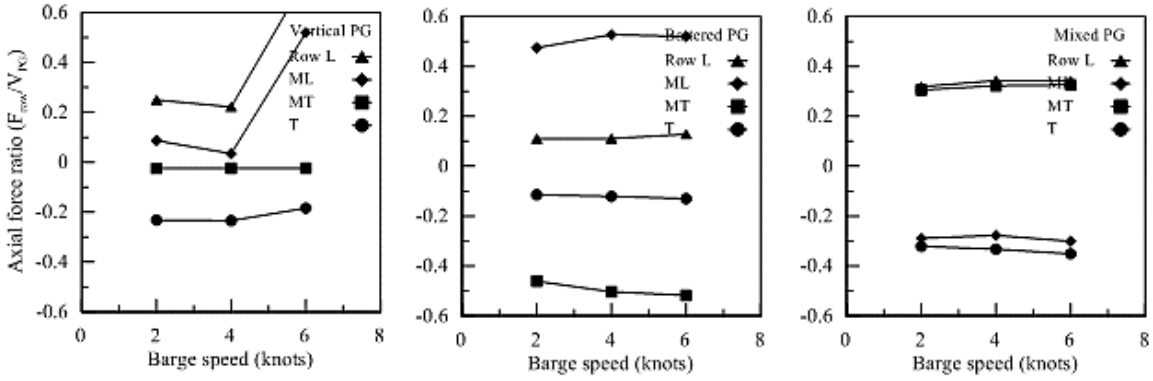

Figure 106. Free body diagram illustrating the bending moments in the piles

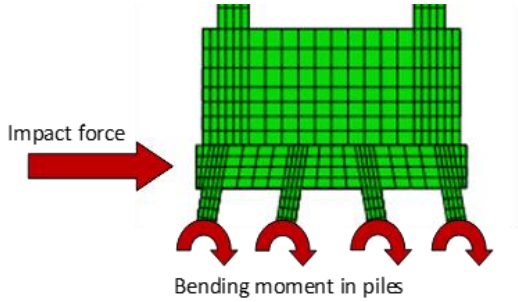

Results for Non-Centric Impact

The case of a non-centric collision with the pile cap was investigated for the three pile groups. The barge's impact location was shifted so that the side of the barge aligns with the side of the pile cap (Figure 110). The non-centric impact simulations were conducted at barge speed of 4 knots only.

The displacement results for the three pile groups are shown in Figure 111. The figure includes the cap displacement at the left (L) and right (R) corners, which shows a slightly higher displacement magnitude (0.2 in.) at the left corner. This small difference indicates that the cap rotation from the impact was minimal. The results of peak displacement from the non-centric impact were closely similar to the centric impacts results, as shown in Figure 112.

Figure 107. Bending moment history results at barge speed = 4 knots

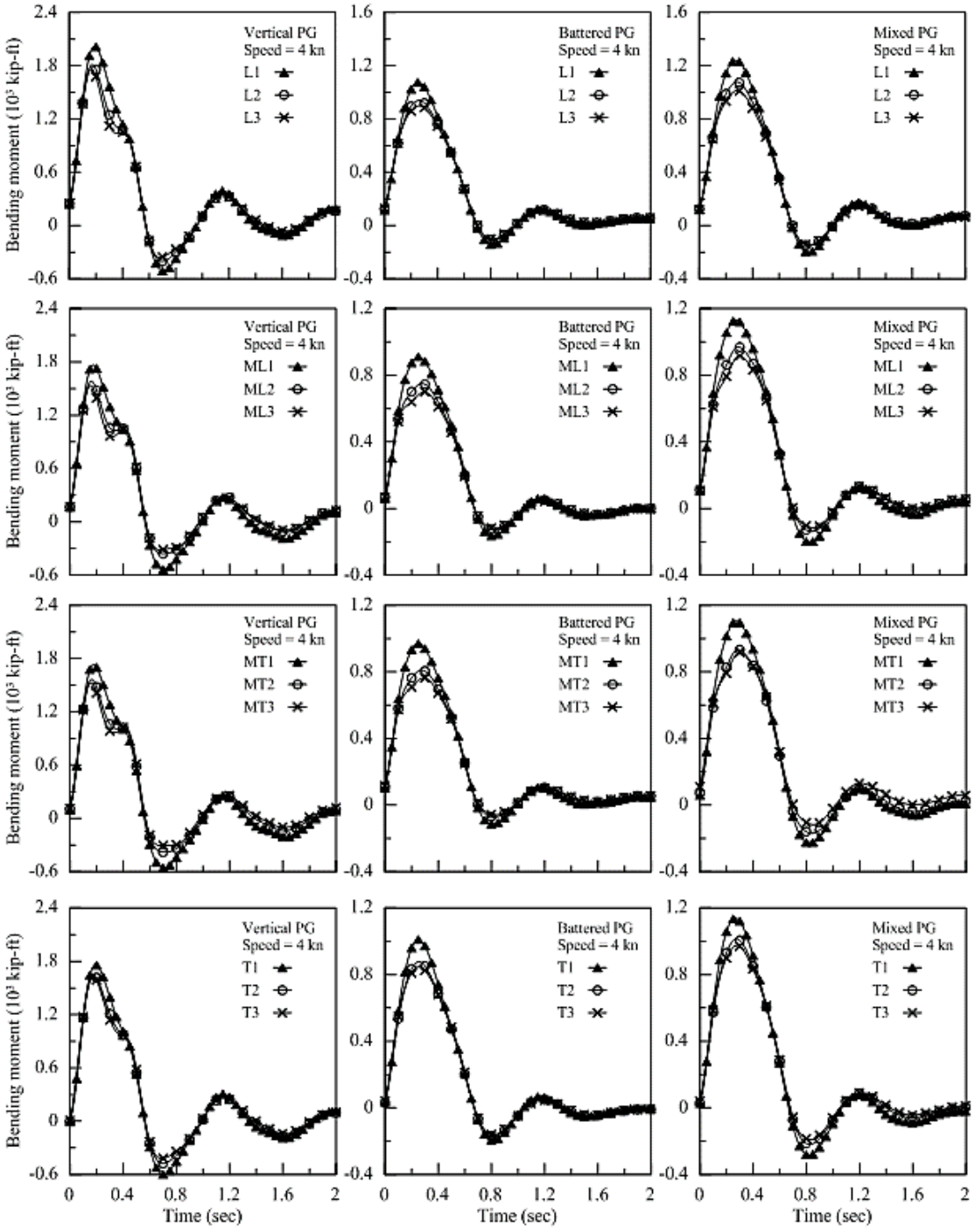

Figure 108. Summary of piles' peak bending moment ratio

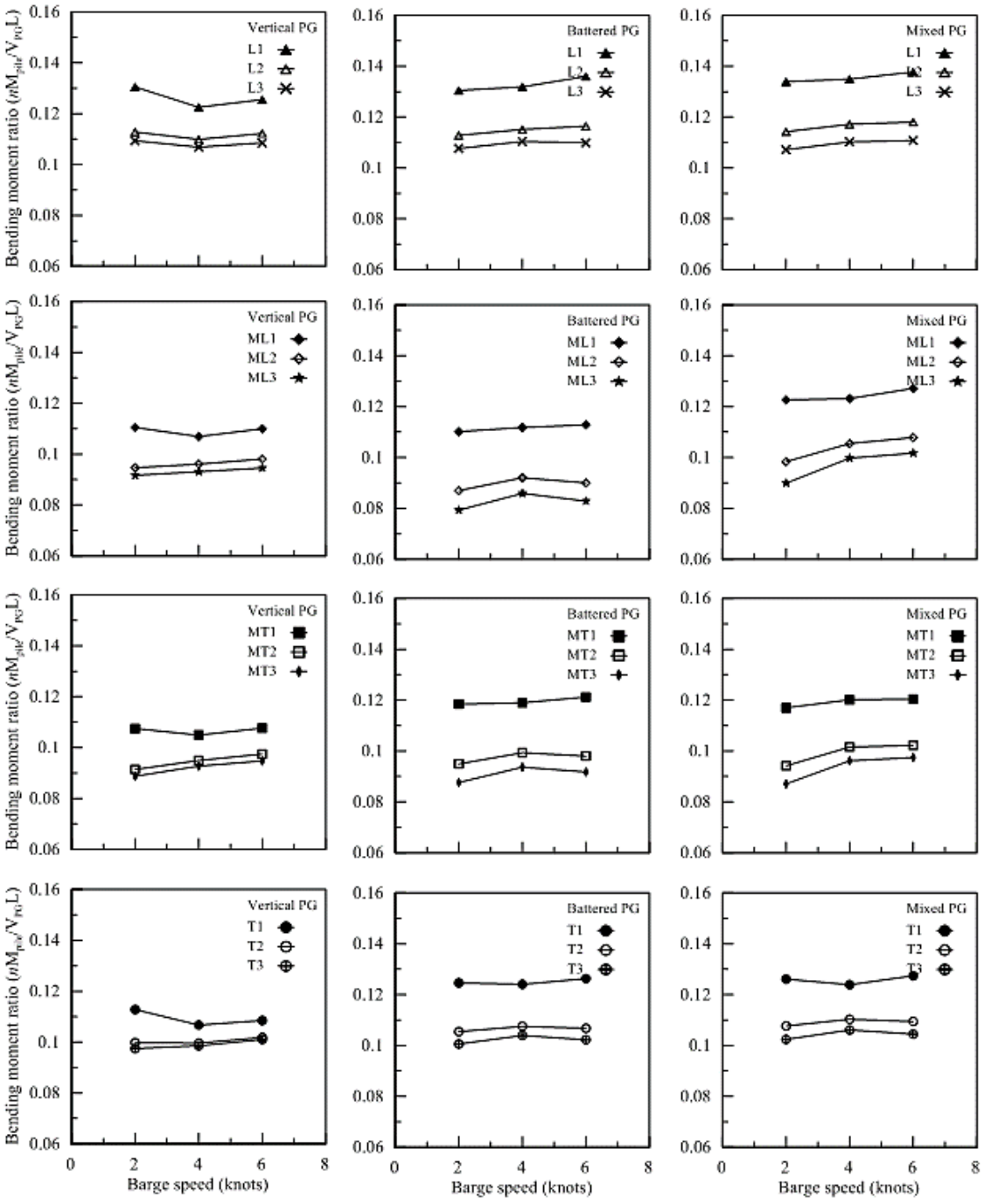

Figure 109. Summary of bending moment ratio per row

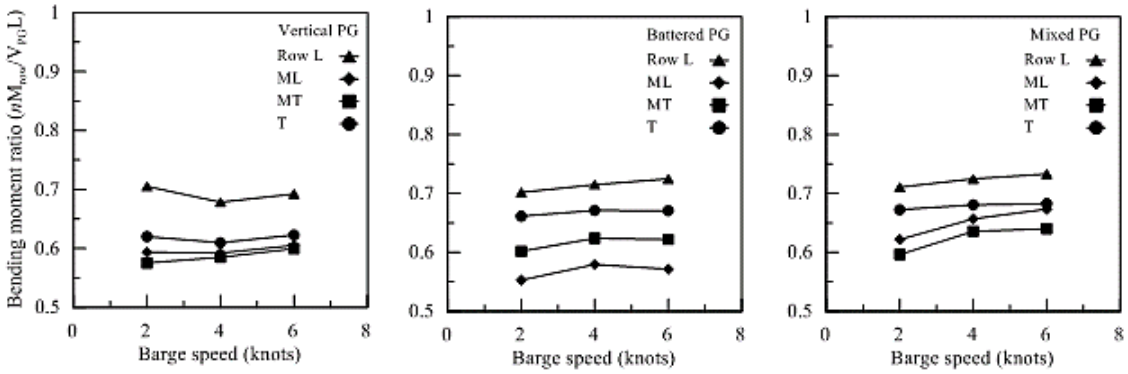

Figure 110. Barge alignment for non-centric impact

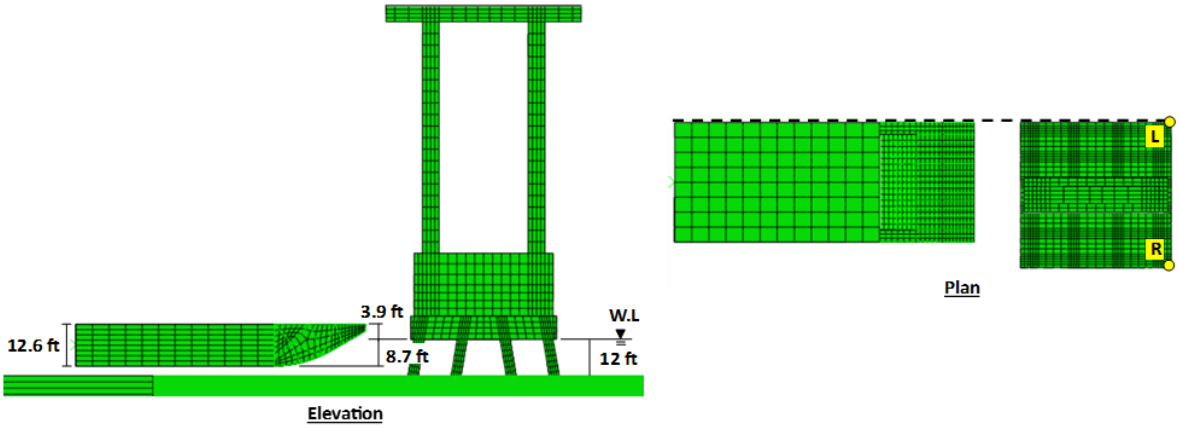

Figure 111. Displacement history for non-centric impact

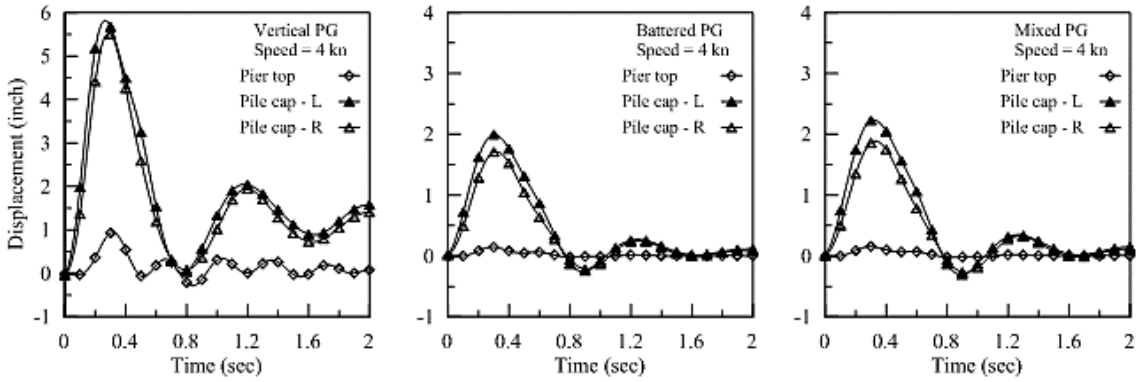

Figure 112. Comparison of peak displacement results for centric and non-centric impacts

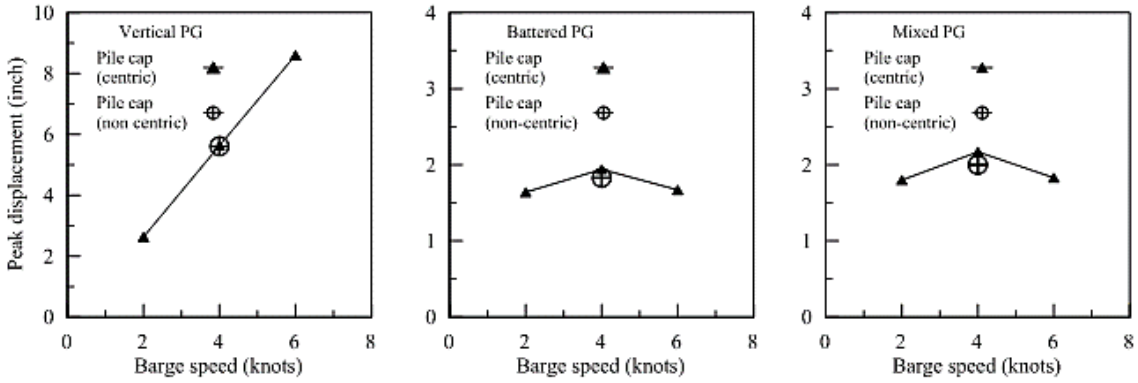

The results of impact force and force distribution in the piles and columns are presented in Figure 113 and Figure 114. The figures show similarity in the impact force results between the centric and non-centric impact cases.

The summary of contribution of each pile in the total shear force is presented in Figure 115, Figure 116, and Figure 117 for the vertical, battered, and mixed PGs, respectively. The figures show that the shear force was unevenly distributed in the piles, as expected, which is noticed in the slightly higher percentages in column 1 piles. However, the deviation in the force distribution was notably higher in the battered and mixed PGs as compared to vertical PG. The percentage difference between column 1 and column 6 piles was 0.2-0.3% in the vertical PG; while it was 1-1.2% in the battered and mixed PGs.

In summary, the influence of barge impact location (with fixed pier contact width) is considered minimal on the displacement response. The similarity in the force results for centric and non-centric impacts indicates that the impact location is not a significant factor on the magnitude of impact force.

Figure 113. Comparison of peak shear force for centric and non-centric impacts

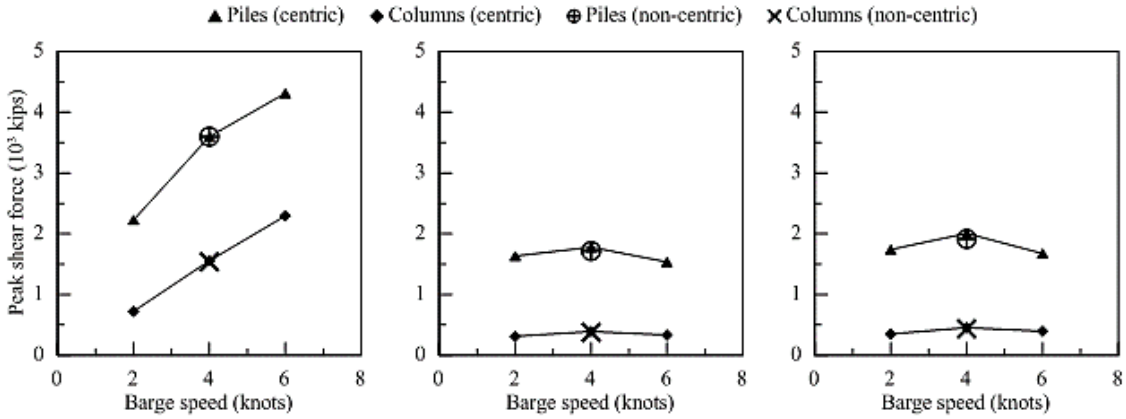

Figure 114. Contribution of piles and pier columns to the resisting force in centric and non-centric impacts

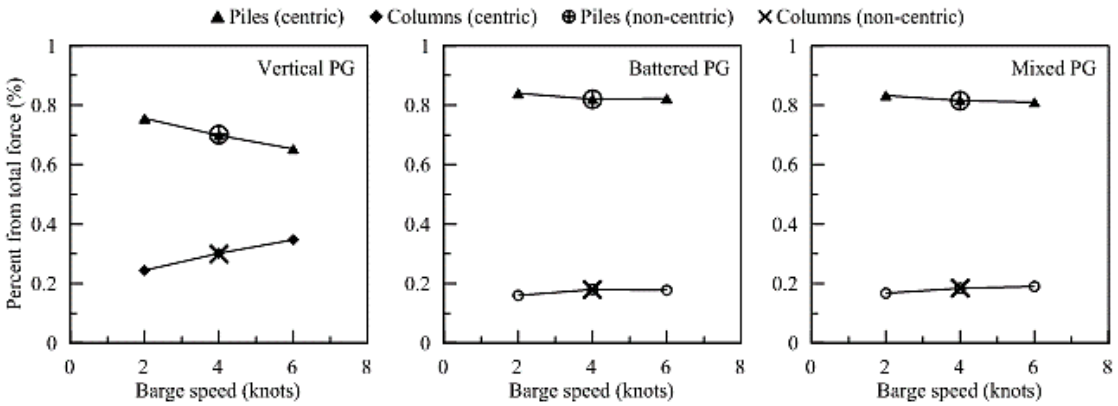

Figure 115. Summary of shear force ratio per pile for non-centric impact in vertical PG

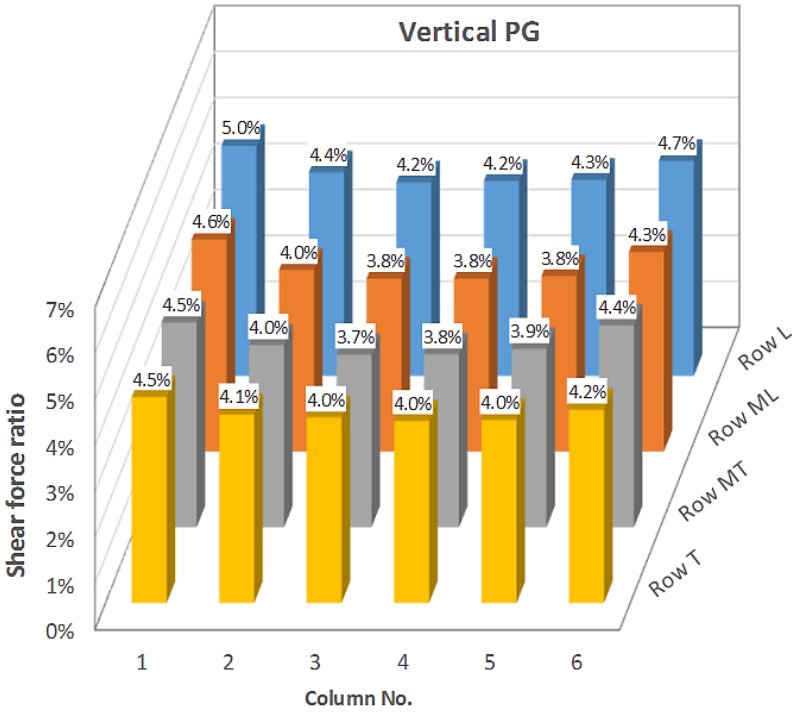

Figure 116. Summary of shear force ratio per pile for non-centric impact in battered PG

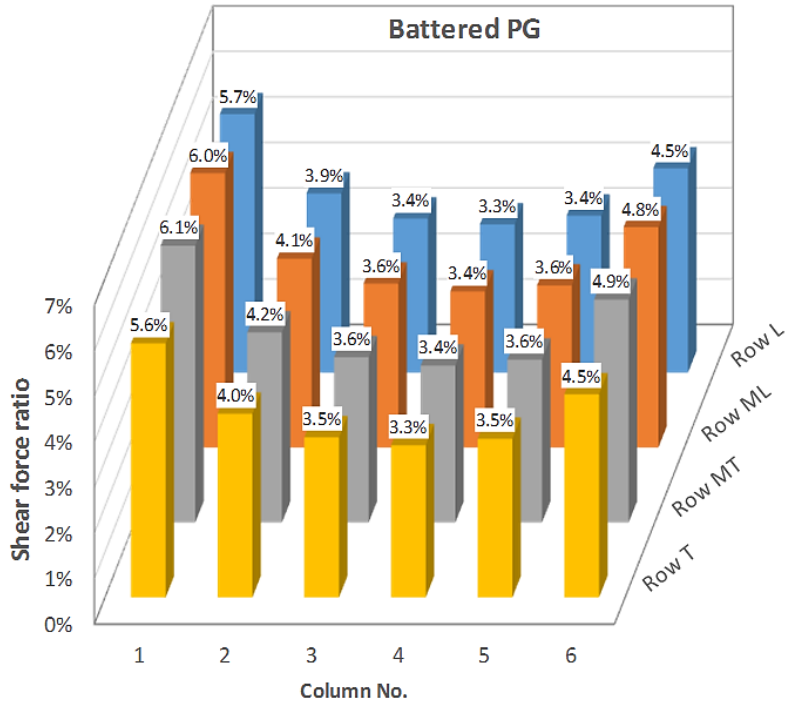

Figure 117. Summary of shear force ratio per pile for non-centric impact in mixed PG

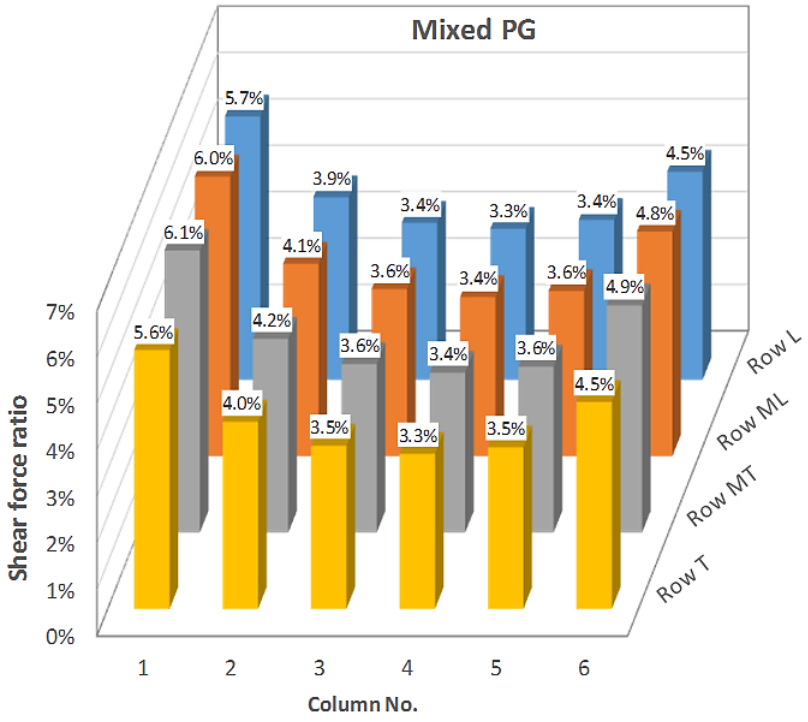

P-y Curve Model in Clays

A p-y curve model for laterally loaded piles in clays under undrained conditions has developed using the results of finite element analysis. Each element of the p-y curve (ultimate lateral soil resistance, initial slope, characteristic shape function) is studied through parametric investigations in which the effect of pile and soil parameters are evaluated. Using the results from the FE parametric study, numerical models for the ultimate resistance, initial slope, and characteristic shape function are verified and compared to existing models.

In clays, the ultimate lateral soil resistance is a function of the undrained shear strength (S_u), pile width (D), and the lateral bearing capacity factor (N_p). The initial slope in the p-y curve is controlled by the parameter y_{50}, which is a function of the soil strain level at $0.5S_u$ in the triaxial test (ε_{50}), pile width (D), and N_p. A hyperbolic function is used to describe the characteristic shape of p-y curve following the existing models in the literature.

Ultimate Soil Resistance p_u

The ultimate lateral soil resistance (p_u) is related to the soil strength and pile width as:

$$p_u = N_p S_u D \quad [67]$$

The bearing capacity factor, N_p, varies with depth due to the two failure mechanisms in the soil (wedge failure and flow around failure), as discussed earlier. The upper-bound values of N_p (or N_{pu}) for the flow around failure mechanism was estimated in the analytical solution by Randolph and Houlsby [114], and later revised by Martin and Randolph [115]. N_{pu} values range from 9.2 to 11.94, and are dependent on the pile adhesion factor (μ), which ranges between 0 and 1.0. The N_p varies with depth such that it increases from the ground surface to the critical depth, after which it reaches the upper bound limit N_{pu}. The actual variation of N_p is debatable as different models in the literature exist for clays (soft or stiff) and above or below water. In the study, the FE modeling was used to study the factors affecting N_p, and to develop a generalized model for N_p in clays in undrained condition.

To estimate N_p, we need to evaluate the ultimate soil resistance (p_u) first, which is then normalized to obtain N_p using S_u and D. The FE model used to study N_p is presented in Figure 118. The 3-D FE model comprised of the pile surrounded by semi-infinite soil domain. Only half of the pile and soil was modeled due to symmetry. The pile and the soil were modeled using solid continuum elements (C3D8R) and the FE mesh density was varied so that it is denser near the pile. The undrained clay constitutive behavior was modeled as linear elastoplastic material with Mohr-Coulomb yield criteria ($c=S_u$, $\phi=0$). The total depth of the soil domain was taken as 15 times the pile width (D), which was sufficient to study the N_p variation. The soil side boundary was placed far from the pile (at 40D) to eliminate the effect of boundary conditions. The soil's side boundary was constrained in the x and y directions; while the bottom boundary was constrained in the z direction. For the symmetry plane, only the y direction was constrained.

The pile width (D) was varied in the study and its length was extended above and below the soil boundaries (Figure 118). The pile was pushed laterally so that the ultimate soil resistance is mobilized over the entire depth. This approach is more efficient than loading the pile at the top, which allows to estimate the ultimate soil resistance along the entire depth in a single run. The pile constitutive behavior was modeled as linear elastic with properties of concrete as: f_c' = 5500 psi, Young's modulus, $E_p = 57000\sqrt{f_c'}$, and ν = 0.2.

The pile-soil interaction was modeled using the interface model available in ABAQUS. The FE simulation was performed in two steps. In the first step, the geostatic stress in the soil was established by applying gravity load (g = 32.2 ft/s2) in the global z-direction until the global stress equilibrium is achieved. In the second step, the pile was pushed laterally a distance of 0.15D, which was found to be sufficient to mobilize the ultimate soil resistance.

Figure 118. Geometry and mesh of the FE model used to study the bearing capacity factor (N_p)

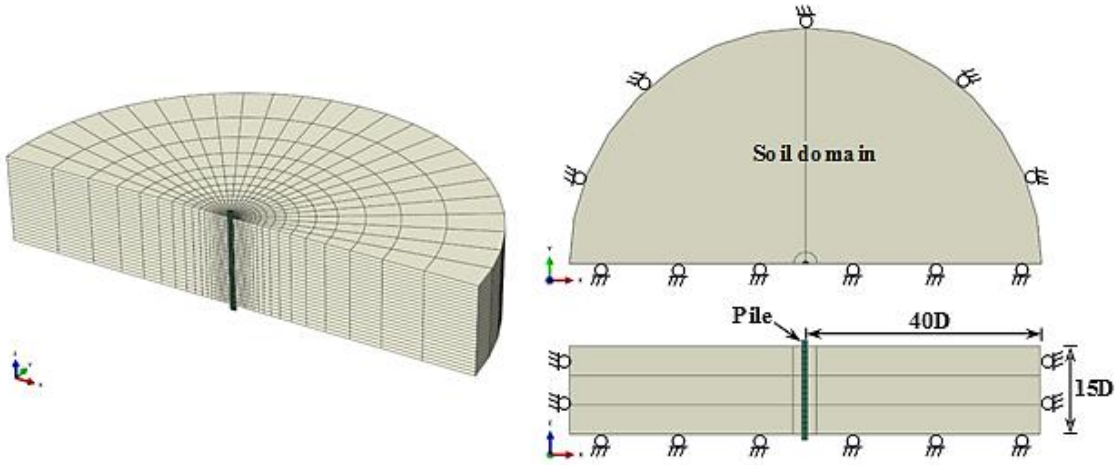

To estimate the variation of N_p with depth, the soil resistance (p) profile is needed. The p represents the net soil resistance (i.e. the net normal stress and pile surface friction) acting against the lateral pile movement at certain depth. The common approach to obtain the soil resistance profile is by differentiation of the bending moment or shear force functions. The soil resistance (p) is related to bending moment and shear force as:

$$-p(z) = \frac{d^2M(z)}{dz^2} = \frac{dV(z)}{dz} \quad [68]$$

where $M(z)$ is the bending moment function, $V(z)$ is the shear force function, and z is the depth. The bending moment or shear force measurements are obtained at several points over the pile length, and then a high order polynomial or cubic spline fit is used to obtain a differentiable function (e.g., [108], [68], [116]). Georgiadis & Georgiadis [68] obtained the soil resistance profile by differentiation of the shear force profile; while Np & Ng [108] obtained the soil resistance by double differentiation of bending moment profile. Haiderali & Madabhushi [116] studied and compared the accuracy of high order polynomials and cubic splines for constructing the bending moment profile from

instrumented piles and then obtaining the soil resistance profiles by differentiation. They concluded that cubic splines are generally more accurate than polynomial fits. Therefore, in this study cubic spline fits were used to create the shear force profile and then perform differentiation to obtain the soil resistance profile.

In the FE model, the shear force was obtained at equidistant points (1D spacing) for a total of 15 points starting from the ground surface. Then the shear force profile was obtained using a cubic spline fit, as shown in the example in Figure 119.

Figure 119. Example for FE results for pile shear and the profile using cubic spline fit

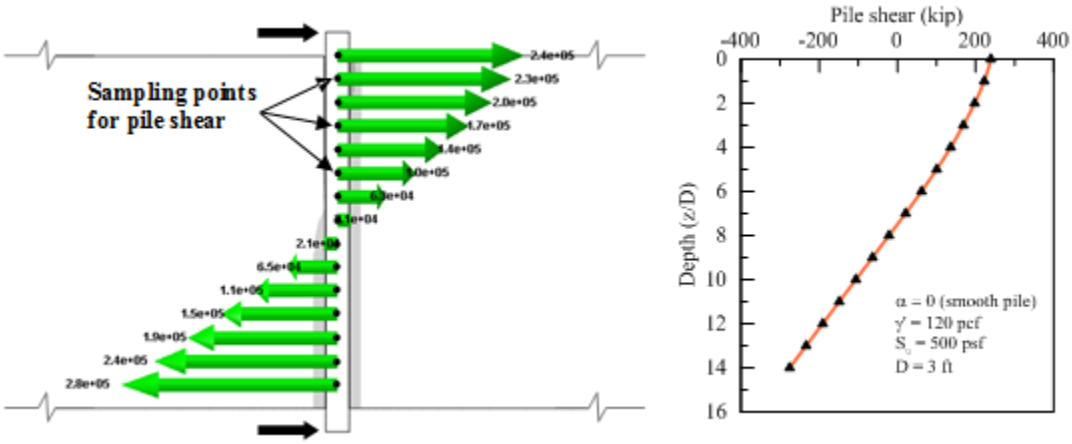

The soil resistance profile (p) was obtained from the slope (first derivative) of the cubic spline function. Finally, the bearing capacity factor (N_p) was estimated by normalizing the soil resistance using the S_u and D [N_p=p/(S_u D)], as shown in Figure 120. The soil resistance profile in the figure shows that N_p is nonlinearly increasing till the depth at which the flow around failure mechanism limits the value of N_p.

Figure 120. Example showing the steps to obtain the soil resistance profile and bearing capacity factor N_p

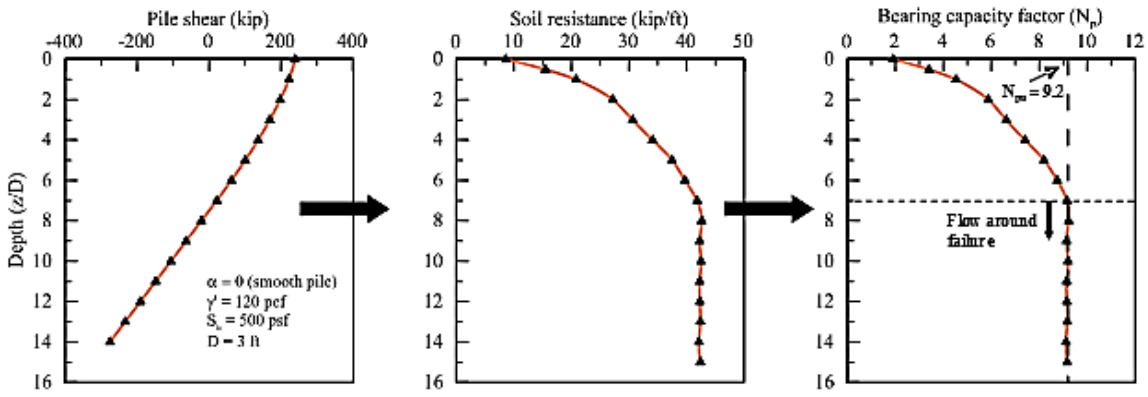

FE parametric study was conducted to evaluate the effect of several parameters on the variation of N_p with depth. For undrained clay conditions, the parameters include the effects of undrained shear strength (S_u), effective unit weight of soil (γ'), pile width (D), and pile adhesion (μ) ([3], [22], [117]).

Effect of Undrained Shear Strength (S_u). The variation of N_p at different S_u (ranging from 170 to 2000 psf) are shown in Figure 121. The selected values for S_u cover the range from soft (< 250 psf) to very stiff (> 2000 psf) clays. It can be seen that S_u has a strong influence on N_p. The results show that the rate of N_p increase with depth decreases as the value of S_u increases, and consequently the depth at which the upper-bound limit for N_p (N_{pu}) is reached became deeper. This indicates that the conditions for flow around failure requires greater confinement (or overburden stress) in stiffer clays. The observation is also in agreement with prediction models for N_p by Matlock [22], Reese et al. [3], and Sullivan et al. [117]. The results near the ground surface show that N_p values were approximately equal to 2.0 (1.8 – 2.2), which is similar to Reese et al. [3] proposed but lower than Matlcok's [22] value of 3.0.

Effect of Soil Effective Unit Weight (γ'). The effect of soil effective unit weight γ' on the variation of N_p is shown in Figure 122. The results show that the rate of N_p increase with depth decreases as γ' decreases. This is because γ' directly affects the rate of increase in overburden stress. In addition, the depth at which the upper-bound value for N_p is reached becomes deeper with the decrease of γ'. The effect of γ' is milder than S_u, which is due to the fact that γ' values are bounded in nature (70-130 pcf) and it is linearly related to N_p as will be discussed later.

Figure 121. Effect of undrained shear strength on N_p variation

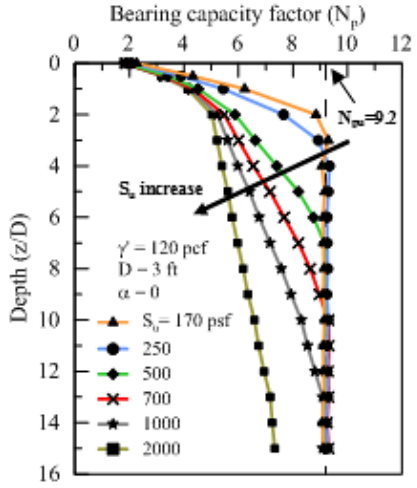

Figure 122. Effect of soil effective unit weight on N_p variation

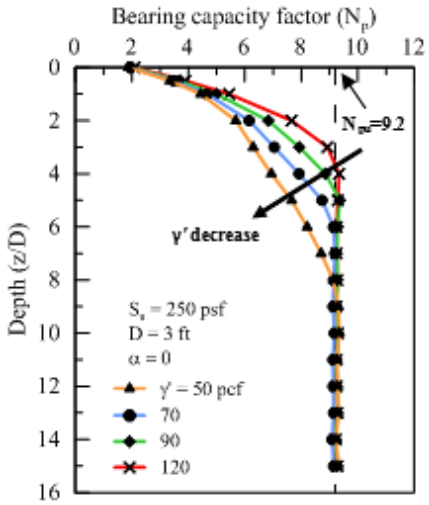

Effect of Pile Adhesion (μ). The effect of μ on N_p variation for three pile cases (μ = 0.0 (smooth), 0.5 (intermediate), 1.0 (rough)) and for different γ' (120, 90, 50 pcf) is depicted in Figure 123. An increase of μ is expected to increase N_p due to additional resistance from surface friction. Following the analytical solution by Randolph & Houlsby [114] and Martin & Randolph [115], the upper-bound limits N_{pu} at μ = 0.0, 0.5, 1.0 are 9.2, 10.8, 11.94, respectively, as indicated by the dashed lines in Figure 123. The N_p increases at slightly higher rate initially (up to z/D=2) as μ is increases, and then it reaches a constant value at the depth when N_{pu} is reached. Moreover, the N_p value at the ground

surface increased slightly when μ increases (on average, +0.3 at μ = 0.5, +0.55 at μ = 1.0 relative to μ = 0.0).

Figure 123. Effect of pile adhesion (μ) on N_p variation

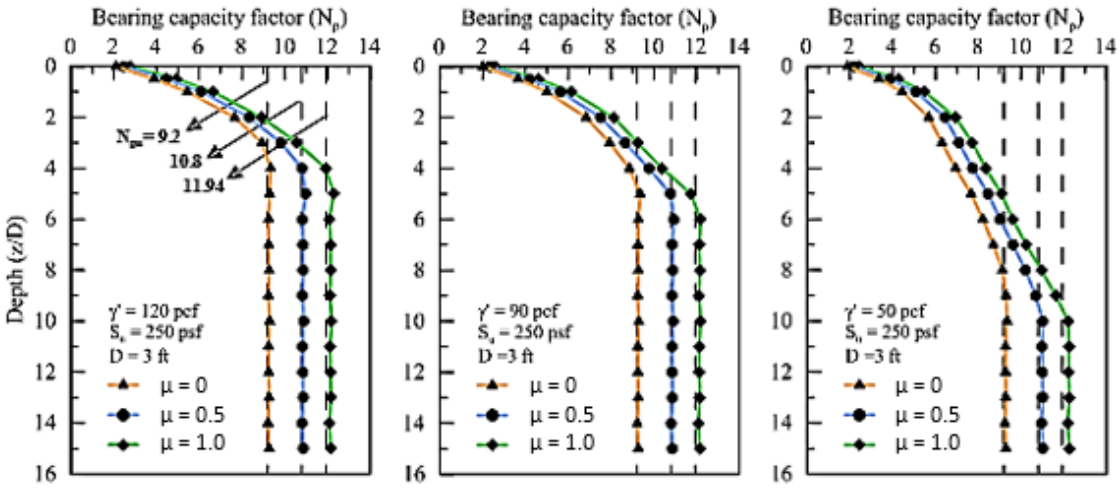

Effect of Pile Width (D). The effect of pile width (D) on N_p variation were studied for three pile widths (2, 3, and 4 ft.) as shown in Figure 124. The results show that the rate of N_p increase with depth increases as the pile width increases, which is due to the fact that larger pile width mobilizes greater soil resistance at the same relative depth (z/D). The N_p value at the ground surface was not affected by the increase in pile width.

Figure 124. Effect of pile width (D) on N_p variation

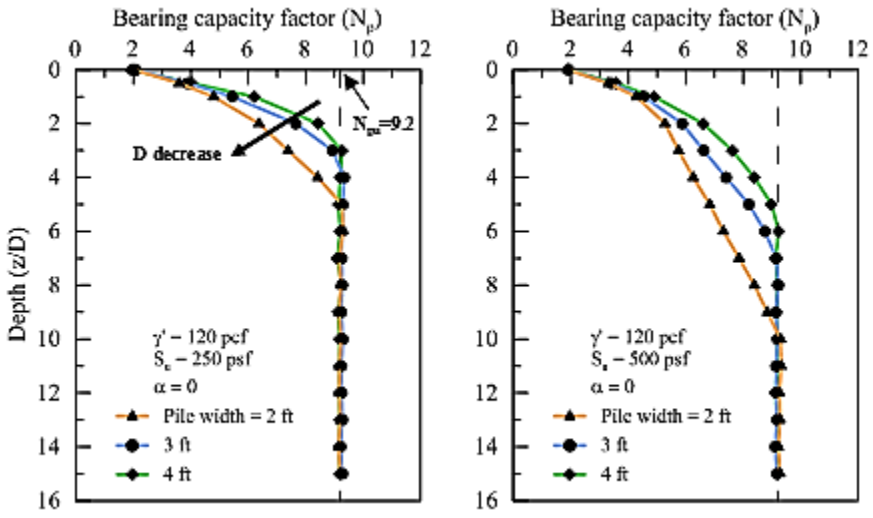

Development of N_p Model with Depth

Using the results of FE parametric study, a unified model for N_p variation with depth is developed. Several models are available in the literature to estimate N_p. However, some of these models were given for a specific clay type (soft or stiff clay), and others were given for cases with soil above water table or below water table (e.g., [3], [22], [117]). Other developed N_p models for Np in clays that don't incorporate the effects of undrained shear strength, effective unit weight, and pile width, which are considered inadequate (e.g., [68], [118], [119]). The developed N_p model in this study is applicable for all clay types (soft or stiff), soil conditions (above or below water), and pile sizes.

The characteristics of N_p model was selected following the observations from the FE parametric study, which can be summarized as follows:

1. Within the depth range ($0 < z < 2D$), N_p increases nonlinearly with depth starting at a value of about 2.0 for smooth piles ($\mu = 0.0$). The rate of increase is a function of S_u, γ', and D.
2. Within the depth range ($2D < z < Z_c$), N_p increases linearly with depth until it reaches the upper-bound limit, N_{pu}. The rate of increase is a function of S_u, γ', and D.
3. For non-smooth piles ($\mu > 0$), N_p increases at higher rate within the shallow depth ($0 < z < 2D$). For depths $z > 2D$, N_p increases at the same rate regardless of μ

value. The depth at which N_{pu} is reached increased slightly at higher μ due to higher N_{pu} value corresponding to the value of μ.

Figure 125 summarizes the characteristics of N_p variation considered in the model development as a function of normalized depth, z/D.

In nonlinear zone ($0 < z < 2D$), the variation of N_p follows a power function starting from N_{po} value at the ground surface.

$$N_p\left(\frac{z}{D}\right) = N_{po} + k\left(\frac{z}{D}\right)^n \quad [69]$$

where k and n are model parameters, z is the depth from the ground surface, D is pile width.

Figure 125. General characteristics of N_p variation used for model development

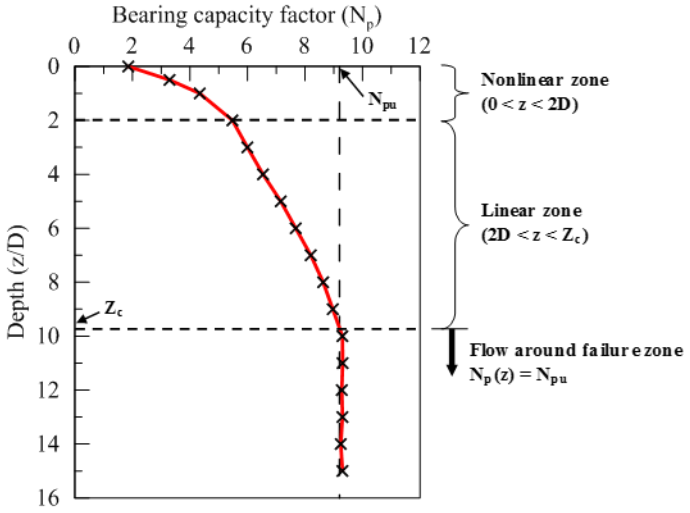

The model function is initially developed using the results for smooth piles (μ = 0.0) and then adjusted for non-smooth piles (μ > 0.0). The results of N_p for smooth piles from the FE parametric study was used to evaluate the parameters k and n in equation 69. The function was fitted to N_p results using an iterative scheme, and the parameters k and n were found to correlate with the ratio $(\gamma' D)/S_u$. A linear regression was used to obtain a relation for k and n as follows:

$$k = 0.82\frac{\overline{\gamma'}D}{\overline{S_u}} + 1.95 \quad [70]$$

$$n = 0.13\frac{\overline{\gamma'}D}{\overline{S_u}} + 0.6 \quad [71]$$

where $\overline{\gamma'}$ and $\overline{S_u}$ are the average values within the depth 0 < z < 2D.

The above equations make the N_p model in the shallow zone dependent on (γ' D)/S_u ratio, which is consistent with the observations from FE results. The ratio of (γ' D)/S_u defines a unique N_p variation for all cases with different values of D, S_u, γ', but with similar (γ' D)/S_u ratio. For instance, a pile with D =3 ft., S_u=500 psf, and γ'=120 pcf would have the same N_p variation with z/D as for the pile with D =2 ft., S_u=250 psf, and γ'=90 pcf, since both have the same (γ' D)/S_u =0.72. This however doesn't mean that the two cases would have similar ultimate lateral capacity, since $p_u$is a function of N_p, S_u, and D.

For non-smooth piles (μ> 0), the values of N_{po} and the k parameter increase when μ increases, while the parameter n remains fairly unchanged. The adjustment N_{po} as function of μ was obtained using linear regression, as follows:

$$N_{po} = 2.0 + 0.6\mu \quad [72]$$

Similarly, the adjustment k parameter as function of μ was obtained as follows:

$$k_{(\mu)} = k_{(0)} + (1 - \exp[-0.71\mu]) \quad [73]$$

where $k_{(0)}$ is the value of k for μ = 0 obtained using equation 70.

In the linear zone (2D < z < Z_c), the results of FE parametric study showed that N_p increased linearly with depth. The slope of N_p in the linear zone for smooth and non-smooth piles was obtained and plotted against the (γ' D)/S_u ratio. The results were found to closely align along the 1:1 line leading to the conclusion that the slope is (γ' D)/S_u, as shown in Figure 126.

Figure 126. Slope of N_p in the linear zone ($2D < z < Z_c$) as function of $(\gamma' D)/S_u$

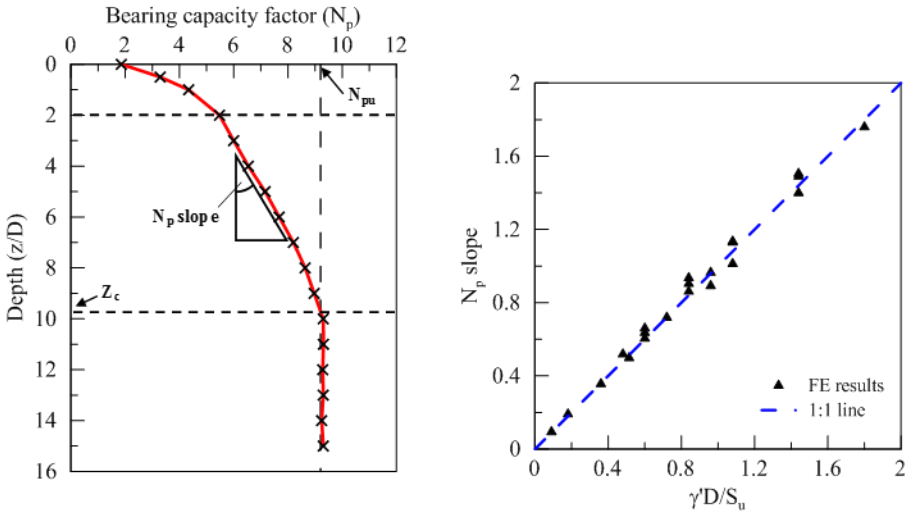

Following to the observation in Figure 126, the N_p model for the linear zone ($2D < z < Z_c$) can be evaluated as follows:

$$N_p\left(\frac{z}{D}\right) = N_{p_{@z/D=2}} + \frac{\gamma' D}{S_u}\left(\frac{z}{D} - 2\right) \leq N_{pu} \qquad [74]$$

where $N_{p@z/D=2}$ is the N_p value at depth z/D = 2 obtained from equation 69, N_{pu} is the upper-bound limit for N_p, which depends on pile adhesion (μ), γ', and S_u values correspond to the depth z.

The N_p value continue to increase with depth until it reaches the upper bound limit N_{pu} at the critical depth (Z_c). The value of Z_c (for smooth piles only (μ = 0)) were found to correlate with $(\gamma' D)/S_u$ that was fitted into the following relation:

$$\frac{Z_c}{D} = \frac{5.36}{\gamma' D/S_u} \qquad [75]$$

It is not necessary to estimate the critical depth (Z_c) to establish the N_p variation with depth, since the critical depth is indirectly determined by enforcing the upper bound limit N_{pu}. It should be noted here that the relation for Z_c is based on N_p for homogenous soil properties, and therefore would be inaccurate for non-homogenous soils.

Comparison of the Developed N_p Model with Other Models

The developed N_p model was first compared with other models in literature for a pile with D = 3 ft., soil properties γ'= 120 pcf, and S_u = 250 (soft clay), 500 (medium stiff clay), and 1000 psf (stiff clay) as shown in Figure 127. The comparison is focused on the rate of N_p increase with depth (or "N_p slope") and the critical depth (Z_c/D). Matlock [22] and Sullivan [73] models produced a fairly similar N_p variations; while Dunnavant and O'Neill [74] model had greater Z_c/D due to the smaller constant in the third term (0.4 z/D). The results of Reese's model show slight change in N_p variation with different S_u, which indicates that the model is lightly sensitive to S_u. This is because the Reese et al. [3] model includes a relatively large constant in the third term (2.83 z/D), which dominates the N_p slope as compared to the contribution from the second term ((γ' z)/S_u).

The N_p results for the proposed model were higher in the shallow zone (0 < z/D < 2) as compared to Matlock and Sullivan models (+1 at z/D=2), and notably higher than the Dunnavant and O'Neill model (+1.8 at z/D=2). The critical depth in the soft clay (250 psf) for the proposed model was similar to Matlock and Sullivan models (z/D=3.3). For medium stiff clay (500 psf), the Z_c/D for the proposed model was at z/D=6.3, which was similar to the Dunnavant and O'Neill model. For stiff clay (1000 psf), the Z_c/D was notably greater in the proposed model (z/D=12) as compared to the Dunnavant and O'Neill model (z/D= 9). One should recall that Matlock and Sullivan models were developed for soft clays; while Dunnavant's model was developed for stiff clays.

Figure 127. Comparison of N_p variation between the proposed and literature models at different undrained shear strengths (S_u)

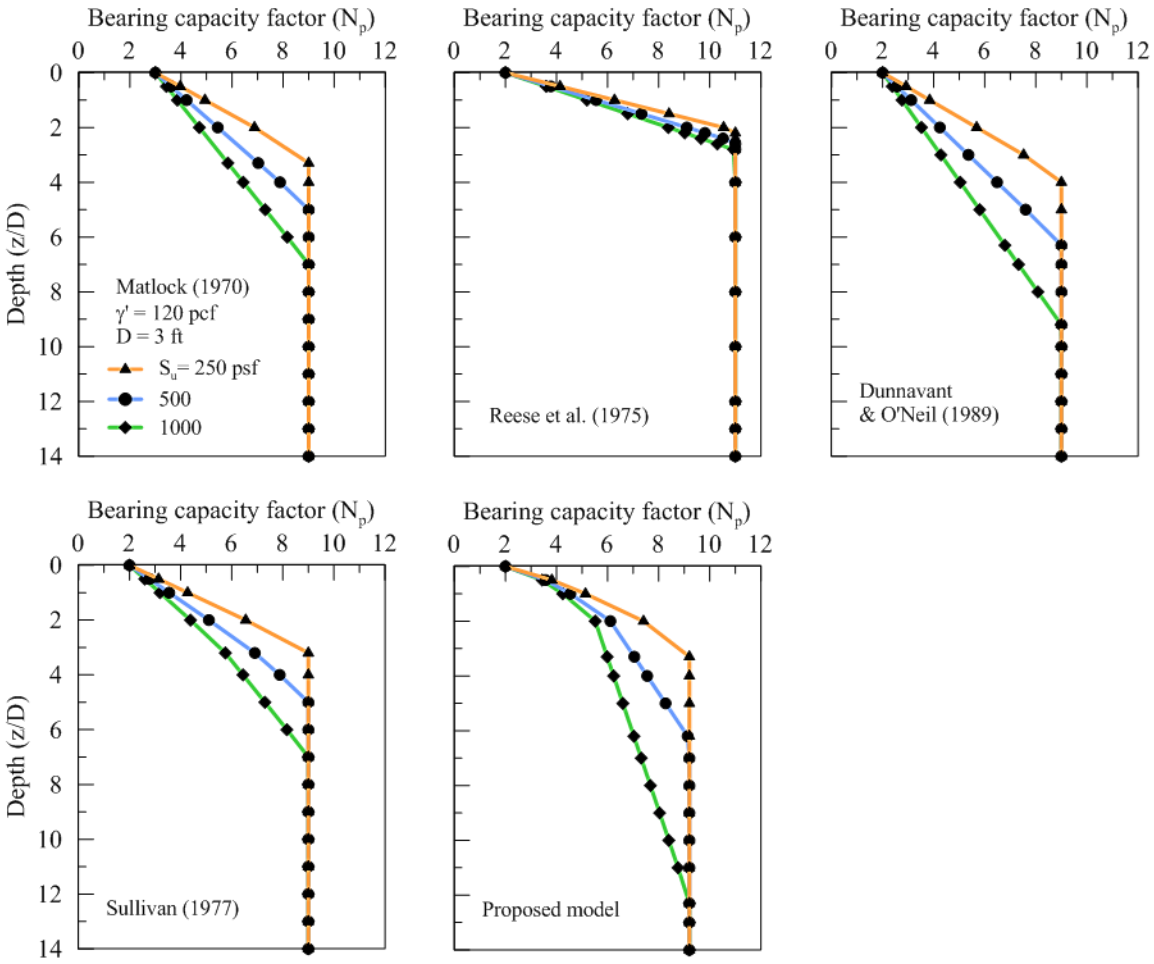

The proposed model was compared with other models for different pile widths (D = 1, 2, 3 ft.) for S_u = 250 psf and γ'= 120 pcf, and the results are depicted in Figure 128. The variations of N_p from the proposed model were slightly higher in the shallow zone ($0 < z/D < 2$) as compared to the Matlock [22], Sullivan [73], and Dunnavant and O'Neill [74] models. All models predicted greater Z_c/D when the pile width was decreased. The results from the proposed model were closely similar to Matlock and Sullivan models at D = 3 ft. only; while it was closer to the result of the Dunnavant and O'Neill model at D = 2 ft. For D = 1 ft., the proposed model had large Z_c/D at 9.3, which was +2 than Matlock [22] and Sullivan [73] models and +1.3 than the Dunnavant and O'Neill [74] model. The Reese et al. [3] model predictions shows that the model is not sensitive to the change in pile width, which is due to the large constant in the third term.

Figure 128. Comparison of N_p variation between the proposed and literature models at different pile widths (D)

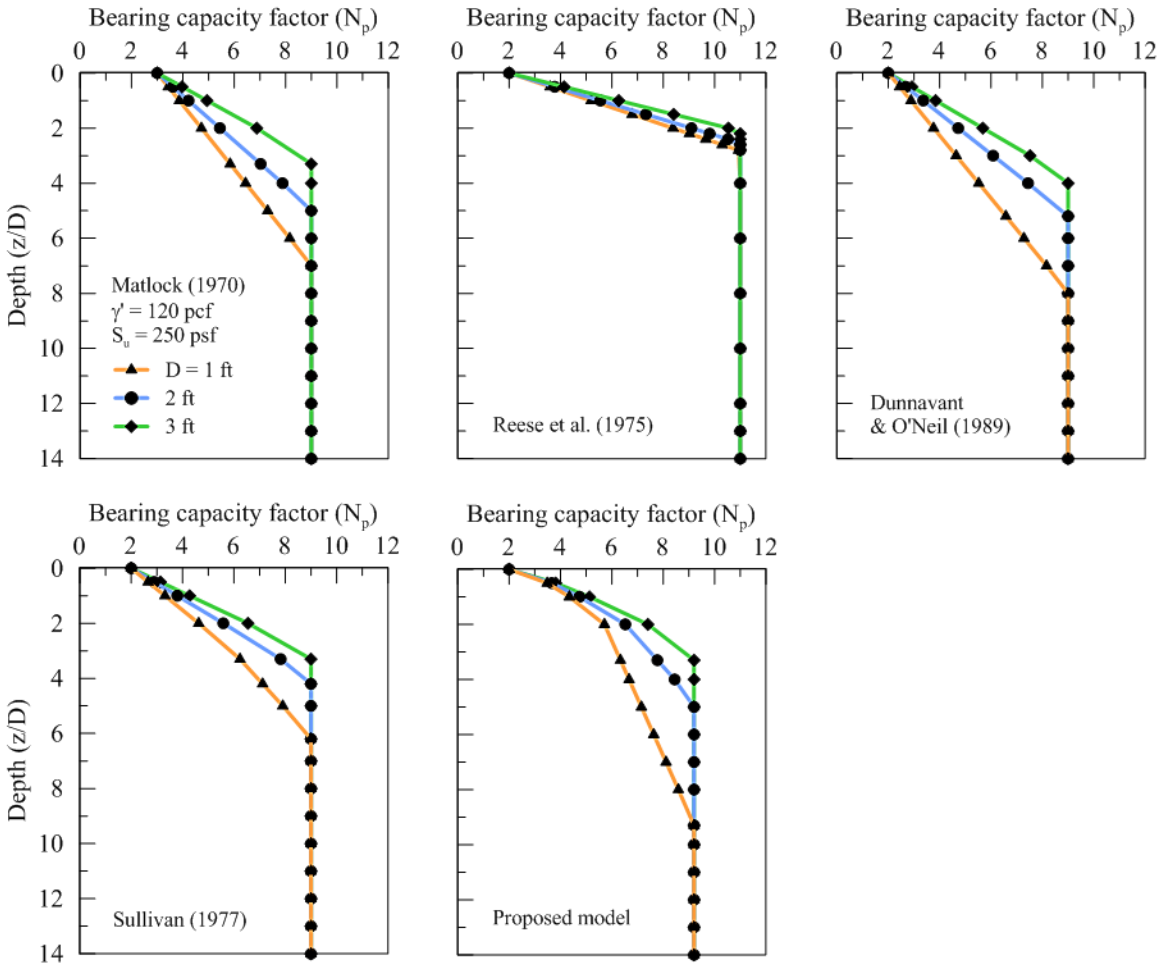

The proposed N_p model was also compared to other models at different effective soil unit weight (γ') for S_u = 250 pcf and D = 3 ft., and the results are presented in Figure 129. The N_p results for all models show decrease in N_p values with the decrease in γ'. The Z_c/D results from the proposed model was similar to Matlock [22] and Sullivan [73] models at γ' = 120 pcf; while it was closer to the result of the Dunnavant and O'Neill [74] model at γ' = 90 and 60 pcf. The results of the Reese et al. [3] model were insensitive to γ', similar to the observations for the cases at different S_u and different D values.

In summary, the response of the proposed N_p model was closely similar to the literature models except for the Reese et al. [3] model. The minor differences come from the difference in formulation and the semi-empirical nature induced by the constant in third term. Moreover, the literature models were developed based on a small number of experimental studies, which are limited as compared to the FE numerical modeling.

Figure 129. Comparison of N_p variation between the proposed and literature models at different effective soil unit weights (γ′)

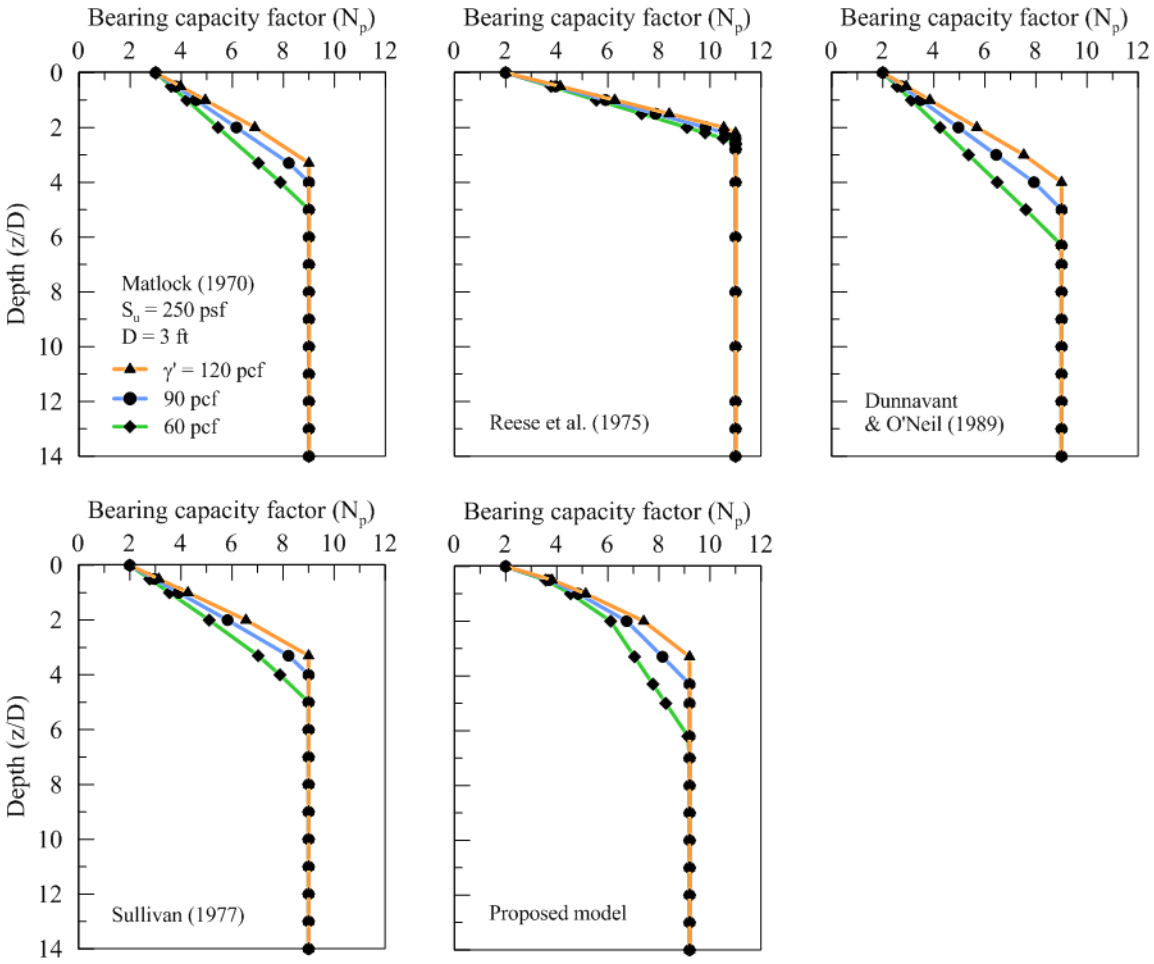

Initial Slope and y_{50}

The second element needed toward the development of the p-y curve is the initial slope, which can be defined using either the coefficient of horizontal subgrade reaction (k) or the reference deflection y_{50} in the p-y curve. Here y_{50} refers to the pile deflection at 50% of the ultimate soil resistance (p_u) in the p-y curve. It is commonly used in the p-y curve models for clays (e.g., [3], [22], [73], [74]) [75]. It can be estimated using the soil strain property (ε_{50}) and the pile width (D) as follows:

$$y_{50} = A\varepsilon_{50}D \quad [76]$$

where A is a constant, ε_{50} is the axial strain at 50% of undrained shear strength in UU test.

Different values for A were proposed in the literature; Matlock [22] assumed A = 2.5, Reese et al. [3] used A = 1.0, and Stevens and Audibert [76] suggested A = 8.9 D-0.5. However, Dunnavant and O'Neill [74] found out A is dependent on the pile-soil relative stiffness, and proposed $A = 0.0063 ((E_p I_p)/(E_s L^4))^{-0.875}$, where $E_p I_p$ is the pile rigidity, E_s is the soil modulus, and L is the pile length. Wu et al. [75] argued that A is approximately equal to the bearing capacity factor for normally consolidated clays.

In this study, the reference deflection y_{50} was studied as part of the FE parametric study. The p-y curves were first obtained from the FE simulations for laterally loaded single pile, and then y_{50} was determined from the curves. Potential factors affecting the y_{50} parameter are: ε_{50}, E_p, S_u, and pile width (D).

The FE model used to study the y_{50} was for a flexible pile with circular cross section as shown in Figure 130. The pile width (D) was varied in the analysis and the length was chosen as 30D to ensure flexible pile behavior. Similar to the study for N_p, only half of the pile and soil domain was modeled to reduce the solution time. The pile and the soil were modeled using solid continuum elements (C3D8R) and the FE mesh density was varied so that it is denser near the pile. The pile and soil constitutive models were selected the same as in previous FE modeling. The simulation was performed in two steps. In the first step, the geostatic stress in the soil was established by applying gravity load in the global z-direction. In the second step, the pile top was pushed laterally a distance of 0.3D, which was selected to fully develop the p-y curves within a 15D depth.

The soil resistance and pile deflection at certain depth were combined to form the p-y curve. To evaluate y_{50}, the deflection corresponding to half of the ultimate soil resistance (0.5pu) is found from the constructed p-y curve. The factors affecting the y_{50} in the p-y curve are: pile's material stiffness (E_p), pile width (D), undrained shear strength (S_u), and the reference strain (ε_{50}). The value of ε_{50} in the FE model is controlled by Young's modulus (E_s), which is related to ε_{50} as $\varepsilon_{50}=0.5S_u/E_s$.

Effect of Soil Stiffness (E_s). The soil stiffness was varied with respect to S_u. The base value for S_u was 250 psf. For each case, y_{50} was obtained from the p-y curves at several depths (z/D = 1, 2, 3, 4, 5, 6), which was limited at 6D due to the p-y curves not being fully developed below this depth. Figure 131 present the results of y_{50} with the normalized depth (z/D). In general, the y_{50} decreases with increasing the soil stiffness, E_s, and the rate of y_{50} decrease is nonlinear. Another observation is that y_{50} varied with depth although E_s was constant for the whole soil profile. The latter indicates that y_{50} depends on another variable beside E_s, which was found to be the N_p as will be shown later.

Figure 130. Geometry and mesh of the FE model used to study y_{50}

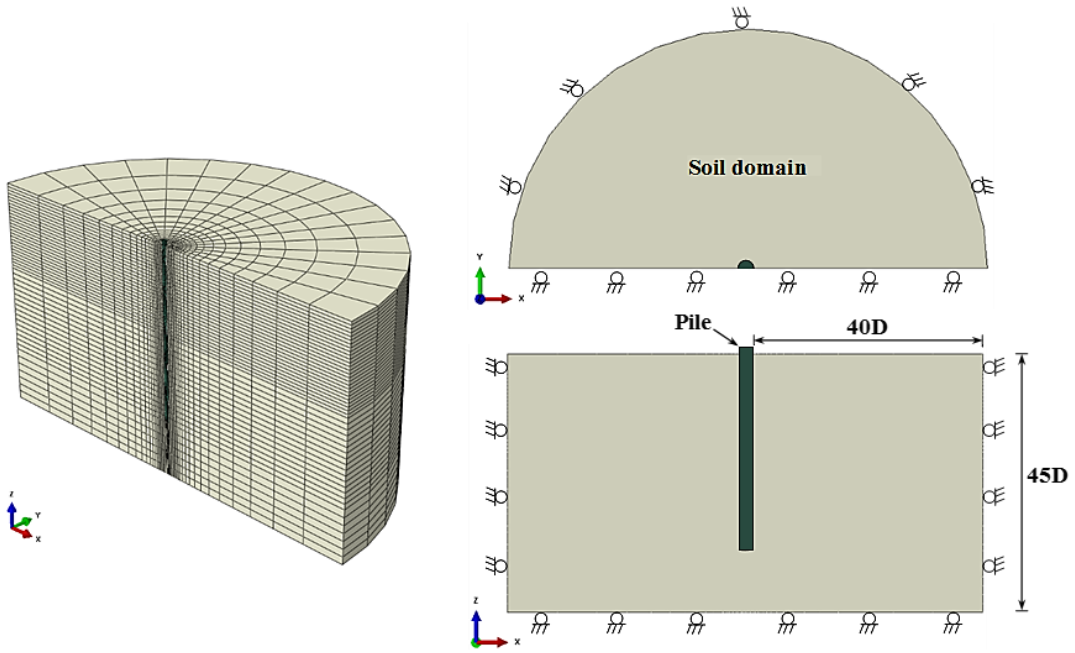

Figure 131. Effect of soil stiffness on y_{50}

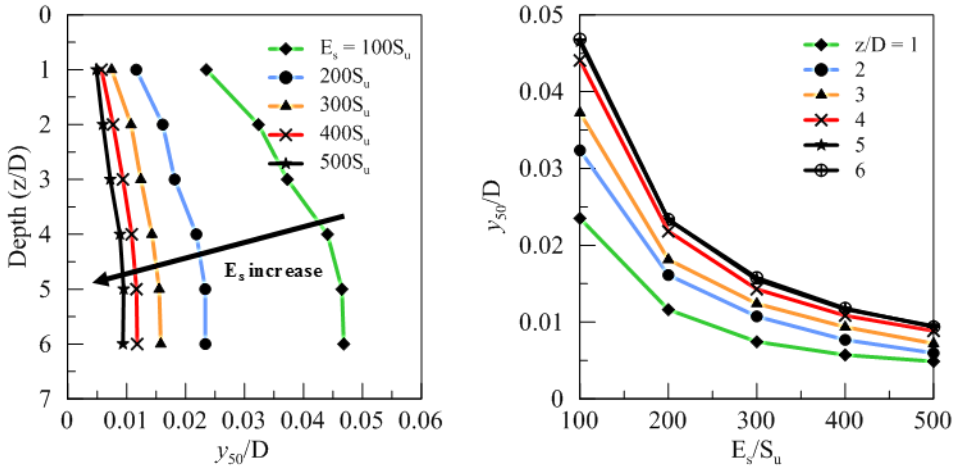

Effect of Pile Stiffness (E_p). The effect of pile stiffness, E_p, was investigated by varying the reference value ($E_{p\text{-ref}}$ = 6.08 x10^8 psf) by ±25% and ±50% (Figure 132). The reference E_p value was estimated for a concrete pile using f_c'=5500 psi and $E_p = 57000\sqrt{f_c'}$ [120]. The results show that the y_{50} increases with increasing the E_p. However, the effect is negligible as noticed in the percent change in y_{50}, which lies within ±3%. Therefore, y_{50} can be considered independent of the E_p value without introducing significant error.

Figure 132. Effect of pile stiffness (E_p) on y_{50}

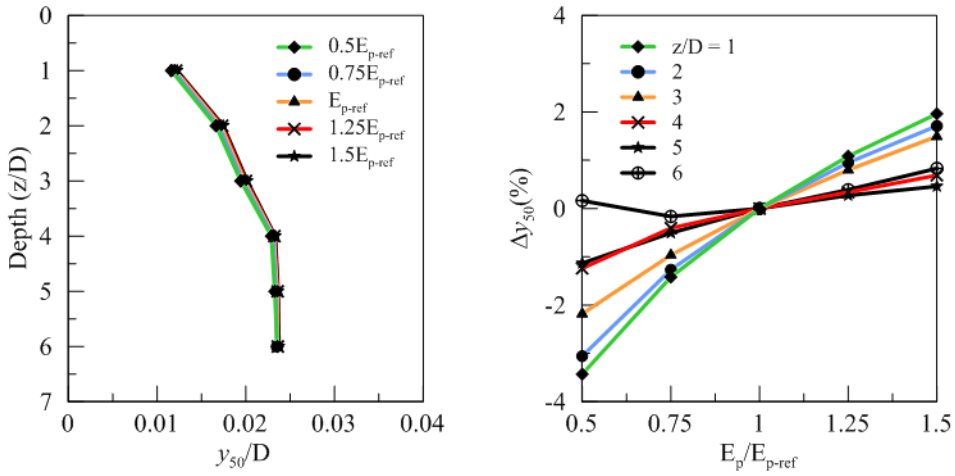

Effect of Undrained Shear Strength (S_u). The effect of S_u on y_{50} was investigated for different S_u values representing soft clay (250 psf), medium stiff clay (500, 750 psf), and stiff clay (1000 psf). Figure 133 shows that, in general, the y_{50} decreases with increasing the S_u value. In addition, the increasing in S_u resulted in a different variation for y_{50} with depth. For example, for S_u = 250 psf, the y_{50} increased up to depth z/D = 4 and then remained fairly constant. Meanwhile, for S_u = 500, 750, and 1000 psf, the y50 kept increasing with depth at different rates. Closely examining the results show that the variation in y_{50} looks similar to the N_p variation for each case. Recall that the ultimate soil resistance (p_u) reaches its limit value at the critical depth (Z_c), and for the presented cases Z_c was 4D for S_u = 250 psf, 7.4D for 500 psf, 11D for 700 psf, and 14.7D for 1000 psf. So for S_u = 250 psf, Z_c= 4D, which is the depth after which y_{50} remained constant. This indicates that there might be some relationship between y_{50} and Np.

Effect of Pile Width (D). The effect of pile width (D) on y_{50} was investigated for three sizes; 2, 3, and 4 ft. as shown in Figure 134. The results show that y_{50} increases with larger pile width. However, the variation of y_{50} with depth was not identical in each case and have similarities with N_p variation, which depends on D. It can be seen that the y_{50} values stopped increasing at a certain depth in each case; at z/D = 3, 4, 6 for D = 4, 3, 2 ft., respectively. These depth values are closely similar to Z_c depths for N_p in each case (Z_c/D = 2.8, 3.7, 5.5 for D = 4, 3, 2 ft., respectively). This is another indication that y_{50} is somehow related to N_p.

Figure 133. Effect of undrained shear strength (S_u) on y_{50}

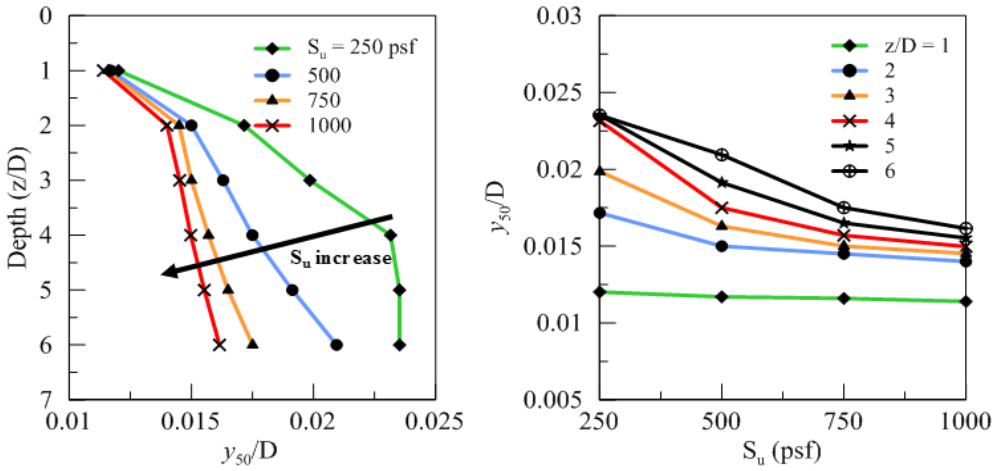

Figure 134. Effect of pile width (D) on y_{50}

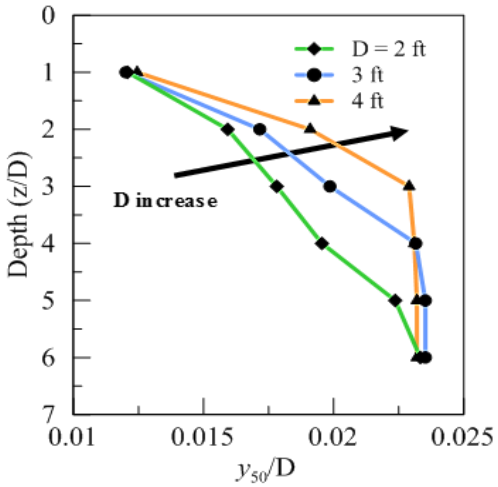

Development of a Model for y_{50}

Using the results of FE parametric study, a model for y_{50} was proposed as follows:

$$y_{50}/_D = AN_p \, S_u/_{E_s} \qquad [77]$$

Using the linear regression analysis, the value for parameter A was obtained as 0.5. The comparison between the y_{50} obtained from the proposed model and FE results is presented in Figure 135, which demonstrates that the proposed model is able to estimate accurate and precise values for y_{50}.

The value of S_u/E_s can be replaced by ε_{50}, leading to the following relationship:

$$y_{50} = 0.5DN_p\varepsilon_{50} \quad [78]$$

Figure 135. Comparison between y_{50} obtained from proposed model and FE results

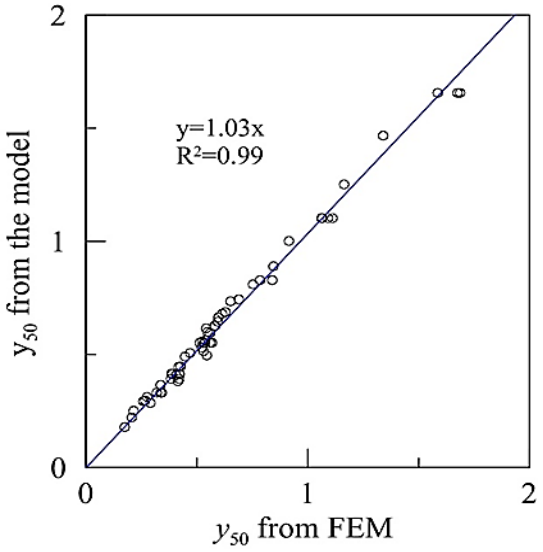

Characteristic Shape of p-y Curve

In this study, nonlinear regression was used for obtaining the constants of A, B, and n in Equation 79. By minimizing the Mean Squared Error in the results, the values of A, B, and n were obtained as 1.11, 0.49, and 0.89. Therefore, the characteristic shape of p-y curves is as follows:

$$p = 1.11p_u \tanh(0.49\left(\frac{y}{y_{50}}\right)^{0.89}) \quad [79]$$

The comparison between the p-y curves obtained from FE analysis and the proposed model for a case of pile in clay is shown in Figure 136. The results suggest that the proposed model is able to capture the results of FE analysis accurately.

Figure 136. P-y curves obtained from FE Analysis and proposed model for piles in clay with S_u = 300 psf, γ = 110 pcf, D= 3 ft., $E_s=200S_u$, and μ=0

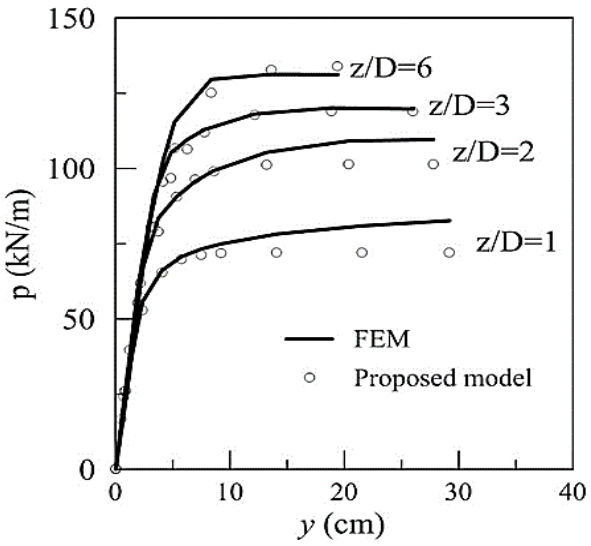

Model for Predicting p-y Curves in Overconsolidated Clays

The p-y model developed in this study can be used for predicting the lateral behavior of overconsolidated clay. For this purpose, the model in equation 79 should be used for two different values of friction angle: peak and critical state. Using the values of $S_{u\text{-}peak}$ and $S_{u\text{-}cs}$, two different curves are obtained. Then a linear decrease from the upper curve (related to $S_{u\text{-}peak}$) to lower one (related to $S_{u\text{-}cs}$) is added as shown in Figure 137. The values of $8y_{50}$ and $30y_{50}$ in Figure 137 are suggested by some researchers, while some others suggest $3y_{50}$ and $15y_{50}$ for these values.

Figure 137. Schematic of p-y curve for overconsolidated clays

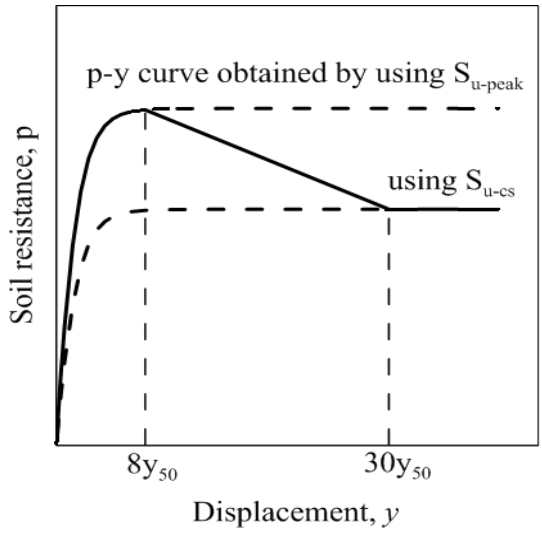

Finite Element Analysis of Laterally Loaded Piles in Sands

A p-y curve model for laterally loaded piles in sands has been developed using the results of finite element analysis. Each element of the p-y curve (ultimate lateral soil resistance, initial slope, characteristic shape function) is studied through parametric investigations, in which the effect of both the soil and parameters were evaluated. Using the results from the parametric study, numerical models for the ultimate resistance, initial slope, and characteristic shape function were verified and compared to existing models

Finite Element Model

A finite element model similar to the 3-D FE model used for p-y curve in clays (Figure 118) was also used here to develop p-y curve for sands. The only difference is in using an appropriate constitutive model to describe the behavior of sand instead of clay constitutive model.

The sand constitutive behavior was modeled as linear elastoplastic material with Mohr-Coulomb yield criteria (ϕ, c = 0). The pile constitutive behavior was modeled as linear elastic and the properties of concrete of f_c'=5500 psi with Young's modulus, $E_p=57000\sqrt{f_c'}$, and Poisson's ratio, ν = 0.2. The effect of pile-soil interaction (adhesion) was accounted for by using an interface model available in ABAQUS. The interface

element has a zero-thickness and transfers normal and tangential stresses (with respect to the interface) between the pile and soil.

Parametric Study for p-y Curves in Sands

The following hyperbolic equation was assumed for p-y curves in sands by introducing a power function inside the hyperbolic tangent function, as shown below:

$$p = p_u \, tanh\left[\left(\frac{\alpha y}{y_{ref}}\right)^n\right] \quad [80]$$

where p is the soil reaction, y is the displacement, p_u is the ultimate soil resistance, and y_{ref} is the reference deflection. When $y = y_{ref}$ in the above equation, the value of p becomes equal to $p_u.\tanh(\alpha^n)$. For the value of $\alpha = 2$, the soil resistance reach to about $0.96p_u$ at $y = y_{ref}$. Accordingly, the value of y_{ref} can be defined as the displacement when the soil reaction, p reaches to the ultimate value, p_u.

The benefit of using equation 80 is that it is easy to evaluate p_u and y_u for each p-y curve in the FE parametric study. The initial slope of p-y curves can be obtained from the derivative of p at y=0, as follows:

$$k_{ini} = \frac{\partial p}{\partial y}|_{y=0} = \frac{\alpha p_u}{y_u} \quad [81]$$

The influence of several factors on the ultimate soil resistance, p_u, and ultimate displacement, y_u, was investigated in FE parametric study. For sands, the influencing factors can be summarized as: the soil elastic modulus (E_s), angle of friction (ϕ), effective unit weight of the soil (γ'), coefficient of lateral earth pressure (K), pile width (D), and the soil-pile interface coefficient (μ).

Effect of Sand Modulus of Elasticity (E_s). Typical values for modulus of elasticity for sandy soils range from 150,000 to 1,700,000 psf. In this parametric study, the values of E_s equal to 200,000, 500,000, 1,000,000, and 2,000,000 (psf) was conducted, which represents silty, loose, medium, and dense sands; respectively. Figure 138 presents the p-y curves for piles in sands with modulus of elasticity. It can be noticed that the value of p_u does not change with E_s, however the value of y_u decreases with increasing E_s. The change of y_u at depth x=12 ft. for the different E_s values is shown in Figure 139. The variation of p_u with depth is shown in Figure 140. The figure shows that the value of p_u

increases initially in quadratic shape to a specific depth, and then increases linearly; which is the same form of the analytical solution proposed by Reese et al. [24].

As shown in Figure 138, the value of y_u increases with increasing depth. Finding the values of y_u from different curves is not an easy task. For developing a p-y model, we assume that y_u increases with x^{n1}, and then we find the value of n1 that gives us the best regression.

Figure 138. P-y curves for piles in sands with (E_s) (a) 200,000 (b) 500,000 (c) 1,000,000, and (d) 2,000,000 (psf)

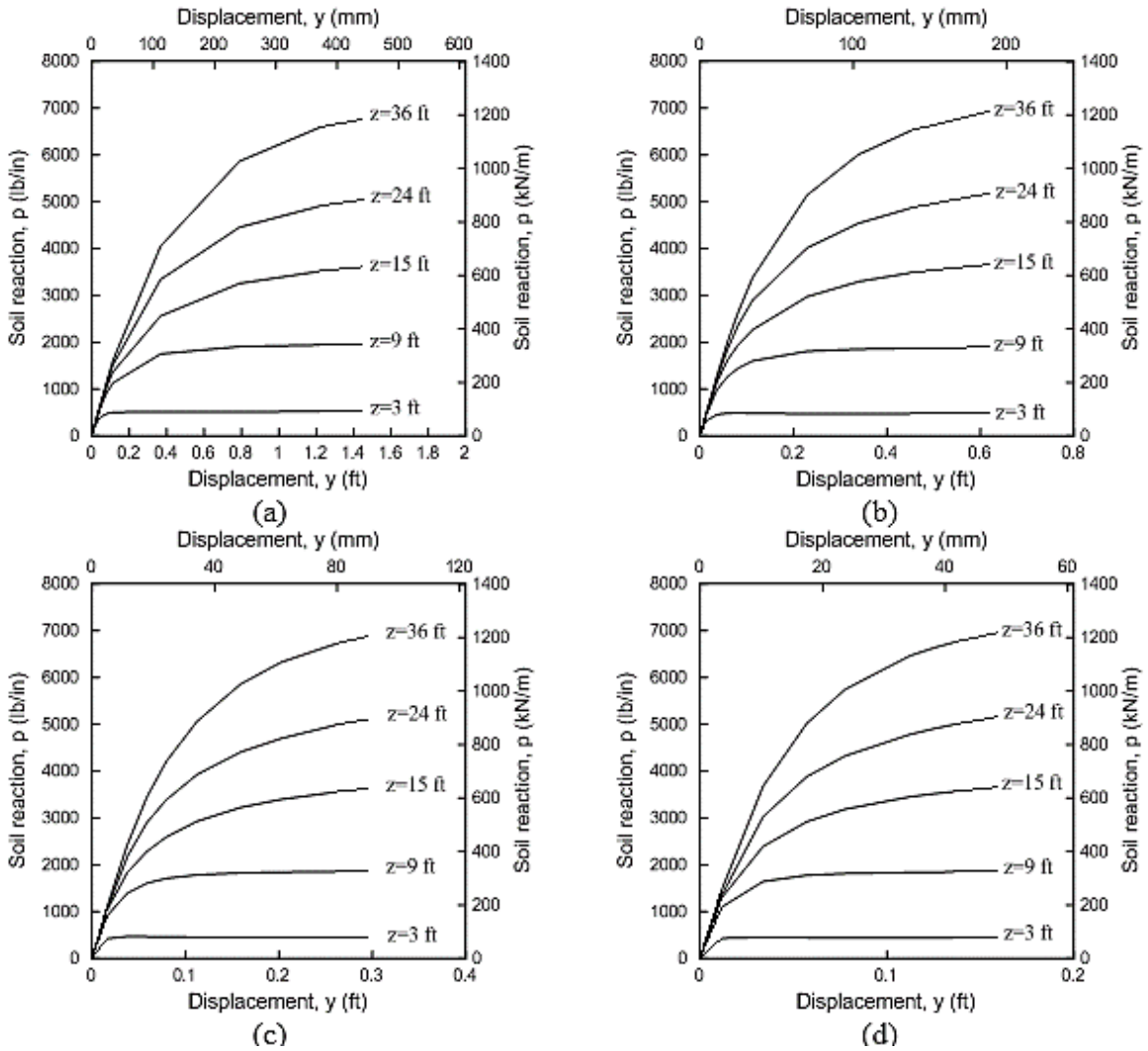

Figure 139. Changes in the ultimate displacement, y_u at depth x=12 ft. with modulus of elasticity (E_s)

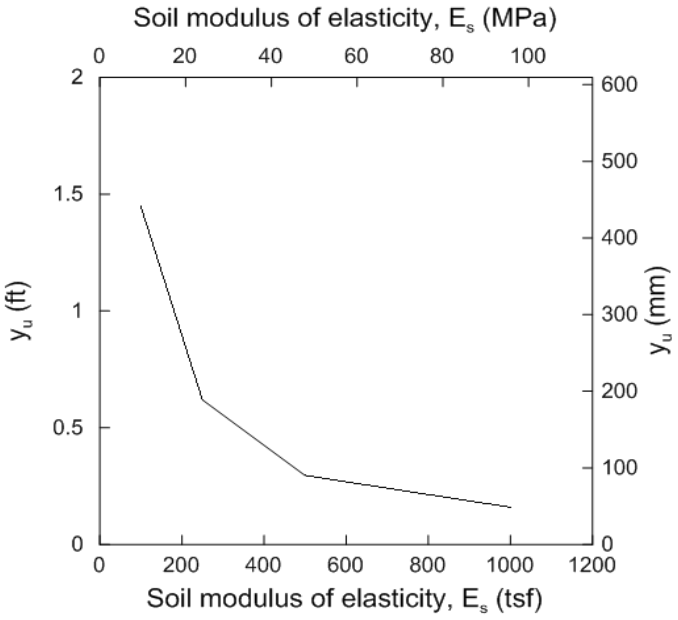

Figure 140. The variation of p_u with depth for piles in sands

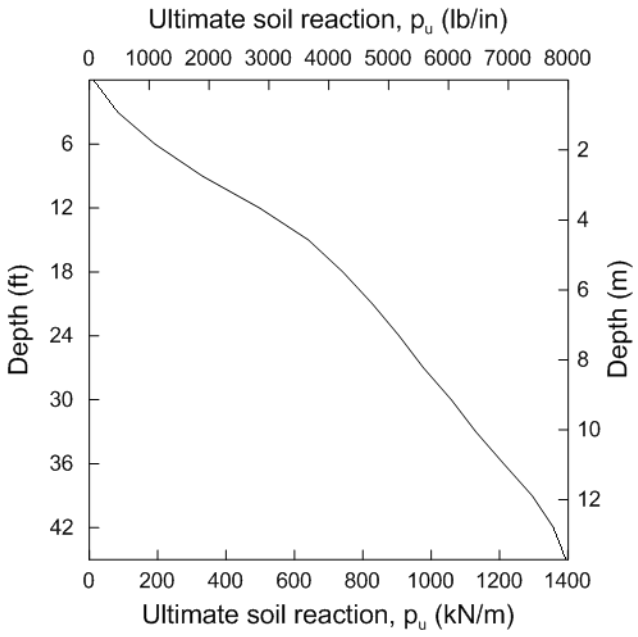

Effect of Soil Friction Angle (ϕ'). The typical range of friction angle for sands varies from < 29° for loose sand to > 41° for very dense sand [121]. In this study, the p-y curves for ϕ = 25, 30, 35, and 40 were studied, as shown in Figure 141. The figure demonstrates that the value of p_u increases with increasing ϕ'. The figure also shows that the p-y curves

are not fully mobilized at high values of ϕ', which implies that y_u has increased. A comparison of p-y curves for different depths of 12 and 30 ft. are shown in Figure 142. The increase in the p_u with depth for different values of ϕ' is depicted in Figure 143. In our model, the best fit regression for p-y curves for p_u and y_u values with $(\tan \phi')^n$ were determined.

Figure 141. P-y curves for piles in sands for ϕ: (a) 25 (b) 30 (c) 35 (d) 40 (degrees)

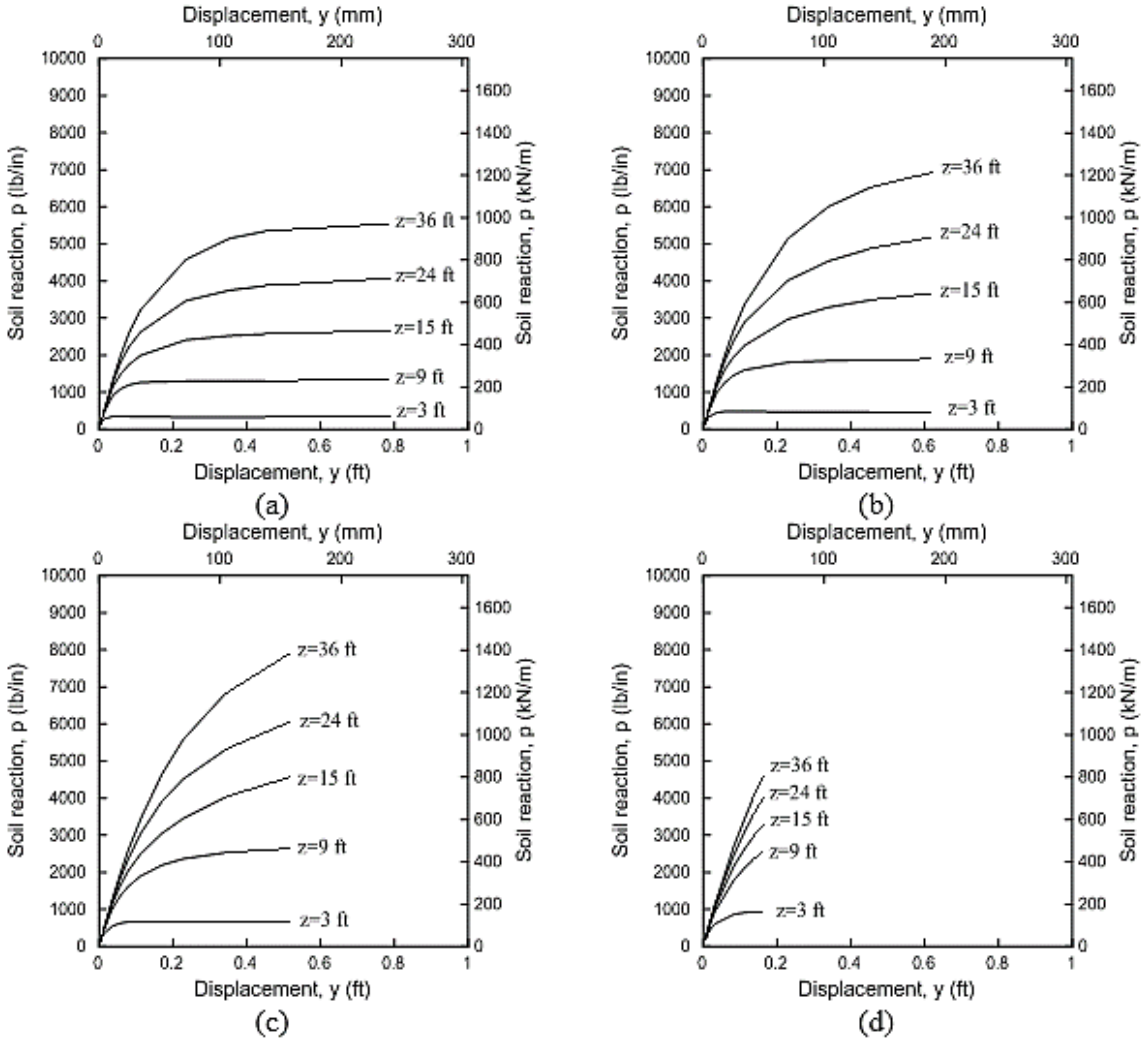

Effect of Effective Unit Weight (γ'). The typical values of unit weight (γ) for different soils ranges from 110 to 130 pcf. Having the value of unit weight of water equals 62.43 (pcf), the p-y curves for different values of effective unit weight, γ' of 60, 80, 100, and 120 (pcf) were obtained as shown in Figure 144. The comparison between p-y curves in different depths for different values of γ' is presented in Figure 145. The figure shows that

the value of ultimate soil reaction, p_u, and ultimate deflection, y_u, increases with increasing γ'. For the case of soils with different unit weights, a simple approach like Georgiadis method can be used as will be discussed later [122]. The results obtained from the proposed model will be modified by the Georgiadis method and compared with the results of finite element analysis.

Figure 142. P-y curves for piles in sands with different ϕ' at depth: (a) x=12 ft. (b) x=30 ft.

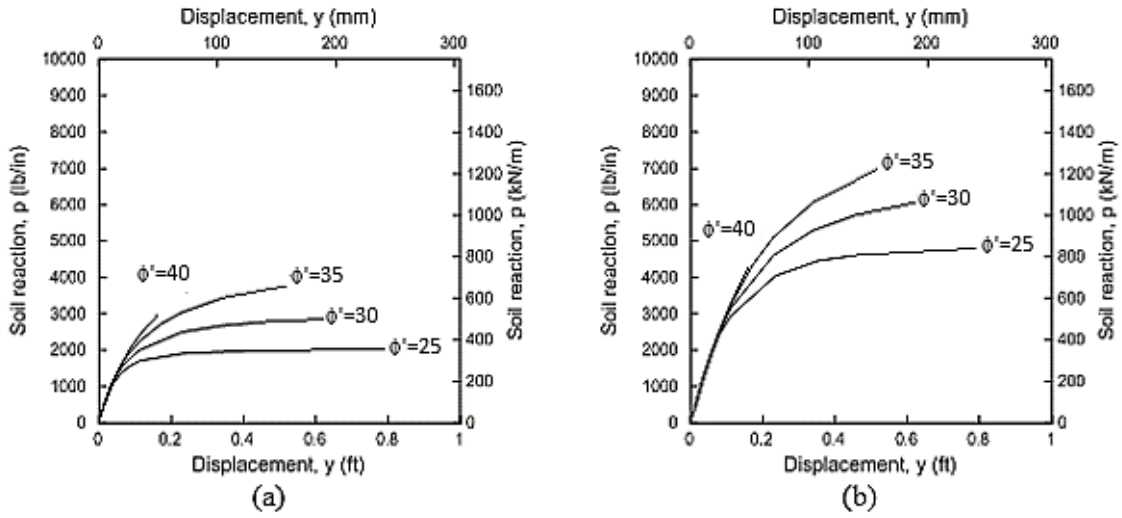

Figure 143. The value of ultimate soil reaction, p_u for piles in sands with different ϕ'

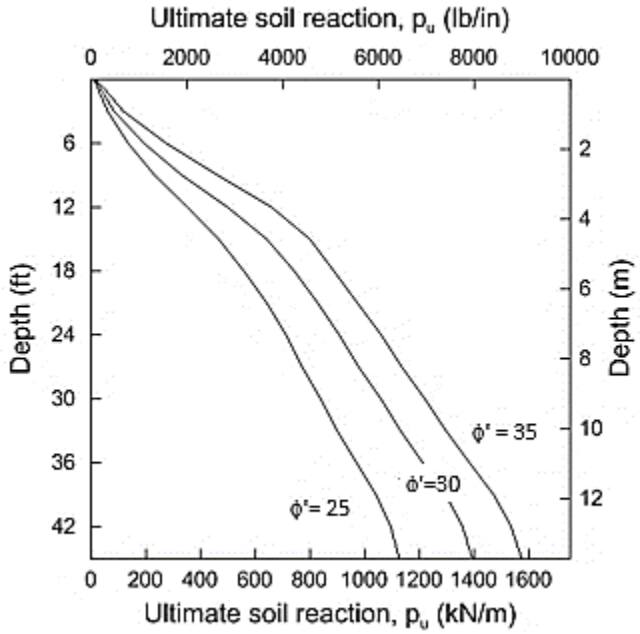

Figure 144. P-y curves for piles in sands with γ': (a) 60 (b) 80 (c) 100 (d) 120 (pcf)

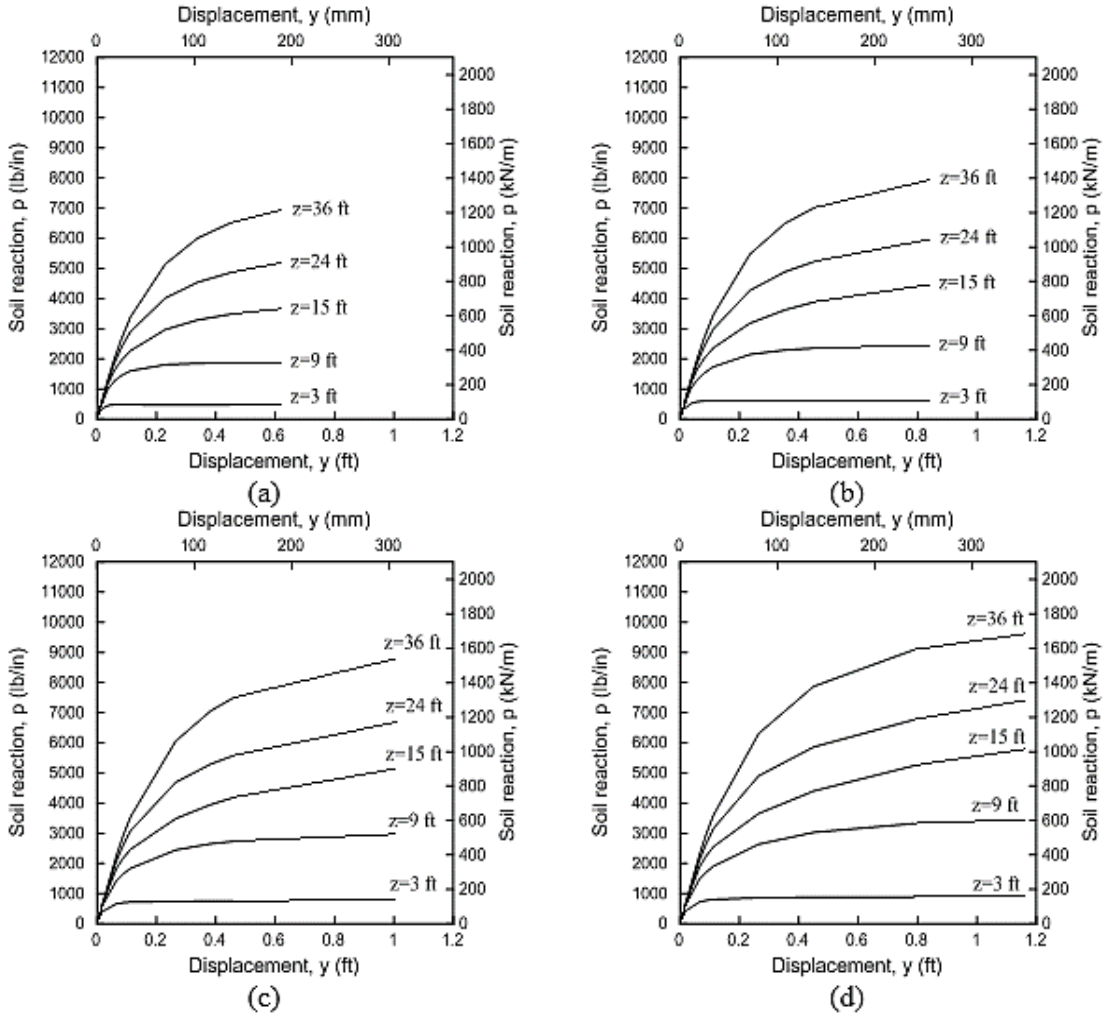

Effect of Coefficient of Lateral Earth Pressure (K). In this study, different values of coefficient of lateral earth pressure (K) of 0.5, 0.75, 1, and 2 were investigated, and the corresponding p-y curves are presented in Figure 146. The comparison between p-y curves at different depths of 12 and 30 ft. is shown in Figure 147.

Effect of Pile Diameter (D). Different pile diameters of 2, 3, and 4 ft. were investigated in this study. The p-y curves for depths, D=2 and 4 ft. are presented in Figure 148. The comparison of p-y curves at different depths of 12 ft. and 30 ft. are shown in Figure 149. It can be seen that increasing the pile diameter lead to an increase in the p_u value; while the effect of diameter on the value of y_u is not obvious.

Figure 145. P-y curves for piles in sands with different γ' at depth: (a) x=12 ft. (b) x=30 ft.

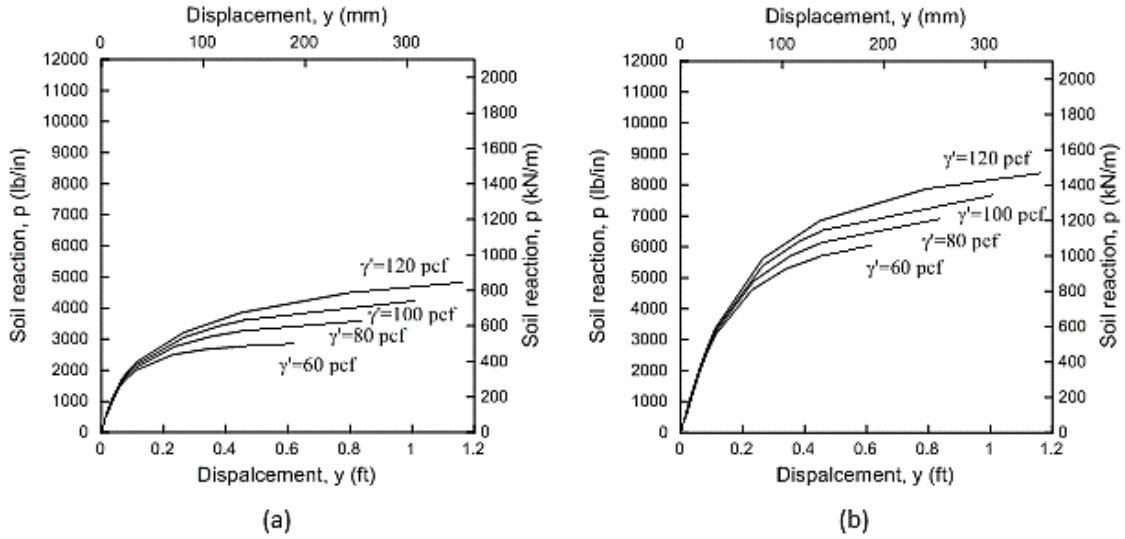

Effect of Interface Friction Coefficient (μ). The surface to surface master-slave contact model was used to simulate the soil-pile interface using the Mohr Coulomb frictional criteria. The typical values of interface friction angle, δ, in literature ranges from 14^o to 30^o. In this study, δ values of 17, 22, and 27 were selected. Defining the interface friction coefficient, μ, as: μ=tan δ, leads to corresponding μ values of 0.3, 0.4, and 0.5. The p-y curve for μ=0.4 and 0.5 are presented in Figure 150. A comparison between p-y curves at two different depths of 12 ft. and 30 ft. are shown in Figure 151. It can be seen from the figure that the interface friction angle, δ, does not have any significant effect on the p-y curves in sands.

Developing a Model for p-y Curves in Sands

In developing a nonlinear hyperbolic model for p-y curves in sands, regression analysis was used to calibrate the following hyperbolic relationship with power function using the results of FE parametric study:

$$p = p_u \tanh\left(\left(\frac{\alpha y}{y_{ref}}\right)^{no}\right) \qquad [82]$$

By fitting the above equation to the p-y curves obtained from FE parametric study, and using α = 2.0, the values of p_u and y_{ref} can be evaluated. The estimation of reference

deflection, y_{ref}, in the p-y curve is easier compared to estimating the value of initial slope of p-y curve, k_{ini}, which is determined by the derivation of equation 82 at y=0.

Figure 146. P-y curves for piles in sands with different K values of (a) 0.5 (b) 0.75 (c) 1.0 (d) 2.0

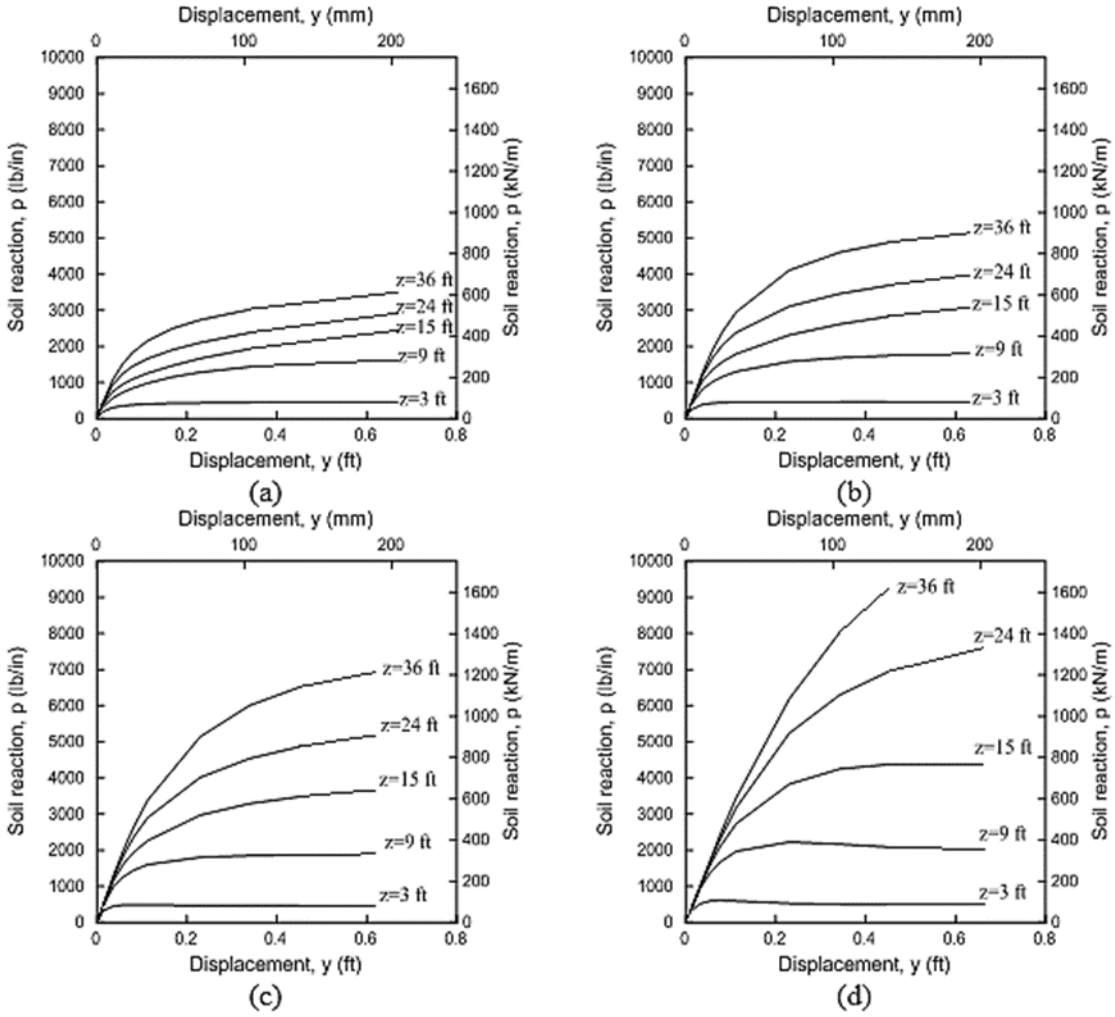

Figure 147. P-y curves for piles in sands with different K values at depth (a) x=12 ft. (b) x=30 ft.

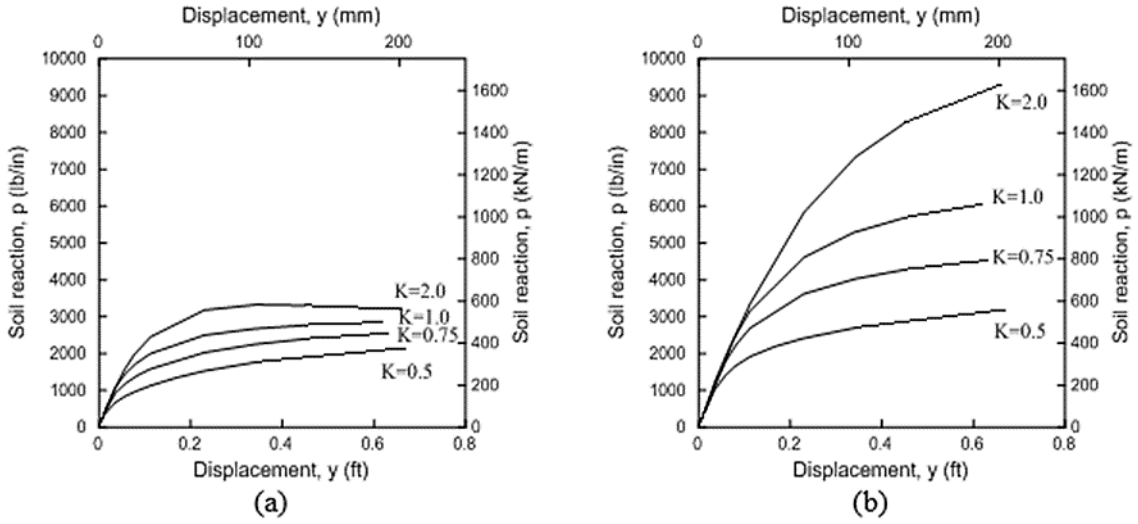

Figure 148. P-y curves for piles in sands with diameter (D): (a) 2 ft. and (b) 4 ft.

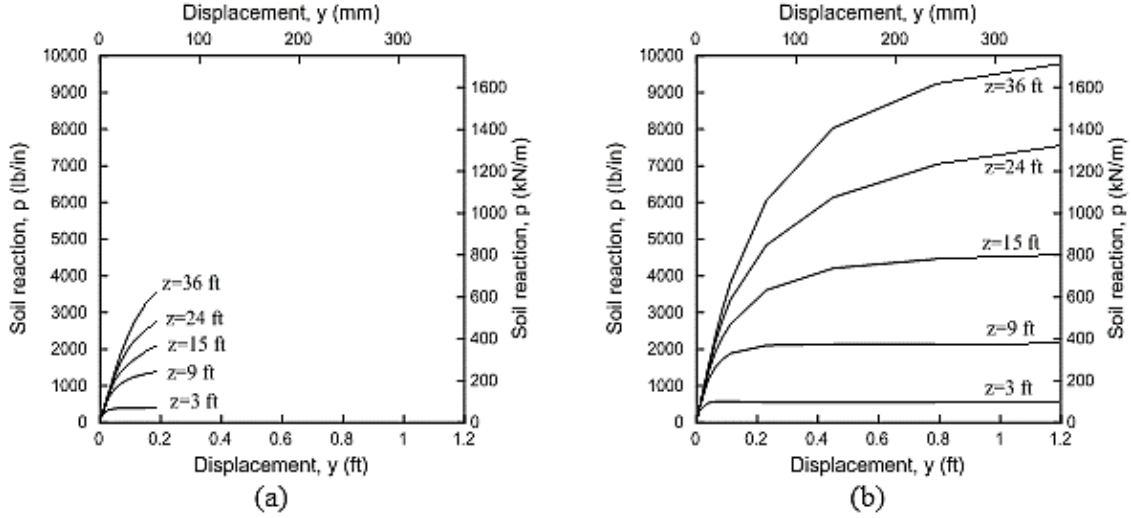

Figure 149. P-y curves for piles in sands with different pile diameter (D) at depth (a) x=12 ft., and (b) x=30 ft.

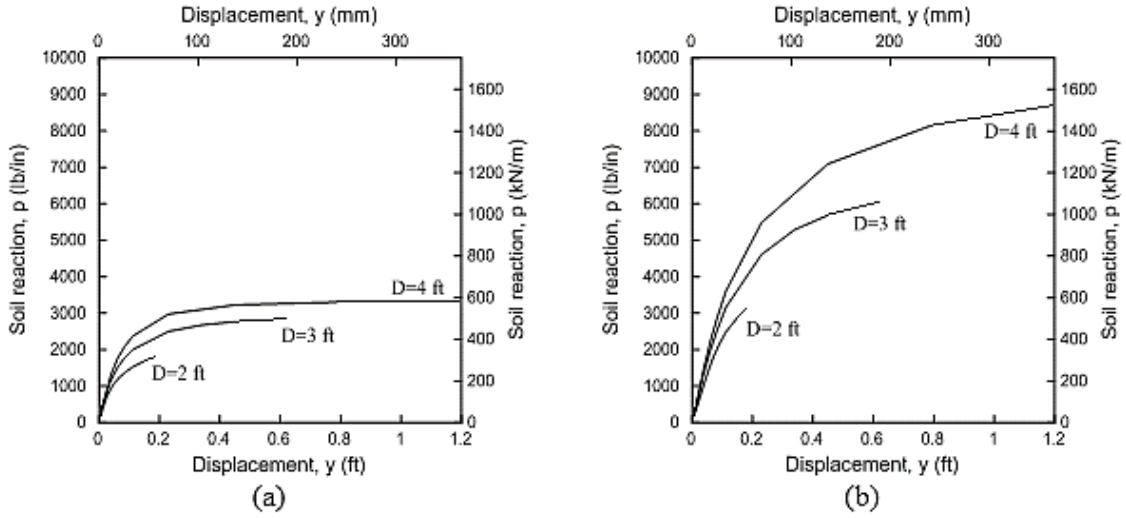

Figure 150. P-y curves for piles in sands with interface friction coefficient (μ) of: (a) 0.4 and (b) 0.5

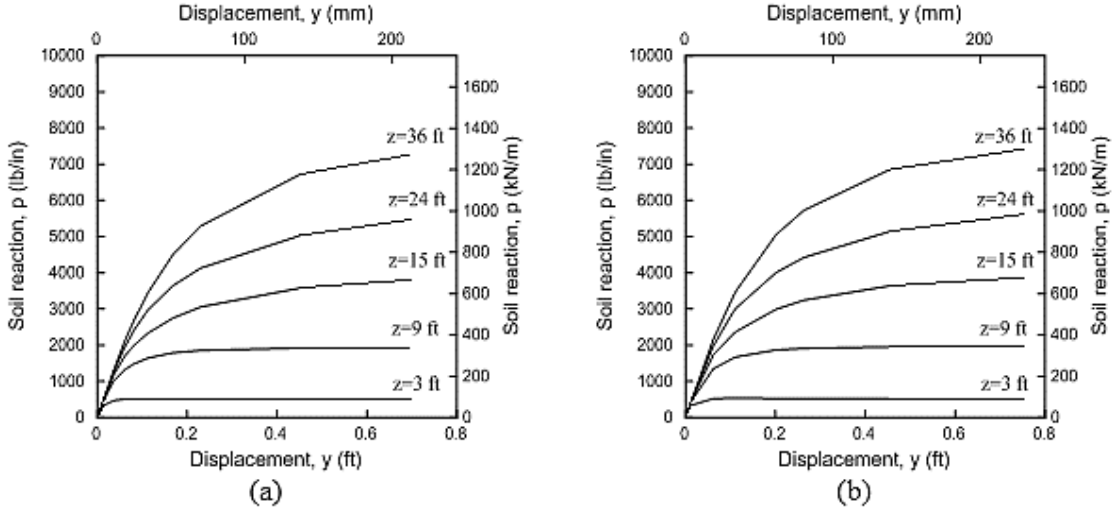

Figure 151. P-y curves for piles in sands with different μ values at depth: (a) x=12 ft. and (b) x=30 ft.

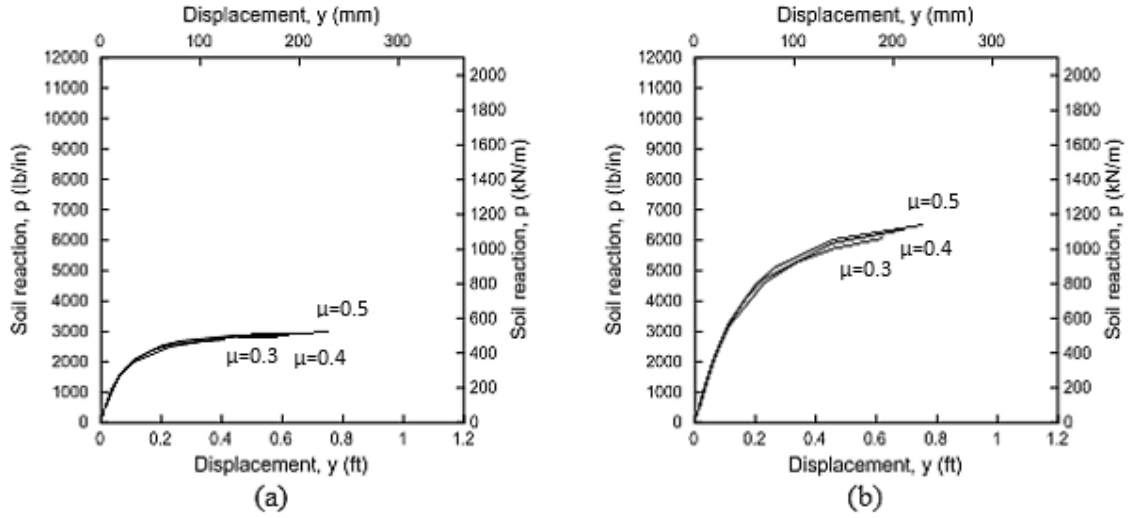

The ultimate soil resistance, p_u, and reference displacement, y_{ref}, were assumed to follow the following equations:

$$p_u = \alpha \times (z/L_0)^{n1} \times \tan^{n2}\varphi' \times (\gamma'/\gamma_w)^{n3} \times K^{n4} \times (D/L_0)^{n5} \quad [83]$$

$$y_{ref} = \beta \times (z/L_0)^{n6} \times (E_s/P_{atm})^{n7} \times \tan^{n8}\varphi' \times (\gamma'/\gamma_w)^{n9} \times K^{n10} \times (D/L_0)^{n11} \quad [84]$$

In developing the regression models for p_u and y_{ref}, the terms L_0 = 3.28 ft. (1 m), γ_w = 62.43 pcf (9.81 kN/m^3), and P_{atm} = 2116 psf (101 kPa) were added to make the equations dimensionless. K in the equation is the coefficient of lateral earth pressure. The results of regression analysis for equations 82, 83, and 84 reveals the following:

$$p = p_u \tanh\left(\left(\frac{2y}{y_{ref}}\right)^{0.66}\right) \quad [85]$$

$$p_u = 24044 \times (z/L_0)^{0.8} \times \tan^{1.2}\varphi' \times (\gamma'/\gamma_w)^{0.5} \times K^{0.8} \times (D/L_0) \quad [86]$$

$$y_{ref} = 117.6 \times (z/L_0)^{0.5} \times (E_s/P_{atm}) \times \tan^{1.4}\varphi' \times (\gamma'/\gamma_w)^{0.6} \times K^{0.9} \times (D/L_0)^{0.9} \quad [87]$$

Verification of the Developed p-y Model in Layered Sands

The developed model in equations 85 to 87 was verified using two different cases: increase in modulus of elasticity (E_s) of sands with depth, and sand layers with different E_s values.

Increasing Modulus of Elasticity (E_s) with Depth. In this case, the E_s value was increased from zero at the ground surface to different values [200,000; 500,000; 1,000,000; and 2,000,000 (psf)] at depth x = 54 ft. As can be seen from equation 86, the value of p_u does not change with E_s; while according to equation 87, the value of y_{ref} increases with increasing E_s. The comparison between the p-y curves obtained from finite element analysis and those from proposed p-y model are presented in Figure 152. As can be seen from the figure, the p-y model in equations 85 to 87 was able to accurately capture the results of finite element analysis.

Figure 152. Comparison between p-y curves from FE analysis and developed model for the case of increasing with depth

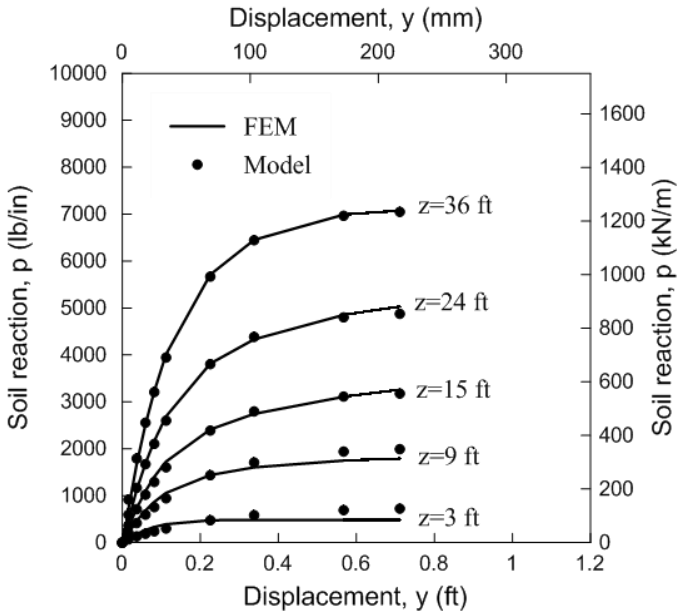

Sand Layers with Different E_s Values. For this case, the subsurface soil was divided into three layers (0 to 18 ft., 18 to 33 ft., and 33 to 54 ft.) with different E_s values. Two examples were considered. The first example consists of top and bottom sand layers with E_s = 1,000,000 psf and a middle layer with E_s = 200,000 psf. The second example consists of top and bottom sand layers with E_s = 200,000 psf and a middle layer with E_s = 500,000

psf. Figure 153a and Figure 153b present the comparison of the profiles of p_u with depth obtained using the FE analysis and the proposed p-y model for examples 1 and 2, respectively. The results show that the p-y model is able to predict the lateral behavior of piles in layered sand soils, accurately.

Figure 153. Comparison between FE analysis and developed model of p_u for piles in layered sands

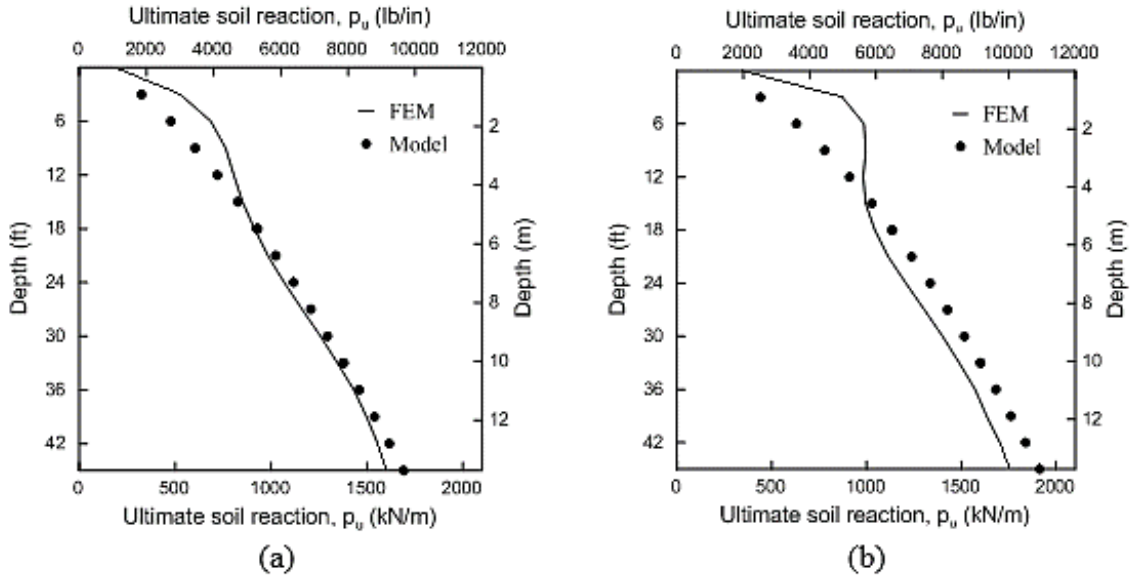

Model for Predicting p-y Curves in Dense Sands

The p-y model developed in this study can be used to predict the lateral behavior of piles in dense sands. In this case, the p-y model in equations 85 to 87 need to be used for two different values of friction angles: the peak friction angle, ϕ_{peak}, and the critical state friction angle, ϕ_{cs}. Using the values of ϕ_{peak} and ϕ_{cs} yield two different curves. Then a linear decrease from the upper curve at y_1 (related to ϕ_{peak}) to the lower one at y_2 (related to ϕ_{cs}) is added as shown in Figure 154. The values of y_1 and y_2 in the figure are suggested to be y_{ref} and $2y_{ref}$.

Figure 154. Schematic of p-y curve for dense sands

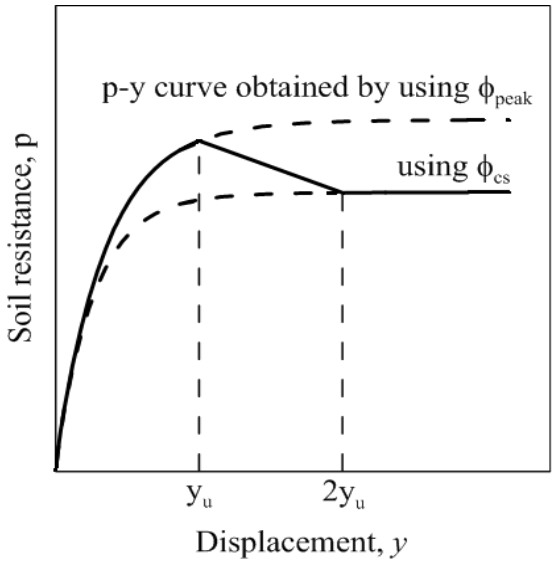

Developing Models for Estimating ε_{50} and Coefficient of Subgrade Reaction, k

Models for Estimating ε_{50}

Regression analyses were first performed on the collected UU test data from the material laboratory and LTRC geotechnical laboratory to evaluate any possible correlation between the different soil parameters and ε_{50}, as shown in the correlation matrix presented in Figure 155. It is obvious that γ_d, w (water content), e_o, PI, LL, LI, and S_u are correlated with ε_{50}. The correlation matrix suggests that LI can be an important correlated parameter, in addition to su and PI. Figure 156 presents the relationship between S_u and ε_{50} with the comparison with FHWA recommendation. The figure shows that the S_u versus ε_{50} correlation is more scattered for using the FHWA guidelines for estimating ε_{50}. On the figure, the purple dots representing samples with LI>1, which might suggest that using LI parameter can provide better criteria for categorizing the UU tests.

A regression model was developed between ε_{50} and S_u as shown in Figure 157. The proposed ε_{50}-S_u model can be summarized as follows:

For $S_u < 500$ psf: $\varepsilon_{50} = 2.5$ %

For $S_u > 2250$ psf: $\varepsilon_{50} = 0.7$ %

For 500 psf < S_u < 2250 psf:

$$\varepsilon_{50} = \frac{1150}{Su(psf)} + 0.19 \quad [88]$$

Another model was developed between ε_{50} and PI as shown in Figure 158, which is given as:

For PI > 25: ε_{50} = 0.7 %

For PI < 25:

$$\varepsilon_{50} = \frac{25}{10 + PI} \quad [89]$$

As shown in Figure 157 and Figure 158, there are large scatters between the developed ε_{50} models based on S_u and PI and the measured ε_{50} from UU tests.

Figure 155. Correlation matrix between soil parameters and ε_{50}

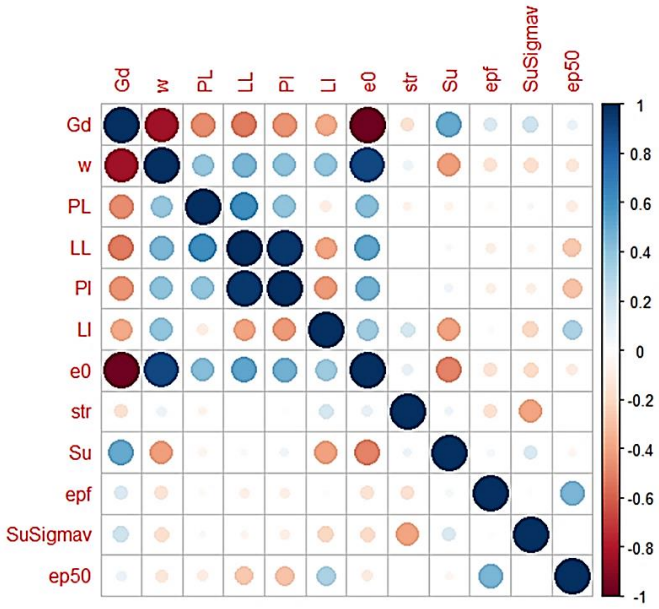

Figure 156. Su versus ε_{50} with comparison with FHWA recommendation

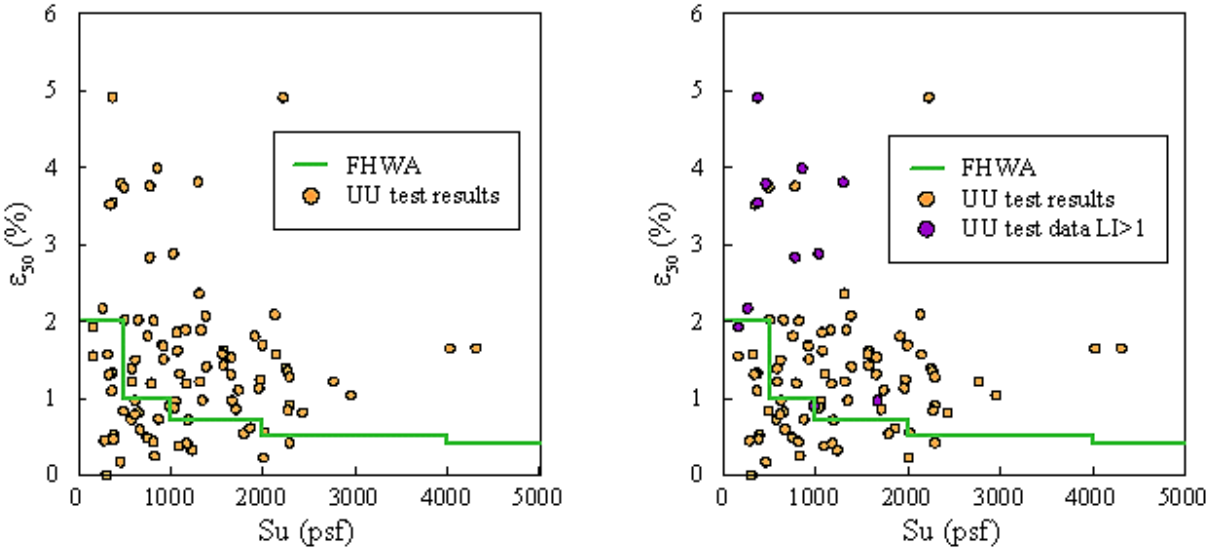

Figure 157. Proposed model for ε_{50} based on S_u

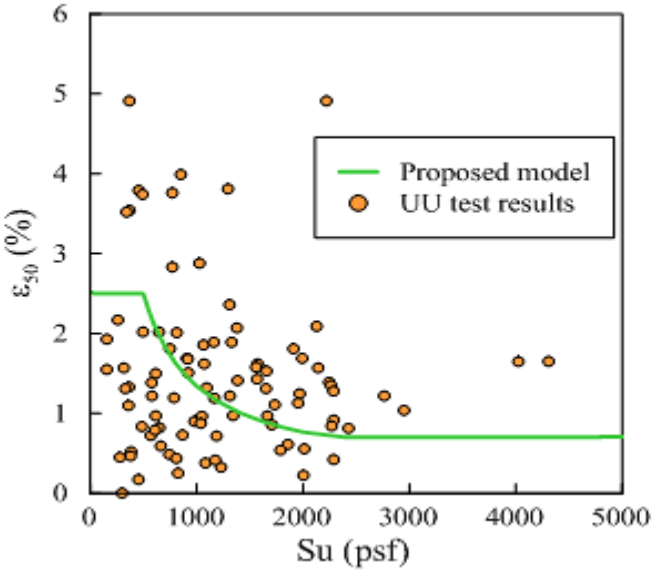

Figure 158. Proposed model for ε_{50} based on PI

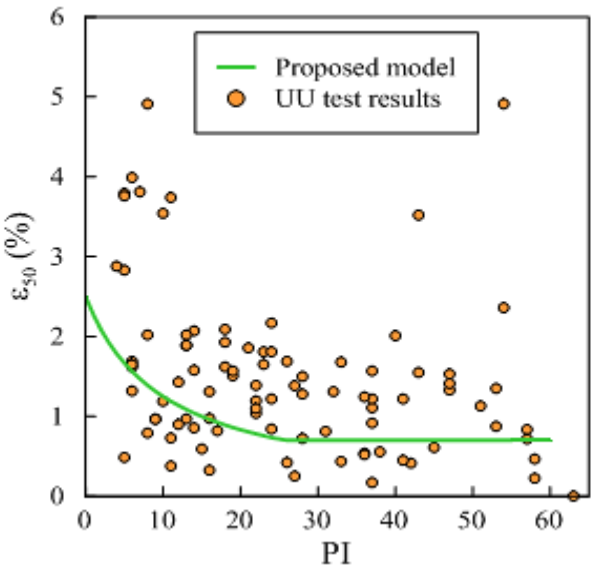

As stated earlier, it seems that LI is the most effective correlated parameter for estimating ε_{50}. The collected results from UU tests were divided into four different categories based on the value of LI as follows: (1) LI > 1, (2) 0.5 < LI < 1, (3) 0 < LI < 0.5, and (4) LI < 0. The correlations between ε_{50} and LI for the 4 different categories are presented in Figure 159.

Figure 159. Correlation between ε_{50} and LI

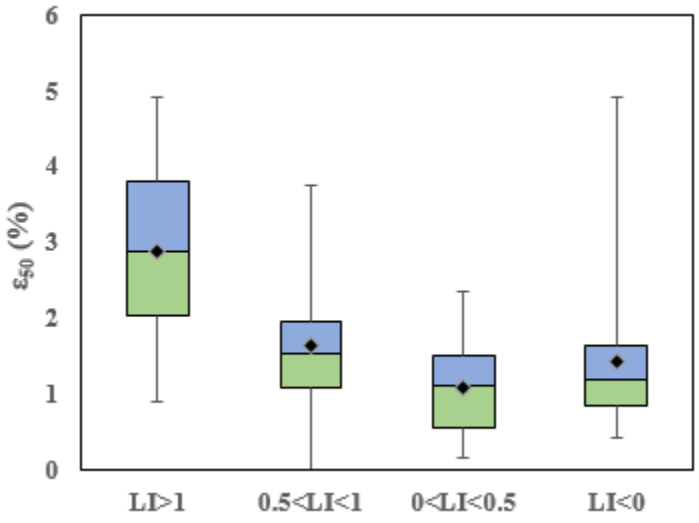

Table 19 summarized the statistical data of UU tests for ε_{50}-LI in Figure 159. Basically, the UU data show that: For LI > 1, ε_{50} ranges between 2 and 4%; for 0.5 < LI < 1, ε_{50} ranges between 1 and 2%; For 0 < LI < 0.5, ε_{50} ranges between 0.5 and 1.5%; and for LI < 0, ε_{50} ranges between 0.75 and 1.75%.

Conducting statistical t-tests between the different LI groups shows that groups 1 and 2, and groups 2 and 3 are different, but no difference between groups 3 and 4 (Table 19).

Table 19. The table for the above box-plot is shown here:

	LI>1	0.5<LI<1	0<LI<0.5	LI<0
Min	0.899	0.002	0.173	0.437
Q1	2.05	1.0845	0.556	0.858
Median	2.88	1.55	1.108	1.19
Mean	2.88	1.64	1.08	1.44
Q3	3.8	1.95	1.51	1.65
Max	4.91	3.76	2.36	4.91

Table 20. Results of t-test between LI groups

	G1 & G2	G2 & G3	G3 & G4
t-test (eq)	0.33%	0.33%	11.48%
t-test (uneq)	1.15%	1.54%	28.78%
Different group?	yes	yes	No

A general regression model was developed between ε_{50} and LI as shown in Figure 160. The model can be summarized as follows:

For LI < 0.28: $\varepsilon_{50} = 0.7$

For LI > 1: $\varepsilon_{50} = 2.5$

For 0.28 < LI < 1: $\varepsilon_{50} = 2.5.LI$

To find a better model for estimating ε_{50}, the UU test results in each LI category were studied separately. It should be noted here that many soil parameters including: w, PL, LL, w-LL, S_u/σ_v, and LI were studied. However, among these parameters the highest values of R^2 among all 4 categories were S_u and PI. Therefore, the following two models are proposed for estimating ε_{50} for each LI category:

Figure 160. Model for ε_{50} based on LI

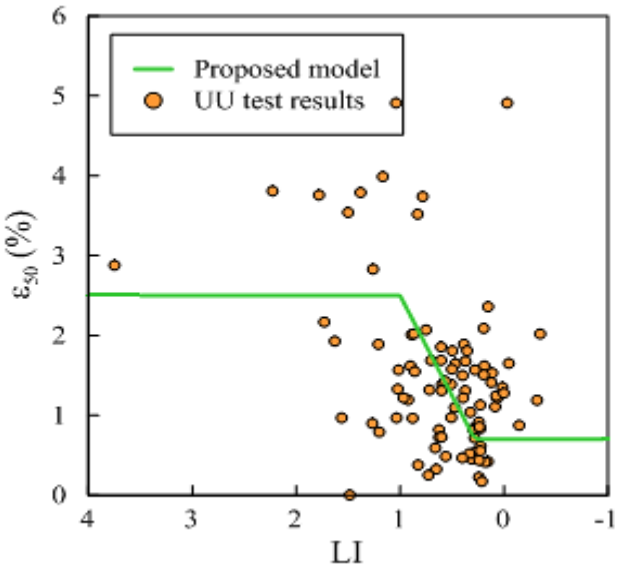

1) Model 1 based on Su (psf):

$$\varepsilon_{50} = \begin{cases} 2 < 3.54 - 0.0009S_u < 4 & LI > 1 \\ 1 < 1.77 - 0.0002S_u < 2 & 0.5 < LI < 1 \\ 0.5 < 0.87 + 0.0001S_u < 1.5 & 0 < LI < 0.5 \\ 0.75 < 0.86 + 0.0004S_u < 1.75 & LI < 0 \end{cases} \quad [90]$$

2) Model 2 based on PI:

$$\varepsilon_{50} = \begin{cases} 2 < 4 - 0.11(PI) < 4 & LI > 1 \\ 1 < 1.96 - 0.01(PI) < 2 & 0.5 < LI < 1 \\ 0.5 < 1.37 - 0.01(PI) < 1.5 & 0 < LI < 0.5 \\ 0.75 < 0.76 + 0.027(PI) < 1.75 & LI < 0 \end{cases} \quad [91]$$

Figure 161 and Figure 162 present the models for estimating ε_{50} based on S_u and PI, respectively, and LI category. For the cases when LI > 0.5, ε_{50} decreases with increasing S_u, and when LI < 0.5, ε_{50} increases with increasing S_u. However, when LI > 0, ε_{50} decreases with increasing PI, and when LI < 0, ε_{50} increases with increasing PI. It is difficult to explain such behavior.

The two models were compared with each other using the value of mean of square errors, MSE $= \frac{\sum diff^2}{n}$. For model 1, MSE = 0.668; while for Model 2, MSE = 0.612. This indicates that using Model 2 (based on PI and LI categories) gives better estimation of ε_{50}

than Model 1. It should be noted here that the value of MSE from using FHWA criteria equals to 1.372, which is very high.

Figure 161. Model 1 for ε_{50} based on S_u and LI category

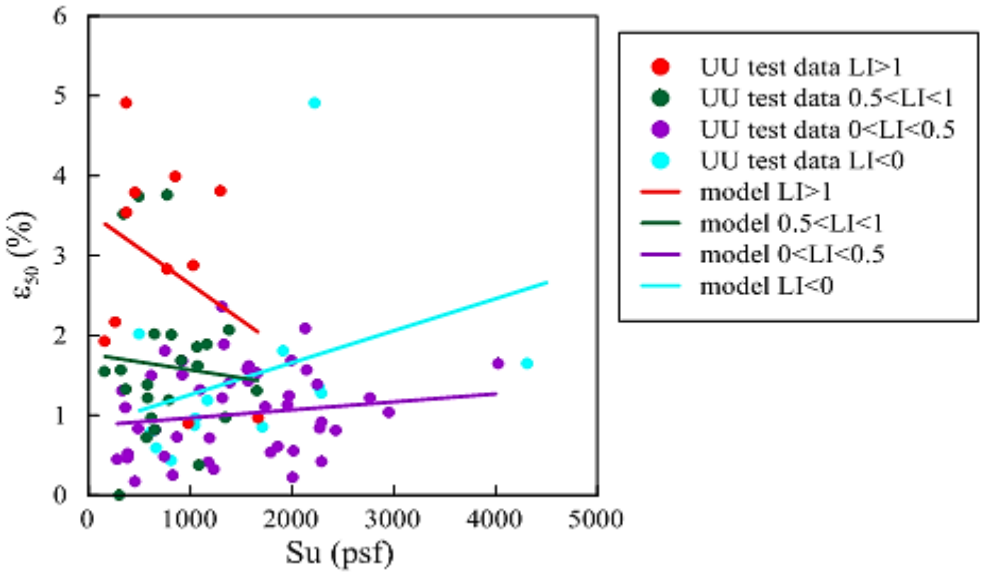

Figure 162. Model 2 for ε_{50} based on PI and LI category

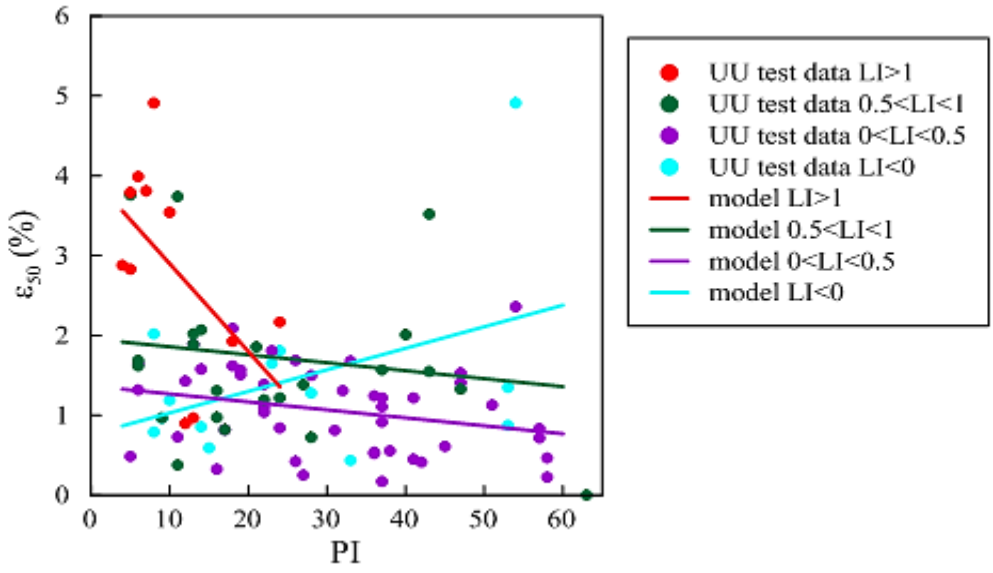

Models for Estimating k

Conducting FE analysis on sands with different parameters led to following equation for p-y curves in sands:

$$p = p_u \tanh\left(\left(\frac{2y}{y_{ref}}\right)^{0.66}\right) \quad [92]$$

With p_u and y_{ref} were defined earlier in equations 86 and 87. Knowing that the value of k is the initial slope of p-y curve, we can calculate k with good accuracy as follows:

$$\frac{\partial p}{\partial y}|_{y=0} = \frac{2p_u}{y_{ref}} \quad [93]$$

The use of Equation 93 and regression analysis on the results of FE parametric study of p-y curves on sand leads to the following equation to estimate the coefficient of subgrade reaction, k (in lb/in^3):

$$k = 0.017 \times E_s \times (z/z_{ref})^{0.3} \times \tan^{0.28}\varphi' \times (\gamma'/\gamma_w)^{0.65} \times K^{0.15} \times (D/D_{ref})^{-0.6} \quad [94]$$

where E_s in lb/in^2, Z and D in ft., z_{ref} = 3 ft., D_{ref} = 3 ft., and K is the coefficient of lateral earth pressure.

The elastic modulus for soil, E_s, can be estimated from results of SPT and CPT, relative density, D_r, or ϕ. It should be noted here that the value of k is dependent on E_s. E_s can be considered as a constant per soil layer, or linearly increasing with depth along the soil layer.

Schmertman [123] proposed the following correlation to estimate E_s from the cone tip resistance, q_c, as:

$$E_s = n \,.\, q_c \quad [95]$$

where n = 2.5-3.5 for young normally consolidated clean sand, n = 3.5-6 for aged normally consolidated clean sand, n = 6-10 for overconsolidated clean sand, n = 1.5 for normally consolidated silty or clayey sands, and n = 3 for overconsolidated silty or clayey sands.

Several correlations were developed between E_s and the standard penetration N_{60}. However, these values are not as accurate as E_s from CPT data [124]. The following relationship can be used to evaluate E_s from N_{60}, which gives approximate conservative values [124]:

$$E_s = \beta_0\sqrt{OCR} + \beta_1 N_{60} \quad [96]$$

where β_0 and β_1 are correlation factors. The value of β_0 = 100,000 lb/ft.^{2} for clean sand (SW and SP), and β_0 = 50,000 lb/ft.^{2} for silty sands and clayey sand (SM and SC); and the value of β_1 = 24,000 lb/ft.^{2} for clean sand (SW and SP), and β_1 = 12,000 lb/ft.^{2} for silty sands and clayey sand (SM and SC).

To simplify the estimation of the coefficient of subgrade reaction, k, for use in p-y curves of sands, the values of k were presented in Table 21 and Figure 163 as a function of the angle of internal friction, ϕ, for sand.

Table 21. Suggested values for coefficient of subgrade reaction, k

Soil Type	Friction Angle, ϕ	Soil Condition Relative to Water Table	Coefficient of Subgrade Reaction, k (pci)	Recommended FHWA k Values
Very loose sand	< 28	Above	< 40	< 25
Very loose sand		Submerged	< 25	< 20
Loose sand	28 - 32	Above	40	25
Loose sand		Submerged	25	20
Medium dense sand	32 - 38	Above	130	90
Medium dense sand		Submerged	85	60
Dense sand	38 – 42	Above	235	225
Dense sand		Submerged	150	125
Very dense sand	> 42	Above	> 235	> 225
Very dense sand		Submerged	> 150	> 125

Figure 163. Coefficient of subgrade reaction, k, versus friction angle, ϕ

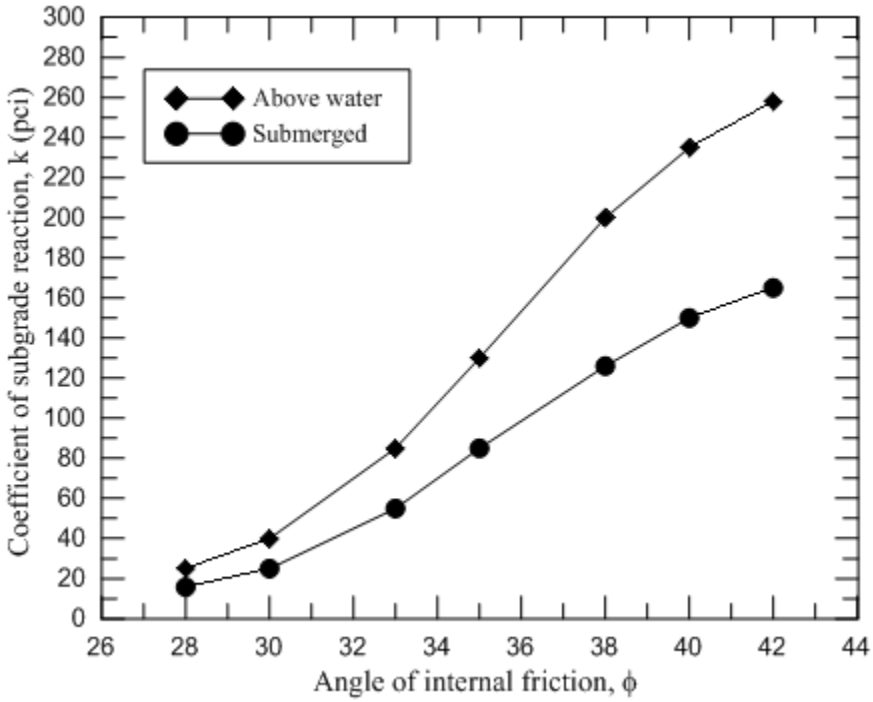

Summary and Conclusions

Summary

In this study, the finite element (FE) modeling was used to investigate the behavior of pile groups under lateral loading. The nonlinear behavior of soils was incorporated using nonlinear constitutive models. The pile-soil interface was modeled using the zero-thickness surface-surface interaction, which provided the capability for modeling the gap behind the piles, and the transfer of interface normal and frictional stresses. The group interaction was incorporated through the interaction of stress fields around the piles. The lateral behavior of three pile group (PG) configurations (vertical, battered, mixed) with a similar number of piles were evaluated under static and dynamic loading conditions. The full-scale lateral load test that was conducted at the M19 eastbound pier foundation of the I-10 Twin Span Bridge was used to verify the FE models. A FE was conducted to investigate the effect of pile spacing and clay soil type on the performance of pile groups.

The developed p-multipliers averaged over the displacement for the vertical, battered, and mixed pile groups are presented in the following tables.

Table 22. Average p-multipliers for vertical PG at depth z/D=4.6

	Row			
Column	L	ML	MT	T
1	0.73	0.49	0.48	0.59
2	0.51	0.32	0.34	0.44
3	0.49	0.30	0.32	0.42
Row average	0.58	0.37	0.38	0.48

Table 23. Average p-multipliers for battered PG at depth z/D=4.6

	Row			
Column	L	ML	MT	T
1	0.89	0.81	0.62	0.77
2	0.67	0.60	0.46	0.61
3	0.64	0.55	0.43	0.58
Row average	0.73	0.65	0.51	0.65

Table 24. Average p-multipliers for mixed PG at depth z/D=4.6

	Row			
Column	L	ML	MT	T
1	0.87	0.54	0.57	0.61
2	0.63	0.37	0.39	0.47
3	0.61	0.35	0.37	0.44
Row average	0.70	0.42	0.44	0.51

The results of p-multipliers versus spacing (averaged per row) are presented in Figure 164; while the effect of clay soil type on p-multipliers (averaged per row) in the pile groups are shown in Figure 165.

Figure 164. Effect of pile spacing on p-multipliers for vertical, battered, and mixed pile groups

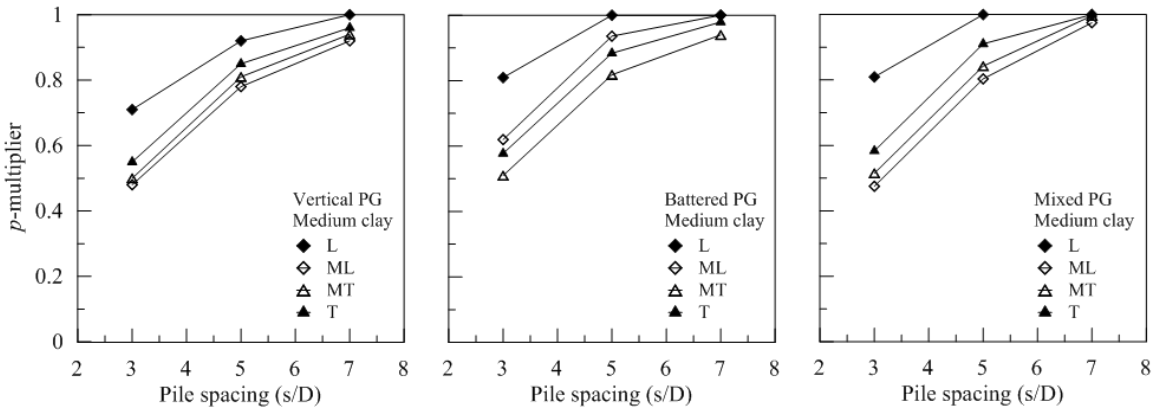

The contribution of axial reaction per pile versus the group lateral load (F_{axial}/H_{PG}) is presented in Figure 166. The influence of pile cap displacement on the normalized axial reaction of piles (F_{axial}/H_{PG}) is presented in Figure 167, and the effect of pile spacing on the normalized axial reaction (F_{axial}/H_{PG}) is depicted in Figures 168 and 169.

The distribution of normalized lateral load per pile (H_{pile}/H_{PG}) for the three PGs presented in Figure 170.

Figure 165. Effect of clay soil type on p-multipliers for vertical, battered, and mixed pile groups

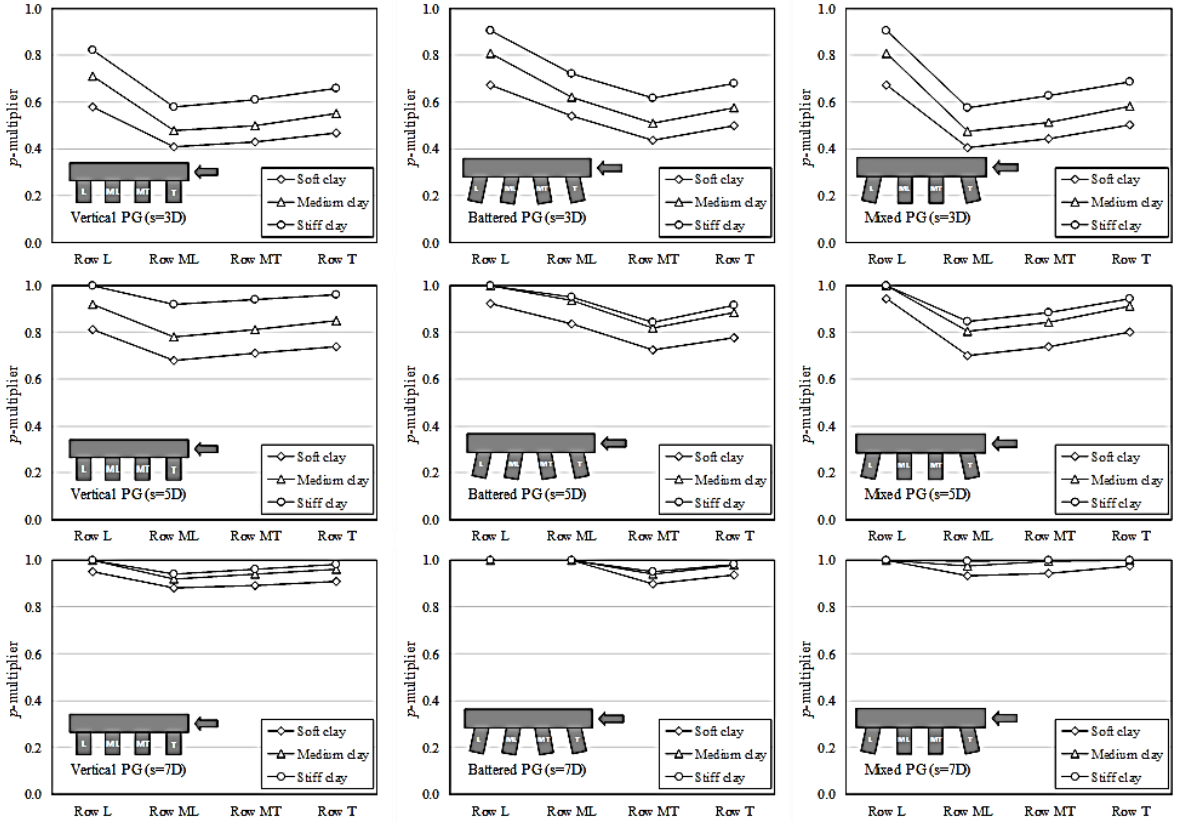

Figure 166. Variation of the axial reaction in the piles

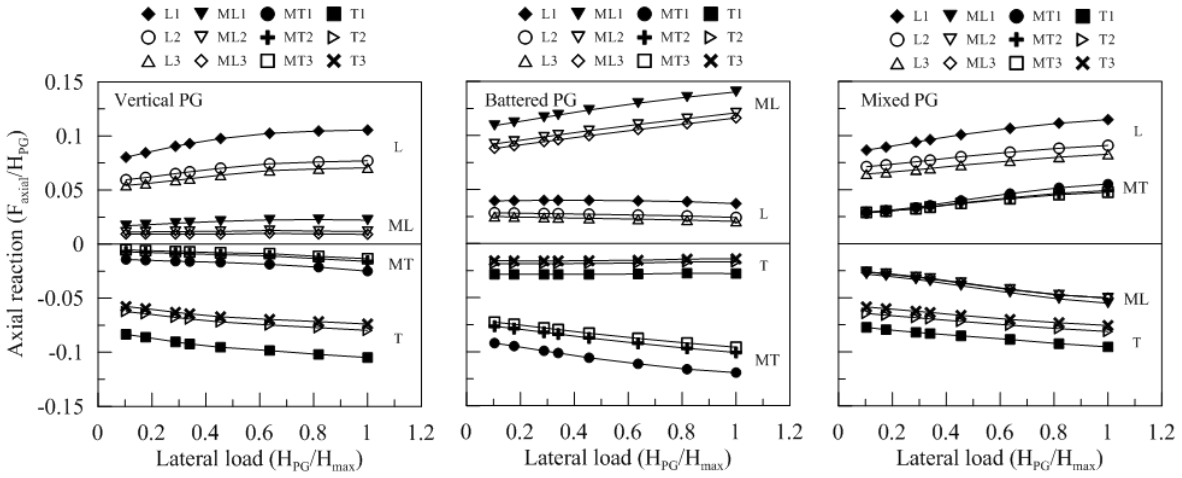

Figure 167. Effect of pile cap displacement on axial reaction

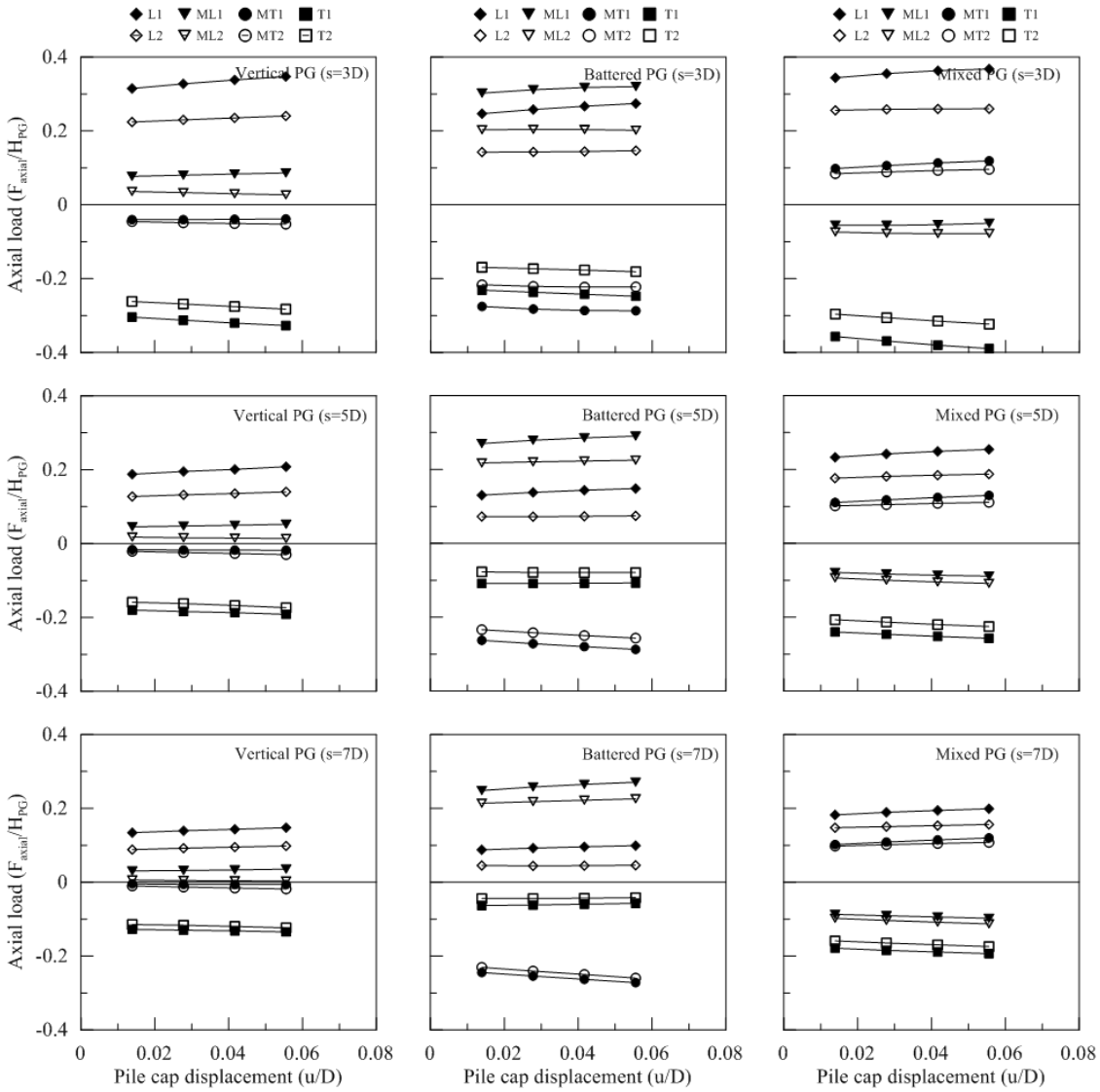

Figure 168. Effect of pile spacing on normalized axial reaction per pile

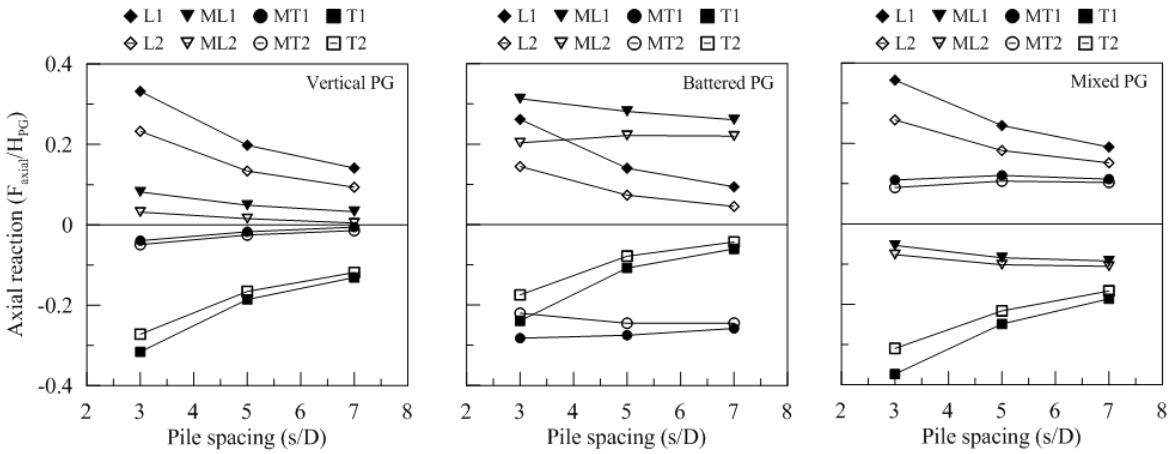

Figure 169. Effect of pile spacing on normalized axial reaction per row

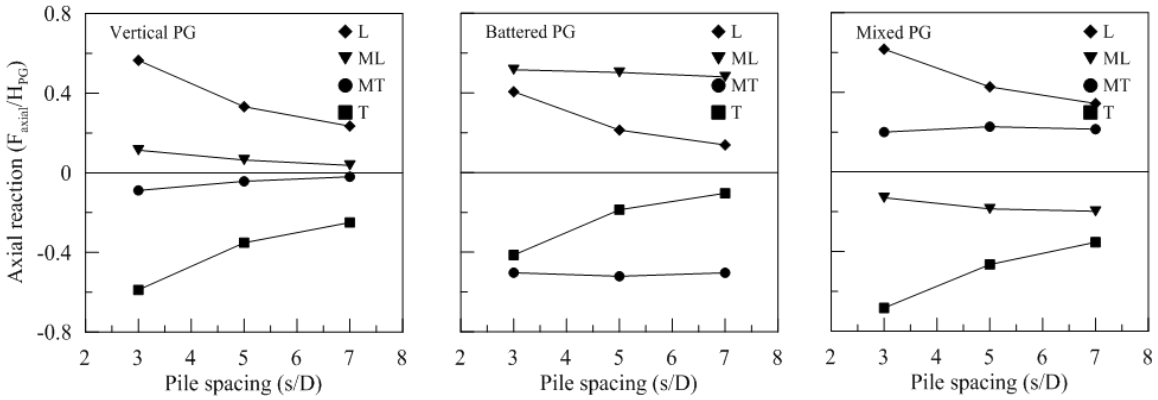

Figure 170. Comparison of the lateral load distribution

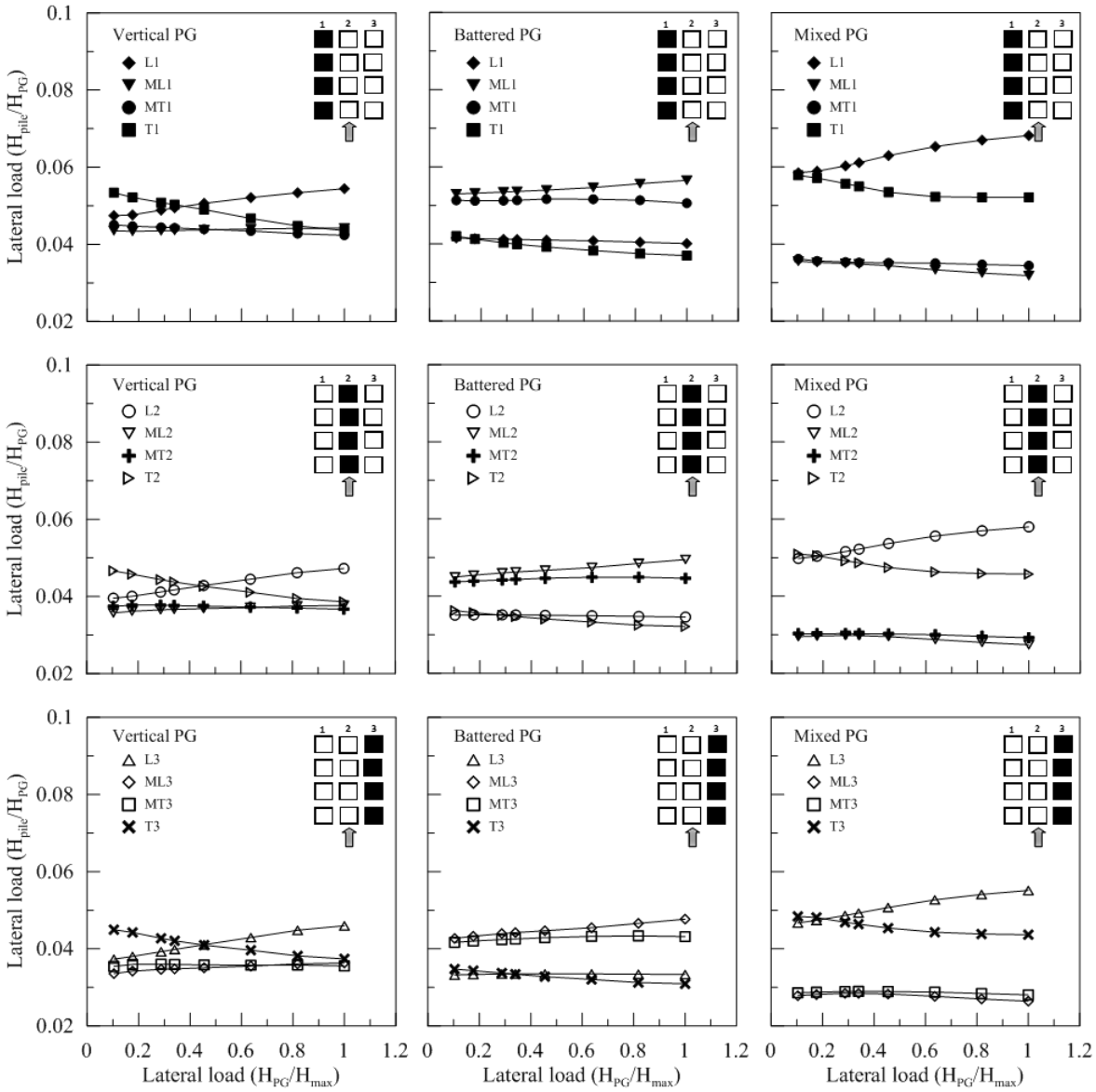

The effect of barge speed impact on the piles' peak lateral displacement, the piles' peak shear force, the distribution of shear force per row, the contribution of piles and pier columns to the total resisting force, and ratio of axial force per row, and the contribution of piles' peak axial force for the different PG configurations are presented in Figures 171, 172, 173, 174, 175, and 176, respectively.

Figure 171. Peak displacement at different barge speeds

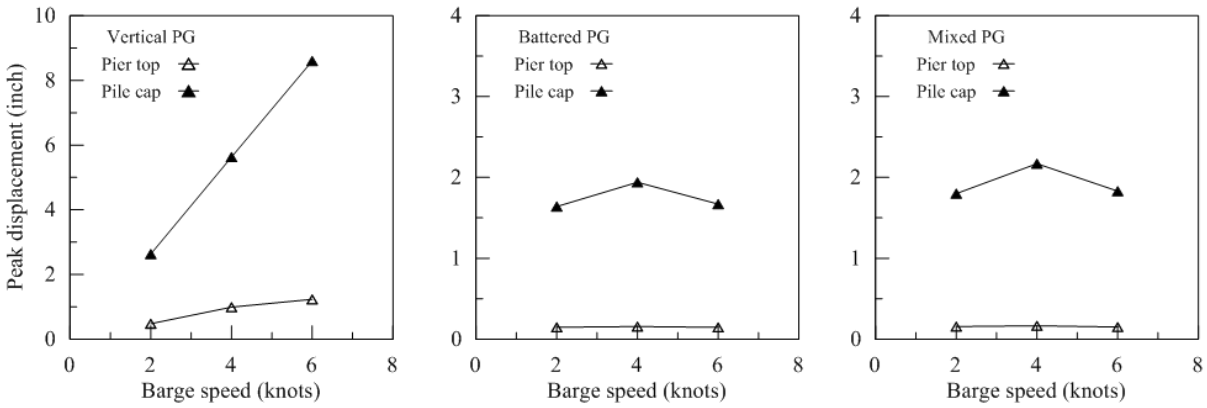

Figure 172. Results of peak shear versus barge speed

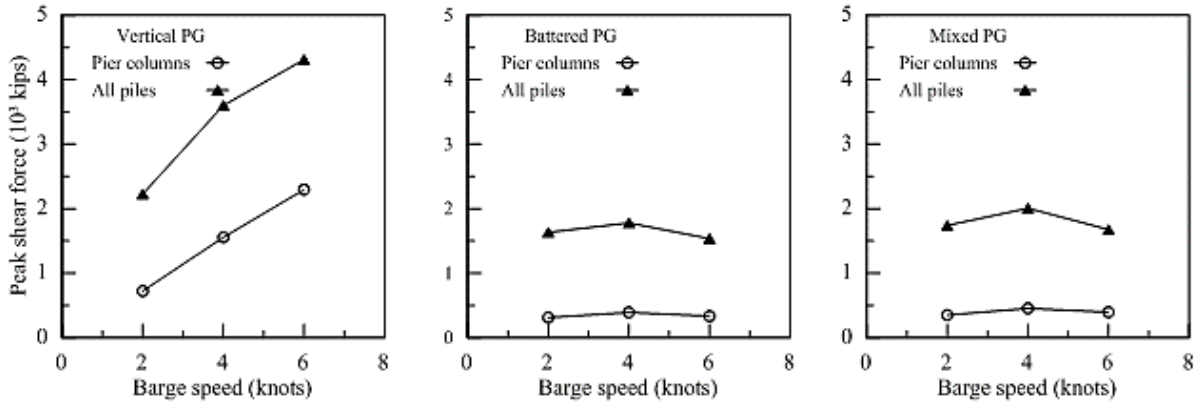

Figure 173. Distribution of shear force per row

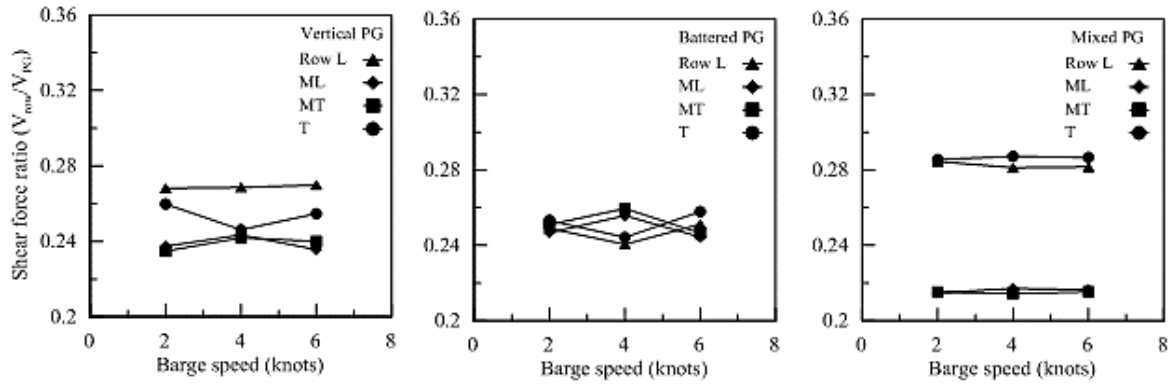

Figure 174. Contribution of piles and pier columns in the resisting force

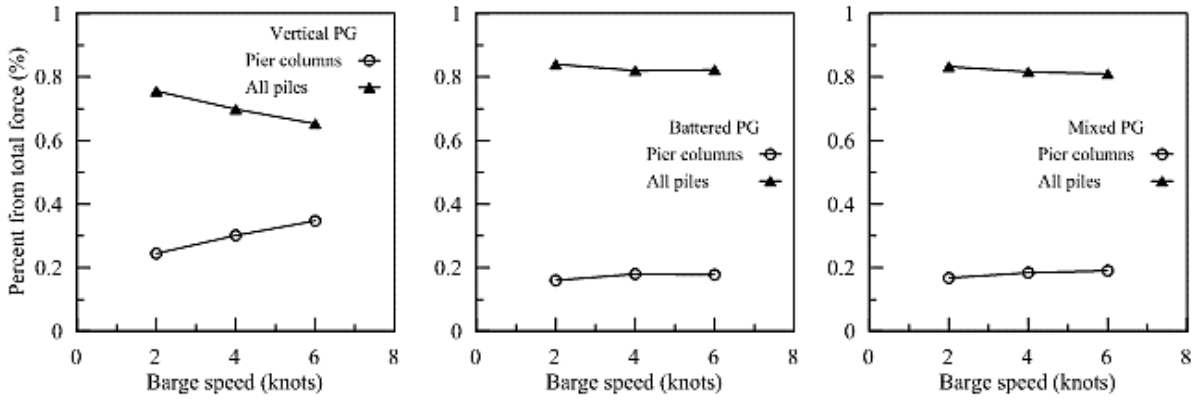

Figure 175. Summary of axial force ratio per row

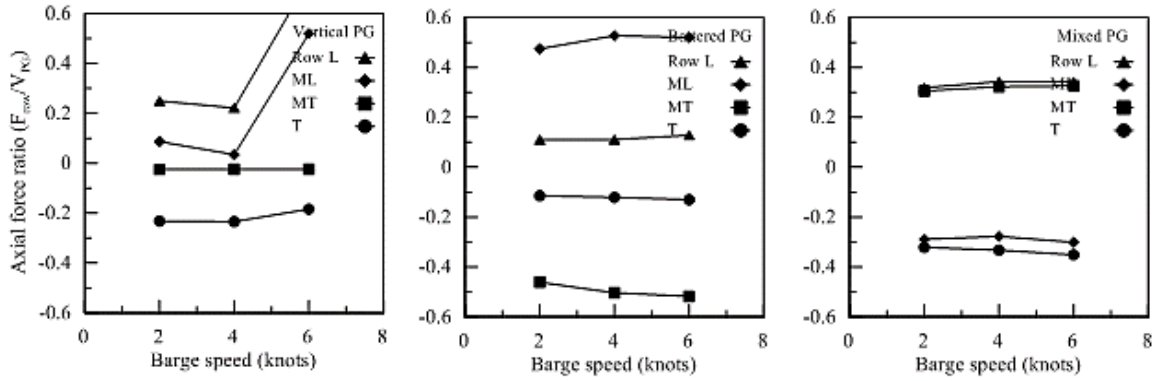

The effect of non-centric barge impact on the peak lateral displacement, peak shear force, and the contribution of piles and pier columns to the resisting force, are presented in Figures 177, 178, and 179, respectively.

Figure 176. Summary of piles' peak axial force ratio

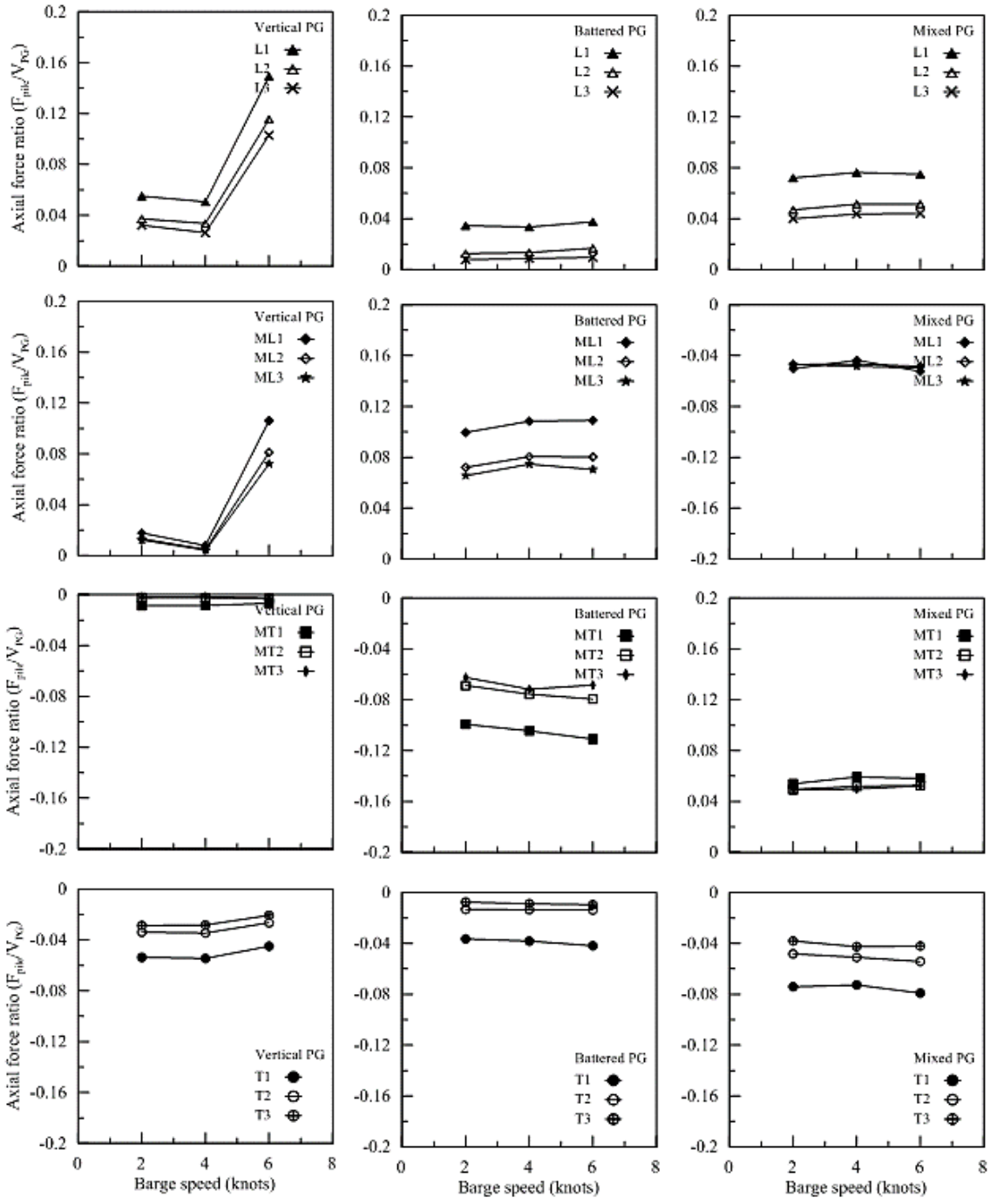

Figure 177. Comparison of peak displacement results for centric and non-centric impacts

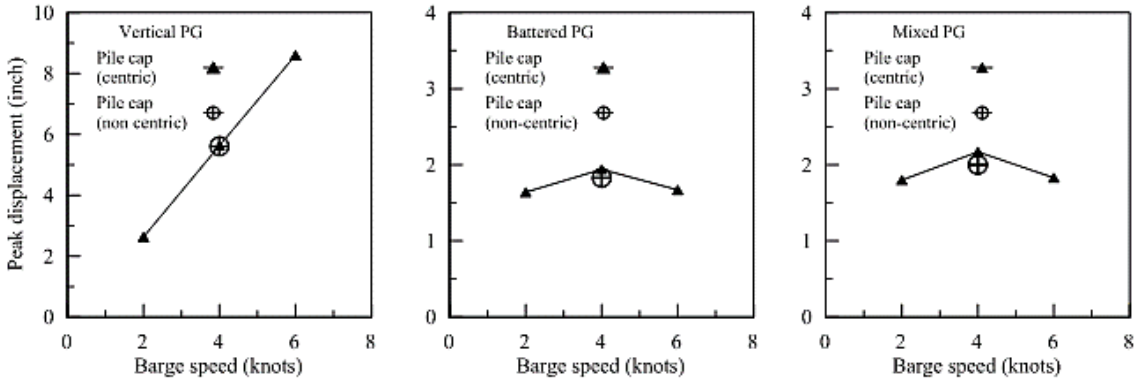

Figure 178. Comparison of peak shear force for centric and non-centric impacts

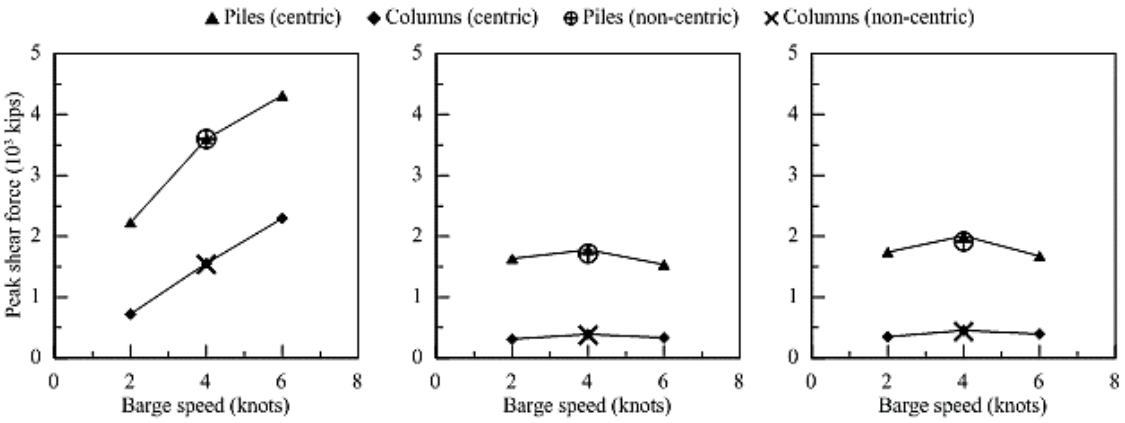

Figure 179. Contribution of piles and pier columns to the resisting force in centric and non-centric impacts

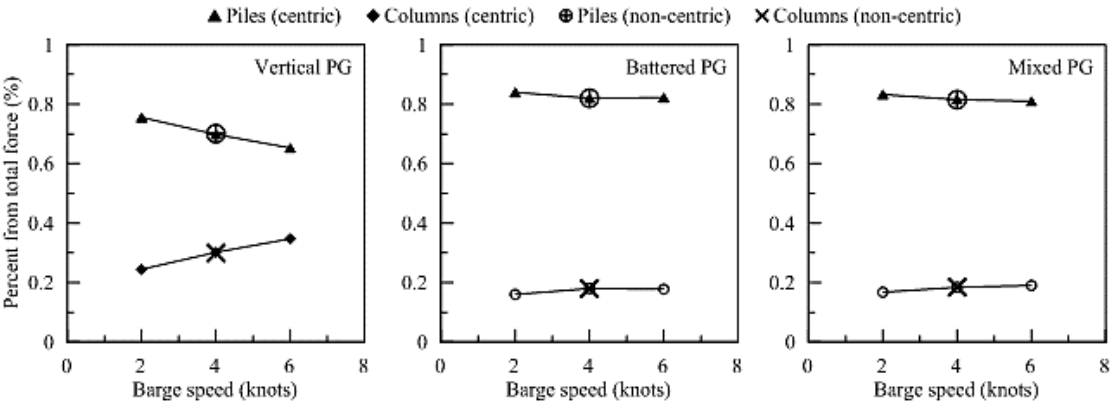

3D FE parametric studies were performed to develop models to evaluate the p-y curves for clayey and sandy soils using tangent hyperbolic models based on soil and pile properties. Regression analyses were performed on the results of FE parametric study to develop formulas for evaluating the lateral bearing capacity factor (N_p) with depth and reference displacement of p-y curve (y_{50}) in clay soils. A combination of tangent hyperbolic and power function model was developed to evaluate the p-y curves in sandy soils based soil and pile properties.

The results of FE parametric study on lateral loading of piles in clayey soils in combination with the nonlinear regression analyses were used to develop the following nonlinear tangent hyperbolic model for p-y curve in clayey soils:

$$p = 1.11 p_u \tanh(0.49 \left(\frac{y}{y_{50}}\right)^{0.89}) \quad [97]$$

where

$$p_u = N_p S_u D \quad [98]$$

$$y_{50} = 0.5\ D\ N_p \varepsilon_{50} \quad [99]$$

The value of N_p can be calculated based on the depth (z) below surface with respect of pile width (D) as follows:

1. For depth range of ($0 < z < 2D$), N_p increases nonlinearly with depth starting at a value of about 2.0 for smooth piles ($\mu = 0.0$), as given by the following equation:

$$N_p \left(\frac{z}{D}\right) = N_{po} + k \left(\frac{z}{D}\right)^n \quad [100]$$

$$k = 0.82 \frac{\bar{\gamma}' D}{\overline{S_u}} + 1.95 \quad [101]$$

$$n = 0.13 \frac{\bar{\gamma}' D}{\overline{S_u}} + 0.6 \quad [102]$$

For non-smooth piles ($\mu > 0$), the values of N_{po} and the k parameter increase when μ increases, as follows:

$$N_{po} = 2.0 + 0.6\mu \quad [103]$$

$$k_{(\mu)} = k_{(0)} + (1 - \exp[-0.71\mu]) \quad [104]$$

where $k_{(0)}$ is the value of k for $\mu = 0$ obtained using equation 101.

2. For the depth range ($2D < z < Z_c$), N_p increases linearly with depth until it reaches the upper-bound limit, N_{pu}. The N_p model for the linear zone ($2D < z < Z_c$) can be evaluated using the following equation:

$$N_p\left(\frac{z}{D}\right) = N_{p_{@z/D=2}} + \frac{\gamma' D}{S_u}\left(\frac{z}{D} - 2\right) \leq N_{pu} \quad [105]$$

where $N_{p@z/D=2}$ is the N_p value at depth $z/D = 2$ obtained from equation 100, N_{pu} is the upper-bound limit for N_p.

The N_p value continues to increase with depth until it reaches the upper bound limit N_{pu} at the critical depth (Z_c). The value of Zc (for smooth piles only ($\mu = 0$)) were found to correlate with $(\gamma' D)/S_u$ as follows:

$$\frac{Z_c}{D} = \frac{5.36}{\gamma' D/S_u} \quad [106]$$

3. For non-smooth piles ($\mu > 0$), N_p increases at higher rate within the shallow depth ($0 < z < 2D$). For depths $z > 2D$, N_p increases at the same rate regardless of μ value. The depth at which N_{pu} is reached increased slightly at higher μ due to higher N_{pu} value corresponding to the value of μ. The value of the upper-bound limits N_{pu} are 9.2, 10.8, and 11.94 for the μ values of 0.0, 0.5, and 1.0 respectively.

Figure 180 presents the characteristics of N_p variation as a function of the normalized depth, (z/D).

Figure 180. General characteristics of N_p variation used for model development

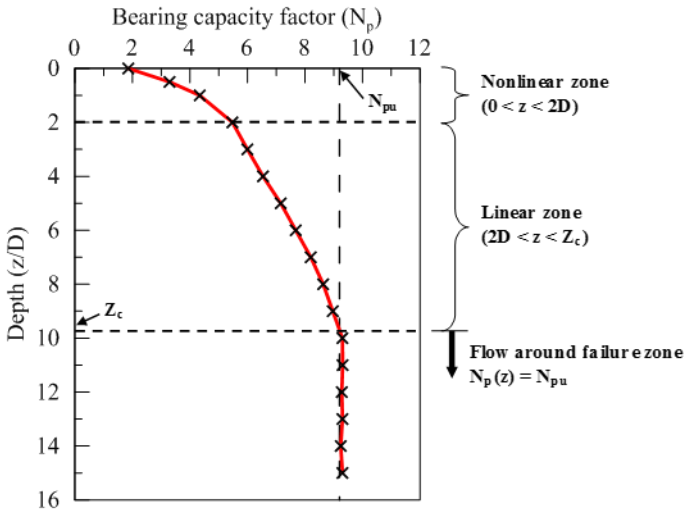

The results of FE parametric study on lateral loading of piles in sandy soils in combination with the nonlinear regression analyses were used to develop the following nonlinear tangent hyperbolic model for p-y curve in sandy soils:

$$p = p_u \tanh\left(\left(\frac{2y}{y_{ref}}\right)^{0.66}\right) \quad [107]$$

$$p_u = 24044 \times (z/L_0)^{0.8} \times \tan^{1.2}\phi' \times (\gamma'/\gamma_w)^{0.5} \times K^{0.8} \times (D/L_0) \quad [108]$$

$$y_{ref} = 117.6 \times (z/L_0)^{0.5} \times (E_s/P_{atm}) \times \tan^{1.4}\phi' \times (\gamma'/\gamma_w)^{0.6} \times K^{0.9} \times (D/L_0)^{0.9} \quad [109]$$

where z = depth, L_o = 3.28 ft. (1 m), ϕ'= effective friction angle of sand, γ' = effective unit weight of sand, γ_w = water unit weight, K = coefficient of lateral earth pressure, D = pile width, and E_s = modulus of elasticity of sands.

The results of laboratory UU tests were used to develop correlations to estimate the strain at 50% stress level (ε_{50}) based on soil properties (i.e., Su, PI, LI). A regression model was developed between ε_{50} and undrained shear strength, S_u, as shown in Figure 181. The proposed ε_{50}-S_u model can be summarized as follows:

For S_u < 500 psf: ε_{50} = 2.5 %

For $S_u > 2250$ psf: $\varepsilon_{50} = 0.7$ %

For 500 psf < S_u < 2250 psf: $\varepsilon_{50} = \frac{1150}{Su(psf)} + 0.19$

Figure 181. Proposed model for ε_{50} based on S_u

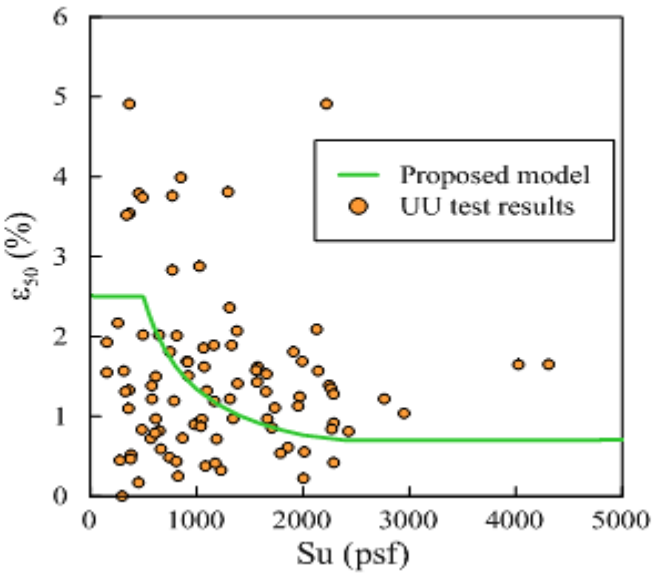

Another model was developed between ε_{50} and PI as shown in Figure 182, which is given as follows:

For PI > 25: $\varepsilon_{50} = 0.7$ %

For PI < 25: $\varepsilon_{50} = \frac{25}{10+PI}$

A general regression model was developed between ε_{50} and LI as shown in Figure 183. The model can be summarized as follows:

For LI < 0.28: $\varepsilon_{50} = 0.7$

For LI > 1: $\varepsilon_{50} = 2.5$

For 0.28 < LI < 1: $\varepsilon_{50} = 2.5.LI$

Figure 182. Proposed model for ε_{50} based on PI

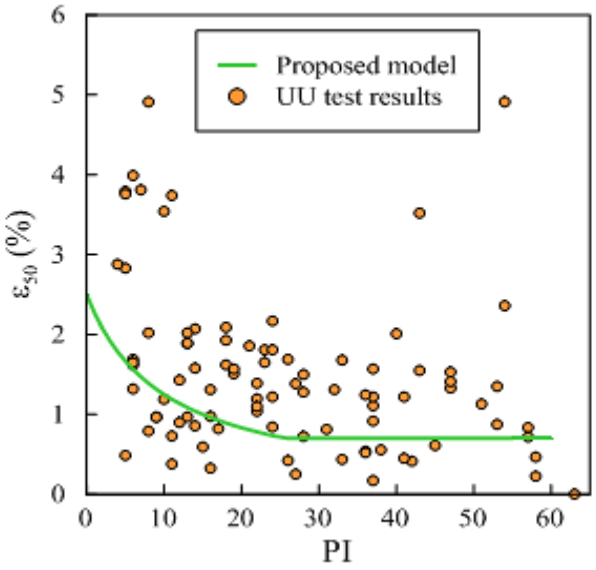

The UU test results were divided into 4 LI categories (LI < 0, 0 < LI < 0.5, 0.5 < LI < 1, and LI > 1), and regression models were developed between ε_{50} and S_u and PI for each LI category as shown in Figure 184 and Figure 185, respectively. The two models are presented in the following equations:

Model 1 based on Su (psf):

$$\varepsilon_{50} = \begin{cases} 2 < 3.54 - 0.0009S_u < 4 & LI > 1 \\ 1 < 1.77 - 0.0002S_u < 2 & 0.5 < LI < 1 \\ 0.5 < 0.87 + 0.0001S_u < 1.5 & 0 < LI < 0.5 \\ 0.75 < 0.86 + 0.0004S_u < 1.75 & LI < 0 \end{cases}$$

Model 2 based on PI:

$$\varepsilon_{50} = \begin{cases} 2 < 4 - 0.11(PI) < 4 & LI > 1 \\ 1 < 1.96 - 0.01(PI) < 2 & 0.5 < LI < 1 \\ 0.5 < 1.37 - 0.01(PI) < 1.5 & 0 < LI < 0.5 \\ 0.75 < 0.76 + 0.027(PI) < 1.75 & LI < 0 \end{cases}$$

Figure 183. Model for ε_{50} based on LI

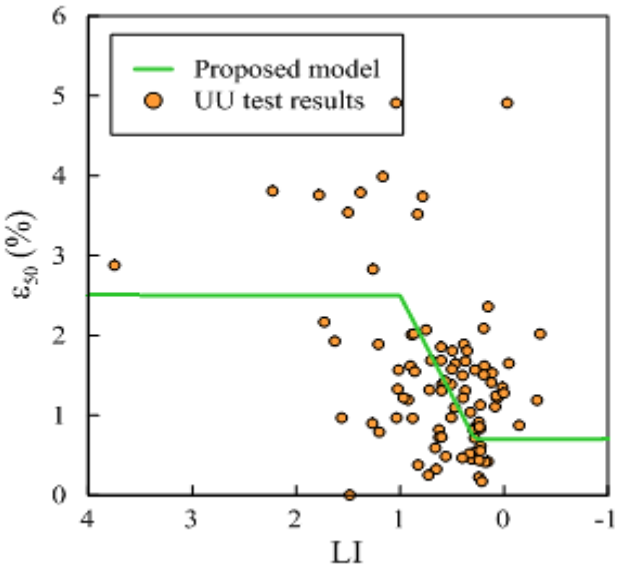

Figure 184. Model 1 for ε_{50} based on S_u and LI category

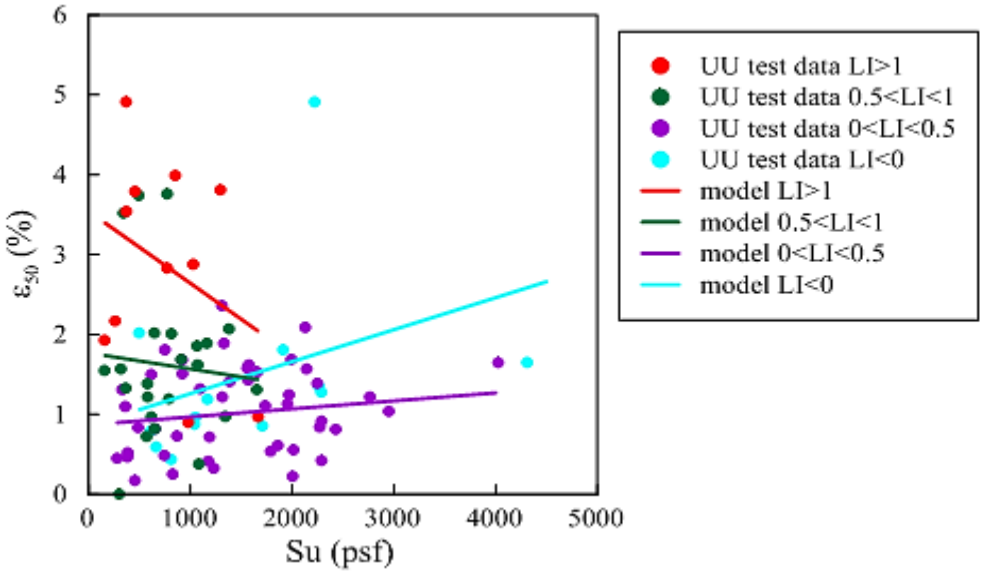

Figure 185. Model 2 for ε_{50} based on PI and LI category

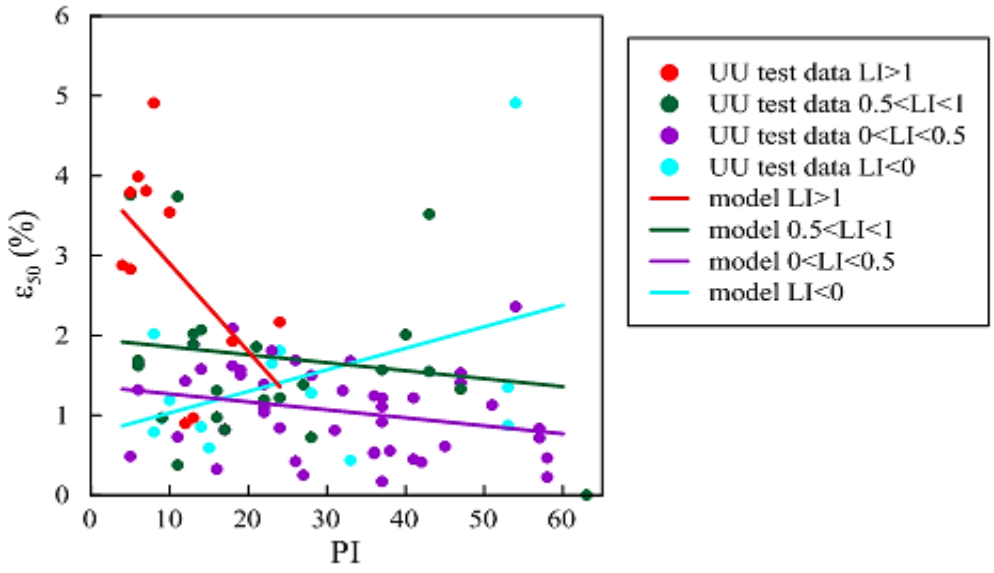

The results of FE parametric study for p-y curve in sand were analyzed to develop a formula to estimate the coefficient of subgrade reaction (k) based on soil and pile properties. The following equation was developed to estimate the coefficient of subgrade reaction, k (in lb/in^3):

$$k = 0.017 \times E_s \times (z/z_{ref})^{0.3} \times \tan^{0.28}\varphi' \times (\gamma'/\gamma_w)^{0.65} \times K^{0.15} \times (D/D_{ref})^{-0.6} \quad [110]$$

where E_s in lb/in^2, Z and D in ft., Z_{ref} = 3 ft., D_{ref} = 3 ft., and K is the coefficient of lateral earth pressure.

For simplification, the estimation of k for different sand consistency, soil condition and friction angle were presented in Table 25 and Figure 186.

Table 25. Suggested values for coefficient of subgrade reaction, k

Soil Type	Friction Angle, ϕ	Soil Condition Relative to Water Table	Coefficient of Subgrade Reaction, k (pci)	Recommended FHWA k Values
Very loose sand	< 28	Above	< 40	< 25
Very loose sand		Submerged	< 25	< 20
Loose sand	28 - 32	Above	40	25
Loose sand		Submerged	25	20
Medium dense sand	32 - 38	Above	130	90
Medium dense sand		Submerged	85	60
Dense sand	38 – 42	Above	235	225
Dense sand		Submerged	150	125
Very dense sand	> 42	Above	> 235	> 225
Very dense sand		Submerged	> 150	> 125

Figure 186. Coefficient of subgrade reaction, k, versus friction angle, ϕ

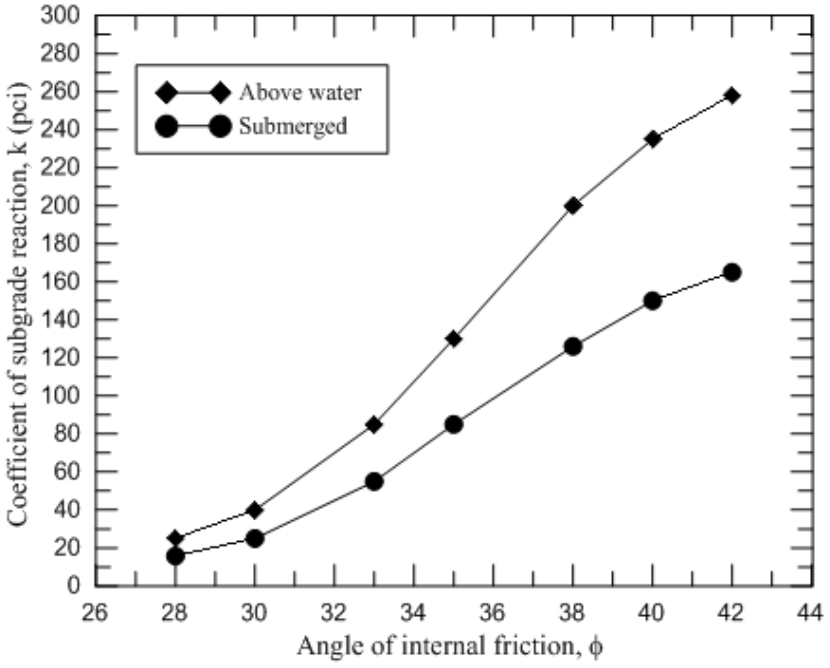

Conclusions

Based on the findings of this study, the following conclusions can be made:

- The use of FE modeling is a viable alternative to experimental testing for studying the lateral behavior of pile groups comprehensively. The comparison between the results of FE analyses and the field measurements (lateral displacements and moments) during the lateral load test at the M19 eastbound pier I-10 of the Twin Span Bridge were in good agreement.
- The comparison between the different pile group configurations showed that the battered pile group had the largest lateral stiffness followed by the mixed and vertical pile groups. The improvement of lateral stiffness relative to the vertical pile group was 120% for the battered pile group and 50% for the mixed pile group.
- The lateral load distribution in the pile group rows differed in each configuration. In the vertical pile group, the first (leading) row carried 30%, while it was 23.3% in each of the remaining rows. In the battered pile group, the percentage was equal in the first and fourth rows at 22%, while it was higher in the middle rows (second and third) at 28%. In the mixed pile group, the percentage was 36% in the first row, 18% in the second and third rows, and 28% in the fourth row.
- The lateral load generated significant axial reactions in the piles in which the row percentage differed in each configuration. The mixed pile group generated the highest percentage of axial force followed by the battered and vertical pile groups. In the vertical pile group, the average axial force ratio (relative to the lateral load) per pile was 8.5% in the first and fourth rows and 1.5% in the second and third rows. In the battered pile group, the axial force ratio was 2.5% in the first and fourth rows, whereas it was 12.5% in the second and third rows. In the mixed pile group, the first and fourth rows had axial force ratio of 9.6%, whereas the second and third rows had 5%. It was noticed that each row in the pile group coupled with its mirror row so that the axial reaction magnitude was similar in the two rows but with opposite sign.
- The results of bending moment showed that the vertical pile group generated higher bending moment at the bottom of pile cap as compared to the battered and mixed pile groups under the same lateral load. In addition, the bending moment was increased linearly with pile cap displacement in the vertical pile group. The mixed pile group had the second highest bending moment with linearly increasing trend. The battered pile group had the lowest bending moment values with fairly constant magnitude.

- The results of soil resistance showed that the shape of soil resistance profiles is closely similar for all piles in a pile group, but they differ between the different pile group configurations.
- The results of p-multipliers showed that the battered pile group had the highest p-multipliers followed by the mixed and vertical pile groups, respectively, which indicates a weaker influence from the group effect in the battered and mixed pile groups.
- The piles in the edge columns had a greater contribution (up to 2%) to the lateral resistance than the interior columns, which was consistently observed in the results of shear and axial forces, bending moment, and soil resistance. This translated in 0.2 raise in the p-multipliers for the edge columns over the interior columns.
- The results of FE parametric study showed that the increase in pile spacing resulted in the following:
  - Decreases in the axial reaction in the first and fourth rows only in all pile groups.
  - Negligible influence on the lateral load distribution between the piles.
  - Increase in the pile group efficiency in all pile groups. The largest increase in the group efficiency was observed in the vertical pile group (+38%).
  - Increases in p-multipliers in all piles in the pile groups, in which the p-multipliers increase 0.3-point when the spacing increased from 3D to 5D.
- The FE parametric study using single row/column pile groups showed that the pile row spacing had a greater influence on the p-multipliers than the column spacing. This was concluded after the vanishing of influence from pile column spacing at spacing greater than 5D.
- Studying the effect of clay soil type showed that the p-multipliers are higher in stiffer clays. In the vertical pile group, the p-multipliers increased 0.1-point when the clay soil type was changed from soft to medium and from medium to stiff at pile spacing of 3D and 5D. In the battered and mixed pile groups, a similar increase was noticed at pile spacing 3D only. Changing the clay soil at pile spacing > 5D showed no influence on the p-multipliers in all pile groups.
- Study of the pile group subjected to barge impact showed that the vertical pile group had the lowest lateral stiffness, while the battered and mixed pile groups had similar stiffness.
- The large stiffness of battered and mixed pile groups forced the barge bow to deform significantly, so that the peak impact force magnitude remained fairly constant for all barge speeds.

- The results of shear force showed that the foundation contributed up to 82% of the total lateral force. In the vertical pile group, the force distribution was 76-65% in the foundation and 24-35% in the pier columns. In the battered and mixed pile groups, the force distribution was 82% in the foundation and 18% in the pier columns.
- The distribution of lateral force showed that in the vertical pile group the first row had slightly higher percentage (28%) compared to other rows, which had similar percentage (24-26%). In the battered pile group, the load percentage was evenly distributed between the rows at 25%. A large contrast in the percentage was observed in the mixed pile group. The first and fourth rows had 28% each, while the second and third rows had 22% each.
- The axial reaction results showed that only the first and fourth rows were axially active in the vertical pile group with axial force ratio of 23%. In the battered pile group, all rows were axially active with the second and third rows having 38% higher axial force ratio than the first and fourth rows. In the mixed pile group, all rows had similar axial reaction ratio at 33%.
- The FE analysis was used to develop a model for obtaining three basic elements of the p-y curve for clays: ultimate soil resistance, initial slope, and characteristic shape function. The ultimate soil resistance, p_u is obtained from the bearing capacity factor, N_p as: $p_u = N_p S_u D$. The reference deflection, y_{50} is given as: $y_{50} = 0.5D N_p \varepsilon_{50}$. Having the values of p_u and y_{50}, the p-y curve for clays can be evaluated using the combined power and hyperbolic tangent function given in equation 79.
- The FE analysis was used to develop a model to evaluate the p-y curve for sands. Nonlinear regression analyses were performed to develop relationships to evaluate p_u and y_{ref} in terms of the soil and pile properties as described in equations 86 and 87, respectively. The p-y curve for sands can be evaluated using the combined power and hyperbolic tangent function given in equation 85.
- The results of laboratory UU tests were used to develop correlations to estimate the strain at 50% stress level (ε_{50}) based on soil properties (i.e., S_u, PI, LI). The comparison between the models' values and measurements are somehow reasonable with some scatters, which are comparable with the values recommended by FHWA.
- The results of FE parametric study and the proposed p-y model in equation 85 were used to develop a relationship to estimate the coefficient of subgrade reaction (k) based on soil and pile properties as shown in equation 94. To simplify the estimation of k, the values for different sand consistency, soil condition, and friction angle were presented in a table and a figure. The results of k values are comparable with the values recommended by FHWA.

Recommendations

Based on the findings of this research study, the following recommendations are offered to DOTD engineers:

- It is recommended that the DOTD design engineers start using the developed p-multipliers presented in Tables 13 through 15 and Figures 74 through 78 for the battered, mixed, and vertical pile groups.

- It is recommended that the DOTD design engineers start applying the results presented in Figures 51, 61 and 62 to estimate the contribution of axial force per each pile (F_{axial}/H_{PG}) within the row/column of the pile group for inclusion in pile design.

- It is recommended that the DOTD design engineers start applying the distribution of lateral load per pile presented in Figure 52 for the three PGs to calculate the contribution of lateral load for each pile for use in the lateral analysis and design of piles.

- The DOTD design engineers can use the results presented in Figure 92, Figures 96, Figure 97, Figure 100, Figures 104, and Figure 105 to evaluate the effect of barge speed impact on the piles' peak lateral displacement, the contribution of piles and pier columns to the total resisting force, the piles' peak shear force, the piles' peak axial force, and the axial force ratio per row, respectively.

- The DOTD design engineers can use the results presented in Figures 112, 113, and 114 to evaluate the effect of non-centric barge impact on the peak lateral displacement, peak shear force, and the contribution of piles and pier columns to the resisting force, respectively.

- It is recommended to implement the developed nonlinear hyperbolic tangent function model for p-y curve in clay soil (Equation 79) in a selected pile design software, and start using it to evaluate the lateral behavior of piles driven in clayey soils.

- It is recommended to implement the developed nonlinear hyperbolic tangent tangent/power function model for p-y curve in sandy soil (Equation 85) in a selected pile design software, and start using it to evaluate the lateral behavior of piles driven in sandy soils.

- It is recommended to start using the models presented in Figures 157, 158, 160, 161, and 162 to estimate the strain at 50% stress (ε_{50}), which are based on typical soil properties (i.e., S_u, PI, LI), as an input parameter for different p-y curve models in clays. Compare the results with values recommended by FHWA.

- It is recommended to start using the models presented Table 21 and Figure 163 to estimate the coefficient of subgrade reaction, k, for different sand consistencies and soil conditions for use as an input parameter for use in different p-y curve models in sands.

- It is recommended to study the effect of the sequence of pile installation on the lateral resistance of pile groups for future research work.

- It is recommended to study the effect of pier height on the barge impact force for future research work.

Acronyms, Abbreviations, and Symbols

Term	Description
1-D	One dimensional
2-D	Two dimensional
3-D	Three dimensional
AASHTO	American Association of State Highway and Transportation Officials
AMCC	Anisotropic modified Cam clay
BM	Bending moment
CDP	Concrete damaged plasticity model
cm	centimeter(s)
CPT	Cone penetration test
c(x)	Soil's viscous damping coefficient
D	Pile width
d	Pile diameter
d_c, d_t	Damage variables at compression and tension
D_{el}, D_0^{el}	Damaged and undamaged elastic stiffness
DP	Drucker-Prager
Eff_{PG}	Pile group efficiency
e_o	Void ratio
E_p	Pile modulus of elasticity
$E_{p\text{-}ref}$	Reference value of E_p
E_{py}	Modulus of subgrade reaction
E_s	Soil modulus
E_{st}	Young's modulus for steel
FE	Finite element
FHWA	Federal Highway Administration
ft.	foot (feet)
f_c'	Compressive strength of concrete
f_{ij}	Flexibility factor for displacement at node i
g	Gravity
H_{PG}	Group lateral load
in.	inch(es)
IPI	In-place inclinometer

I_p	Pile stiffness
J_2	Second invariant of the deviatoric stress tensor
K	Coefficient of Lateral Earth Pressure
K_a	Coefficient of lateral earth pressure at rest
K_o	Active coefficient of lateral earth pressure
K_p	Stiffness matrix for the pile
K_s	Stiffness matrix for the soil
K	Coefficient of subgrade reaction
k_h	Lateral subgrade reaction modulus
k(x)	Static soil stiffness
L	Leading row
LL	Liquid limit
LI	Liquidity index
DOTD	Department of Transportation and Development
LTRC	Louisiana Transportation Research Center
LVDT	Linear variable differential transformer
lb.	pound(s)
M	Bending moment
M	meter(s)
M_c, M_e	Slope of critical state line in compression and tension
MCC	Modified Cam-clay
ML	Middle-leading row
MSE	Mean of square errors
MT	Middle-trailing row
N_{60}	Corrected stand penetration count number
NC	Normally consolidated
N_p	Lateral bearing capacity factor
N_{pu}	Upper-bound limits
OCR	Overconsolidation ratio
P	Soil reaction
PI	Plasticity index
$\bar{p}$	Hydrostatic effective stress
P_d, P_s	Dynamic and static soil reactions
PG	Pile group
P_g	Soil resistance for a pile-in-group
P_i	Load on pile i

P_{single}	Soil resistance for an isolated single pile
P_{sj}	Horizontal force at node j
p'_0	Preconsolidation pressure
p_u	Ultimate resistance
Q	External horizontal forces
$\bar{q}$	Deviatoric effective stress
q_c	Cone tip resistance
r	Radial distance
R_j	Ratio between the length of overlapped portion of passive wedge face and total length of the passive wedge face from neighboring pile j
S	Spacing
SC	Clayey sand
SG	Strain gauge
s_{ij}	Deviatoric stress
SL	Stress level
SM	Silty sand
SP	Poorly graded sand
SPT	Standard penetration test
S_u	Undrained shear strength
SW	Well graded sand
T	Trailing row
y	Deflection
u_i	Total displacement of pile i in group
u_o	Unit displacement of single pile
UU	Unconsolidated undrained
V	Shear
W	Load
w	Water content
y_{50}	Pile deflection at 50% of ultimate soil resistance
y_u	Ultimate displacement
Z_c	Critical depth
α, β	Rayleigh damping parameters
ω	Cyclic frequency
α_{ij}	Deviatoric anisotropy tensor
β	Friction angle for the Drucker-Prager model
ε_{50}	Axial strain at 50% of undrained shear strength

Term	Description
ε_t^{ck}	Cracking strain
$\varepsilon_t^{pl}, \varepsilon_c^{pl}$	Plastic strains at tension and compression
ϕ	Soil friction angle
ϕ_{cs}	Critical state friction angle
ϕ_m	Mobilized friction angle
ϕ_p	Peak friction angle
μ	Coefficient of interface friction, or pile adhesion factor
γ_d	Dry unit weight
ν	Poisson's ratio
ψ	Angle of dilation
σ	Cauchy stress
σ_{co}	Initial yield stress
σ_n	Mean stress at the interface
$\hat{\sigma}_{max}$	Maximum principal stress
σ_{vo}	Effective overburden stress
η	Hysteretic damping ratio
τ_{lim}	Maximum shear stress limit
τ_{max}	Ultimate friction stress

References

[1] H. Poulus and E. Davis, Pile foundation analysis and design, New York: Wiley, 1980.

[2] H. Matlock and L. Reese, "Generalized solutions for laterally loaded piles," *Journal of the Soil Mechanics and Foundations Division,* vol. 86, no. 5, p. 63–94, 1960.

[3] L. Reese, W. Cox and F. and Koop, "Field testing and analysis of laterally loaded piles om stiff clay," in *Offshore Technology Conference*, Houston, TX, 1975.

[4] L. Reese and R. Welch, "Lateral loading of deep foundations in stiff clay," *Journal of the Geotechnical Engineering Division,* vol. 101, no. 7, p. 633–649, 1975.

[5] D. Brown, L. Reese and M. O'Neill, "Lateral load behavior of pile group in sand," *Journal of Geotechnical Engineering,* vol. 114, no. 11, p. 1261–1276, 1988.

[6] M. McVay, T. Shang and R. Casper, "Centrifuge testing of fixed-head laterally loaded battered and plumb pile groups in sand," *Geotechnical Testing Journal,* vol. 19, no. 1, pp. 41-50, 1996.

[7] A. Trochanis, J. Bielak and P. Christiano, "Three-dimensional nonlinear study of piles," *Journal of Geotechnical Engineering,* vol. 117, no. 3, p. 429–447, 1991.

[8] M. Ashour, G. Norris and P. Pilling, "Lateral loading of a pile in layered soil using the strain wedge model," *Journal of geotechnical and geoenvironmental engineering,* vol. 124, no. 4, p. 303–315, 1998.

[9] Z. Yang and B. Jeremić, "Numerical analysis of pile behaviour under lateral loads in layered elastic–plastic soils," *International Journal for Numerical and Analytical Methods in Geomechanics,* vol. 26, no. 14, p. 1385–1406, 2002.

[10] M. Hetényi, Beams on elastic foundation: theory with applications in the fields of civil and mechanical engineering, Ann Arbor, MI: University of Michigan Press, 1946.

[11] E. Winkler, Die Lehre von der Elastizität und Festigkeit., Dominicus, Prague, 1867.

[12] L. Palmer and J. Thompson, "The earth pressure and deflection along the embedded lengths of piles subjected to lateral thrust," in *Second International Conference on Soil Mechanics and Foundation Engineering,*, Vol 5, pp156-161., 1948.

[13] K. Terzaghi, " Evalution of conefficients of subgrade reaction," *Géotechnique,* vol. 5, no. 4, p. 297–326, 1955.

[14] H. Gill and K. Demars, "Displacement of laterally loaded structures in nonlinearly responsive soil," Naval Civil Engineering Lab, Port Hueneme, California, 1970.

[15] L. Reese, W. Isenhower and S. Wang, Analysis and design of shallow and deep foundations, Hoboken, New Jersy: John Wiley, 2006.

[16] H. Matlock and E. Ripperger, "Procedures and instumentation for tests on a laterally-loaded pile," in *Eighth Texas Conference on Soil Mechanics and Foundation Engineering*, Austin, TX, 1956.

[17] L. Reese and W. Cox, "Soil behavior from analysis of tests of uninstrumented piles under lateral loading," in *Performance of Deep Foundations, ASTM International,*, West Conshohocken, PA, 1969.

[18] P. Robertson, M. Davies and R. Campanella, "Design of laterally loaded driven piles using the flat dilatometer," *Geotechnical Testing Journal,* vol. 12, no. 1, pp. 30-38, 1989.

[19] P. Robertson, J. Hughes, R. Campanella and A. Sy, "Design of laterally loaded displacement piles using a driven pressuremeter.” Laterally Loaded Deep Foundations: Analysis and Performance, 229-229–10.," in *Laterally Loaded Deep Foundations: Analysis and Performance*, West Conshohocken, PA, 1984.

[20] P. Ruesta and F. Townsend, "Evaluation of laterally loaded pile group at roosevelt bridge," *Journal of Geotechnical and Geoenvironmental Engineering,* vol. 123, no. 12, p. 1153–1161, 1997.

[21] B. McClelland and J. Focht, " Soil modulus for laterally loaded piles," *Journal of the Soil Mechanics and Foundations Division,* vol. 82, no. 4, pp. 1-22, 1956.

[22] H. Matlock, "Correlation for design of laterally loaded piles in soft clay," in *Offshore Technology Conference*, Houston, TX, 1970.

[23] R. Welch and L. Reese, "Lateral load behavior of drilled shafts," Center for Highway Research, The University of Texas at Austin, Austin, Texas, 1972.

[24] L. Reese, W. Cox and F. Koop, "Analysis of laterally loaded piles in sand," in *Offshore Technology Conference*, Houston, TX, 1974.

[25] H. Poulos and E. Davis, "Pile foundation analysis and design," in *Series in geotechnical engineering*, New York, NY, 1980.

[26] K. Sun, "Laterally loaded piles in elastic media," *Journal of Geotechnical Engineering,* vol. 120, no. 8, p. 1324–1344, 1994.

[27] C. Vallabhan and Y. Das, "Modified vlasov model for beams on elastic foundations," *Journal of Geotechnical Engineering,* vol. 117, no. 6, p. 956–966, 1991.

[28] D. Basu, R. Salgado and M. Prezzi, "A continuum-based model for analysis of laterally loaded piles in layered soils," *Géotechnique,* vol. 59, no. 2, p. 127–140, 2009.

[29] W. Guo and F. Lee, " Load transfer approach for laterally loaded piles," *International Journal for Numerical and Analytical Methods in Geomechanics,* vol. 25, no. 11, p. 1101–1129, 2001.

[30] G. Norris, "Theoretically based BEF laterally loaded pile analysis," in *3rd International Conference on Numerical Methods in Offshore Piling, TECHNIP Ed.*, Paris, France, 1986.

[31] M. Ashour, P. Pilling and G. Norris, "Lateral behavior of pile groups in layered soils," *Journal of Geotechnical and Geoenvironmental Engineering,* vol. 130, no. 6, pp. 580-592, 2004.

[32] M. Ashour and G. Norris, "Modeling lateral soil-pile response based on soil-pile interaction," *Journal of Geotechnical and Geoenvironmental Engineering,* vol. 126, no. 5, p. 420–428, 2000.

[33] C. Leung and Y. Chow, "Response of pile groups subjected to lateral loads," *International journal for numerical and analytical methods in geomechanics,* vol. 11, no. 3, p. 307–314, 1987.

[34] D. Brown, L. Reese and M. O'Neill, "Cyclic lateral loading of a large-scale pile group," *Journal of Geotechnical Engineering,* vol. 113, no. 11, p. 1326–1343, 1987.

[35] M. McVay, L. Zhang, T. Molnit and P. Lai, "Centrifuge testing of large laterally loaded pile groups in sands," *Journal of Geotechnical and Geoenvironmental Engineering,* vol. 124, no. 10, p. 1016–1026, 1988.

[36] S. Rao, V. Ramakrishna and G. Raju, "Influence of rigidity on laBehavior of pile-supported dolphins in marine clay under lateral loading," *Journal of Geotechnical and Geoenvironmental Engineering,* vol. 122, no. 8, pp. 607-612, 1996.

[37] N. Patra and P. Pise, "Ultimate lateral resistance of pile groups in sand," *Journal of Geotechnical and Geoenvironmental Engineering,* vol. 127, no. 6, p. 481–487, 2001.

[38] K. Rollins, T. Gerber, J. Lane and S. Ashford, "Lateral resistance of a full-scale pile group in liquefied sand," *Journal of Geotechnical and Geoenvironmental Engineering,* vol. 131, no. 1, p. 115–125, 2005.

[39] M. Ashour and H. Ardalan, "Employment of the p-multiplier in pile-group analysis," *Journal of Bridge Engineering,* vol. 16, no. 5, p. 612–623, 2011.

[40] M. McVay, R. Casper and T. Shang, "Lateral response of three-row groups in loose to dense sands at 3D and 5D pile spacing," *Journal of Geotechnical Engineering,* vol. 121, no. 5, p. 436–441, 1995.

[41] K. Rollins, R. Olsen, J. Egbert, K. Olsen, D. Jensen and B. Garrett, "Response, analysis, and design of pile groups subjected to static and dynamic lateral loads," Utah Department of Transportation Research Division, Salt Lake city, UT, 2003.

[42] T. Ilyas, C. Leung, Y. Chow and S. Budi, "Centrifuge model study of laterally loaded pile groups in clay," *Journal of Geotechnical and Geoenvironmental Engineering,* vol. 130, no. 3, p. 274–283, 2004.

[43] S. Chandrasekaran, A. Boominathan and G. Dodagoudar, "Group interaction effects on laterally loaded piles in clay," *Journal of geotechnical and geoenvironmental engineering,* vol. 136, no. 4, p. 573–582, 2009.

[44] AASHTO, "AASHTO LRFD Bridge Design Specifications.," American Association of State Highway and Transportation Officials, Washington, D.C., 2012.

[45] S. Rao, V. Ramakrishna and M. Rao, "Influence of rigidity on laterally loaded pile groups in marine clay," *Journal of Geotechnical and Geoenvironmental Engineering,* vol. 124, no. 6, p. 542–549, 1998.

[46] K. Rollins, K. Peterson and T. Weaver, "Lateral load behavior of full-scale pile group in clay," *Journal of Geotechnical and Geoenvironmental Engineering,* vol. 124, no. 6, p. 468–478, 1988.

[47] D. Brown, L. Reese and M. O'Neill, "Lateral load behavior of pile group in sand," *Journal of Geotechnical Engineering,* vol. 114, no. 11, p. 1261–1276, 1988.

[48] M. Novak, "Dynamic stiffness and damping of piles," *Canadian Geotechnical Journal,* vol. 11, no. 4, p. 574–598, 1974.

[49] T. Nogami and M. Novak, "Resistance of soil to a horizontally vibrating pile," *Earthquake Engineering & Structural Dynamics,* vol. 5, no. 3, p. 249–261, 1977.

[50] G. Gazetas and R. Dobry, "Horizontal response of piles in layered soils," *Journal of Geotechnical Engineering,* vol. 110, no. 1, pp. 20-40, 1984.

[51] T. Nogami and K. Konagai, "Time domain flexural response of dynamically loaded single piles," *Journal of Engineering Mechanics,* vol. 114, no. 9, p. 1512–1525, 1988.

[52] T. Nogami, J. Otani, K. Konagai and H. Chen, "Nonlinear soil-pile interaction model for dynamic lateral motion," *Journal of Geotechnical Engineering,* vol. 118, no. 1, p. 89–106, 1992.

[53] M. El Naggar and M. Novak, "Nonlinear analysis for dynamic lateral pile response," *Soil Dynamics and Earthquake Engineering,* vol. 15, no. 4, p. 233–244, 1996.

[54] M. a. S. B. Novak, "Approximate Approach to Contact Effects of Piles," in *Proceedings of Session on Dynamic Response of Pile Foundations: Analytical Aspects*, Florida, 1980.

[55] M. El Naggar and K. Bentley, "Dynamic analysis for laterally loaded piles and dynamic p-y curves," *Canadian Geotechnical Journal,* vol. 37, no. 6, p. 1166–1183, 2000.

[56] A. Kaynia and E. Kausel, "Dynamics of piles and pile groups in layered soil media," *Soil Dynamics and Earthquake Engineering,* vol. 10, no. 8, p. 386–401, 1991.

[57] R. Dobry and G. Gazetas, "Simple method for dynamic stiffness and damping of floating pile groups," *Geotechnique,* vol. 38, no. 4, p. 557–574, 1988.

[58] G. Gazetas, K. Fan, A. Kaynia and E. Kausel, "Dynamic interaction factors for floating pile groups," *Journal of Geotechnical Engineering,* vol. 117, no. 10, p. 1531–1548, 1991.

[59] N. Makris and G. Gazetas, "Dynamic pile-soil-pile interaction. part ii: lateral and seismic response," *Earthquake Engineering & Structural Dynamics,* vol. 21, no. 2, p. 145–162, 1992.

[60] G. Mylonakis and G. Gazetas, "Lateral vibration and internal forces of grouped piles in layered soil," *Journal of Geotechnical and Geoenvironmental Engineering,* vol. 125, no. 1, p. 16–25, 1999.

[61] Y. Mostafa and M. El Naggar, "Dynamic analysis of laterally loaded pile groups in sand and clay," *Canadian Geotechnical Journal,* vol. 39, no. 6, p. 1358–1383, 2002.

[62] J. Murchison and M. and O'Neill, "Evaluation of py relationships in cohesionless soils," in *Analysis and design of pile foundations*, 1984.

[63] A. Vesic, "Bending of beams resting on isotropic elastic solid," *Journal of the Engineering Mechanics Division,* vol. 87, no. 2, pp. 35-54, 1961.

[64] API, "2A-WSD, Planning, Designing and Constructing Fixed Offshore Platforms-Working Stress Design, 2014.," 2014.

[65] B. Kim, N. Kim, W. Lee and Y. Kim, "Experimental load–transfer curves of laterally loaded piles in Nak-Dong River sand," *Journal of Geotechnical and Geoenvironmental Engineering,* vol. 130, no. 4, pp. 416-425, 2004.

[66] M. Georgiadis, C. Anagnostopoulos and S. Saflekou, "Centrifugal testing of laterally loaded piles in sand," *Canadian Geotechnical Journal,* vol. 29, no. 2, pp. 208-216, 1992.

[67] S. Rajashree and T. Sitharam, "Nonlinear finite-element modeling of batter piles under lateral load," *Journal of Geotechnical and Geoenvironmental Engineering,* vol. 127, no. 7, pp. 604-612, 2001.

[68] K. Georgiadis and M. Georgiadis, "Undrained lateral pile response in sloping ground," *Journal of Geotechnical and Geoenvironmental Engineering,* vol. 136, no. 11, pp. 1489-1500, 2010.

[69] R. Klinkvort and O. Hededal, "Effect of load eccentricity and stress level on monopile support for offshore wind turbines," *Canadian Geotechnical Journal,* vol. 51, no. 9, pp. 966-974, 2014.

[70] H. Li, L. Tong, S. Liu, H. Liu and M. Zhang, "Construction and verification of a unified p–y curve for laterally loaded piles," *Bulletin of Engineering Geology and the Environment,* vol. 77, no. 3, pp. 987-997, 2018.

[71] S. Sørensen, L. Ibsen and A. Augustesen, "Effects of diameter on initial stiffness of py curves for large-diameter piles in sand," in *Numerical Methods in Geotechnical Engineering*, CRC Press., 2010, pp. 923-928.

[72] D. Kallehave, B. Byrne, C. Thilsted and K. Mikkelsen, "Optimization of monopiles for offshore wind turbines," *Philosophical Transactions of The Royal Society A Mathematical Physical and Engineering Sciences,* vol. 373, no. 2035, 2015.

[73] W. Sullivan, Development and evaluation of a unified method for the analysis of laterally loaded piles in clay, Houston: University of Texas, 1977.

[74] T. Dunnavant and M. O'Neill, "Experimental p-y model for submerged, stiff clay," *Journal of Geotechnical Engineering,* vol. 115, no. 1, pp. 95-114, 1989.

[75] D. Wu, B. Broms and V. Choa, "Design of laterally loaded piles in cohesive soils using py curves," *Soils and foundations,* vol. 38, no. 2, pp. 17-26, 1998.

[76] J. Stevens and J. Audibert, "Re-examination of py curve formulations," in *Offshore technology conference*, 1979.

[77] A. Skempton, "The bearing capacity of clay," in *Proc. of Building Research Congress*, ICE, 1951.

[78] P. Hannigan, F. Rausche, G. R. B. Likins and M. Becker, "Design and Construction of Driven Pile Foundations - Volume 1, Report No. FHWA-NHI-16-009," National Highway Institute, U.S. Department of Transportation, Federal Highway Administration, Washington, D.C., 2016.

[79] ASTM, A416/A416M-12a. Specification for steel strand, uncoated seven-wire for prestressed concrete, ASTM International, 2012.

[80] Abaqus, "Abaqus Documentation," Dassault Systèmes, Providence, RI., 2011.

[81] J. Mander, M. Priestley and R. Park, "Theoretical stress-strain model for confined concrete," *Journal of Structural Engineering,* vol. 114, no. 8, p. 1804–1826, 1988.

[82] T. Jankowiak and T. Lodygowski, "Identification of parameters of concrete damage plasticity constitutive model," *Foundations of civil and environmental engineering,* vol. 6, no. 1, p. 53–69, 2005.

[83] H. Pam and R. Park, "Flexural strength and ductility analysis of spirally reinforced prestressed concrete piles," *PCI Journal,* vol. 35, no. 4, p. 54–83, 1990.

[84] J. Lubliner, J. Oliver, S. Oller and E. Oñate, "A plastic-damage model for concrete," *International Journal of Solids and Structures,* vol. 25, no. 3, p. 299–326, 1989.

[85] J. Lee and G. Fenves, "Plastic-damage model for cyclic loading of concrete structures," *Journal of Engineering Mechanics,* vol. 124, no. 8, p. 892–900, 1998.

[86] W. Chen and D. Han, Plasticity for Structural Engineers, J. Ross Publishing, 2007.

[87] L. Zdravković, D. Potts and D. Hight, "The effect of strength anisotropy on the behaviour of embankments on soft ground," *Géotechnique,* vol. 52, no. 6, p. 447–457, 2002.

[88] K. Roscoe and J. Burland, "On the generalized stress-strain behaviour of 'wet' clay," in *Engineering Plasticity*, Cambridge, UK, 1968.

[89] M. Abu-Farsakh, F. Rosti and A. Souri, "Evaluating pile installation and subsequent thixotropic and consolidation effects on setup by numerical simulation for full-scale pile load tests," *Canadian Geotechnical Journal,* vol. 52, no. 11, p. 1734–1746, 215.

[90] Y. Dafalias, M. Manzari and A. Papadimitriou, "SANICLAY: simple anisotropic clay plasticity model," *International Journal for Numerical and Analytical Methods in Geomechanics,* vol. 30, no. 12, p. 1231–1257, 2006.

[91] J. Argyris, G. Faust, J. Szimmat, E. Warnke and K. Willam, "Special issue: papers presented at the conference recent developments in the finite element analysis of

prestressed concrete reactor vessels," *Nuclear Engineering and Design,* vol. 28, no. 1, 1974.

[92] G. Consolazio, R. Cook, M. McVay, D. Cowan, A. Biggs and L. Bui, "Barge Impact Testing of the St. George Island Causeway Bridge, Phase III: Physical Testing and Data Interpretation," University of Florida, Gainesville, 2006.

[93] O. Larsen, "Ship collision with bridges: the interaction between vessel traffic and bridge structures. International Association for Bridge and Structural Engineering," International Association for Bridge and Structural Engineering, Zürich, Switzerland, 1993.

[94] G. Consolazio and D. Cowan, "Nonlinear analysis of barge crush behavior and its relationship to impact resistant bridge design," *Computers & Structures, K.J Bathe 60th Anniversary Issue,* vol. 81, no. 8-11, p. 547–557, 2003.

[95] P. Yuan and I. Harik, "Equivalent barge and flotilla impact forces on bridge piers," *Journal of Bridge Engineering,* vol. 15, no. 5, p. 523–532, 2010.

[96] Y. Sha and H. Hao, "Nonlinear finite element analysis of barge collision with a single bridge pier," *Engineering Structures,* vol. 41, p. 63–76, 2012.

[97] G. Kantrales, G. Consolazio, D. Wagner and S. Fallaha, "Experimental and analytical study of high-level barge deformation for barge–bridge collision design," *Journal of Bridge Engineering,* vol. 21, no. 2, 2016.

[98] J. Zhang, X. Chen, D. Liu and X. Li, "Analysis of bridge response to barge collision: refined impact force models and some new insights," *Advances in Structural Engineering,* vol. 19, no. 8, p. 1224–1244, 2016.

[99] G. Consolazio, M. Davidson and D. Cowan, "Barge Bow Force-Deformation Relationships for Barge-Bridge Collision Analysis," *Transportation Research Record,* vol. 2131, no. 3-14, pp. 1-12, 2009.

[100] B. Hardin and V. Drnevich, "Shear modulus and damping in soils: design equations and curves," *Journal of the Soil Mechanics and Foundations Division,* vol. 98, no. SM7, p. 667–692, 1972.

[101] M. Liu and D. Gorman, "Formulation of Rayleigh damping and its extensions," *Computers & Structures,* vol. 57, no. 2, p. 277–285, 1995.

[102] A. Zerwer, G. Cascante and J. Hutchinson, "Parameter estimation in finite element simulations of rayleigh waves," *Journal of Geotechnical and Geoenvironmental Engineering,* vol. 128, no. 3, p. 250–261, 2002.

[103] D. Winter, Biomechanics and motor control of human movement, Hoboken, New Jersey: John Wiley & Sons, Inc., 2009.

[104] K. Jackson, "Fitting of Mathematical Functions to Biomechanical Data," *IEEE Transactions on Biomedical Engineering,* vol. 26, no. 2, p. 122–124, 1979.

[105] M. Abu-Farsakh, S. Yoon, D. Ha, W. Marr, Z. Zhang and X. Yu, "Development of a substructure instrumentation system at the new I-10 twin span bridge and its use to investigate the lateral behavior of batter piles," *Geotechnical Testing Journal,* vol. 34, no. 4, pp. 332-343, 2011.

[106] P. Robertson and K. and Cabal, Guide to cone penetration testing for geotechnical engineering., Signal Hill, CA: Gregg Drilling & Testing, Inc., 2015.

[107] M. McVay, L. Zhang, T. Molnit and P. Lai, "Centrifuge testing of large laterally loaded pile groups in sands," *Journal of Geotechnical and Geoenvironmental Engineering,* vol. 124, no. 10, p. 1016–1026, 1998.

[108] D. Nip and C. Ng, "Back-analysis of laterally loaded bored piles," in *Proceedings of the Institution of Civil Engineers - Geotechnical engineering*, UK, 2005.

[109] M. Abu-Farsakh, X. Yu, B. Pathak, K. Alshibli and Z. Zhang, "Field testing and analyses of a batter pile group foundation under lateral loading," *Journal of the Transportation Research Board,* vol. 2212, no. 1, p. 42–55, 2011.

[110] A. Souri, M. Abu-Farsakh and G. Voyiadjis, "Study of static lateral behavior of battered pile group foundation at I-10 Twin Span Bridge using three-dimensional finite element modeling," *Canadian Geotechnical Journal,* vol. 53, no. 6, p. 962–973, 2015.

[111] B. Das, Geotechnical engineering handbook, Ft. Lauderdale, FL: J. Ross Pub, 2011.

[112] R. Day, Geotechnical engineer's portable handbook, New York, NY: McGraw-Hill Professional, 2012.

[113] K. Rollins, K. J. Olsen, D., B. Garrett, R. Olsen and J. Egbert, "Pile spacing effects on lateral pile group behavior: analysis," *Journal of Geotechnical and Geoenvironmental Engineering,* vol. 132, no. 10, p. 1272–1283, 2006.

[114] M. Randolph and G. Houlsby, "The limiting pressure on a circular pile loaded laterally in cohesive soil," *Géotechnique,* vol. 34, no. 4, pp. 613-623, 1984.

[115] C. Martin and M. Randolph, "Upper-bound analysis of lateral pile capacity in cohesive soil," *Géotechnique,* vol. 56, no. 2, pp. 141-145, 2006.

[116] A. Haiderali and G. Madabhushi, "Evaluation of curve fitting techniques in deriving p–y curves for laterally loaded piles," *Geotechnical and Geological Engineering,* vol. 34, no. 5, pp. 1453-1473, 2016.

[117] W. Sullivan, L. Reese and C. Fenske, "Unified method for analysis of laterally loaded piles in clay," in *In Numerical methods in offshore piling*, Thomas Telford Publishing, 1980, pp. 135-146.

[118] J. Murff and J. Hamilton, "P-ultimate for undrained analysis of laterally loaded piles," *Journal of Geotechnical Engineering,* vol. 119, no. 1, pp. 91-107, 1993.

[119] J. Yu, M. Huang and C. Zhang, "Three-dimensional upper-bound analysis for ultimate bearing capacity of laterally loaded rigid pile in undrained clay," *Canadian Geotechnical Journal,* vol. 52, no. 11, pp. 1775-1790, 2015.

[120] A. C. Institute, "Building Code Requirements for Structural Concrete (ACI 318-08) and Commentary.," ACI, 2008.

[121] R. Peck, W. Hanson and T. Thornburn, Foundation engineering (Vol. 10), New York: John Wiley , 1974.

[122] M. Georgiadis, "Development of py curves for layered soils," in *Geotechnical practice in offshore engineering*, Austin, Texas, 1983.

[123] J. Schmertmann, "Guidlines for Cone Penetration Test: Perdormance and Design, Report FHWA-TS-78-209," Federal Highway Administration, Washington, D.C., 1978.

[124] D. Coduto, Foundation Design, Principles and Practices, 2nd Edition, Upper Saddle River, New Jersey: Prentice-Hall, Inc., 2001.

This public document is published at a total cost of $200.
29 copies of this public document were published in this first printing at a cost of $200. The total cost of all printings of this document including reprints is $200. This document was published by Louisiana Transportation Research Center to report and publish research findings as required in R.S. 48:105. This material was duplicated in accordance with standards for printing by state agencies established pursuant to R.S. 43:31. Printing of this material was purchased in accordance with the provisions of Title 43 of the Louisiana Revised Statutes.